# Uniform, 1-Dimensional Polymer Nanofibers for Applications in Nanomedicine

by

**Hayley C. Parkin**

BSc. (Hons.), University of Victoria, 2020

A Dissertation Submitted for Fulfillment of the Requirements for the Degree of

DOCTOR of PHILOSOPHY

in the

DEPARTMENT of CHEMISTRY

UNIVERSITY OF VICTORIA

# Uniform, 1-Dimensional Polymer Nanofibers for Applications in Nanomedicine

by

**Hayley C. Parkin**

BSc. (Hons.), University of Victoria, 2020

**Supervisory Committee**
Prof. Ian Manners (Supervisor)
Department of Chemistry

Prof. Cornelia Bohne (Acting Supervisor)
Department of Chemistry

Prof. Jeremy Wulff (Departmental Member)
Department of Chemistry

Prof. Stephanie M. Willerth (Outside Member)
Department of Biomedical Engineering

# Abstract

Polymer nanomaterials have garnered increased attention over the past several decades due to their ability to perform in a variety of applications, depending on the chemical functionality of the material used. Of note, polymers have been used increasingly for biomedical applications, from drug and gene delivery vehicles, to contrast agents and therapeutics themselves. Living crystallization-driven self-assembly (CDSA) provides a novel pathway for the preparation of morphologically pure, length-controlled, 1-dimensional (1D) polymer nanofibers. In this thesis, the applications of these nanofibers for applications in nanomedicine is explored.

Chapter 1 provides an introduction into polymer self-assembly, living CDSA, and a brief literature review of nanoparticles explored for biomedical applications. Chapter 2 describes the synthesis and self-assembly of biodegradable and cationic poly(fluorenetrimethylenecarbonate)-*block*-poly(dimethylaminoethylmethacrylate) (PFTMC-*b*-PDMAEMA) 1D nanofibers, and evaluates the length and shape dependence on antibacterial activity against *Escherichia coli.* A comparison to neutral 1D poly(ethylene glycol) nanofibers is made. Chapter 3 then investigates the antibacterial mechanism of action of 1D nanofibers relative to nanospheres of identical composition. This pathway is explored through the use of confocal laser scanning electron microscopy and flow cytometry, as well as transmission electron microscopy and scanning electron microscopy. Chapter 4 expands upon preliminary drug-loading results to explore the addition of the anticancer therapeutic paclitaxel to the core-corona interface of PFTMC-*b*-PDMAEMA seed nanofibers. These are then evaluated as a delivery vehicle in 2D and 3D cell models containing glioblastoma cells. Chapter 5 then extends the scope of antibacterial activity of 1D PFTMC-*b*-PDMAEMA nanofibers against gram-positive *Staphylococcus epidermidis*, as well

as explores the ability of these nanofibers for treating the extremely drug-resistant organism *Burkholderia vietnamiensis*. Chapter 6 concludes this thesis with an outlook as well as proposes future directions that could expand on the projects presented herein.

# Table of Contents

# List of Figures

# List of Schemes

# List of Tables

# List of Abbreviations

| | |
|---|---|
| °C | Degrees celsius |
| 1D | One-dimensional |
| $^{1}$H NMR | Proton nuclear magnetic resonance |
| 2D | Two-dimensional |
| 3D | Three-dimensional |
| *a* | Solvophilic head group area |
| Å | Angstrom |
| ABX | Abraxane |
| AFM | Atomic force microscopy |
| AMP | Antimicrobial peptide |
| -*b*- | Block |
| BCP | Block copolymer |
| BD | BODIPY$^{630/650\text{-}X}$ |
| *B. vietnamiensis* | *Burkholderia vietnamiensis* |
| ca. | Circa |
| CDSA | Crystallization-driven self-assembly |
| CFDA-SE | Carboxyfluorescein diacetate succinimidyl ester |
| CI | Confidence interval |
| CLSM | Confocal laser scanning microscopy |
| CTA | Chain transfer agent |
| $Đ$ | Dispersity |
| $Đ_M$ | Dispersity (mass) |
| $Đ_L$ | Dispersity (length) |
| $Đ_W$ | Dispersity (width) |
| $d_{core}$ | Core diameter |
| DAPI | 4′,6-Diamidino-2-phenylindole |
| DBU | 1,8-Diazabicyclo[5.4.0]undec-7-ene |
| DCM | Dichloromethane |
| DLS | Dynamic light scattering |

| | |
|---|---|
| DMEM/F-12 | Dulbecco's Modified Eagle Medium/Nutrient Mixture F-12 |
| DMSO | Dimethyl sulfoxide |
| DNA | Deoxyribonucleic acid |
| $DP_n$ | Number average degree of polymerization |
| $EC_{50}$ | Half maximal effective concentration |
| *E. coli* | *Escherichia coli* |
| e.g. | *Exempli gratia*: for example |
| EtOH | Ethanol |
| Eq. | Equation |
| FTMC | Fluorenetrimethylenecarbonate |
| g | Gram |
| GBM | Glioblastoma |
| GPC | Gel permeation chromatography |
| H | Hydrophobic |
| h | Hour |
| HEPES | 2-(4-(2-hydroxyethyl)piperazin-1-yl)ethanesulfonic acid |
| $IC_{50}$ | Half maximal inhibitory concentration |
| i.e., | *Id est*: that is |
| iPrOH | Isopropanol |
| l | Solvophobic tail length |
| LB | Lysogeny broth |
| LCST | Lower critical solution temperature |
| $L_i$ | Individual contour lengths |
| $L_n$ | Number average length |
| $L_w$ | Weight average length |
| -m- | Nanofiber or micelle segment |
| m | Meter |
| m/z | Mass over charge |

| | |
|---|---|
| MALDI-TOF MS | Matrix-assisted laser desorption ionization time of flight mass spectrometry |
| MBC | Minimum bactericidal concentration |
| MeOH | Methanol |
| mg | Milligram |
| MG | Malignant glioma |
| MIC | Minimum inhibitory concentration |
| min | Minute |
| mL | Milliliter |
| mmol | Millimole |
| $M_n$ | Number average molar mass |
| mol | Mole |
| mol% | Mole percentage |
| mRNA | Messenger RNA |
| $m_{unimer}/m_{seed}$ | Unimer-to-seed mass ratio |
| mv | Millivolts |
| $M_w$ | Weight average molecular weight |
| nm | Nanometer |
| $OD_{600}$ | Absorbance at 600 nm |
| P | Polar |
| PBMA | Poly(butyl methacrylate) |
| PCL | Poly(ε-caprolactone) |
| PDMAEMA | Poly(dimethylaminoethyl methacrylate) |
| PEG | Poly(ethylene glycol) |
| PEO | Poly(ethylene oxide) |
| PFS | Polyferrocenyldimethylsilane |
| PFr | Poly(fructose) |
| PFTMC | Poly(fluorenetrimethylenecarbonate) |
| PHPMA | Poly(*N*-2-hydroxypropyl methacrylamide) |

| | |
|---|---|
| PLLA | Poly(L-lactide) |
| PNIPAM | Poly(N-isopropylacrylamide) |
| PNSL | Preformed nanoparticle solvent-switch |
| ppm | Parts per million |
| PS | Poly(styrene) |
| PTX | Paclitaxel |
| RAFT | Reversible addition-fragmentation chain-transfer |
| Ref | Reference |
| RI | Refractive index |
| $R_h$ | Hydrodynamic radius |
| RNA | Ribonucleic acid |
| ROP | Ring-opening polymerization |
| s | Second |
| *S. epi* | *Staphylococcus epidermidis* |
| siRNA | Small interfering RNA |
| SEM | Scanning electron microscopy |
| TEM | Transmission electron microscopy |
| THF | Tetrahydrofuran |
| TMS | Trimethylsilane |
| UV | Ultraviolet |
| UV-Vis | Ultraviolet-visible |
| $v$ | Solvophobic tail volume |
| $v/v$ | Volume by volume |
| $W_n$ | Width-average length |
| wt % | Weight percentage |
| δ | Chemical shift |
| λ | Wavelength |
| $\lambda_{abs}$ | Absorption wavelength |
| $\lambda_{em}$ | Emission wavelength |
| $\lambda_{ex}$ | Excitation wavelength |

| | |
|---|---|
| μm | Micrometer |
| σ | Standard deviation |
| χ | Flory-Huggins parameter |

# Acknowledgements

I'd like to begin by expressing my sincerest gratitude to my supervisor, Prof. Ian Manners, for his mentorship over the past four years. To say he has made an impact on my life is an understatement. Having someone to look up to that was so incredibly passionate and understanding, was truly inspirational. His encouragement and direction improved my confidence and I have accomplished things that would not have been possible without him. I'd also like to thank Deborah O'Hanlon-Manners for all the help she has offered throughout my time at UVic. The group would not run without her.

Next, I thank my committee members, Prof. Cornelia Bohne, Prof. Jeremy Wulff, Prof. Stephanie Willerth and Prof. Hanadi Sleiman, as well as Manners group alumni Prof. Ali Nazemi and Prof. Zachary Hudson, for their support especially towards the end of this degree. I'd also like to thank everyone from the Manners group past and present. Dr. Steven Street and Dr. Diego Garcia-Hernandez were instrumental in my training and welcoming into the group. I'd like to thank those I've worked with in both Elliott and Bob Wright: Hannah, Harvey, Marcus, Ayesha, Hill, Charlotte, Lei, Jiandong, Chen, Chuanqi, Liam, Matt, Mitch, Harrison, and Etienne. I also had the pleasure of working with Lennard Shopperly, without whom Chapter 4 would not be possible.

I need to thank my best friend, Margarita, who I have been laughing with for as long as I can remember, and who has made the good times great and the bad times better. Anamika, Dani, and Paige, you three are the absolute loves of my life. Big thanks to Audrey for always checking in, arranging to meet up, and never forgetting to bring sunscreen. Thank you to the Buckley lab group chat for the numerous coffees, superfluxes, and dance parties. And finally to Chris, for getting me through the sleepless nights.

I'd like to thank my family for their unwavering support. These four years have been extremely difficult, but their love has eased some of the hardship. To my mom, the strongest lady I know and who has given everything for us. To my dad, who always knows the right advice to give, and also what movies to watch. To my sisters, Chloe and Tessa, who I can always count on. And to my favourite nieces Lucy and Poppy, I'm so happy to be Auntie H.

Finally, to my Granny who never failed to encourage me, and to my Auntie Deedee who was the brightest light. I know you are both somewhere in the universe, cheering me on. I hope I am making you proud.

# Dedication

*I dedicate this thesis to everyone that I have lost.*

# Chapter 1

# Introduction

## 1.1 Self-assembly in nature and synthetic approaches

### 1.1.1 Natural self-assembly and templated synthesis

Self-assembly is the spontaneous and reversible organization of smaller subunits through non-covalent interactions without intervention from external forces.[1] It underpins most of the complex systems in everyday life, from cellular organisms, our bones, the complex universe, to musical compositions.[2] While great strides have been made in small molecule synthesis, many challenges remain. Notably, synthetic access to complex structures on the order of 10 nm – 100 μm remains elusive; in contrast, these structures are ubiquitous in nature.

In what appears to be great ease, deoxyribonucleic acid (DNA) strands are precisely synthesized in a well-defined fashion, assembled into higher order structures, coiled into chromosomes, and then routinely unwound, copied, and wound again.[3–6] What is a simple task for every single mammalian cell remains elusive to synthetic chemists. Furthermore, where we have failed to achieve such controlled hierarchical self-assembly, viruses have excelled.[7] The assembly of the tobacco mosaic virus results in an ordered array of proteins with a pore perfectly sized to contain a strand of ribonucleic acid (RNA), with each virus measuring 300 nm in length (Figure 1.1A).[7,8] Biological assemblies do not stop there, with human bones containing at least 7 orders of hierarchical structure which is essential for their development, growth, and regeneration.[9,10]

Likewise, muscles contain several components which work together to slide along each other to cause contraction or relaxation (Figure 1.1B).[11] This is possible through the cooperation of adenosine triphosphate, actin, and myosin to create movement through the release of energy.[12]

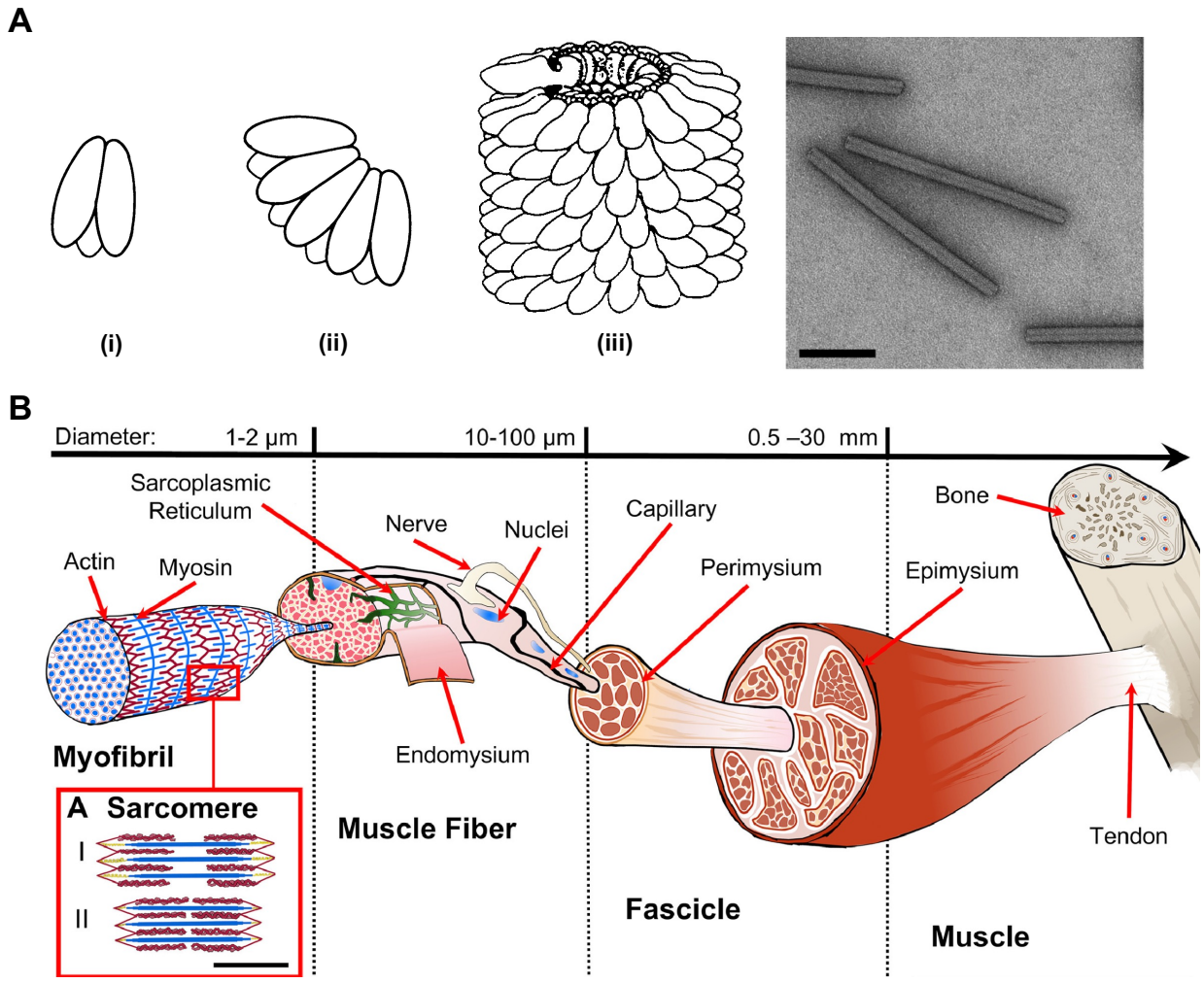


**Figure 1.1.** Examples of self-assembled complex systems in natural biological environments. (A) The self-assembly of the tobacco mosaic virus to demonstrate that (i) small nuclei form first which together create larger building blocks (ii), which assemble into the final spiral form (iii) as demonstrated in the transmission electron microscopy micrograph on the right-hand side. Scale bar = 100 nm. Reproduced with permission from the American Society for Microbiology, *Bacteriol. Rev*. **1969**, *33* (2), 302 – 309. (B) Hierarchical self-assembly of multiple individual

components which ultimately form muscle tissue. Reproduced with permission from Elsevier, *Appl. Mater. Today* **2020**, *20*, 10077.

The defining trait of these complex assemblies is the presence of emergent properties.[13,14] Each individual component of the described systems does not sum to the total properties that are revealed upon their coalescence. The cooperation of the individual parts leads to hierarchical function that allows for life on Earth to exist. Therefore, if we can access such assemblies through synthetic approaches, an array of new materials with an untold number of applications becomes possible.

### 1.1.2 Synthetic approaches to self-assembled systems

Two categories of self-assembled systems exist, those at equilibrium, or those out of equilibrium (Figure 1.2A).[15–17] Equilibrium assemblies are said to be static, as no energy is dissipated to maintain their state (Figure 1.2B).[15] While the term static is slightly misleading, as local dynamic processes are occurring to maintain the overall state, no macroscopic changes are observable. Out of equilibrium assemblies either expend energy in order to maintain homeostasis, or are kinetically trapped, and are considered to be dynamic, and static processes respectively (Figure 1.2B).[16,17] The more elaborate morphologies previously discussed are normally not at equilibrium, and this allows for the generation of structures with higher-order properties. The question to then ask, is how can these complex systems be fabricated.

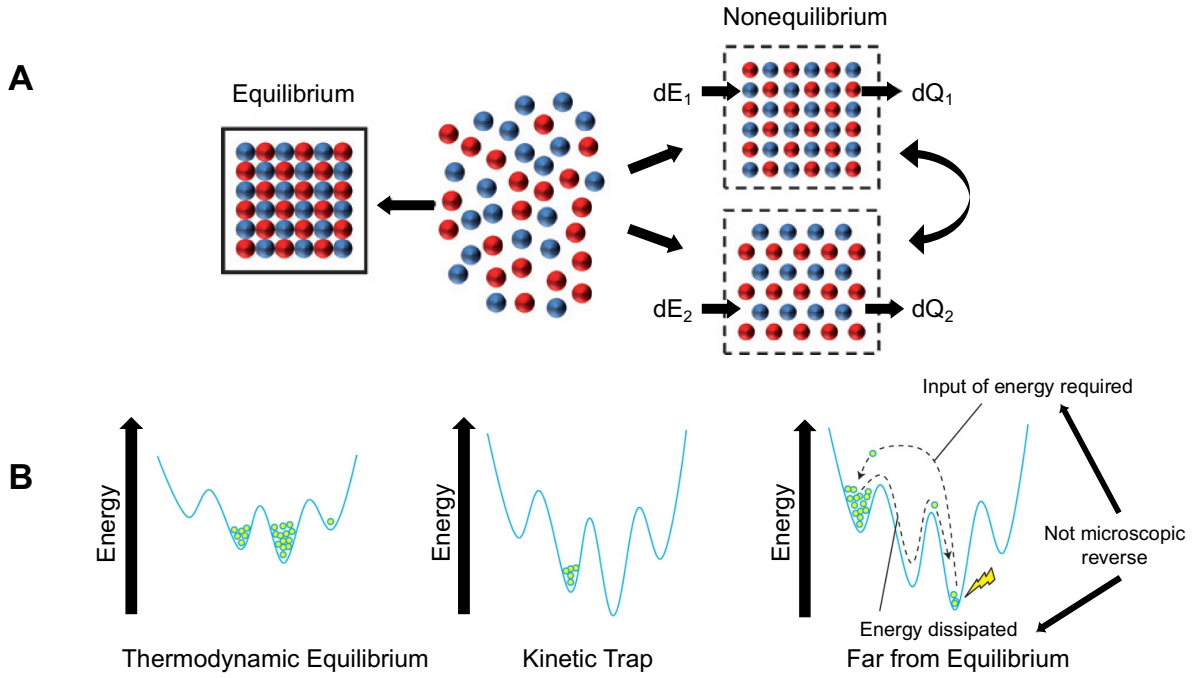


**Figure 1.2.** Schematics to demonstrate the differing types of self-assembled systems, including equilibrium and non-equilibrium assemblies. (A) From a disordered state in the center of the figure, either an equilibrium assembly can form (left) which does not require an input of energy to maintain homeostasis, or non-equilibrium assemblies are generated where exchange occurs, and energy is dissipated to maintain the system (right). Reproduced with permission from the Royal Society of Chemistry, *Soft Matter* **2009**, *5* (6), 1110–1128. (B) Energy landscapes showcasing thermodynamic equilibrium, kinetically trapped assemblies, or far-from-equilibrium assemblies. Block copolymer self-assembly generally falls into kinetically trapped structures, whereas small molecule self-assembly is generally equilibrium self-assembly, where monomer exchange occurs, and a thermodynamically favoured product is obtained. Reproduced with permission from Springer Nature BV, *Nat. Nanotechnol*. **2015**, *10* (2), 111–119.

Top-down approaches begin with a larger material and trimming, etching, shaping, or molding it to the desired final structure.[18–20] On the macroscale, this could be represented by

carving a statue from a piece of marble. Such techniques on the nanoscale include lithography, where etching is performed on a surface to create a smaller patterned array (Figure 1.3A).[21] The limit of this technique is the size in which the pattern can be made, which depends on the use of smaller and smaller wavelengths of photons, or electrons being employable.[21] Another technique which has been developed for top-down self-assembly is thin-film stretching.[22] Polymers are suspended in aqueous media and applied to a stretchable material. Upon evaporation of the solvent, the film is stretched to yield various morphologies, in particular anisotropic shapes. (Figure 1.3B).[22]

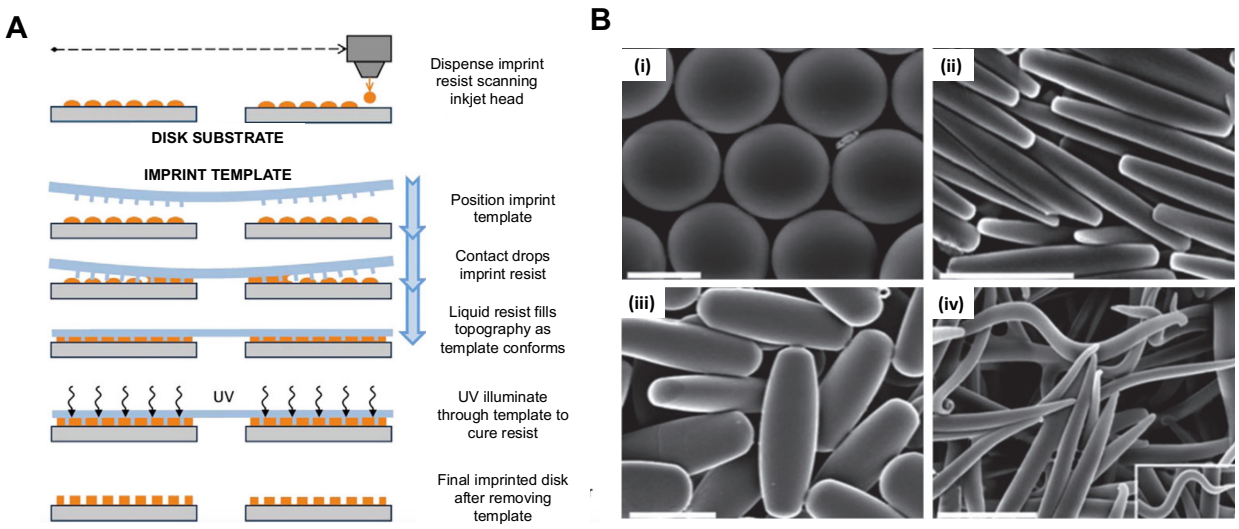


**Figure 1.3.** Top-down methods commonly employed for the generation of morphologically controlled nanoparticles. (A) Lithographic approach to creating patterned surfaces. This involves creation of a template, which is placed on top of a resist, which is then cured into the desired pattern and the template is removed. Reproduced with permission from Elsevier, *Adv. Colloid Interface Sci*. **2012**, *170*, 2–27. (B) Nanoparticles formed by thin-film stretching, giving spherical or oblong nanoparticles which can be stretched or modified to form intermediate structures shown in i-iv. Reproduced with permission from John Wiley & Sons, *Wiley Interdiscip. Rev. Nanomed. Nanobiotechnol*. **2016**, *8* (2), 191–207.

In contrast, bottom-up techniques begin with small monomers containing features which encode the final assembly to yield the target particle.[18,23–25] A macroscale example of bottom-up assembly would be the building of the pyramids, one brick at a time; on the nanoscale, this includes polymerizations, and small molecule and block copolymer self-assembly.[26,27] This method holds more potential for achieving complexity compared to top-down self-assembly approaches, if the components can be made to behave cooperatively as required. Supramolecular chemistry provides a framework for bottom-up assembly on smaller scale. Awarded the Nobel prize in 1987, the ability to form host-guest complexes or ordered arrays has revolutionized the fields of medicinal chemistry, catalysis and more, with one example shown below where the antiparallel packing of perylene monoamide monomers forms supramolecular ribbons, which can be impregnated with a photocatalyst for hydrogen production (Figure 1.4A-D).[28–32] Small molecule self-assembly is also a somewhat well-understood process.[33] Surfactants and lipids are utilized to form high-curvature morphologies, owing to the presence of polar head groups and non-polar tails which drives the assembly to find the lowest energy conformation.[33] This process is largely governed by the entropic expulsion of water from the hydrophobic components of the molecule into the bulk solution, but other contributing factors include enthalpy, the concentration and the overall geometry of the surfactant, and the conditions of the solution such as temperature.[34] The morphology of the resulting particle can be predicted utilizing an equation to calculate the packing parameter, which takes into account the area of the hydrophilic head group, and the volume and the length of the hydrophobic tail.[33] While these assemblies find many useful applications, they are inherently limited by the overall instability of the self-assembled particles. As their assembly is reliant on reaching a high molecular concentration, known as the critical micelle concentration,

they can easily collapse upon dilution leaving only molecularly dissolved compounds.[33] Therefore, particles that possess greater colloidal stability need to be developed.

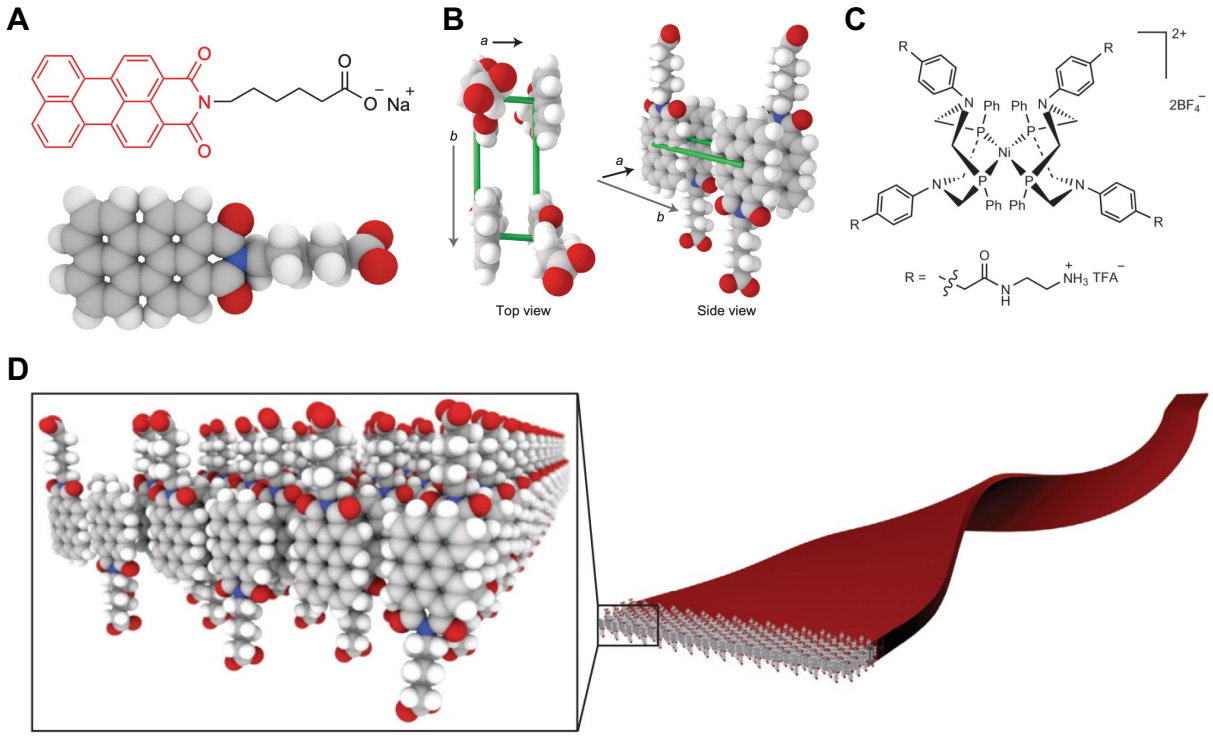


**Figure 1.4.** Supramolecular assembly for photocatalytic hydrogen production.[32] (A) Chemical structure of the perylene monoimide building block, and space filling model of such structure. (B) Packing model demonstrating interactions which govern ordered assembly. (C) Chemical structure of the photocatalyst which embeds within the ordered array of monomer. (D) Supramolecular ribbons generated from tight antiparallel packing of building blocks. Reproduced with permission from Springer Nature BV, *Nat. Chem*. **2014**, *6*, 964–970.

## 1.2 Block copolymer self-assembly

Polymers are chemical moieties repetitively joined together through covalent bonding, to create long chain, high molecular weight structures.[35] Several synthetic methods have been developed to

access polymers from a variety of starting materials, including addition, condensation, and radical polymerizations, as well as living polymerizations.[36–39] Living polymerization techniques are especially useful as they result in high molecular weight materials with relatively low molecular weight dispersities, meaning there are only small discrepancies in the overall degree of polymerization of each polymer chain, leading to greater predictability of the self-assembly.[36,38,40,41] Additionally, as they are termed "living", the chain-ends of the polymers remain active to further growth, and so sequential block copolymers (BCPs) can be made by employing such synthetic strategies.[36,40] Importantly, there need not be chemical similarity between the two blocks, and thus self-assembly of BCPs can yield structures with unique and tunable morphologies and properties.[40]

### 1.2.1 Solid-state self-assembly

BCPs can assemble in the solid state into amorphous or semi-crystalline phase separated materials, with the latter possessing desirable properties such as increased mechanical strength and stiffness, but lower impact resistance and solubility.[42–46] The phase separation is driven by the energy of the interactions occurring between the blocks in the bulk state or in thin-films.[42,44] Several different morphologies are obtainable depending on how those interactions are controlled. For example, the volume fraction of each block will contribute to the final morphology (Figure 1.5A).[47] If the volume fractions are one-to-one, gyroid or lamellar morphologies are more commonly obtained. An imbalance in the volume fractions between the blocks results in the formation of body-centered cubic or hexagonal structures.[47] This is largely related to the interfacial curvature of the resulting morphology, as the volume fraction indirectly represents interface crowding effects (Figure 1.5B).[47] The self-assembly is also driven by the free energy of mixing of the blocks.[48,49] Enthalpic contributions are usually unfavourable and there is net repulsion between the two blocks,

especially if their solubilities differ significantly. The entropy of mixing for many BCPs is favourable, but only slightly, and thus this term is outweighed by the enthalpic contributions.[48] Thus, the free energy of BCP mixing is normally positive and non-spontaneous, unless performed at elevated temperatures. Another parameter that is commonly utilized to describe BCP self-assembly is the Flory-Huggins interaction parameter. This considers the net repulsion between the two blocks and is proportional to enthalpy and inversely proportional to temperature.[48] The output is a segregation factor, with values over 100 indicating very strong segregation between the blocks, and values near 10 indicating weak segregation.[48] These tenets are applicable to diBCPs, as well as BCPs of higher orders, although the number of morphologies and overall complexity of the system increases as the number of blocks increases.

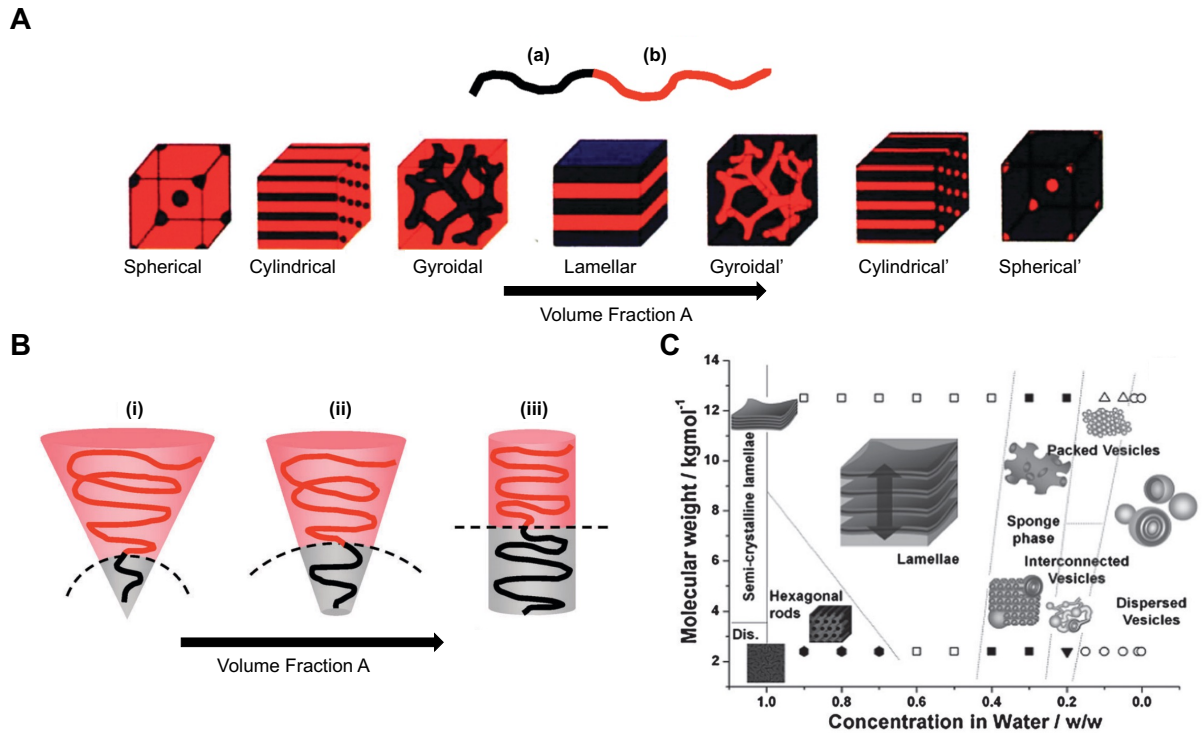


**Figure 1.5.** Amorphous solid- and solution-phase self-assembly as influenced by various parameters. (A) Solid-phase self-assembly morphologies of a diblock copolymer, with changes corresponding to increases in the volume fraction of B. (B) Solid-phase self-assembly of a diblock

copolymer demonstrating that as the volume fraction of A increases towards a 1:1 block ratio, lower interfacial curvature structures are obtained. (C) Solution-phase assembly morphology map of an example amorphous diblock copolymer demonstrating that the resulting morphology is highly dependent on the concentration, and molecular weight of the polymer, and that morphological purity is difficult to access. Reproduced with permission from the Royal Society of Chemistry, *Chem. Soc. Rev*. **2012**, *41*, 5969–5985.

### 1.2.2 Solution-state self-assembly

Solution-phase self-assembly of BCPs is also possible if the solubilities of the blocks differ. The complexity of the self-assembly process further increases relative to the solid-state, as now the solvent also plays a significant role in the thermodynamics. Additionally, unlike small-molecule assemblies which may be at chemical equilibrium, block copolymer solution assemblies are normally kinetically trapped.[17] Thus, mixtures of shapes and sizes can be obtained under the same self-assembly conditions such as spheres, cylinders, and platelets (Figure 1.5C). As the rate of unimer exchange is very low in these kinetically-trapped structures, a low energy equilibrium structure is not obtained even over extended periods of time or range of temperatures.[50–52] Similarly to solid-state self-assembly, the resulting morphologies are governed by several factors. Most notably, these include the block ratio, the solvent, the temperature, and the processing method.[47] Pioneering work was performed in the 1990s and early 2000s by the Eisenberg group which demonstrated this phenomenon beautifully (Figure 1.6).[53–55] It is important to note that high-curvature structures are formed in the majority, with low-curvature interface structures much more difficult to obtain.

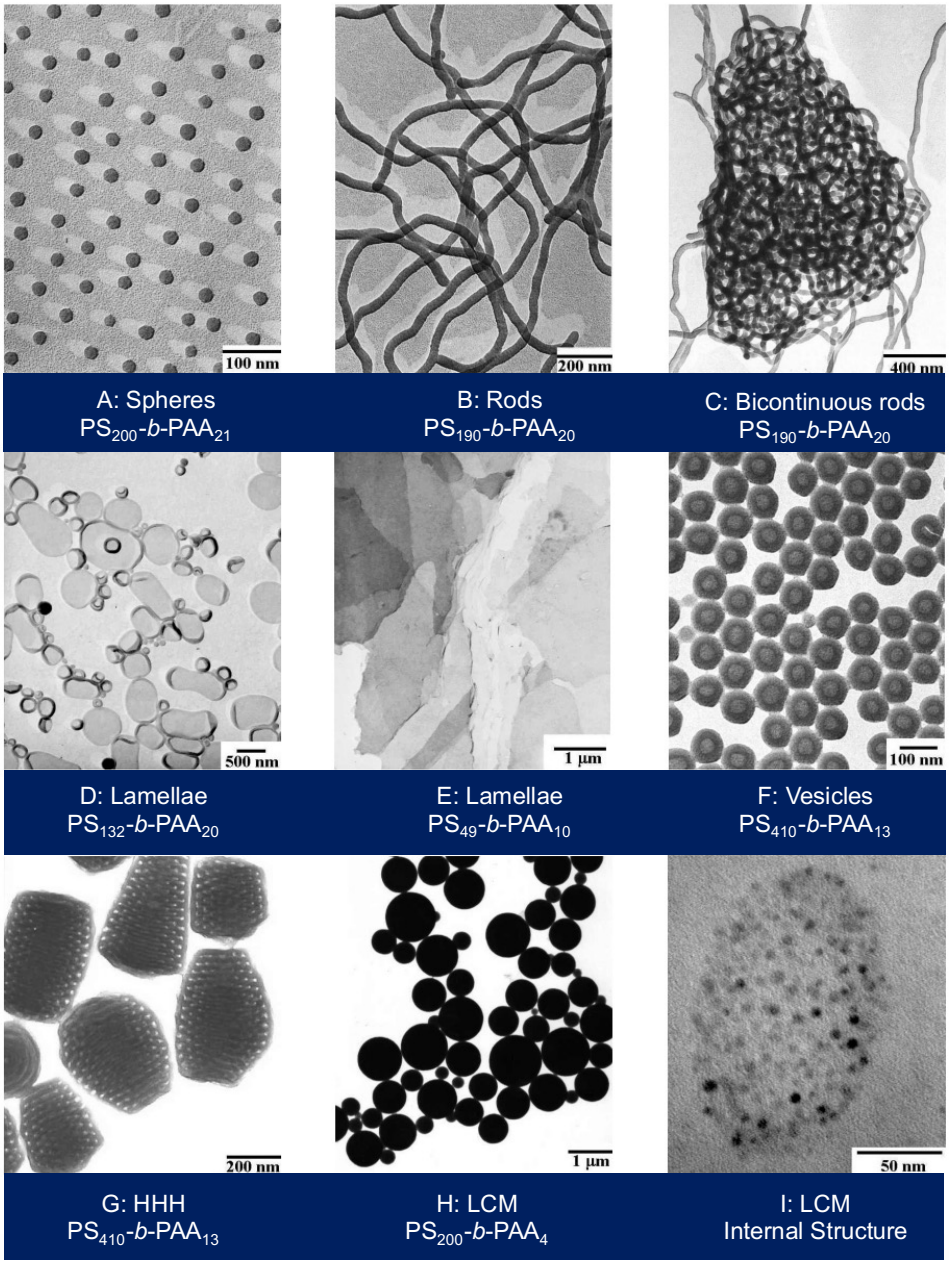


**Figure 1.6.** Pioneering work performed by the Eisenberg group on solution-state self-assembly. Through subtle variations in the core-forming and corona-forming block degrees of polymerization vast morphological space is accessed. HHH = hexagonally packed hollow loops. LCM = large compound micelles. Adapted with permission from the Royal Society of Chemistry, *Chem. Soc. Rev*. **2012**, *41*, 5969–5985.

Several thermodynamic factors contribute to the overall free energy of micellization, including the energy of the intercoronal chain repulsions, the core-chain stretching, and the interfacial energy.[53] Intercoronal chain repulsion is an enthalpic contribution arising from the repulsions occurring between the coronal chains in solution. This repulsion is increased when electrostatic interactions are present, or when the coronal chains are sufficiently long. To minimize repulsions, high curvature interface structures are favoured, with spheres preferentially forming over cylinders and vesicles. In contrast, the core-chain stretching is an entropic contribution which is governed by the requirement for the core-chains to undertake fewer and less favourable (with fewer degrees of freedom) conformations upon assembly. Normally, this is minimized in larger-core structures as the core chains can freely interact with one another in the interior of the core. For spherical particles, this instead leads to the generation of a large number of very small particles, rather than a small number of large particles. Finally, the interfacial energy is a parameter that describes the enthalpic penalty associated with the core-segments interacting with the solvent that is selective for the corona. These interactions are minimized in larger particles, as the overall surface area of the exposed core is lower. Together, these parameters can explain why different morphologies are accessible under differing conditions,[53,56] and importantly, it highlights the level of complexity present in BCP self-assembly, which limits rational prediction of the final shape and size of the particles.

## 1.3 Crystallization-driven self-assembly

### 1.3.1 Self-assembly of block copolymers with a crystallizable core-forming block

Crystallization of the core-forming block of a BCP can offer control over the resulting assembly morphology, as a new term is introduced into the thermodynamic equation[57–60] The free energy

associated with the formation of the crystal structure lattice now needs to be considered.[61] This term contributes to the free energy of the core-chain-stretching as outlined in the previous section. The stability granted by formation of the crystal lattice is now able to compete with the other thermodynamic parameters to favour low interfacial curvature structures such as 1-dimensional (1D) nanofibers and 2-dimensional (2D) nanoplatelets. Polymers that contain a regular, symmetric structure are often able to crystallize in solution. The regularity can arise due to many factors, such as single enantiomeric forms present in the backbone, the presence of hydrogen bonds between the chains, or π-π stacking interactions.[60] All of these contribute to the ability of a polymer to form a rigid crystalline material. This does not only apply to crystalline homopolymers, but also to BCPs when the crystallizable core-forming block is present at an adequate degree of polymerization. For example, the crystal structure of poly(ethylene oxide)-*b*-poly(styrene) (PEO-*b*-PS) was studied in the 1960s by Keller and coworkers.[58] Through brightfield microscopy and X-ray analysis, they were able to conclude that the platelet-like structures they were observing contained crystalline cores (Figure 1.7A). Furthermore, in the late 1990s it was determined that the morphology of the BCP assembly can be influenced by the crystallization of the core-forming block.[62,63] In this work, polyferrocenylsilanes were employed as the core-forming block. Importantly, polyferrocenylsilanes are only crystallizable upon symmetric substitution at the silyl group (Figure 1.7B); if one of the groups is substituted for an alternative functional group, the polymer no longer contains the structural regularity required to crystallize (Figure 1.7B).[63] When crystallization of the core was favourable upon introduction of a poor solvent long nanofiber micelles were observed. Alternatively, when crystallization was not possible, spherical nanoparticles were observed, similarly to many amorphous-core BCPs. The nanofiber morphology contains a very low interfacial curvature, a feature that is not normally accessible with amorphous core-forming

blocks.[64] This discovery of morphological control governed by the crystallization of the core gave rise to the term crystallization-driven self-assembly (CDSA).[61]

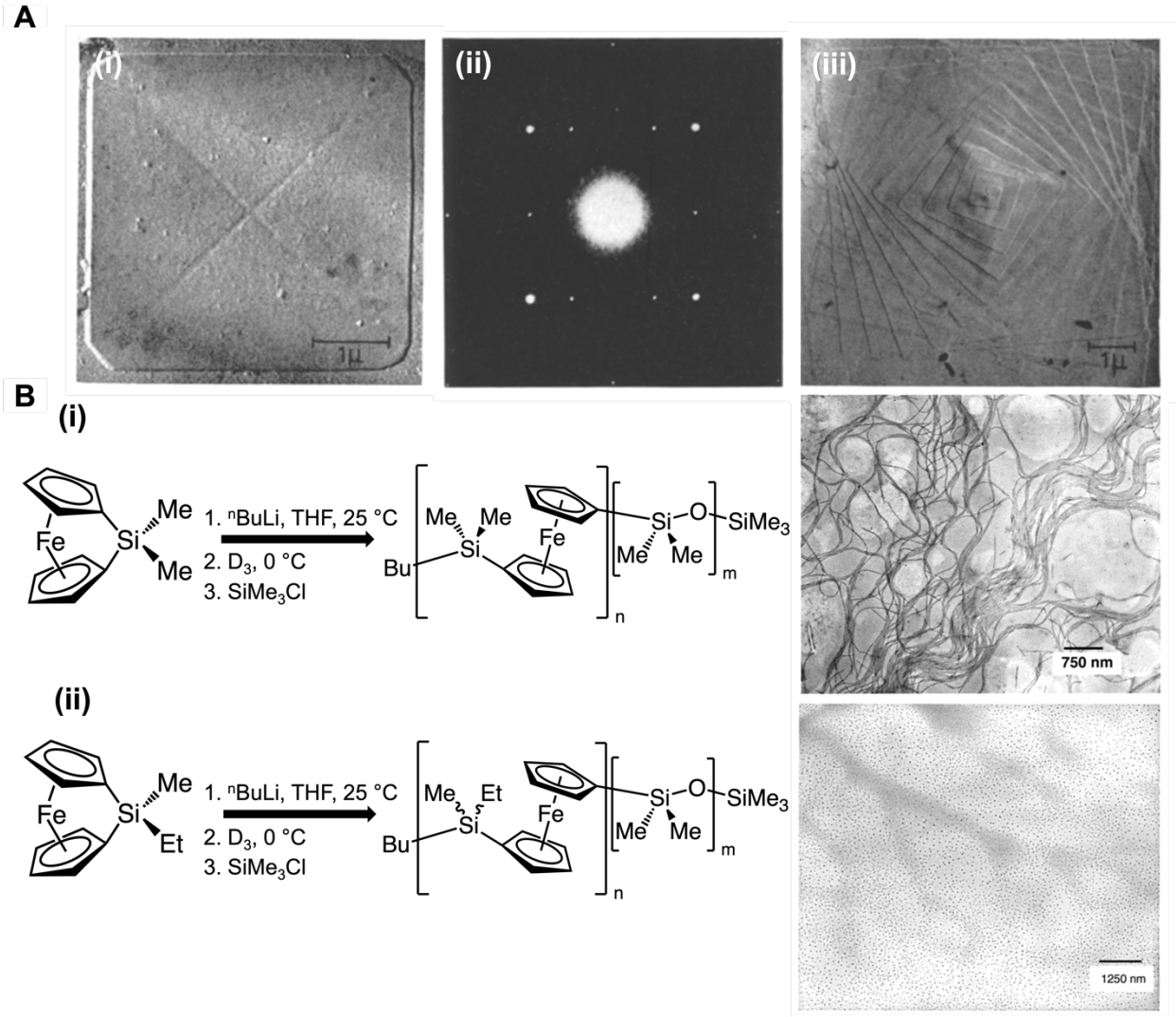


**Figure 1.7.** Images demonstrating the influence of core-crystallization on nanoparticle morphology. (A) (i) PEO-*b*-PS block copolymer self-assembled micelles with low interfacial curvature. (ii) X-ray diffraction pattern of the micelle in (i), demonstrating the crystalline nature of the core. (iii) Stacked flat core-curvature morphologies obtainable due to the crystallinity of the PEO core-forming block. Reproduced with permission from Springer Nature BV, *Kolloid- Z.u.Z. Polymere* **1966**, *209* (2), 115–128. (B) Pioneering work performed by the Manners group

demonstrating that upon ring-opening of ferrocenophane monomers with the silicon substituted with two methyl groups, length disperse crystalline-core nanofibers are generated in mixtures of $CH_2Cl_2$ and hexanes, whereas in (ii) when one methyl is substituted for an ethyl group, core crystallization does not occur and spherical micelles are obtained. Reproduced with permission from the American Chemical Society, *J. Am. Chem. Soc*. **2000**, *122* (47), 11577–11584.

### 1.3.2 Living CDSA

Core-crystallization offers further opportunities for the generation of controlled nanoparticles. As discovered in 2007, the crystalline core of 1D nanofibers is susceptible to physical stress which can cause fracture.[57,59,65] Commonly, sonication is utilized to induce breakage of the core. Longer structures tend to break more easily, akin to breaking a long twig versus a much shorter one.[65,66] Therefore, if the power is great enough and the sonication proceeds for a sufficient time, the population of nanofibers gradually approach the same length (ca. 25 nm). While some variations exist in the final nanofiber length due to differences in the crystal lattice of the individual nanoparticles, adequate sonication normally results in a reasonably uniform population of very short nanofibers, termed “seeds”. These seeds can then act as crystal nuclei, where the ends remain active for epitaxial growth upon the addition of further dissolved polymer (unimer) (Figure 1.8A).[59] This process is analogous to living polymerization, and similarly, the final length of the resultant nanofibers is directly dependent on the unimer/seed mass ratio. This process is known as seeded-growth living CDSA, and can also be applied to the formation of controlled 2D nanoplatelet micelles, which are favoured when the core-to-corona block ratio is near to on-to-one (Figure 1.8B).

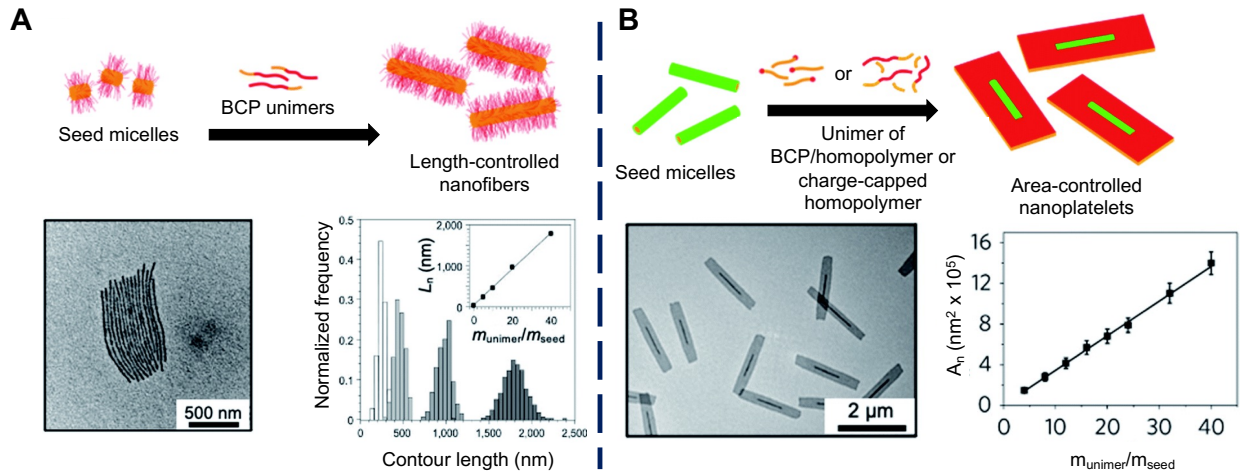


**Figure 1.8.** Schematic to illustrate the morphological control of nanoparticles produced via living CDSA. (A) For 1D nanofibers, unimer is added to seed micelles which grows epitaxially from the seed termini. The final length is directly dependent on the ratio of unimer to seed. (B) Area control is achievable for the formation of 2D nanoplatelet structures, through the use of either homopolymer seeds or charge-capped homopolymer. Unimer is added and grows in two dimensions from the seed, to a size that is directly dependent on the amount of unimer added. Reproduced with permission from the Royal Society of Chemistry, *Chem. Sci*. **2021**, *12*, 4661–4682.

Self-seeding living CDSA is also well known.[64,67–69] In this case, the polymer is dissolved in a solvent in which both blocks of the BCP are soluble at high temperatures, but in which the core-forming block selectively crystallizes upon cooling. Upon cooling of the unimer solution small crystalline nuclei precipitate and act as in situ seeds for epitaxial growth. This process also can yield length-controlled structures with low overall dispersity, however, less control is obtained over the final length as the amount of crystalline nuclei depends on both the temperature upon heating and cooling, and reproducibility is limited.[64] These methods can be utilized for the

formation of 1D nanofibers and 2D platelets, and the presence of active termini in both lends to the formation of higher order structures.

### 1.3.3 Hierarchical assembly via living CDSA

Living CDSA has been demonstrated to be a versatile method for creating segmented and hierarchical structures.[70–72] The former structures can be generated through the sequential addition of BCPs containing the same core chemistry but different coronal chemistry. In few instances, if the core-crystal lattice is sufficiently similar, then two different core-forming blocks may be used for heteroepitaxial growth.[73,74] In either case, the ability to create segmented structures with well-defined coronal spaces of unique chemical composition affords the development of structures such as non-centrosymmetric micelles,[75–77] barcode micelles,[77] and multiblock patchy platelet comicelles.[78] For example, hierarchical assemblies can be obtained through tuning of the coronal-block chemistries; in studies published in 2015 and 2016, hydrophobic and polar corona segments are exploited to drive association between chemically similar blocks to form higher order structures such as cross-like micelles and train-track-like micelles (Figure 1.9A).[70,71] Importantly, control over the final morphology is dictated by the overall degree of polymerization of the BCP and through solvent selection. Patchy 2D block comicelles can be made through the dissolution of a central segment which contains a different solubility profile than the external segment (Figure 1.9B).[79] Non-centrosymmetric micelles are accessible upon utilization of a cross-linkable corona forming block (Figure 1.9C).[75] The cross-linking renders one side of the central micelle inactive to epitaxial growth, and thus unidirectional growth can occur upon the addition of further unimer. The discovery of numerous such higher-order synthetic nanostructures highlight the vast utility and versatility of the living CDSA method.

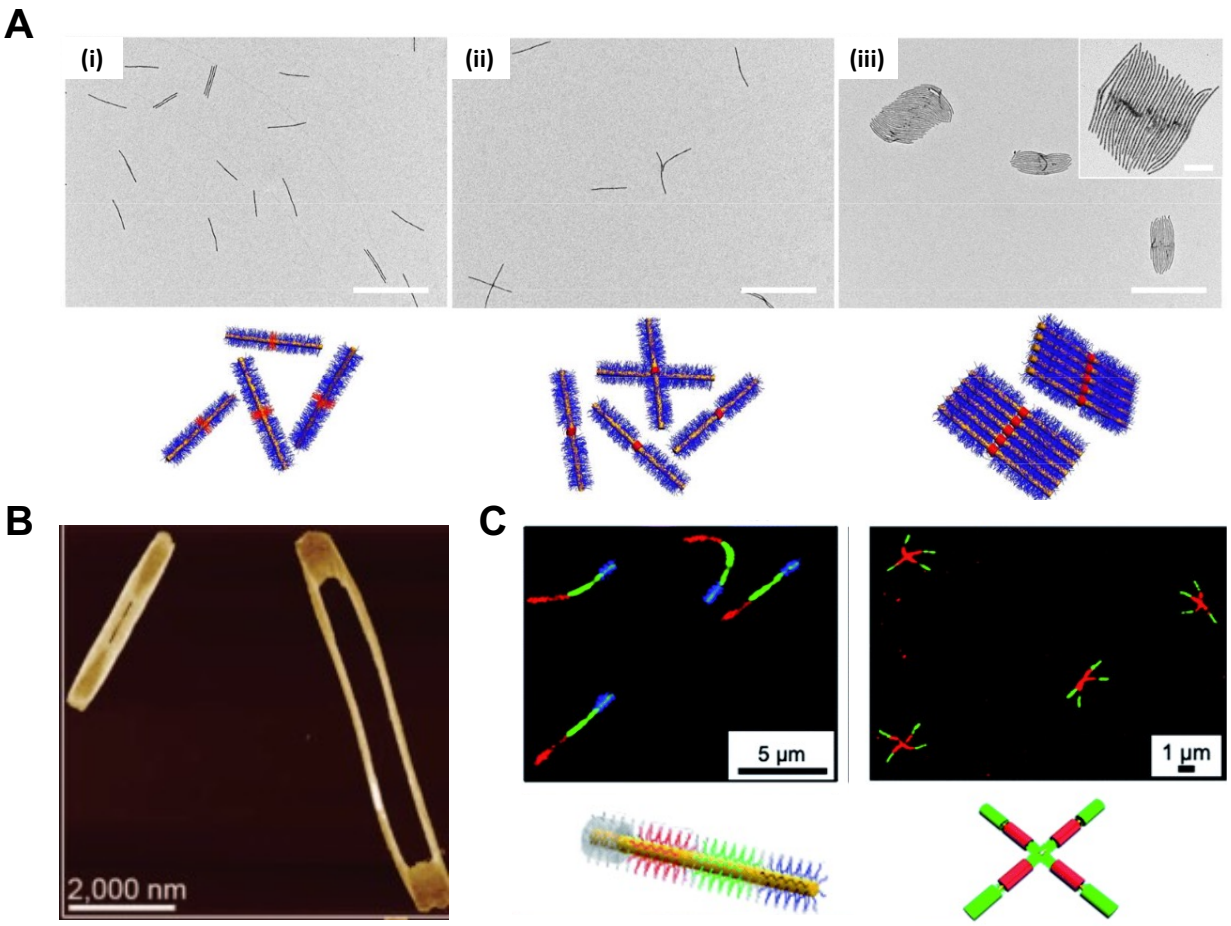


**Figure 1.9.** Hierarchical assemblies accessible through living CDSA. (A) P-H-P triblock comicelles, where P = polar and H = hydrophobic blocks. As the solvent polarity increases (left to right) the hydrophobic segments of the nanofibers associate together to form higher order structures. (B) Patchy 2D block comicelles, generated from alternate addition of unimers with different solubilities. Upon addition of THF into the mixture, the central segment dissolves. (C). Barcode micelles with dyes attached to the respective corona-forming block. Non-centrosymmetric micelles were generated through cross-linking of the central segment, followed by sonication to fragment the disperse nanofiber. Reproduced with permission from the Royal Society of Chemistry, *Chem. Sci*. **2021**, *12*, 4661–4682.

## 1.4 Nanoparticles and their applications in nanomedicine

### 1.4.1 General applications and considerations

Nanomedicine describes the use of nanoscopic structures with dimensions from ca. 10 – 200 nm for disease diagnosis and treatment,[80–82] and since its inception, many nanoparticles with medicinal uses have been developed (Figure 1.10).[82] While compositionally these nanoparticles are chemically distinct, the physiochemical properties of the nanoparticles are all largely dependent on their size, shape, and surface chemistry.[81] Owing to their unique and tunable properties, nanoparticles have been exploited for uses as bioimaging agents, high-throughput diagnostics, and disease treatments.[80] However, despite the increase in reports detailing the development of novel nanomedicine treatments, relatively few have successfully reached clinical trials for purposes of directly treating diseases, such as cancer, or for drug-delivery.[83–85] Their clinical applications currently are limited to acting as protective drug-delivery vectors which offer few enhancements to specific targeting and potency.[84–87] Overall, the approved treatments are confined to those spherical in shape, and are based on increased solubilization of an already prescribed therapeutic to increase the bioavailability. Unfortunately, it is clear that the full potential of nanomedicine has not yet been reached,[84,86,88] and more fundamental information is needed in order to increase the diversity of applications available for nanoparticle use and facilitate rational design. Increasing targeting capabilities and rendering the nanoparticles themselves more useful and potent for therapeutic applications may be mediated through tuning of the size and the shape of the nanoparticle.

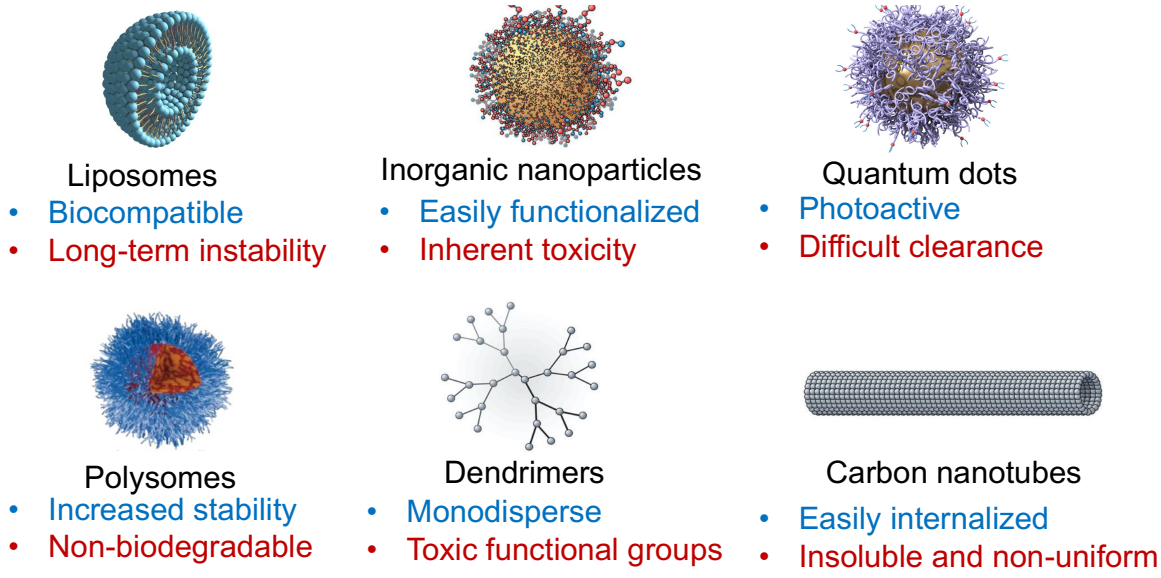


**Figure 1.10.** Nanoparticles of various compositions, commonly employed for biomedical applications. Each is associated with respective advantages and disadvantages.

### 1.4.2 Size-dependent properties

Upon injection of a nanoparticle into the body, several processes occur. Immediately, a protein corona forms around the nanoparticle,[89,90] which can block any targeting groups present on the surface and mark the particle for degradation. The nanoparticles then circulate through the bloodstream, become opsonized by the immune system, or extravasate into different organs and tissues, which more often than not unfortunately involves sequestration into the kidneys or liver (Figure 1.11A, B).[89] The details of these processes are dependent on the nanoparticle size.[91] The formation of the protein coat and which substrates are adhered to the surface of the nanoparticle is partially dictated by the size of the nanoparticle. If the cells of the body recognize the object as foreign, this can trigger targeting by macrophages or the complement system, leading to inadequate circulation of the nanoparticles due to their destruction by the immune system.[87] The circulation half-life of the particle is greatly dependent on the nanoparticle size as well.[89] As mentioned, if the

nanoparticle is too large or too small, this can lead to immediate filtration by the renal or waste systems. Medium sized particles can persist longer in circulation due to avoidance of these mechanisms. Importantly, extravasation into tissues or organs is thought to be governed by the size of the intercellular gaps present between specific cell types.[89,90] This means that for example, if the particle is between 50 – 100 nm, it could accumulate in the liver, whereas particles between 2 – 5 μm in size have been proposed to accumulate in the lungs (Figure 1.11B).[89] Overall, particles approximately 100 nm in size have been suggested to be the most long lasting in circulation, which can be advantageous for therapeutic delivery so long as they reach their target eventually.[89] Finally, the size of the nanoparticle can also influence its ability to penetrate into a tumor.[89,90] The tumor microenvironment can be extremely variable between types of cancer, with some possessing increased vasculature, while others contain a dense and fibrous extracellular matrix.[90] If the tumor is characterized by increased and leaky vasculature, larger particles can be advantageous for extravasating into the tumor; in contrast, it has been noted that much smaller nanoparticles are more adept at penetrating into more complex and packed tumor environments.[89,92] Evidently, the size of the nanoparticle employed will depend on the desired accumulation location and pathology of the targeted disease. It should be noted that all the outlined trends are dependent on the composition of the particle as well, and deviations can be observed depending on the material studied. Additionally, the pathway the particle will take is incredibly complex and of course, is not simply controlled by the size of the nanoparticle alone; the shape also plays a pertinent role in the ultimate fate of the nanoparticle.

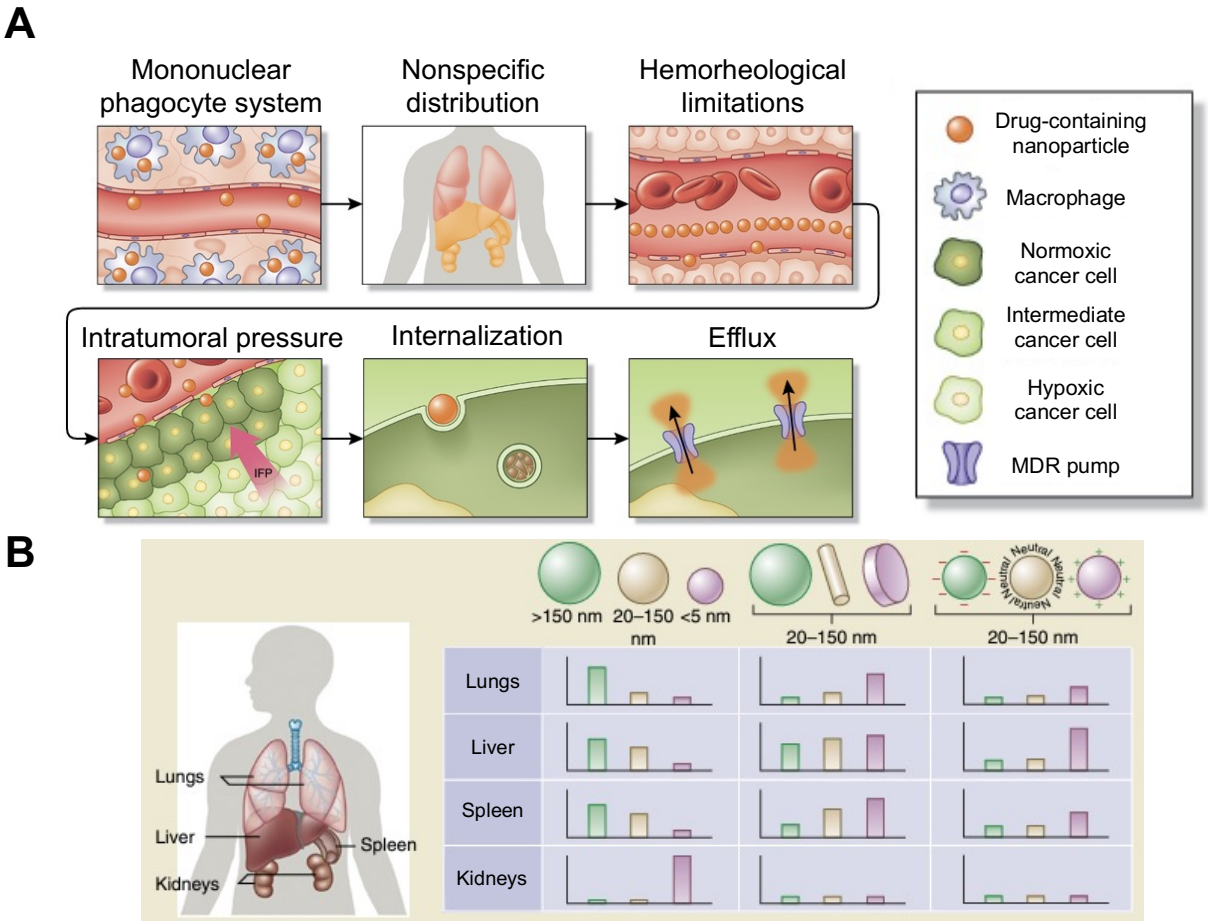


**Figure 1.11.** Biological barriers encountered by nanoparticles upon injection into the body. (A) Immunological and physical barriers that nanoparticles must surpass to reach the tumor site, including recognition by the immune system, off-target distribution, red blood cell interactions, high intravascular pressures, and cellular internalization. (B) Size, shape, and surface-charge dependence on particle accumulation in the body. Smaller nanoparticles (< 5 nm) are largely excreted through the kidneys, whereas larger (> 150 nm) preferentially accumulate in the lungs. Reproduced with permission from *Nat. Biotechnol*. **2015**, *33* (9), 941 – 951.

### 1.4.3 Shape-dependent properties

The idea that "form follows function" has been discussed in many academic areas, but particularly in biological fields for many decades. This statement is true not only to the structure of proteins,

chromosomes, and cells, but also for nanoparticles. Spherical nanoparticles are the most commonly produced and studied, largely due to the thermodynamic properties discussed in section 1.2.2 leading to their preferential formation over lower curvature morphologies. However, other shapes are also obtainable and have been studied in biological applications, albeit much less frequently. If we consider spherical, cylindrical, and discoidal nanoparticles being the most relevant for discussion, we can rationalize how these shapes affect the biodistribution and pharmacokinetics of the injected nanoparticles (Figure 1.11B).[89] Importantly, how the nanoparticle behaves in the laminar flow of the bloodstream will affect its circulation half-life and margination to tissues. For example, spherical particles do not disrupt the bloodstream and circulate for approximately 2 – 3 days, while long cylindrical micelles, on the other hand, are capable of aligning with the blood flow, and this allows them to persist in the blood stream for much longer periods of time (> 1 week).[93,94] Shorter cylindrical and discoidal shapes experience "tumbling" in the blood stream, and this promotes their margination to the blood vessel walls.[89] This can increase their adherence to endothelial cells and increase extravasation into surrounding tissues, allowing for enhanced penetration and accumulation at tumor sites. Finally, the shape of the nanoparticle can also dictate the bioaccumulation sites, with spherical particles showing higher concentrations in the liver, relative to cylindrical and discoidal shapes of a given composition, which appear to be increased in the lungs and spleen (Figure 1.11B).[89] Overall, it is clear that total control over the nanoparticle shape and size is critical for addressing specific diseases of interest, as targeting to an organ, tissue, or cell type will be greatly impacted by these nanoparticle parameters. Thus far, discrepancies between the desired impact of the nanoparticle and the physiological *in vivo* activity have greatly hindered the widespread use of nanoparticles for medicinal purposes, and thus more fundamental knowledge is required to resolve these issues.

### 1.4.4 Anisotropic nanoparticles in nanomedicine

Anisotropic nanoparticles have been garnering intense attention for medicinal applications due to their multi-dimensionality, allowing for more unique biological interactions to occur. Many materials have been utilized, but those that are especially common are metal nanoparticles, likely due to their manufacturability.[95–97] Many methods exist for creating anisotropic nanoparticles, including both top-down and bottom-up approaches. The former includes methods such as thin-film stretching and electron beam lithography for mold-making, whereas the latter usually involves self-assembly, or microfluidics.[98] As mentioned in the previous section, anisotropic particles behave less predictably *in vivo*, as multiple different orientations are able to interact with a cell due to the differing dimensions present in a single structure. This angle of contact can then dictate the level of cellular uptake or adherence.[99,100] For example, ellipsoidal particles (both prolate and oblate) have been demonstrated to have increased adherence to cells over spherical particles.[101] Interestingly, despite increased adherence in both ellipsoidal particles, only those with an oblate shape experienced increased uptake over spherical nanoparticles, with the prolate-ellipsoids having reduced cellular uptake.[101] Therefore, control over the aspect ratio is also needed when designing nanoparticles for biological applications.

Nanoparticle anisotropy has been experimentally demonstrated to offer several additional advantageous biological properties. It was determined that rod-like nanoparticles elicited lower cytokine release from macrophages (Figure 1.12A).[102] Additionally, delivery of therapeutics using anisotropic iron oxide nanoparticles in mice resulted in increased drug-retention in the blood stream, as well as lower levels of white blood cells, relative to nanospheres (Figure 1.12B).[103] In another study, polystyrene anisotropic nanoparticles displayed higher accumulation in their target organs relative to nanospheres, along with increased diffusion through the extracellular matrix of

the tumor microenvironment.[104] Furthermore, rod-like particles have shown increased accumulation in the lungs and the brain, the latter target being traditionally very difficult to reach due to the blood-brain-barrier.[104] Anisotropic nanoparticles generated from both top-down and bottom-up approaches have been utilized for efficient delivery of cargo, including nucleic acids (siRNA, mRNA, DNA) and chemotherapeutics, and oxygen.[98] In one such example, it was demonstrated that the employment of worm-like polymer micelles (polyethyleneglycol-*b*-polyphosphoramidate) enhanced transfection efficiency 10,000× relative to spherical particles of identical composition (Figure 1.12B).[105] Therefore, it becomes clear that anisotropic nanoparticles have several advantages over their isotropic counterparts, yet, to date, only a very small fraction of nanoparticles undergoing clinical trials or approved for use are anisotropic. This is likely due to the materials employed (majority liposomal) favouring spherical structures, as well as the ease of obtaining this morphology. Therefore, if uniform, controllable, anisotropic nanoparticles can be fabricated in a reproducible, predictable, and facile manner, then their employment for clinical use may become more widespread. This can be achieved using living CDSA to generate the nanoparticles containing crystalline cores, of controlled length.

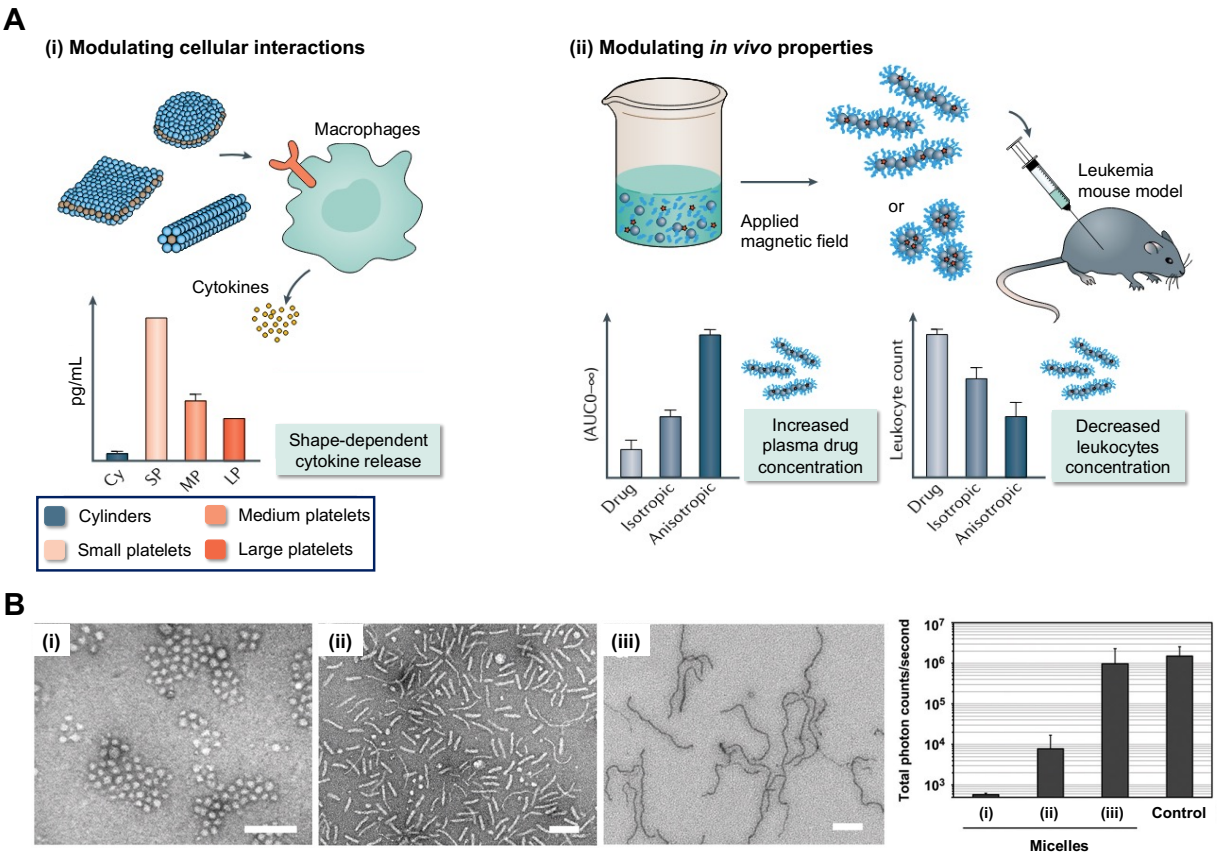


**Figure 1.12.** Advantageous cellular interactions and biological properties of anisotropic nanoparticles. (A) (i) Cylindrical nanoparticles were demonstrated to cause a much lower amount of cytokine release from macrophages and (ii) anisotropic nanoparticles aided in prolonging drug circulation and resulted in decreased white blood cell counts. Reproduced with permission from *Nat. Rev. Chem*. **2017**, *5*, 21 – 45. (B) Three different nanoparticle morphologies were analyzed including (i) spherical (ii) short rods and (iii) long rods and the transfection efficiency was measured. It was demonstrated that long rod-like nanoparticles were able to reach a 10,000 x higher transfection efficiency relative to spherical counterparts. Reproduced with permission from John Wiley & Sons, *Adv. Mater*. **2013**, *25* (2), 227 – 232.

## 1.5 PFTMC-based block copolymers

### 1.5.1 Advantages of polycarbonate-based nanoparticles

Living CDSA has been shown to be a useful tool for the creation of near monodisperse nanoparticles, but most of the examples described in the literature involve the use of polyferrocene core-forming blocks or $\pi$-conjugated core-forming blocks such as polythiophenes.[68,69,106–113] While these crystallize superbly, their self-assembly takes place in solvent mixtures such as dichloromethane/hexanes, which are not conducive for biomedical applications. Such nanofibers are also not dispersible nor colloidally stable in water; therefore, new core-forming blocks are needed for living CDSA to be useful for nanomedicine.

Some of the first described biocompatible and biodegradable core-forming blocks include polylactides and polycaprolactones. The O'Reilly and Dove groups pioneered work in this area, demonstrating that these polymers could be utilized as crystallizable core-forming blocks, and were eventually able to perform controlled living CDSA under aqueous conditions.[66,67,74,114–117] However, these core-forming blocks favoured 2D assemblies, and accessing 1D nanofibers required great control over the block ratios and the solvents selected. Additionally, the biodegradation of these materials occurs through bulk hydrolysis, which in turn releases large amounts of acidic byproducts which can trigger an immune response and catalyse further degradation, and they are therefore not ideal for biomedical applications.[118] Poly(trimethylene carbonate) had also been explored for use in block copolymers due to its hydrophobicity and low glass transition temperature;[119,120] however, the polymer structure is not rigid enough to crystallize. Therefore, in 2014 Hedrick and Yang described the synthesis of a new polycarbonate-based core-forming block, poly(fluorenetrimethylene carbonate) (PFTMC).[121] This compound was initially of interest for its electroactivity and biodegradability. The article outlined the monomer synthesis and

the subsequent ring-opening polymerization using poly(ethylene glycol) (PEG) as a macroinitator for the controlled polymerization (Figure 1.13A), generating BCPs of high-molecular weight and of low dispersity. The self-assembly was then attempted through the direct dialysis of the unimer BCP from THF into water. When the degree of polymerization of the PEG corona-forming block was lower, almost exclusively low interfacial curvature tape-like micelles were observed by transmission electron microscopy (Figure 1.13B).[121] Upon increasing the fraction of the hydrophilic block, the morphology transitioned to give mostly spherical micelles. Normally upon solution self-assembly of amorphous-core structures, where thermodynamic parameters (e.g. short corona-forming block) favour the formation of low interfacial curvature structures, vesicles are formed. It was not yet realized in this work that the tape-like structures observed were a result of PFTMC crystallization.

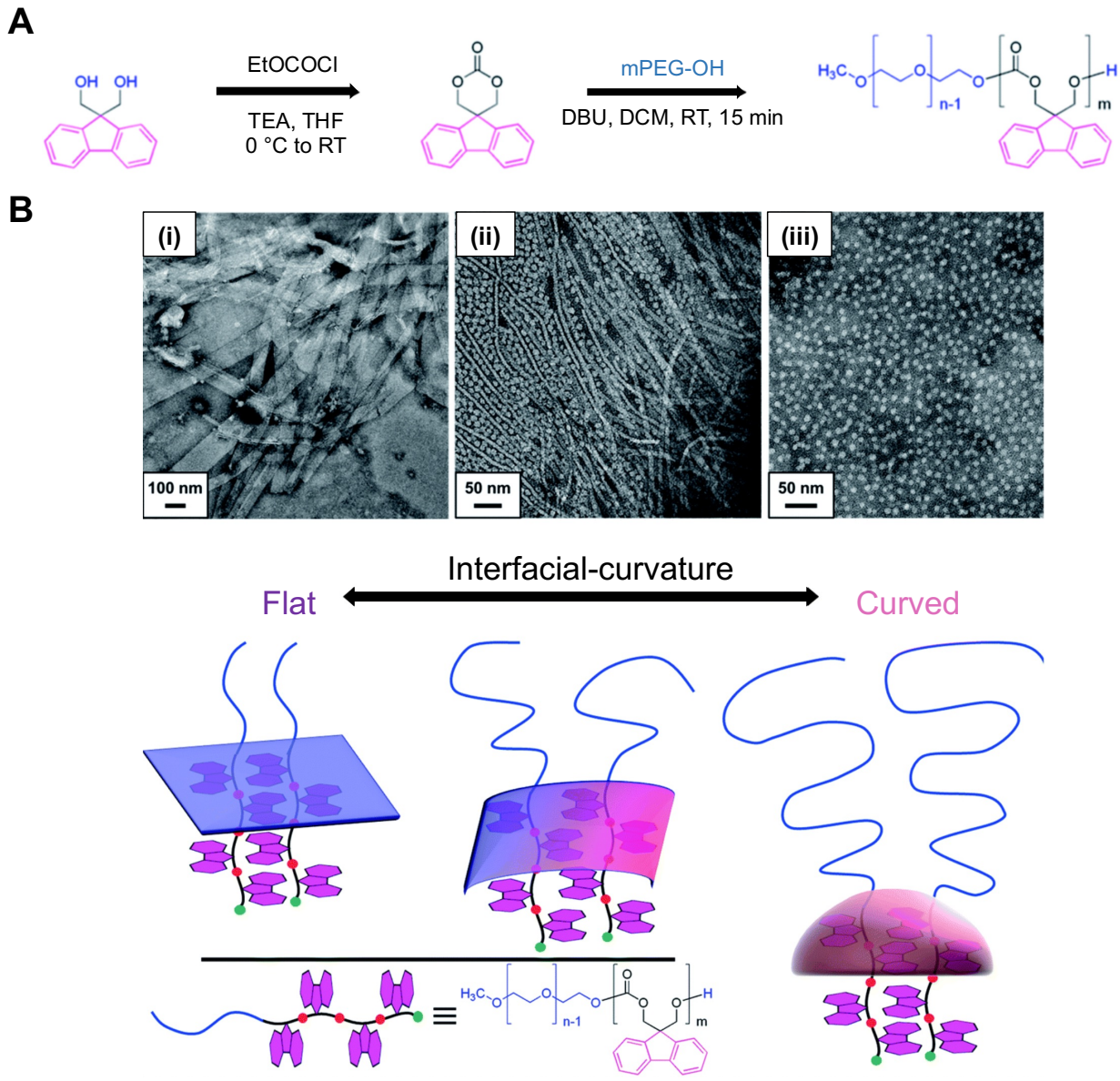


**Figure 1.13.** First synthesis and investigative self-assembly of diblock copolymers containing a PFTMC core-forming block. (A) Synthetic route to ring-strained fluorene monomer, which undergoes ring-opening polymerization upon macroinitiation by PEG-OH. (B) Morphologies obtained under various self-assembly conditions, ranging from flat interfacial curvature morphologies (i) to highly curved morphologies (iii), and the mixture obtained during the transition (ii). Reproduced with permission from the Royal Society of Chemistry, *Polym. Chem.* **2010**, *5* (6), 2035 – 2040.

Subsequently, in 2018 it was reported that the BCP PFTMC$_{20}$-*b*-PEG could undergo living CDSA in mixtures of DMSO:MeOH to yield length controlled nanofibers with low dispersity (Figure 1.14A, B).[122] The BCP was synthesized through the procedure reported by Hedrick & Yang, and various molecular weight PEG macroinitiators were employed for creating BCPs with differing block ratios. Only when the block ratio was close to 1:2 (20:44) were 2D structures formed. Spherical micelles were only observed upon direct addition of unimer solution into water. 1D nanofibers formed in mixtures of DMSO:MeOH could be readily transferred into water through dialysis, and remained colloidally stable (> 2 years in $H_2O$) upon doing so. The crystallinity of the core was confirmed through a combination of small- and wide-angle X-ray scattering experiments. Molecular dynamics also elucidated the number of chain folds and chain orientation of the PFTMC polymers within the core, with 1 chain fold occurring when the PFTMC degree of polymerization was 20. The BCP nanofibers were evaluated for cytotoxicity against WI-38 and HeLa cells in 2D cell culture using AlamarBlue™ to assess cellular metabolism. No cytotoxicity was observed at concentrations less than or equal to 100 μg/mL (Figure 1.14C). The degradation product, 9H-fluorene-9,9-dimethanol, which is assumed to arise from surface erosion, was also evaluated for cytotoxicity. It was determined that cell viability only decreased at concentrations above 0.45 mM or 1.01 mM, for WI-38 or HeLa cells respectively. The discovery of this new biodegradable and biocompatible crystallizable core-forming block unlocked the potential to explore vast applications of PFTMC 1D nanofibers in nanomedicine.

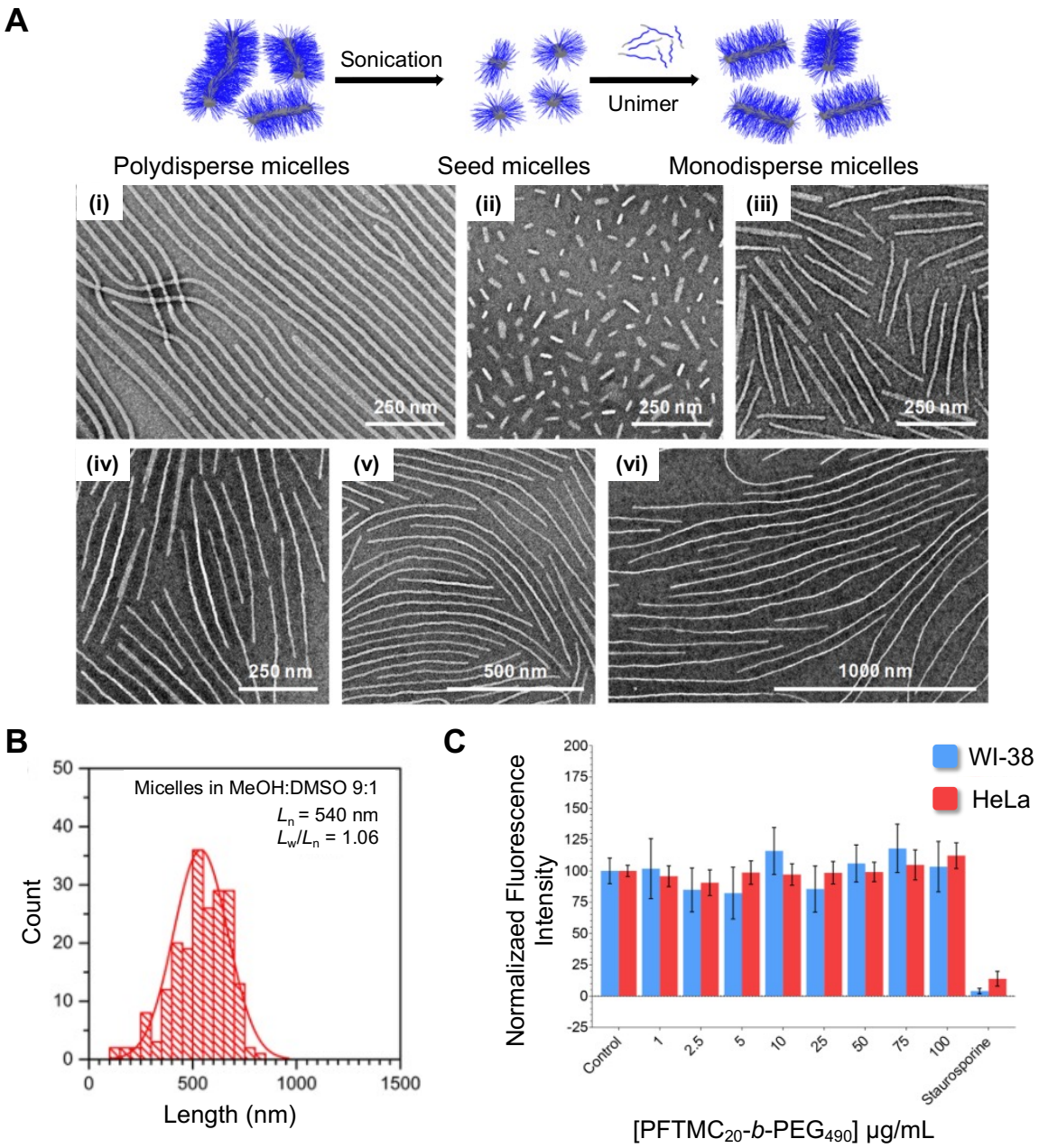


**Figure 1.14.** First report of diblock copolymers containing a PFTMC core-forming block undergoing living CDSA. (A) Schematic demonstrating the process of obtaining seeds from polydisperse micelles through sonication, followed by addition of polymer unimer to generate near monodisperse micelles. This process can be followed by TEM as demonstrated in (i) through (vi), and the final length of the polymer nanofibers is dependent on the amount of added unimer. (B)

Histogram of the count *vs* length of the nanofibers, demonstrating a low-length dispersity sample is obtained in mixtures of MeOH:DMSO. (C) Cell viability of WI-38 and HeLa cells upon incubation with PFTMC-*b*-PEG nanofibers from 100 μg/mL to 0 μg/mL, with no toxicity observed. Reproduced with permission from the American Chemical Society, *J. Am. Chem. Soc*. **2018**, *140* (49), 17127–17140.

### 1.5.2 Previous work employing PFTMC nanomaterials for nanomedicine

Since the publishing of this article in 2018, our group has explored the use of PFTMC-based nanofibers for biomedical applications such as drug delivery and nucleic acid delivery.[123–127] The nanofibers employed have expanded from PFTMC-*b*-PEG to include a variety of corona forming blocks, most notably poly(*N*-isopropylacrylamide) (PNIPAM), poly(dimethylaminoethyl methacrylate) (PDMAEMA), poly(*N*-2-hydroxypropyl methacrylamide) (PHPMA), and polyfructose (PFr), each with their own unique advantage for biological applications. For example, PNIPAM exhibits a low critical solution temperature which allows it to undergo morphological changes around 37 °C, which may be useful for drug delivery applications.[128] PDMAEMA is partially protonated at physiological pH, allowing for the complexation of anionic cargos as well as targeting of anionic cell membranes.[129] PHPMA readily undergoes polymerization-induced self-assembly, making it a promising candidate of scaffolding applications. PFr contains fructose moieties which are proposed to specifically interact with the GLUT5 receptor commonly upregulated on breast-cancer cells, allowing for more specific targeting.[130] The majority of our previous work, however, relies on PFTMC-*b*-PEG, PFTMC-*b*-PNIPAM, and PFTMC-*b*-PDMAEMA.

Drug loading has been performed on both tri- and di-BCPs.[123,124] Initially, it was believed that the addition of a hydrophobic, yet amorphous middle block would allow for better

encapsulation of hydrophobic cargo in the micelle, as in amorphous core structures the drug is typically encapsulated within the hydrophobic core. Therefore, triblock copolymer micelles of composition PFTMC-*b*-poly(butyl methacrylate)-*b*-PEG (PFTMC-*b*-PBMA-*b*-PEG) were synthesized and prepared by living CDSA, and the model compound Nile red was encapsulated in the core (Figure 1.15A, B).[123] It was demonstrated that the maximum drug loading capacity was 1 wt.%, representing an encapsulation efficiency of 6.7 % (Figure 1.15C). It was then discovered that nanoparticles which did not include the middle amorphous core could also load cargo.[124] Therefore, the ability to load Nile red at the core-corona interface of crystalline core PFTMC-*b*-PEG and PFTMC-*b*-PNIPAM nanofibers was also explored.[124] Here, it was identified that the maximum drug-loading capacity was also 1 wt%, and that the chemical composition of the corona-forming block did not dramatically affect this drug-loading capacity.

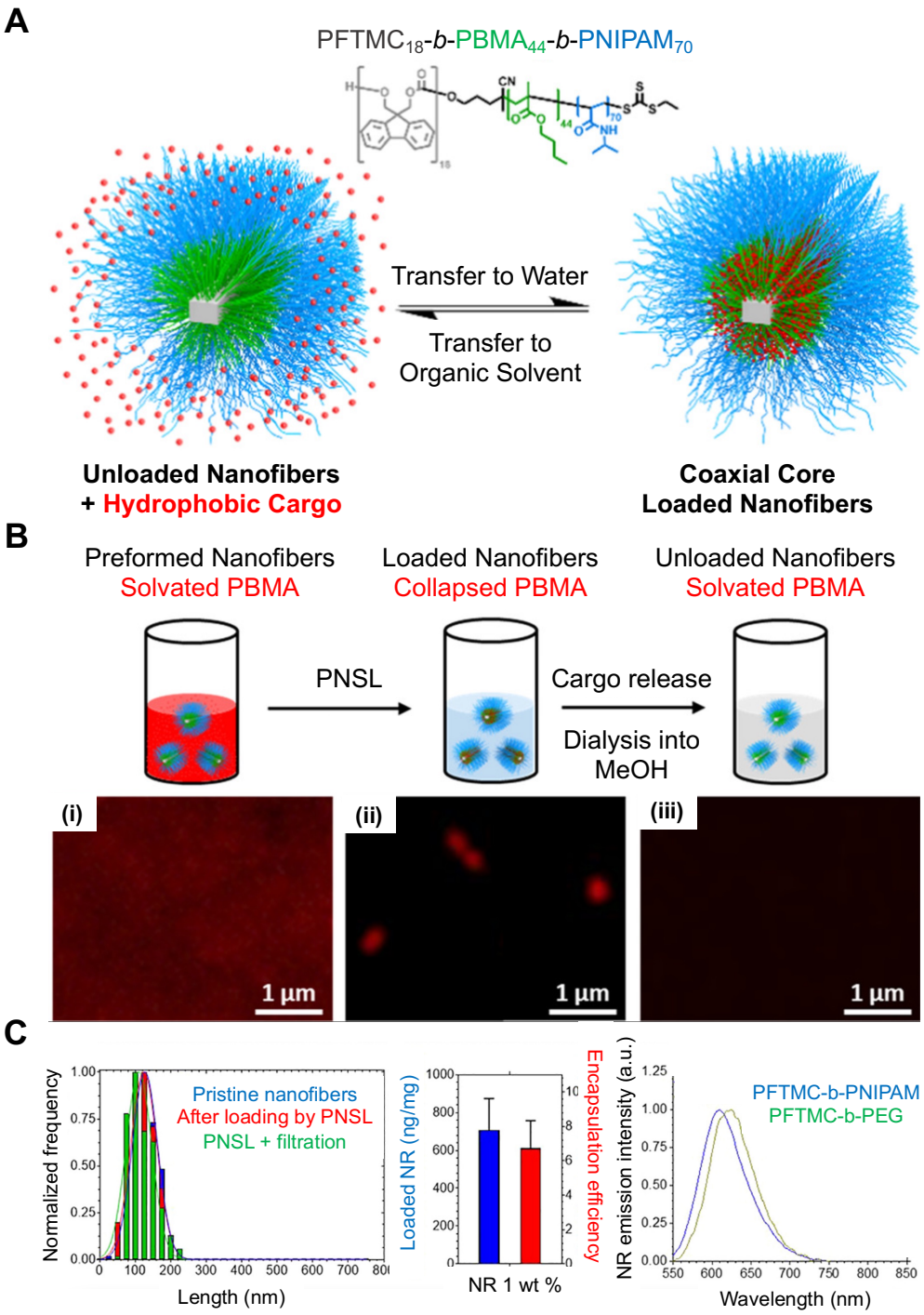


**Figure 1.15.** PFTMC-*b*-PNIPAM based nanofibers developed for drug-delivery applications. (A) Triblock copolymer nanofibers derived from PFTMC-*b*-PBMA-*b*-PNIPAM, where PBMA is an additional hydrophobic non-crystalline core which is able to encapsulate hydrophobic cargo upon

transfer into water. (B) Preformed-nanoparticle solvent-switch loading system developed in the reported literature, which involves the drug, and the nanoparticles present in a good solvent, which is then slowly transferred into water by syringe-pump, and the organic solvent is allowed to evaporate, localizing the hydrophobic cargo to the hydrophobic core-corona interface. (C) Length contour analysis of drug-loaded nanofibers, encapsulation efficiency and quantitative drug-loading capacity of triblock copolymer nanofibers, and fluorescence emission upon loading with Nile red, as reported by Garcia-Hernandez et al.[123] Reproduced with permission from the American Chemical Society, *Macromolecules* **2021**, *54* (12), 5784–5796.

Nucleic acid complexation has also been extensively investigated in our group over the past few years.[125–127] For this purpose, the BCP PFTMC-*b*-PDMAEMA is utilized, as the cationic PDMAEMA corona complexes to the anionic DNA with ease, resulting in the formation of stable "micelleplexes". The effect of nanofiber length on the DNA delivery was explored, with short seed nanofibers of approximately 25 nm in length exhibiting the highest transfection efficiencies relative to those > 70 nm in length, and greater than nanospheres (Figure 1.16A).[126] Further work determined that upon increasing the length of the PDMAEMA corona, more DNA can be complexed resulting in transfection efficiencies more than 1000× higher than the lipid industry standard lipofectamine (Figure 1.16B).[127] Both PFTMC-*b*-PDMAEMA nanofibers utilized for transfection displayed low toxicity at the concentrations of interest (Figure 1.16C, D). These results demonstrate that BCP nanofibers containing a PFTMC core-forming block are particularly promising for biomedical applications, and thus they are further explored in the remaining chapters of this thesis.

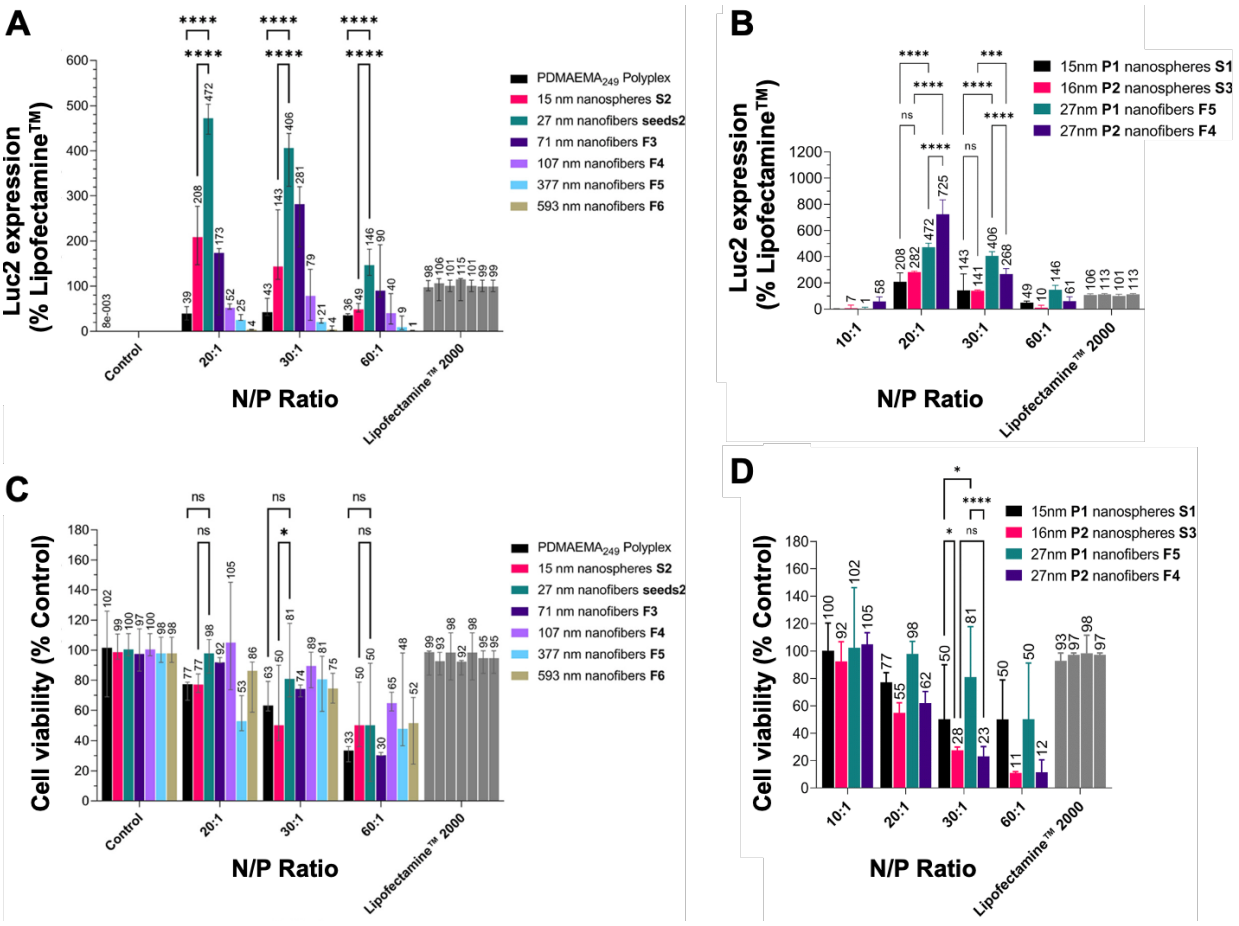


**Figure 1.16.** Transfection efficiency of PFTMC-*b*-PDMAEMA based nanofibers. (A) Transfection levels of PFTMC-*b*-PDMAEMA nanofibers in U87 GBM cells, as dependent on the length and the shape of the nanoparticles, with short seed nanofibers displaying the highest transfection levels at an N/P ratio of 20. (B) Transfection efficiency of PFTMC-*b*-PDMAEMA nanofibers with a longer coronal block degree of polymerization, enabling higher transfection than shorter coronal counterparts. (C) and (D) represent the relative cell viability determined for U87 GBM cells upon incubation with the PFTMC-*b*-PDMAEMA nanofiber samples, with shorter coronal lengths displaying lower overall cytotoxicity at higher N/P ratios. Reproduced with permission from the American Chemical Society, *J. Am. Chem. Soc*. **2022**, *144*, 19799–19812; Reproduced with permission from the Royal Society of Chemistry, *Biomater. Sci*. **2022**, *11*, 3512–3523.

## 1.6 Thesis objectives

This introduction has outlined the fundamental principles underlying block copolymer self-assembly, living CDSA, and nanomedicine. Recent work has demonstrated the potential utility of controlled, morphologically pure, and anisotropic nanoparticles for biomedical applications.[97,99,115,116,126,131] Nevertheless, further studies are required to determine the full therapeutic capabilities of these 1D nanofibers, with the key objectives of this thesis outlined below.

### 1.6.1 Investigate the antibacterial activity of cationic 1D nanofibers

Antibiotic resistance is an ever-growing, yet ancient issue facing today's generations worldwide. Traditional small molecules commonly target a very specific feature of either the bacterial membrane or a metabolic pathway, and small deviations in these structures arising from random mutations can render the entire family of antibiotics ineffective. Resistance can be triggered by the over-prescription of such therapies, as this can lead to constitutive exposure to low levels of therapeutics, which provide a selection pressure for resistant organisms and, eventually, ineffective eradication of disease. Thus, treatments with more general mechanisms of action are direly needed, as resistance is much more difficult to acquire when a broad characteristic of the bacterium is targeted. Polymeric materials have the potential to address this need. Various polymer assemblies have been previously synthesized for antibacterial applications, but these are limited to homopolymers or BCPs which undergo uncontrolled assembly in solution. This non-uniformity makes pin-pointing contributions from specific variables extremely difficult and can lead to erroneous conclusions being made. Therefore, the development of controlled polymeric assemblies which actively and generally target bacteria is of great interest. Furthermore, we wish

to explore the scope of antibacterial activity of such treatments, and if 1D particles can prevent the formation of resistance.

### 1.6.2 Understand bacteria-nanoparticle interactions

A critical hinderance to the universal implementation of nanomedicine treatments is the lack of understanding of the ultimate fate of the nanoparticle. As previously outlined, antibacterial polymer materials have been previously reported in the literature. Several observations have been made, with certain cationic groups appearing to have higher antibacterial activity than others, or different levels of activity observed against different strains of bacteria. Despite such publications, no details of why this occurs have yet to be reported. Therefore, a major goal of this work is to identify why we measure differential activity based on the assembly properties, through studies of their fundamental interactions with bacteria. This information will inform the design of polymer nanomaterials to enhance their potency, hopefully allowing for the next generation of antibacterial therapeutics to be developed.

### 1.6.3 Explore the clinical relevance of 1D nanomaterials for cargo delivery

Many polymeric drug-delivery vehicles have been developed, with several finding moderate degrees of success due to their ability to increase the bioavailability of the therapeutic, mostly through solubilization. However, these carriers are all spherical in shape and encapsulate the cargo within the amorphous core. Therefore, the development of a carrier which offers intrinsic advantages in delivery capability may not only increase the solubility of the drug, but also the effectiveness of the treatment if more of it is able to reach the target site. Therefore, we wished to explore the capacity of 1D nanofibers for therapeutic delivery in tumour models and for antibacterial activity, and determine if the 1D shape provides advantageous delivery properties

over traditional drug carriers, with the ultimate goal of achieving not only effective delivery, but increasing the potency of such treatments.

## 1.7 Thesis summary and collaborator acknowledgements

This thesis describes four research projects related to the development of 1D nanofibers, prepared via living CDSA, for applications in nanomedicine. The 5 ensuing chapters are as follows:

- Chapter 2. Uniform, length-tunable antibacterial diblock copolymer nanofibers
- Chapter 3. Mechanism of action and design of antibacterial block copolymer nanoparticles
- Chapter 4. Uniform block copolymer nanoparticles for the delivery of paclitaxel in 2D and 3D glioblastoma tumor models
- Chapter 5. Extending the scope of antibacterial activity of 1D crystalline-core nanofibers for overcoming antibacterial resistance
- Chapter 6. Conclusions and future work

In line with Prof. Ian Manners' research group policy, this thesis is comprised of self-contained chapters, each intended for publication. Each research project involved collaboration, with contributions outlined below, as well as expanded upon at the beginning of each chapter.

Chapter 2. This chapter was reproduced from *Polym. Chem.* **2022**, *13*, 2941-2949. Dr. J. D. Garcia-Hernandez performed the synthesis and self-assembly of PFTMC-*b*-PEG nanomaterials used in this work, as well as provided input on experimental design. Dr. S. T. G. Street performed the synthesis and self-assembly of PFTMC-*b*-PDMAEMA nanomaterials. R. Hof provided input on experimental design of the antibacterial assays.

Chapter 3. This chapter was reproduced from *J. Am. Chem. Soc.* **2024**, *146* (8), 5128-5141. Dr. S. T. G. Street assisted with experimental design and interpretation of results. B. E. Gowan, Department of Biology, University of Victoria, performed bacterial sample preparation for TEM analysis. L. H Da-Silva-Correa, Department of Civil Engineering in the research group of Dr. Heather Buckley, performed SEM microscopy of bacterial samples. R. Hof assisted with training in biological techniques and provided useful advice.

Chapter 4. This chapter was reproduced from *Biomater. Sci*. **2024**, *Submitted.* This work was carried out jointly with L. K Shopperly of the research group of Prof. Stephanie Willerth, University of Victoria. 2D cell culture studies were carried out by L. K Shopperly, and 3D cell culture studies were performed by L. K Shopperly and M. R. Perez, of Prof. Stephanie Willerth's research group, University of Victoria.

Chapter 5. This chapter contains unpublished results. Dr. J. D Garcia-Hernandez performed the synthesis and self-assembly of PFTMC-*b*-PEG and PFTMC-*b*-PNIPAM nanomaterials.

## 1.8 References


1. Whitesides, G. M.; Grzybowski, B. Self-Assembly at All Scales. *Science* **2002**, *295* (5564), 2418–2421. DOI: 10.1126/SCIENCE.1070821
2. Simon, H. A. The Architecture of Complexity. *Proc. Am. Phil. Soc.* **1962**, *106* (6), 467–482.
3. Watson, J. D.; Crick, F. H. The Structure of DNA. *Cold Spring Harb. Symp. Quant. Biol.* **1953**, *18*, 123–131. DOI: 10.1101/SQB.1953.018.01.020.
4. Worcel, A.; Benyajati, C. Higher Order Coiling of DNA in Chromatin. *Cell* **1977**, *12*, 83–100. DOI: 10.1016/0092-8674(77)90187-8.
5. Richmond, T. J.; Davey, C. A. The Structure of DNA in the Nucleosome Core. *Nature* **2003**, *423* (6936), 145–150. DOI: doi.org/10.1038/nature01595.
6. Travers, A.; Muskhelishvili, G. DNA Structure and Function. *FEBS J.* **2015**, *282* (12), 2279–2295. DOI: 10.1111/FEBS.13307.
7. Kushner, D. J. Self-Assembly of Biological Structures. *Bacteriol. Rev.* **1969**, *33* (2), 302–309. DOI: 10.1128/BR.33.2.302-345.1969.
8. Gulati, N. M.; Pitek, A. S.; Steinmetz, N. F.; Stewart, P. L. Cryo-Electron Tomography Investigation of Serum Albumin-Camouflaged Tobacco Mosaic Virus Nanoparticles. *Nanoscale* **2017**, *9* (10), 3408–3415. DOI: 10.1039/C6NR06948G.
9. Fratzl, P.; Weinkamer, R. Nature's Hierarchical Materials. *Prog. Mater. Sci.* **2007**, *52* (8), 1263–1334. DOI: 10.1016/J.PMATSCI.2007.06.001.
10. Ritchie, R. O. The Conflicts between Strength and Toughness. *Nat. Mater.* **2011**, *10* (11), 817–822. DOI: 10.1038/nmat3115.

11. Gotti, C.; Sensini, A.; Zucchelli, A.; Carloni, R.; Focarete, M. L. Hierarchical Fibrous Structures for Muscle-Inspired Soft-actuators: A Review. *Appl. Mater. Today* **2020**, *20*, 100772. DOI: 10.1016/J.APMT.2020.100772.
12. Adelstein, R. S.; Eisenberg, E. Regulation and Kinetics of the Actin-Myosin-ATP Interaction. *Ann. Rev. Biochem.* **1980**, *49*, 921–956. DOI: 10.1146/ANNUREV.BI.49.070180.004421.
13. Ottino, J. M. Engineering Complex Systems. *Nature* **2004**, *427* (6973), 399. DOI: 10.1038/427399a.
14. Bhalla, U. S.; Iyengar, R. Emergent Properties of Networks of Biological Signaling Pathways. *Science* **1999**, *283* (5400), 381–387. DOI: 10.1126/SCIENCE.283.5400.381.
15. Grzybowski, B. A.; Wilmer, C. E.; Kim, J.; Browne, K. P.; Bishop, K. J. M. Self-Assembly: From Crystals to Cells. *Soft Matter* **2009**, *5* (6), 1110–1128. DOI: 10.1039/B819321P.
16. Arango-Restrepo, A.; Barragán, D.; Rubi, J. M. Self-Assembling Outside Equilibrium: Emergence of Structures Mediated by Dissipation. *Phys. Chem. Chem. Phys.* **2019**, *21* (32), 17475–17493. DOI: 10.1039/C9CP01088B.
17. Mattia, E.; Otto, S. Supramolecular Systems Chemistry. *Nat. Nanotechnol.* **2015**, *10* (2), 111–119. DOI: 10.1038/nnano.2014.337.
18. Whitesides, G. M.; Kriebel, J. K.; Mayers, B. T. Self-Assembly and Nanostructured Materials. *Nanoscale Assembly* **2005**, 217–239. DOI: 10.1007/0-387-25656-3_9.
19. Biswas, A.; Bayer, I. S.; Biris, A. S.; Wang, T.; Dervishi, E.; Faupel, F. Advances in Top–Down and Bottom–Up Surface Nanofabrication: Techniques, Applications & Future Prospects. *Adv. Colloid Interface Sci.* **2012**, *170*, 2–27. DOI: 10.1016/J.CIS.2011.11.001.

20. Cook, A. B.; Clemons, T. D. Bottom-Up versus Top-Down Strategies for Morphology Control in Polymer-Based Biomedical Materials. *Adv. Nanobiomed. Res.* **2022**, *2*, 2100087. DOI: 10.1002/ANBR.202100087.
21. Hawker, C. J.; Russell, T. P. Block Copolymer Lithography: Merging "Bottom-Up" with "Top-Down" Processes. *MRS Bull.* **2005**, *30* (12), 952–966. DOI: 10.1557/MRS2005.249.
22. Champion, J. A.; Katare, Y. K.; Mitragotri, S. Making Polymeric Micro- and Nanoparticles of Complex Shapes. *Proc. Natl. Acad. Sci.* **2007,** *104* (29), 11901–11904. DOI: 10.1073/pnas.0705326104
23. Cheng, J. Y.; Ross, C. A.; Smith, H. I.; Thomas, E. L. Templated Self-Assembly of Block Copolymers: Top-Down Helps Bottom-Up. *Adv. Mater.* **2006**, *18* (19), 2505–2521. DOI: 10.1002/ADMA.200502651.
24. Zhang, S. Building from the Bottom Up. *Mater. Today* **2003**, *6* (5), 20–27. DOI: 10.1016/S1369-7021(03)00530-3.
25. Cheng, J. Y.; Mayes, A. M.; Ross, C. A. Nanostructure Engineering by Templated Self-Assembly of Block Copolymers. *Nat. Mater.* **2004**, *3* (11), 823–828. DOI: 10.1038/nmat1211.
26. Ikkala, O.; Ten Brinke, G. Hierarchical Self-Assembly in Polymeric Complexes: Towards Functional Materials. *Chem. Commun.* **2004**, (19), 2131–2137. DOI: 10.1039/B403983A.
27. Tu, R. S.; Tirrell, M. Bottom-Up Design of Biomimetic Assemblies. *Adv. Drug Deliv. Rev.* **2004**, *56* (11), 1537–1563. DOI: 10.1016/J.ADDR.2003.10.047.
28. De Feyter, S.; De Schryver, F. C. Two-Dimensional Supramolecular Self-Assembly Probed by Scanning Tunneling Microscopy. *Chem. Soc. Rev.* **2003**, *32* (3), 139–150. DOI: 10.1039/B206566P.

29. van der Weegen, R.; Teunissen, A. J. P.; Meijer, E. W. Directing the Self-Assembly Behaviour of Porphyrin-Based Supramolecular Systems. *Chem. Eur. J.* **2017**, *23* (15), 3773–3783. DOI: 10.1002/CHEM.201605872.

30. Chakrabarty, R.; Mukherjee, P. S.; Stang, P. J. Supramolecular Coordination: Self-Assembly of Finite Two- and Three-Dimensional Ensembles. *Chem. Rev.* **2011**, *111* (11), 6810–6918. DOI: 10.1021/CR200077M.

31. De Greef, T. F. A.; Smulders, M. M. J.; Wolffs, M.; Schenning, A. P. H. J.; Sijbesma, R. P.; Meijer, E. W. Supramolecular Polymerization. *Chem. Rev.* **2009**, *109* (11), 5687–5754. DOI: 10.1021/CR900181U.

32. Weingarten, A. S.; Kazantsev, R. V.; Palmer, L. C.; McClendon, M.; Koltonow, A. R.; Samuel, A. P. S.; Kiebala, D. J.; Wasielewski, M. R.; Stupp, S. I. Self-Assembling Hydrogel Scaffolds for Photocatalytic Hydrogen Production. *Nat. Chem.* **2014**, *6*, 964–970. DOI: 10.1038/nchem.2075.

33. Lombardo, D.; Kiselev, M. A.; Magazù, S.; Calandra, P. Amphiphiles Self-Assembly: Basic Concepts and Future Perspectives of Supramolecular Approaches. *Adv. Condens. Matter Phys.* **2015**, 151683. DOI:10.1155/2015/151683.

34. Greaves, T. L.; Drummond, C. J. Solvent Nanostructure, the Solvophobic Effect and Amphiphile Self-Assembly in Ionic Liquids. *Chem. Soc. Rev.* **2013**, *42* (3), 1096–1120. DOI: 10.1039/C2CS35339C.

35. Mülhaupt, R. Hermann Staudinger and the Origin of Macromolecular Chemistry. *Angew. Chem. Int. Ed.* **2004**, *43* (9), 1054–1063. DOI: 10.1002/ANIE.200330070.

36. Yagci, Y.; Tasdelen, M. A. Mechanistic Transformations Involving Living and Controlled/Living Polymerization Methods. *Prog. Polym. Sci.* **2006**, *31* (12), 1133–1170. DOI: 10.1016/J.PROGPOLYMSCI.2006.07.003.
37. Asua, J. M. Polymer Reaction Engineering. *Polym. React. Engin.* **2008**, 1–367. DOI: 10.1002/9780470692134.
38. Boyer, C.; Bulmus, V.; Davis, T. P.; Ladmiral, V.; Liu, J.; Perrier, S. Bioapplications of RAFT Polymerization. *Chem. Rev.* **2009**, *109* (11), 5402–5436. DOI: 10.1021/CR9001403
39. Honeyman, C. H.; Manners, I.; Morrissey, C. T.; Allcock, H. R. Ambient Temperature Synthesis of Poly(Dichlorophosphazene) with Molecular Weight Control. *J. Am. Chem. Soc.* **1995**, *117* (26), 7035–7036. DOI: 10.1021/JA00131A040.
40. Webster, O. W. Living Polymerization Methods. *Science* **1991**, *251* (4996), 887–893. DOI: 10.1126/SCIENCE.251.4996.887.
41. Szwarc, M. Living Polymers and Mechanisms of Anionic Polymerization. *Living Polymers and Mechanisms of Anionic Polymerization* **1983**, 1–177. DOI: 10.1007/3-540-12047-5_1.
42. Leibler, L. Theory of Microphase Separation in Block Copolymers. *Macromolecules* **1980**, *13* (6), 1602–1617. DOI: 10.1021/MA60078A047.
43. Peinemann, K. V.; Abetz, V.; Simon, P. F. W. Asymmetric Superstructure Formed in a Block Copolymer via Phase Separation. *Nat. Mater.* **2007**, *6* (12), 992–996. DOI: 10.1038/nmat2038.
44. Farrell, R. A.; Fitzgerald, T. G.; Borah, D.; Holmes, J. D.; Morris, M. A. Chemical Interactions and Their Role in the Microphase Separation of Block Copolymer Thin Films. *Int. J. Mol. Sci.* **2009**, *10* (9), 3671–3712. DOI: 10.3390/IJMS10093671.

45. He, W. N.; Xu, J. T. Crystallization Assisted Self-Assembly of Semicrystalline Block Copolymers. *Prog. Polym. Sci.* **2012**, *37* (10), 1350–1400. DOI: 10.1016/J.PROGPOLYMSCI.2012.05.002.

46. Shiomi, T.; Tsukada, H.; Takeshita, H.; Takenaka, K.; Tezuka, Y. Crystallization of Semicrystalline Block Copolymers Containing a Glassy Amorphous Component. *Polymer* **2001**, *42* (11), 4997–5004. DOI: 10.1016/S0032-3861(00)00894-6.

47. Mai, Y.; Eisenberg, A. Self-Assembly of Block Copolymers. *Chem. Soc. Rev.* **2012**, *41*, 5969–5985. DOI: 10.1039/c2cs35115c.

48. Bates, F. S.; Fredrickson, G. H. Block Copolymer Thermodynamics: Theory and Experiment. **2003**, *41* (1), 525–557. DOI: 10.1146/ANNUREV.PC.41.100190.002521.

49. Tager, A. A.; Adamova, L. V.; Kolmakova, L. K.; Nokhrina, N. N.; Valetskii, P. M.; Rogovina, L. Z.; Starozhuk, I. P. Thermodynamics of the Compatibility of Blocks in Block Copolymers. *Polym. Sci. U.S.S.R.* **1982**, *24* (10), 2331–2339. DOI: 10.1016/0032-3950(82)90104-6.

50. Jain, S.; Bates, F. S. Consequences of Nonergodicity in Aqueous Binary PEO-PB Micellar Dispersions. *Macromolecules* **2004**, *37* (4), 1511–1523. DOI: 10.1021/MA035467J.

51. Lund, R.; Willner, L.; Richter, D.; Dormidontova, E. E. Equilibrium Chain Exchange Kinetics of Diblock Copolymer Micelles: Tuning and Logarithmic Relaxation. *Macromolecules* **2006**, *39* (13), 4566–4575. DOI: 10.1021/MA060328Y.

52. Dormidontova, E. E. Micellization Kinetics in Block Copolymer Solutions: Scaling Model. *Macromolecules* **1999**, *32* (22), 7630–7644. DOI: 10.1021/MA9809029.

53. Cameron, N. S.; Corbierre, M. K.; Eisenberg, A. Asymmetric Amphiphilic Block Copolymers in Solution: A Morphological Wonderland. *Can. J. Chem.* **1999**, *77* (8), 1311–1326. DOI: 10.1139/V99-141.

54. Zhang, L.; Eisenberg, A. Multiple Morphologies of "Crew-Cut" Aggregates of Polystyrene-b-Poly(Acrylic Acid) Block Copolymers. *Science* **1995**, *268* (5218), 1728–1731. DOI: 10.1126/SCIENCE.268.5218.1728.

55. Zhang, L.; Eisenberg, A. Multiple Morphologies and Characteristics of "Crew-Cut" Micelle-like Aggregates of Polystyrene-*b*-Poly(Acrylic Acid) Diblock Copolymers in Aqueous Solutions. *J. Am. Chem. Soc.* **1996**, *118* (13), 3168–3181. DOI: 10.1021/JA953709S.

56. Hayward, R. C.; Pochan, D. J. Tailored Assemblies of Block Copolymers in Solution: It is All About the Process. *Macromolecules* **2010**, *43* (8), 3577–3584. DOI: 10.1021/MA9026806.

57. Wang, X.; Guerin, G.; Wang, H.; Wang, Y.; Manners, I.; Winnik, M. A. Cylindrical Block Copolymer Micelles and Co-Micelles of Controlled Length and Architecture. *Science* **2007**, *317* (5838), 644–647. DOI: 10.1126/SCIENCE.1141382.

58. Lotz, B.; Kovacs, A. J.; Bassett, G. A.; Keller, A. Properties of Copolymers Composed of One Poly-Ethylene-Oxide and One Polystyrene Block - II. Morphology of Single Crystals. *Kolloid-Z.u.Z. Polymere* **1966**, *209* (2), 115–128. DOI: 10.1007/BF01500629.

59. Gilroy, J. B.; Gädt, T.; Whittell, G. R.; Chabanne, L.; Mitchels, J. M.; Richardson, R. M.; Winnik, M. A.; Manners, I. Monodisperse Cylindrical Micelles by Crystallization-Driven Living Self-Assembly. *Nat. Chem.* **2010**, *2* (7), 566–570. DOI: 10.1038/nchem.664.

60. Hamley, I. W. Crystallization in Block Copolymers. *Adv. Polym. Sci.* **1999**, *148*, 114–137. DOI: 10.1007/3-540-48836-7_2.

61. Ganda, S.; Stenzel, M. H. Concepts, Fabrication Methods and Applications of Living Crystallization-Driven Self-Assembly of Block Copolymers. *Prog. Polym. Sci*. **2020**, 101195. DOI: 10.1016/j.progpolymsci.2019.101195.

62. Lammertink, R. G. H.; Hempenius, M. A.; Manners, I.; Vancso, G. J. Crystallization and Melting Behavior of Poly(Ferrocenyldimethylsilanes) Obtained by Anionic Polymerization. *Macromolecules* **1998**, *31* (3), 795–800. DOI: 10.1021/MA9711248.

63. Massey, J. A.; Temple, K.; Cao, L.; Rharbi, Y.; Raez, J.; Winnik, M. A.; Manners, I. Self-Assembly of Organometallic Block Copolymers: The Role of Crystallinity of the Core-Forming Polyferrocene Block in the Micellar Morphologies Formed by Poly(Ferrocenylsilane-b-Dimethylsiloxane) in n-Alkane Solvents. *J. Am. Chem. Soc.* **2000**, *122* (47), 11577–11584. DOI: 10.1021/JA002205D.

64. MacFarlane, L.; Zhao, C.; Cai, J.; Qiu, H.; Manners, I. Emerging Applications for Living Crystallization-Driven Self-Assembly. *Chem. Sci.* **2021**, *12*, 4661–4682. DOI: 10.1039/d0sc06878k.

65. Guérin, G.; Wang, H.; Manners, I.; Winnik, M. A. Fragmentation of Fiberlike Structures: Sonication Studies of Cylindrical Block Copolymer Micelles and Behavioral Comparisons to Biological Fibrils. *J. Am. Chem. Soc.* **2008**, *130* (44), 14763–14771. DOI: 10.1021/ja805262v.

66. Arno, M. C.; Inam, M.; Coe, Z.; Cambridge, G.; Macdougall, L. J.; Keogh, R.; Dove, A. P.; O'Reilly, R. K. Precision Epitaxy for Aqueous 1D and 2D Poly(ε-Caprolactone) Assemblies. *J. Am. Chem. Soc.* **2017**, *139* (46), 16980–16985. DOI: 10.1021/jacs.7b10199.

67. Yu, W.; Foster, J. C.; Dove, A. P.; O'Reilly, R. K. Length Control of Biodegradable Fiber-Like Micelles via Tuning Solubility: A Self-Seeding Crystallization-Driven Self-Assembly of Poly(ε -Caprolactone)-Containing Triblock Copolymers. *Macromolecules* **2020**, *53* (4), 1514–1521. DOI: 10.1021/ACS.MACROMOL.9B02613.

68. Vespa, M.; Hudson, Z. M.; Manners, I. Homogeneous and Segmented Nanofibers with a Conjugated Poly[3-(2′-Ethylhexyl)Thiophene] Core via Living Crystallization-Driven Self-

Assembly. *Macromolecules* **2023**, *57* (4), 1509–1520. DOI: 10.1021/ACS.MACROMOL.3C02357.

69. MacFarlane, L. R.; Shaikh, H.; Garcia-Hernandez, J. D.; Vespa, M.; Fukui, T.; Manners, I. Functional Nanoparticles through π-Conjugated Polymer Self-Assembly. *Nat. Rev. Mater.* **2020**, *6*, 7–26. DOI: 10.1038/s41578-020-00233-4.
70. Li, X.; Gao, Y.; Boott, C. E.; Hayward, D. W.; Harniman, R.; Whittell, G. R.; Richardson, R. M.; Winnik, M. A.; Manners, I. "Cross" Supermicelles via the Hierarchical Assembly of Amphiphilic Cylindrical Triblock Comicelles. *J. Am. Chem. Soc.* **2016**, *138* (12), 4087–4095. DOI: 10.1021/JACS.5B12735.
71. Qiu, H.; Hudson, Z. M.; Winnik, M. A.; Manners, I. Multidimensional Hierarchical Self-Assembly of Amphiphilic Cylindrical Block Comicelles. *Science* **2015**, *347* (6228), 1329–1332. DOI: 10.1126/SCIENCE.1261816.
72. Li, X.; Gao, Y.; Boott, C. E.; Winnik, M. A.; Manners, I. Non-Covalent Synthesis of Supermicelles with Complex Architectures Using Spatially Confined Hydrogen-Bonding Interactions. *Nat. Commun.* **2015**, *6*, 1–8. DOI: 10.1038/ncomms9127.
73. Merg, A. D.; Van Genderen, E.; Bazrafshan, A.; Su, H.; Zuo, X.; Touponse, G.; Blum, T. B.; Salaita, K.; Abrahams, J. P.; Conticello, V. P. Seeded Heteroepitaxial Growth of Crystallizable Collagen Triple Helices: Engineering Multifunctional Two-Dimensional Core-Shell Nanostructures. *J. Am. Chem. Soc.* **2019**, *141* (51), 20107–20117. DOI: 10.1021/JACS.9B09335.
74. He, Y.; Eloi, J. C.; Harniman, R. L.; Richardson, R. M.; Whittell, G. R.; Mathers, R. T.; Dove, A. P.; O'Reilly, R. K.; Manners, I. Uniform Biodegradable Fiber-Like Micelles and Block Comicelles via "Living" Crystallization-Driven Self-Assembly of Poly(l-Lactide) Block

Copolymers: The Importance of Reducing Unimer Self-Nucleation via Hydrogen Bond Disruption. *J. Am. Chem. Soc.* **2019**, *141* (48), 19088–19098. DOI: 10.1021/JACS.9B09885.

75. Rupar, P. A.; Chabanne, L.; Winnik, M. A.; Manners, I. Non-Centrosymmetric Cylindrical Micelles by Unidirectional Growth. *Science* **2012**, *337* (6094), 559–562. DOI: 10.1126/SCIENCE.1221206.
76. Qiu, H.; Cambridge, G.; Winnik, M. A.; Manners, I. Multi-Armed Micelles and Block Co-Micelles via Crystallization-Driven Self-Assembly with Homopolymer Nanocrystals as Initiators. *J. Am. Chem. Soc.* **2013**, *135* (33), 12180–12183. DOI: 10.1021/JA404100W.
77. Hudson, Z. M.; Lunn, D. J.; Winnik, M. A.; Manners, I. Colour-Tunable Fluorescent Multiblock Micelles. *Nat. Commun.* **2014**, *5*, 1–8. DOI: 10.1038/ncomms4372.
78. Nazemi, A.; He, X.; Macfarlane, L. R.; Harniman, R. L.; Hsiao, M. S.; Winnik, M. A.; Faul, C. F. J.; Manners, I. Uniform "Patchy" Platelets by Seeded Heteroepitaxial Growth of Crystallizable Polymer Blends in Two Dimensions. *J. Am. Chem. Soc.* **2017**, *139* (12), 4409–4417. DOI: 10.1021/JACS.6B12503.
79. Qiu, H.; Gao, Y.; Boott, C. E.; Gould, O. E. C.; Harniman, R. L.; Miles, M. J.; Webb, S. E. D.; Winnik, M. A.; Manners, I. Uniform Patchy and Hollow Rectangular Platelet Micelles from Crystallizable Polymer Blends. *Science* **2016**, *352* (6286), 697–701. DOI: 10.1126/SCIENCE.AAD9521.
80. Betty, N.; Kim, Y. S.; Rutka, J. T.; Chan, W. C. W.; Nanomedicine. *N. Engl. J. Med.* **2010**, *363* (25), 2434–2443. DOI: 10.1056/NEJMRA0912273.
81. Chan, W. C. W. Nanomedicine 2.0. *Acc. Chem. Res.* **2017**, *50*, 44, 627–632. DOI: 10.1021/acs.accounts.6b00629.

82. Pelaz, B.; Alexiou, C.; Alvarez-Puebla, R. A.; Alves, F.; Andrews, A. M.; Ashraf, S.; Balogh, L. P.; Ballerini, L.; Bestetti, A.; Brendel, C.; et al. Diverse Applications of Nanomedicine. *ACS Nano* **2017**, *11* (3), 2313–2381. DOI: 10.1021/acsnano.6b06040.

83. Riehemann, K.; Schneider, S. W.; Luger, T. A.; Godin, B.; Ferrari, M.; Fuchs, H. Nanomedicine—Challenge and Perspectives. *Angew. Chem. Int. Ed.* **2009**, *48* (5), 872–897. DOI: 10.1002/ANIE.200802585.

84. Park, K. The Beginning of the End of the Nanomedicine Hype. *J. Control. Release* **2019**, *305*, 221–222. DOI: 10.1016/J.JCONREL.2019.05.044.

85. Patra, J. K.; Das, G.; Fraceto, L. F.; Campos, E. V. R.; Rodriguez-Torres, M. D. P.; Acosta-Torres, L. S.; Diaz-Torres, L. A.; Grillo, R.; Swamy, M. K.; Sharma, S.; Habtemariam, S.; Shin, H. S. Nano Based Drug Delivery Systems: Recent Developments and Future Prospects. *J. Nanobiotechnol.* **2018**, *16*, 1–33. DOI: 10.1186/S12951-018-0392-8.

86. Germain, M.; Caputo, F.; Metcalfe, S.; Tosi, G.; Spring, K.; Åslund, A. K. O.; Pottier, A.; Schiffelers, R.; Ceccaldi, A.; Schmid, R. Delivering the Power of Nanomedicine to Patients Today. *J. Control. Release* **2020**, *326*, 164–171. DOI: 10.1016/J.JCONREL.2020.07.007.

87. Mitchell, M. J.; Billingsley, M. M.; Haley, R. M.; Wechsler, M. E.; Peppas, N. A.; Langer, R. Engineering Precision Nanoparticles for Drug Delivery. *Nat. Rev. Drug Discov.* **2020**, *20* (2), 101–124. DOI: 10.1038/s41573-020-0090-8.

88. Yang, J.; Wang, X.; Wang, B.; Park, K.; Wooley, K.; Zhang, S. Challenging the Fundamental Conjectures in Nanoparticle Drug Delivery for Chemotherapy Treatment of Solid Cancers. *Adv. Drug Deliv. Rev.* **2022**, *190*, 114525. DOI: 10.1016/J.ADDR.2022.114525.

89. Blanco, E.; Shen, H.; Ferrari, M. Principles of Nanoparticle Design for Overcoming Biological Barriers to Drug Delivery. *Nat. Biotechnol.* **2015**, *33* (9), 941–951. DOI: 10.1038/nbt.3330.

90. Chan, W. C. W. Principles of Nanoparticle Delivery to Solid Tumors. *BME Front.* **2023**, *4*, 0016. DOI: 10.34133/BMEF.0016.

91. Jiang, W.; Kim, B. Y. S.; Rutka, J. T.; Chan, W. C. W. Nanoparticle-Mediated Cellular Response Is Size-Dependent. *Nat. Nanotechnol.* **2008**, *3* (3), 145–150. DOI: 10.1038/nnano.2008.30.

92. Cabral, H.; Matsumoto, Y.; Mizuno, K.; Chen, Q.; Murakami, M.; Kimura, M.; Terada, Y.; Kano, M. R.; Miyazono, K.; Uesaka, M.; Nishiyama, N.; Kataoka, K. Accumulation of Sub-100 nm Polymeric Micelles in Poorly Permeable Tumours Depends on Size. *Nat. Nanotechnol.* **2011**, *6* (12), 815–823. DOI: 10.1038/nnano.2011.166.

93. Geng, Y.; Dalhaimer, P.; Cai, S.; Tsai, R.; Tewari, M.; Minko, T.; Discher, D. E. Shape Effects of Filaments versus Spherical Particles in Flow and Drug Delivery. *Nat. Nanotechnol.* **2007**, *2* (4), 249–255. DOI: 10.1038/nnano.2007.70.

94. Christian, D. A.; Cai, S.; Garbuzenko, O. B.; Harada, T.; Zajac, A. L.; Minko, T.; Discher, D. E. Flexible Filaments for in Vivo Imaging and Delivery: Persistent Circulation of Filomicelles Opens the Dosage Window for Sustained Tumor Shrinkage. *Mol. Pharm.* **2009**, *6* (5), 1343–1352. DOI: 10.1021/MP900022M.

95. Yang, L.; Zhou, Z.; Song, J.; Chen, X. Anisotropic Nanomaterials for Shape-Dependent Physicochemical and Biomedical Applications. *Chem. Soc. Rev.* **2019**, *48* (19), 5140–5176. DOI: 10.1039/C9CS00011A.

96. Kohout, C.; Santi, C.; Polito, L. Anisotropic Gold Nanoparticles in Biomedical Applications. *Int. J. Mol. Sci.* **2018**, *19* (11), 3385. DOI: 10.3390/IJMS19113385.

97. Pearce, A. K.; Wilks, T. R.; Arno, M. C.; O'Reilly, R. K. Synthesis and Applications of Anisotropic Nanoparticles with Precisely Defined Dimensions. *Nat. Rev. Chem.* **2020**, *5*, 21–45. DOI: 10.1038/s41570-020-00232-7.

98. Meyer, R. A.; Green, J. J. Shaping the Future of Nanomedicine: Anisotropy in Polymeric Nanoparticle Design. *Wiley Interdiscip. Rev. Nanomed. Nanobiotechnol.* **2016**, *8* (2), 191–207. DOI: 10.1002/WNAN.1348.

99. Song, Y.; Elsabahy, M.; Collins, C. A.; Khan, S.; Li, R.; Hreha, T. N.; Shen, Y.; Lin, Y. N.; Letteri, R. A.; Su, L.; Dong, M.; Zhang, F.; Hunstad, D. A.; Wooley, K. L. Morphologic Design of Silver-Bearing Sugar-Based Polymer Nanoparticles for Uroepithelial Cell Binding and Antimicrobial Delivery. *Nano Lett.* **2021**, *21* (12), 4990–4998. DOI: 10.1021/ACS.NANOLETT.1C00776.

100. Champion, J. A.; Mitragotri, S. Role of Target Geometry in Phagocytosis. *Proc. Natl. Acad. Sci. USA* **2006**, *103* (13), 4930–4934. DOI: 10.1073/PNAS.0600997103.

101. Sharma, G.; Valenta, D. T.; Altman, Y.; Harvey, S.; Xie, H.; Mitragotri, S.; Smith, J. W. Polymer Particle Shape Independently Influences Binding and Internalization by Macrophages. *J. Control. Release* **2010**, *147* (3), 408–412. DOI: 10.1016/J.JCONREL.2010.07.116.

102. Li, Z.; Sun, L.; Zhang, Y.; Dove, A. P.; O'Reilly, R. K.; Chen, G. *ACS Macro Letters* **2016**, *5* (9), 1059–1064. DOI: 10.1021/acsmacrolett.6b00419.

103. Xiong, F.; Tian, J.; Hu, K.; Zheng, X.; Sun, J.; Yan, C.; Yao, J.; Song, L.; Zhang, Y.; Gu, N. *Nanoscale* **2016**, *8* (39), 17085–17089. DOI: 10.1039/C6NR05781K.

104. Kolhar, P.; Anselmo, A. C.; Gupta, V.; Pant, K.; Prabhakarpandian, B.; Ruoslahti, E.; Mitragotri, S. Using Shape Effects to Target Antibody-Coated Nanoparticles to Lung and

Brain Endothelium. *Proc. Natl. Acad. Sci. USA* **2013**, *110* (26), 10753–10758. DOI: 10.1073/PNAS.1308345110.

105. Jiang, X.; Qu, W.; Pan, D.; Ren, Y.; Williford, J. M.; Cui, H.; Luijten, E.; Mao, H. Q. Plasmid-Templated Shape Control of Condensed DNA–Block Copolymer Nanoparticles. *Adv. Mater.* **2013**, *25* (2), 227–232. DOI: 10.1002/ADMA.201202932.

106. Tian, J.; Zhang, Y.; Du, L.; He, Y.; Jin, X. H.; Pearce, S.; Eloi, J. C.; Harniman, R. L.; Alibhai, D.; Ye, R.; Phillips, D. L.; Manners, I. Tailored Self-Assembled Photocatalytic Nanofibres for Visible-Light-Driven Hydrogen Production. *Nat. Chem.* **2020**, *12* (12), 1150–1156. DOI: 10.1038/s41557-020-00580-3.

107. Jin, X. H.; Price, M. B.; Finnegan, J. R.; Boott, C. E.; Richter, J. M.; Rao, A.; Matthew Menke, S.; Friend, R. H.; Whittell, G. R.; Manners, I. Long-Range Exciton Transport in Conjugated Polymer Nanofibers Prepared by Seeded Growth. *Science* **2018**, *360* (6391), 897–900. DOI: 10.1126/SCIENCE.AAR8104.

108. Hayward, D. W.; Lunn, D. J.; Seddon, A.; Finnegan, J. R.; Gould, O. E. C.; Magdysyuk, O.; Manners, I.; Whittell, G. R.; Richardson, R. M. Structure of the Crystalline Core of Fiber-Like Polythiophene Block Copolymer Micelles. *Macromolecules* **2018**, *51* (8), 3097–3106. DOI: 10.1021/ACS.MACROMOL.7B02552.

109. Cai, J.; Li, C.; Kong, N.; Lu, Y.; Lin, G.; Wang, X.; Yao, Y.; Manners, I.; Qiu, H. Tailored Multifunctional Micellar Brushes via Crystallization-Driven Growth from a Surface. *Science* **2019**, *366* (6469), 1095–1098. DOI: 10.1126/SCIENCE.AAX9075.

110. Street, S. T. G.; He, Y.; Jin, X. H.; Hodgson, L.; Verkade, P.; Manners, I. Cellular Uptake and Targeting of Low Dispersity, Dual Emissive, Segmented Block Copolymer Nanofibers. *Chem. Sci.* **2020**, *11* (32), 8394–8408. DOI: 10.1039/D0SC02593C.

111. Tritschler, U.; Pearce, S.; Gwyther, J.; Whittell, G. R.; Manners, I. 50th Anniversary Perspective: Functional Nanoparticles from the Solution Self-Assembly of Block Copolymers. *Macromolecules* **2017**, *50* (9), 3439–3463. DOI: 10.1021/ACS.MACROMOL.6B02767.

112. Lei, S.; Tian, J.; Kang, Y.; Zhang, Y.; Manners, I. AIE-Active, Stimuli-Responsive Fluorescent 2D Block Copolymer Nanoplatelets Based on Corona Chain Compression. *J. Am. Chem. Soc.* **2022**, *144* (38), 17630–17641. DOI: 10.1021/JACS.2C07133.

113. Ellis, C. E.; Fukui, T.; Cordoba, C.; Blackburn, A.; Manners, I. Towards Scalable, Low Dispersity, and Dimensionally Tunable 2D Platelets Using Living Crystallization-Driven Self-Assembly. *Polym. Chem.* **2021**, *12* (25), 3650–3660. DOI: 10.1039/D1PY00571E.

114. Petzetakis, N.; Walker, D.; Dove, A. P.; O'Reilly, R. K. Crystallization-Driven Sphere-to-Rod Transition of Poly(Lactide)-b-Poly(Acrylic Acid) Diblock Copolymers : Mechanism and Kinetics. *Soft Matter* **2012**, *8* (28), 7408–7414. DOI: 10.1039/C2SM25247C.

115. Inam, M.; Foster, J. C.; Gao, J.; Hong, Y.; Du, J.; Dove, A. P.; O'Reilly, R. K. Size and Shape Affects the Antimicrobial Activity of Quaternized Nanoparticles. *J. Polym. Sci. A Polym. Chem.* **2019**, *57* (3), 255–259. DOI: 10.1002/POLA.29195.

116. Li, Z.; Pearce, A. K.; Du, J.; Andrew, |; Dove, P.; O'Reilly, R. K.; Dove, A. P. Uniform Antibacterial Cylindrical Nanoparticles for Enhancing the Strength of Nanocomposite Hydrogels. *J. Polym. Sci.* **2022**, *61* (1), 44–55. DOI: 10.1002/POL.20210853.

117. Inam, M.; Cambridge, G.; Pitto-Barry, A.; Laker, Z. P. L.; Wilson, N. R.; Mathers, R. T.; Dove, A. P.; O'Reilly, R. K. 1D vs. 2D Shape Selectivity in the Crystallization-Driven Self-Assembly of Polylactide Block Copolymers. *Chem. Sci.* **2017**, *8* (6), 4223–4230. DOI: 10.1039/C7SC00641A.

118. Brannigan, R. P.; Dove, A. P. Synthesis, Properties and Biomedical Applications of Hydrolytically Degradable Materials Based on Aliphatic Polyesters and Polycarbonates. *Biomater. Sci.* **2016**, *5*, 9–21. DOI: 10.1039/C6BM00584E.

119. Fukushima, K. Poly(Trimethylene Carbonate)-Based Polymers Engineered for Biodegradable Functional Biomaterials. *Biomater. Sci.* **2015**, *4*, 9–24. DOI: 10.1039/C5BM00123D.

120. Zhu, K. J.; Hendren, R. W.; Jensen, K.; Pitt, C. G. Synthesis, Properties, and Biodegradation of Poly(1,3-Trimethylene Carbonate). *Macromolecules* **1991**, *24* (8), 1736–1740. DOI: 10.1021/MA00008A008.

121. Venkataraman, S.; Hedrick, J. L.; Yang, Y. Y. Fluorene-Functionalized Aliphatic Polycarbonates: Design, Synthesis and Aqueous Self-Assembly of Amphiphilic Block Copolymers. *Polym. Chem.* **2014**, *5* (6), 2035–2040. DOI: 10.1039/C3PY01207G.

122. Finnegan, J. R.; He, X.; Street, S. T. G.; Garcia-Hernandez, J. D.; Hayward, D. W.; Harniman, R. L.; Richardson, R. M.; Whittell, G. R.; Manners, I. Extending the Scope of "Living" Crystallization-Driven Self-Assembly: Well-Defined 1D Micelles and Block Comicelles from Crystallizable Polycarbonate Block Copolymers. *J. Am. Chem. Soc.* **2018**, *140* (49), 17127–17140. DOI: 10.1021/jacs.8b09861.

123. Garcia-Hernandez, J. D.; Street, S. T. G.; Kang, Y.; Zhang, Y.; Manners, I. Cargo Encapsulation in Uniform, Length-Tunable Aqueous Nanofibers with a Coaxial Crystalline and Amorphous Core. *Macromolecules* **2021**, *54* (12), 5784–5796. DOI: 10.1021/ACS.MACROMOL.1C00672.

124. Garcia-Hernandez, J. D.; Parkin, H.; Manners, I. Hydrophobic Cargo Loading of Uniform, Length-Tunable Aqueous Diblock Copolymer Nanofibers with a Crystalline Core. *Polym. Chem.* **2022**, *13*, 4100–4110. DOI: 10.1039/D2PY00395C.

125. Street, S. T. G.; He, Y.; Harniman, R. L.; Garcia-Hernandez, J. D.; Manners, I. Precision Polymer Nanofibers as a Modular, Functionalizable Platform Designed for Nucleic Acid Delivery Applications. *Polym. Chem*. **2022**, *13*, 3009–3025. DOI: 10.1039/D2PY00152G.

126. Street, S. T. G.; Chrenek, J.; Harniman, R. L.; Letwin, K.; Mantell, J. M.; Borucu, U.; Willerth, S. M.; Manners, I. Length-Controlled Nanofiber Micelleplexes as Efficient Nucleic Acid Delivery Vehicles. *J. Am. Chem. Soc.* **2022**, *144*, 19799–19812. DOI: 10.1021/jacs.2c06695

127. Street, S. T. G.; Parkin, H. C.; Shopperly, L.; Chrenek, J.; Letwin, K.; Willerth, S. M.; Manners, I. Optimization of Precision Nanofiber Micelleplexes for DNA Delivery. *Biomater. Sci.* **2022**, *11*, 3512–3523.

128. Akimoto, J.; Nakayama, M.; Sakai, K.; Okano, T. Temperature-induced Intraceullar Uptake of Thermoresponsive Polymeric Micelles. *Biomacromolecules* **2009,** *10* (6), 1331–1336. DOI: 10.1021/bm900032r

129. Van De Watering, P.; Zuidam, N. J.; Van Steenbergen, M. J.; Van Der Houwen, O. A. G. J.; Underberg, W. J. M.; Hennink, W. E. A Mechanistic Study of the Hydrolytic Stability of Poly(2-(Dimethylamino)Ethyl Methacrylate). *Macromolecules* **1998**, *31* (23), 8063–8068. DOI: 10.1021/MA980689G.

130. Zamora-León, S. P.; Golde, D. W.; Concha, I. I.; Rivas, C. I.; Delgado-López, F.; Baselga, J.; Nualart, F.; Vera, J. C. Expression of the Fructose Transporter GLUT5 in Human Breast Cancer. *Proc. Natl. Acad. Sci.* **1996**, *93* (5), 1847–1852. DOI: 10.1073/PNAS.93.5.1847.

131. Parkin, H. C.; Garcia-Hernandez, J. D.; Street, S. T. G.; Hof, R.; Manners, I. Uniform, Length-Tunable Antibacterial 1D Diblock Copolymer Nanofibers. *Polym. Chem.* **2022**, *13* (20), 2941–2949. DOI: 10.1039/D2PY00262K.

# Chapter 2

# Uniform, Length-Tunable Antibacterial 1D Diblock Copolymer Nanofibers

*This chapter has been adapted from:*

Parkin, H. C., Garcia-Hernandez, J. D.[+], Street, S. T. G.[+], Hof, R., Manners, I. *Polym. Chem.* **2022**, *13*, 2941-2949.

*Contributions:*

*Hayley Parkin, Dr. Steven Street, and Prof. Ian Manners conceived the project. Dr. Steven Street synthesized and self-assembled the PFTMC-b-PDMAEMA materials. Dr. Juan Diego Garcia Hernandez synthesized and self-assembled the PFTMC-b-PEG materials. R. Hof provided input on assay design and bacterial culture training. Hayley Parkin developed the antibacterial assays and performed the experiments, and analyzed and interpreted the data. Hayley Parkin wrote the manuscript which was subsequently edited by Prof. Ian Manners and the other authors.*

## 2.1 Abstract

The rapid increase in antibiotic resistant strains of bacteria has led to an urgent need to develop new methods of treating bacterial infections. Antibacterial polymeric nanoparticles are of interest for their more general mechanism of action which involves targeting anionic bacterial membrane structures with cationic functional groups. In this work we utilized living crystallization-driven self-assembly (CDSA) to prepare low dispersity length-controlled block copolymer (BCP) nanofibers that consist of a poly(fluorenetrimethylenecarbonate) (PFTMC) core and a poly(dimethylaminoethyl methacrylate) (PDMAEMA) corona. These nanofibers were shown to function as effective antibacterial agents against *Escherichia coli (E. coli)* W3110. Three different lengths of $PFTMC_{16}$-*b*-$PDMAEMA_{131}$ nanofibers ($L_n$ = 107 nm, 377 nm, 593 nm) with low length dispersities ($Đ$ = 1.04 – 1.14) were investigated. In all three cases the nanofibers were found to have improved antibacterial activity over analogous nanospheres, as well as analogous nanofibers containing a poly(ethyleneglycol) (PEG) corona. The longest nanofibers ($L_n$ = 593 nm) had the highest activity, inhibiting bacterial growth at concentrations as low as 12.5 $\mu$g/mL with a minimum inhibitory concentration (MIC) of 17 $\mu$g/mL. This MIC value falls within the range for antibiotics including erythromycin (32 $\mu$g/mL) and ampicillin (12.5 $\mu$g/mL) against the same strain of *E. coli*. In contrast to other antibacterial polymer systems which require prior quaternization of the PDMAEMA block, $PFTMC_{16}$-*b*-$PDMAEMA_{131}$ nanofibers are protonated in aqueous media and display high levels of antibacterial activity. Our findings indicate that the 1-dimensional (1D) nanofiber shape allows for improved antibacterial activity relative to nanospheres and highlight the role that nanoparticle shape, size, and coronal chemistry play in determining antibacterial activity.

## 2.2 Introduction

The over-use of antibiotics has led to the evolution of multiple antibiotic-resistant strains of bacteria that are difficult or no longer possible to treat, contributing to an estimated 4.95 million deaths in 2019 alone.[1,2] Antibiotic resistance has been recognized since the 1930s,[3–5] and current resistance emerging is partially due to the inherently specific mechanism of action of most traditional antibiotics.[1,3,6] The more specific a treatment is to a certain bacterial structure, the fewer mutations a bacterium needs to accumulate to become resistant, and hence a rapid development of resistance is observed over few replicative cycles.[5] This has led to an increased emphasis on developing more generalized antibacterial treatments.[7] Several alternatives have been proposed including antimicrobial peptides,[8–10] inorganic nanoparticles,[11–13] carbon-nanotubes,[14–16] electrospun nanofibers,[17–19] polymers,[20–22] and polymeric micellar nanoparticles.[23–25]

Molecularly dissolved polymers or assembled polymer-peptide particles have been used as effective antibacterial treatments.[8,26,27] Cationic species are important for targeting the anionic bacterial cell membrane through electrostatic interactions with structures such as teichoic acids and lipopolysaccharides, which localizes the particle to the bacterial membrane.[20,28,29] While multiple different cationic residues have been employed in polymer antibacterials, poly(dimethylaminoethyl methacrylate) (PDMAEMA) remains one of the most widely studied due to its ease of synthesis and quaternization.[9,27,28] Qiao and coworkers observed that the shape of polymer-peptide assemblies can increase antibacterial activity, with star-shaped polymers showing improved activity against both gram-negative and gram-positive bacteria in comparison to globular antimicrobial peptides.[20] The amphiphilic balance along the polymer chain has also been shown to be important for enhancing antibacterial activity.[26] However, molecularly dissolved polymers and polymer-peptide assemblies also suffer from disadvantages such as increased renal clearance

due to their small size,[30,31] and a lack of control over the final size and shape dispersity due to their method of preparation.[26,32] These disadvantages exemplify the importance of considering the size, shape, and surface chemistry of polymeric alternatives to antibiotics.

Polymeric micellar nanoparticles are of considerable interest as antibacterials as they have the potential to be of sufficient size to persist in the body, different accessible shapes, and readily modifiable core and surface chemistries.[33–35] These nanoparticles can be prepared by synthesizing di- or tri-BCPs and performing solution phase self-assembly.[36] However, control over nanoparticle morphology is often a challenge, and thus nanospheres and vesicles are the most commonly accessible.[36,37] In particular, 1D nanofibers and two-dimensional (2D) platelets are challenging to access as a pure morphology and their dimensions cannot be controlled, resulting in samples that are size-disperse.[38] Living crystallization-driven self-assembly (CDSA) can overcome these limitations, producing low dispersity, morphologically pure 1D nanofiber or 2D platelet nanoparticles.[38–40] This method employs a BCP that has a crystallizable solvophobic core-forming block, and a solvophilic corona-forming block (Figure 2.1).[38,41] Upon introduction of a poor solvent for the core, the BCP will assemble into structures with low-curvature core-corona interfaces such as 1D nanofibers or 2D platelets.[38,42] Moreover, living CDSA employs seed nanoparticles, generated from sonication, that can undergo further epitaxial growth upon the introduction of additional molecularly dissolved BCP (unimer) to yield low dispersity, length-controlled nanomaterials such as nanofibers (Figure 2.1).[41,43–46]

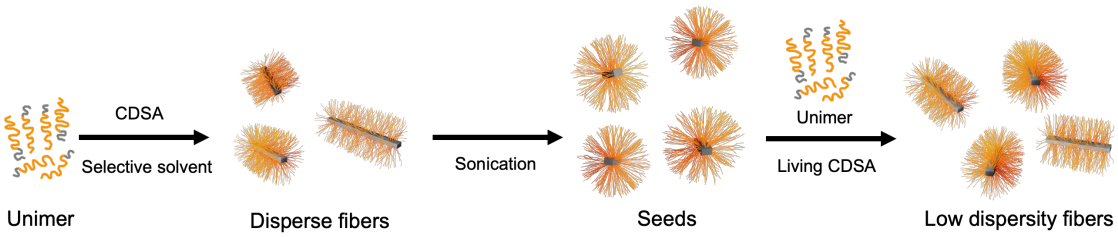


**Figure 2.1** General schematic for CDSA and living CDSA using BCPs with a crystallizable core-forming block to prepare morphologically pure, low dispersity 1D nanoparticles.

Previous studies of antibacterial BCP nanoparticles have led to promising results for both nanospheres and vesicles.[47–50] More recently, Dove, O'Reilly, and coworkers employed CDSA to assemble diamond platelets composed of poly(L-lactide)-*block*-poly(dimethylaminoethyl methacrylate) (PLLA-*b*-PDMAEMA).[25] A difference in antibacterial activity was observed between nanospheres and 2D platelets, with small platelets performing better than nanospheres and large platelets.[25] Quaternization of the PDMAEMA corona was also shown to impact the antibacterial properties, with platelets alkylated with longer dodecyl groups resulting in superior bacterial growth inhibition of gram-negative bacteria in comparison to the analogous methylated platelets and nanospheres.[25]

With size and shape having a critical effect on antibacterial activity,[25,49,51] we set out to investigate if length-controlled 1D nanofibers produced via living CDSA could exhibit enhanced and size-dependent antibacterial properties relative to other nanoparticle compositions. Previous studies have implied that lower surface-area contact points such as those found in 1D materials require less force to penetrate a membrane.[52] This could prove important to the enhancement of the antibacterial properties of a material.[52] The larger surface area to volume ratio of 1D assemblies would be expected to increase the relative charge per particle that would be experienced by the bacterium, thus potentially increasing activity.[27] Varying the length of the nanofiber provides

another size-based parameter for optimizing antibacterial activity. Finally, 1D materials have also been reported to have advantages over other morphologies *in vivo*, for example, they are known to persist longer in the body due to both increased circulation times, and reduced renal clearance and macrophage uptake.[53–55]

Studies of the antibacterial properties of 1D BCP nanofibers are rare but show promising results for length-disperse samples of peptide-based β-sheet forming materials and also silver-loaded systems with a crystalline polylactic acid core and a sugar-based corona prepared by CDSA.[56,57] Furthermore, immediately prior to the submission of the present article an interesting report was published on the promising antibacterial properties of uniform triBCP nanofibers with a crystalline polycaprolactone (PCL) core and a poly(t-butylamino)ethylmethacrylate corona.[58] Herein, we have explored the antibacterial activity of low length dispersity samples of nanofibers prepared from diBCPs with a crystallizable poly(fluorenetrimethylenecarbonate) (PFTMC) core-forming block and either a PDMAEMA or poly(ethylene glycol) (PEG) corona-forming block. These BCPs were used to prepare length-controlled nanofibers over the range ca. 100 – 600 nm via living CDSA (Figure 2.2). The PFTMC block was selected as recent studies have shown it is capable of undergoing CDSA in a robust fashion, easily forming length-controlled nanofibers with a crystalline-core via living CDSA.[59–62] It has also been shown to be noncytotoxic and degradable under conditions relevant to human physiology.[59,62,63] PDMAEMA was selected as a corona-forming block as it has been shown to exhibit antibacterial activity in both polymer and nanoparticle systems.[21,25] PDMAEMA homopolymer was also studied to investigate the difference between nanofibers and molecularly dissolved polymer on antibacterial activity. PEG was selected as a second corona-forming block to yield morphologically pure $PFTMC_{18}$-*b*-$PEG_{530}$ nanofibers

as a negative control system. PEG is known to be well-tolerated *in vivo* and is considered a "stealth" polymer that should interact minimally with cells.[64]

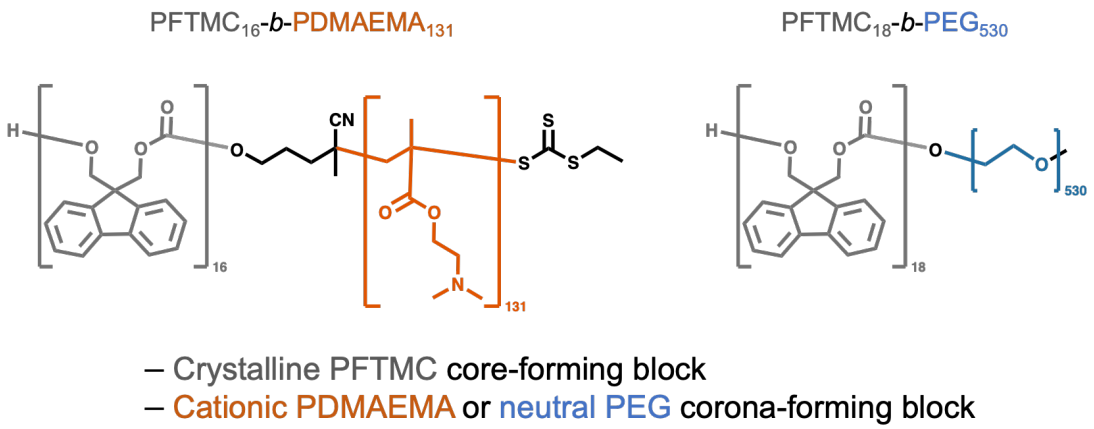


**Figure 2.2.** Structures of the diBCPs used to form the length-controlled nanofibers studied in this work.

## 2.3 Results

### 2.3.1 Design, synthesis, and living CDSA of nanofibers and nanospheres

$PFTMC_{16}$-*b*-$PDMAEMA_{131}$ was prepared through a combination of ring-opening polymerization (ROP) and reversible addition-fragmentation chain-transfer (RAFT) polymerization as previously reported.[62] $PFTMC_{18}$-*b*-$PEG_{530}$ was prepared via ROP as previously described.[59,60,65] Each polymer was characterized by $^1$H NMR, GPC and, in selected cases, MALDI-TOF mass spectrometry. Degrees of polymerization ($DP_n$) were determined by MALDI MS for the PFTMC homopolymers, and by relative $^1$H NMR integration of the corona-forming block to the PFTMC block for the diBCPs. Characterization data can be found in Table S2.1.[60,62,65] Two BCPs were studied: $PFTMC_{16}$-*b*-$PDMAEMA_{131}$ and $PFTMC_{18}$-*b*-$PEG_{530}$ ($M_n$ = 24,900 g/mol and 27,900 g/mol respectively, as determined by NMR $DP_n$'s; $Đ_M$ = 1.55, 1.14 respectively, as determined by GPC, Figure 2.2). The relatively high $Đ_M$ for the aminomethacylate diBCP is attributed to

interactions with the GPC column.[60] Both PFTMC-based diBCPS have been shown previously to form colloidally-stable nanofibers in aqueous media via the living CDSA method although the use of a buffer is recommended for long-term storage of the PDMAEMA materials.[59,62,65]

Nanofibers were prepared from both $PFTMC_{16}$-*b*-$PDMAEMA_{131}$ and $PFTMC_{18}$-*b*-$PEG_{530}$ via living CDSA from the corresponding compositionally identical seeds according to procedures outlined in the supporting information (Figure 2.3, Figure S2.1, Table S2.2).[59,60,62,65] Briefly, each BCP was dissolved in THF to form a unimer solution. The unimer solution was then slowly introduced via a pipette to a poor solvent for the PFTMC core-forming block (MeOH), which afforded morphologically pure length-disperse nanofibers. These were then sonicated for 3 h between 0 °C and 10 °C to yield seeds ($L_n$ = 28 nm, $Đ$ = 1.20 for $PFTMC_{16}$-*b*-$PDMAEMA_{131}$, $L_n$ = 24 nm, $Đ$ = 1.12 for $PFTMC_{18}$-*b*-$PEG_{530}$), which were then able to grow upon addition of further unimer to a final length that was directly dependent on the amount of unimer added (Figure 2.3A). The fibers were subsequently transferred from the THF:MeOH self-assembly solvent mixture into water, either via dialysis for nanofibers of $PFTMC_{16}$-*b*-$PDMAEMA_{131}$ or via the preformed nanoparticle solvent-switch loading (PNSL)[60] system for $PFTMC_{18}$-*b*-$PEG_{530}$ nanofibers. Three samples of nanofibers with different lengths and consistent widths ($W_n$ = 13 nm, $Đ_W$ = 1.03)[62] derived from $PFTMC_{16}$-*b*-$PDMAEMA_{131}$ were prepared: $L_n$ = 107 nm, 377 nm, and 593 nm ($Đ$ = 1.10, 1.04, 1.14 respectively) (Figure 2.3A-C).[62] A small amount of fragmentation was detected only in the case of the longest $PFTMC_{16}$-*b*-$PDMAEMA_{131}$ nanofibers on transfer to water, where the length dispersity increased to 1.14 from 1.05. Together, these 3 samples allowed for an assessment of how antibacterial activity is affected by nanofiber length. $PFTMC_{16}$-*b*-$PDMAEMA_{131}$ nanospheres *(*$R_h$ = 65 nm by dynamic light scattering (DLS), diameter = 15 nm, $Đ$ = 1.05, as determined by TEM) with an amorphous PFTMC core were prepared via dialysis from

THF into water, in order to investigate the effect of morphology on antibacterial activity (Figure 2.3D).[59,62] The PDMAEMA corona was protonated in water, as anticipated. The ζ-potential in 5 mM NaCl was least positive for $PFTMC_{16}$-*b*-$PDMAEMA_{131}$ nanospheres (ζ = +7.4 ± 0.2 mv) and the cationic charge increased with increasing nanofiber length (ζ = +13.4 ± 0.7 mv, +15.7 ± 0.4 mv, +16.1 ± 0.2 mv) (Table S2.2). $PFTMC_{18}$-*b*-$PEG_{530}$ nanofibers ($L_n$ = 114 nm, $Đ$ = 1.06) were prepared via living CDSA as described above in order to assess the effect of the corona-forming block on antibacterial activity (Figure 2.3E).[65]

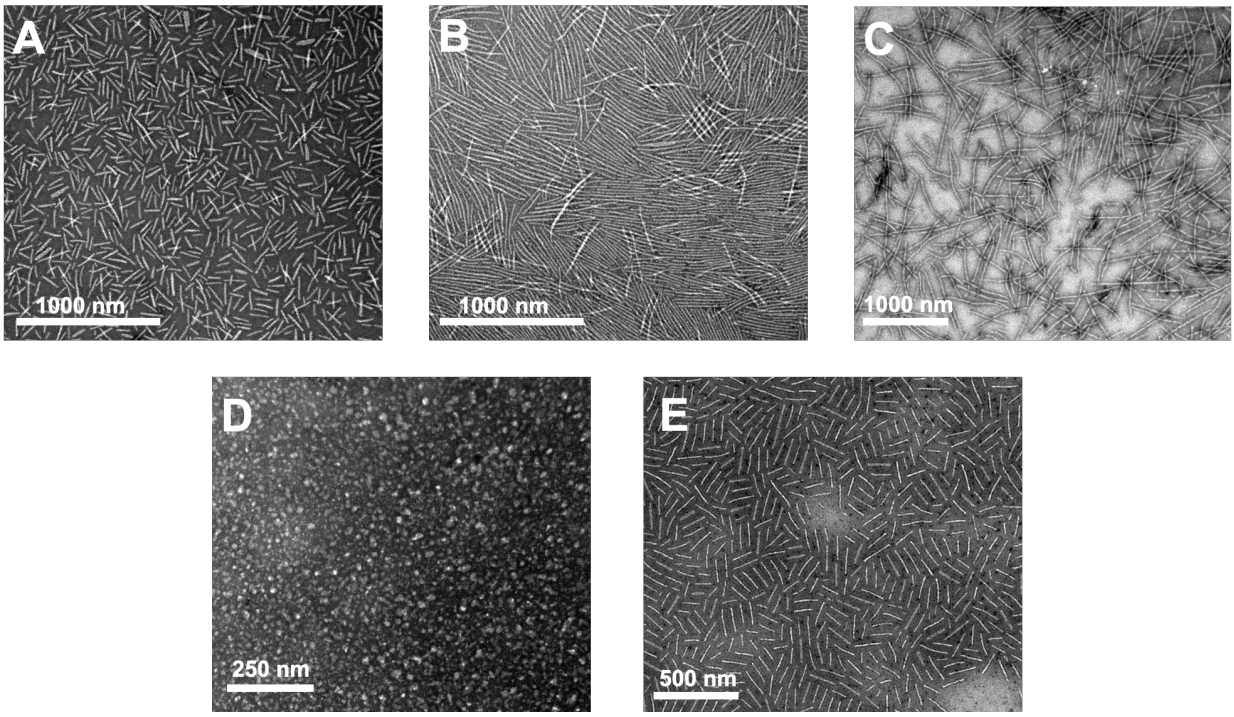


**Figure 2.3.** TEM micrographs of the PFTMC-based diBCP nanoparticles used in this work. All samples were stained using a 3 wt % uranyl acetate solution in EtOH (A-C) Low dispersity $PFTMC_{16}$-*b*-$PDMAEMA_{131}$ nanofibers prepared via the living CDSA method after transfer into water (A) $L_n$ = 107 nm, $Đ$ = 1.10, σ = 34 nm; (B) $L_n$ = 377 nm, $Đ$ = 1.04, σ = 78 nm; (C) $L_n$ = 593 nm, $Đ$ = 1.14, σ = 222 nm). (D) $PFTMC_{16}$-*b*-$PDMAEMA_{131}$ nanospheres ($R_h$ = 65 nm, $Đ$ = 1.05). (E) Low dispersity $PFTMC_{18}$-*b*-$PEG_{530}$ nanofibers ($L_n$ = 114 nm, $Đ$ = 1.06, σ = 28 nm).

### 2.3.2 Antibacterial Assays

Kinetic growth assays were performed in order to evaluate the antibacterial activity of each nanoparticle sample. The common laboratory strain *E. coli* W3110 was chosen as a non-pathogenic, gram-negative model organism as its growth is robust at 37 °C under aerobic and anaerobic conditions. Liquid cultures were diluted to a common Ultraviolet-Visible (UV-Vis) absorbance at 600 nm and were incubated at 37 °C (physiological temperature) with a solution of nanofibers in 2-(4-(2-hydroxyethyl)piperazin-1-yl)ethanesulfonic acid (HEPES) buffer (pH = 7.4) at concentrations from 100 μg/mL – 0 μg/mL. UV-Vis absorbance measurements (at 600 nm) were taken 40 minutes apart over a period of 240 minutes.

### 2.3.4 Bacterial growth inhibition

*E. coli* that was incubated in the absence of nanofibers habitually grew to yield an absorbance between 0.4 – 0.8 at 600 nm (Figure 2.4A-F, black trace). For each of the three PFTMC$_{16}$-*b*-PDMAEMA$_{131}$ nanofiber samples there was initial rise in absorbance followed by a drop off and subsequent plateau of bacterial growth at 100 μg/mL (Figure 2.4A-C, pink trace). Nanofibers of $L_n$ = 107 nm ($Đ$ = 1.10) caused a plateau of bacterial growth at concentrations in excess of 50 μg/mL with no significant effects noted below this threshold (Figure 2.4A). In contrast, 377 nm nanofibers ($Đ$ = 1.04) showed no significant inhibition of bacterial growth at concentrations below 100 μg/mL (Figure 2.4B) with a large variance in growth observed at 50 μg/mL. 593 nm nanofibers ($Đ$ = 1.14) inhibited growth at concentrations in excess of 12.5 μg/mL (Figure 2.4C). Interestingly, PFTMC$_{16}$-*b*-PDMAEMA$_{131}$ nanospheres ($Đ$ = 1.05) showed no significant inhibition of bacterial growth at or below 100 μg/mL (Figure 2.4D). Similarly, 114 nm PFTMC$_{18}$-*b*-PEG$_{530}$ nanofibers ($Đ$ = 1.06) also showed no noteworthy inhibition of bacterial growth at or below 100 μg/mL

(Figure 2.4E). Finally, $PDMAEMA_{91}$ was found to inhibit bacterial growth at 100 µg/mL but not at any lower concentration value (Figure 2.4F).

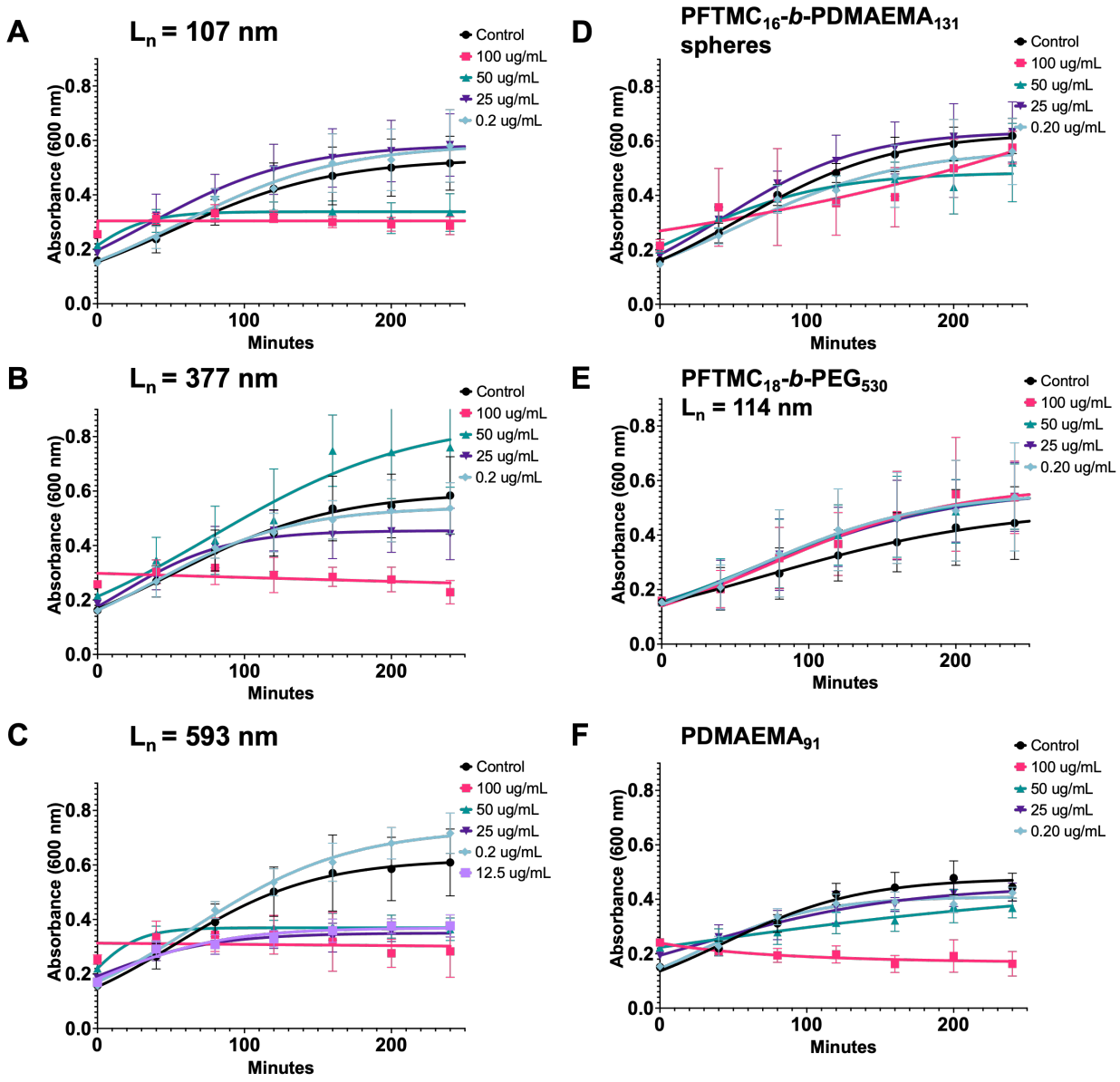


**Figure 2.4.** Kinetic growth data obtained by measuring the $OD_{600}$ from t = 0 mins to t = 240 mins at 37 °C of E. coli W3110 exposed to (A-C) $PFTMC_{16}$-*b*-$PDMAEMA_{131}$ nanofibers ($L_n$ = 107 nm, 377 nm, and 593 nm; $Đ$ = 1.10, 1.04, 1.14 respectively) from 100 µg/mL to 0 µg/mL, (D) $PFTMC_{16}$-*b*-$PDMAEMA_{131}$ nanospheres ($R_h$ = 65 nm, $Đ$ = 1.05) from 100 µg/mL to 0 µg/mL (E) $PFTMC_{18}$-*b*-$PEG_{530}$ nanofibers ($L_n$ = 114 nm, $Đ$ = 1.06) from 100 µg/mL to 0 µg/mL, and (F)

PDMAEMA$_{91}$ homopolymer from 100 μg/mL to 0 μg/mL. Error bars represent the 95% confidence interval (C.I.) across all trials. Control samples showed variable growth between trials but were deemed sufficient if the maximum absorbance reached a value of 0.4 or above. The growth and representative absorbance are most likely limited by the volume of the 96 well-plate and the amount of nutrients available.

### 2.3.5 Minimum inhibitory concentration determinations

Minimum inhibitory concentrations (MICs) were determined by the Lambert and Pearson method using GraphPad Prism software (Figure S2.2).[66] Each experiment was performed in triplicate and repeated on a minimum of three separate occasions. The 107 nm PFTMC$_{16}$-*b*-PDMAEMA$_{131}$ nanofibers were found to have an MIC of 55 μg/mL (Figure S2.2A) whereas the value for the 377 nm analogues was approximately 103 μg/mL (Figure S2.2B). The longer 593 nm PFTMC$_{16}$-*b*-PDMAEMA$_{131}$ nanofibers possessed the lowest MIC of 17 μg/mL (Figure S2.2C), indicating the highest antibacterial activity. In contrast, the PFTMC$_{16}$-*b*-PDMAEMA$_{131}$ nanospheres, PFTMC$_{18}$-*b*-PEG$_{530}$ nanofibers, and PDMAEMA$_{91}$ homopolymer were all found to exhibit MICs in excess of 100 μg/mL (Figure S2.2D-F).

## 2.4 Discussion

### 2.4.1 Effect of nanoparticle shape on antibacterial activity

It has been shown that the shape of polymeric and nanoparticle systems is an important factor for mediating antibacterial activity.[20,25,57,67] With this in mind, we aimed to examine how 1D nanofibers compared to nanospheres and individual polymers in terms of inhibiting bacterial growth. We found that PFTMC$_{16}$-*b*-PDMAEMA$_{131}$ nanofibers exhibited improved antibacterial activity compared to PFTMC$_{16}$-*b*-PDMAEMA$_{131}$ nanospheres at all lengths examined (ca. 100 –

600 nm). The activity of the 107 nm nanofibers and the 593 nm nanofibers against gram-negative bacteria was also greater than that for the previously reported quaternized PLLA-*b*-PDMAEMA platelets and spheres, although different strains were used in each work.[25] The MIC of the 593 nm fibers (17 μg/mL) also falls within the range of MICs for commonly used antibiotics against *E. coli* W3110 (e.g. ampicillin = 12.5 μg/mL, erythromycin = 32 μg/mL), and some previously reported polymer systems against different strains *E.coli*.[20,68,69] In contrast to previous work, the $PFTMC_{16}$-*b*-$PDMAEMA_{131}$ nanofibers used here contain unquaternized PDMAEMA, eliminating the need for an extra synthetic step to alkylate the PDMAEMA corona. Comparison of these findings to previous studies on unquaternized PDMAEMA-based polymers and nanospheres indicates that the 1D morphology of the nanoparticle helps mediate antibacterial activity to a greater extent than other shapes.[51,70,71] The dependence of antibacterial activity on shape exhibited here is analogous to the relationship previously identified between star-shaped polymers and globular antimicrobial peptides, where the star-shape of the former system improved the antibacterial activity.[20] A comparison of the $PFTMC_{16}$-*b*-$PDMAEMA_{131}$ nanofiber activity to that of the $PDMAEMA_{91}$ homopolymer indicates that it is not only the coronal toxicity that is important; clearly, the 1D shape imparts significant advantages in mediating antibacterial activity.

### 2.4.2 Effect of nanoparticle length on antibacterial activity

To further elucidate the dependency of antibacterial activity on nanoparticle size and shape, we prepared $PFTMC_{16}$-*b*-$PDMAEMA_{131}$ nanofibers of three different lengths, ranging from approximately 100 nm to 600 nm. The 593 nm fibers outperformed all other nanoparticle systems tested (Figure 2.5A). It has been previously proposed that the closer the match in nanoparticle size to bacterial size, the higher the antibacterial efficiency.[25] While this trend was not explicitly followed in our findings, the longer 593 nm nanofibers did have the closest match in size to that

of the bacteria (~ 1.5 μm in length).[25] The 107 nm nanofibers showed higher activity than the 377 nm nanofibers (Figure 2.5B), indicating that longer 1D nanoparticles are not always more active, a result that was also observed in the very recently reported PCL-based triBCP system.[58] This could be due to the variability in bacterial growth for the 377 nm fibres around 50 μg/mL, which may be the effective concentration for this material. This refers to a specific concentration that corresponds to halfway between the minimum and maximum response. As this is located on the exponential part of the curve even slight variations in concentration could have a large impact on the observed growth leading to large potential errors. The difference in antibacterial performance may also suggest different mechanisms of action are present. A recent article by Feng and coworkers suggests that longer fibers undergo partial cellular internalization whereas shorter fibers do not.[72] Therefore, the longer nanofibers may affect bacterial growth in a different manner to the shorter examples, with intermediate length nanofibers being less amenable to both of these mechanisms.[72] The shorter 107 nm nanofibers may have an advantage due to their smaller size. A computational study performed by Yang and Ma showed that smaller nanoparticles require less force to penetrate a membrane.[52] This characteristic may explain the increased activity of the 107 nm nanofibers relative to the 377 nm nanofibers. In summary, the 593 nm nanofibers were observed to have the lowest MIC, showcasing that nanoparticle length has a key role in mediating antibacterial activity.

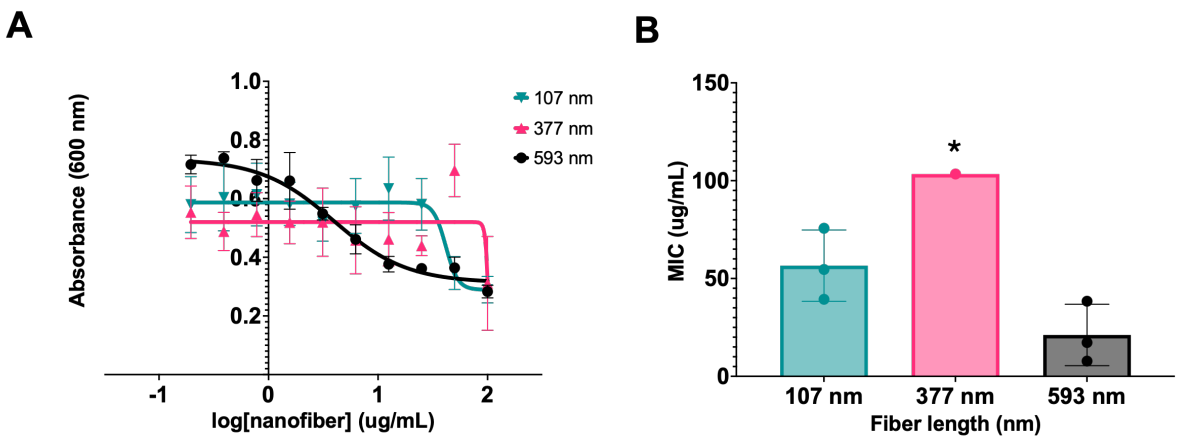


**Figure 2.5.** Relative comparisons of the antibacterial activity of the three samples of $PFTMC_{16}$-*b*-$PDMAEMA_{131}$ nanofibers studied against *E. coli*. W3110 (A) Overlayed MIC curves for each length tested ($L_n$ = 107 nm, 377 nm, 593 nm; $Đ$ = 1.10, 1.04, 1.14 respectively). (B) The determined MIC values for each nanofiber length with representative error bars (95 % C.I) across three trials. *Error bars cannot be shown for $L_n$ = 377 nm due to the variability in readings at 50 μg/mL, therefore, we report the value to be ≥ 100 μg/mL.

### 2.4.3 Effect of nanoparticle corona on antibacterial activity

Finally, this work demonstrates that the nanofiber corona plays a significant role in mediating antibacterial activity. While all of the PDMAEMA-containing nanofibers displayed antibacterial activity to some extent, the PEG-containing nanofibers did not. This is likely because PEG is a hydrophilic, biologically compatible, neutral polymer.[64] On the other hand, protonated PDMAEMA has a $pK_a$ of around 7.5, implying that at physiological pH the terminal amine is at least partially protonated.[70] This partial positive charge is reflected in the recorded ζ-potential of each nanofiber sample (Table S2.2). As nanofiber length increases, so does the zeta potential. This finding confirms that PDMAEMA is an effective antibacterial agent, and suggests that a cationic corona is crucial for mediating antibacterial activity, presumably through association with the

bacterial membrane. It also facilitates the future development of improved antibacterial polymer nanofibers through tuning the cationic, hydrophobic balance of the nanofiber corona.

## 2.5 Conclusion

In this work we have reported a comparative study of the antibacterial activity of samples of uniform, length-controlled PFTMC$_{16}$-*b*-PDMAEMA$_{131}$ nanofibers ($L_n$ = ca. 100 – 600 nm) as well as 15 nm PFTMC$_{16}$-*b*-PDMAEMA$_{131}$ nanospheres, 114 nm PFTMC$_{18}$-*b*-PEG$_{530}$ nanofibers and PDMAEMA$_{91}$ homopolymer against *E. coli W3110.* Whilst all three samples of PFTMC$_{16}$-*b*-PDMAEMA$_{131}$ nanofibers exhibited antibacterial activity, the longest nanofibers tested ($L_n$ = 593 nm, $Đ$ = 1.14) were the most potent, with an MIC of 17 μg/mL. The shortest nanofibers tested ($L_n$ = 107 nm, $Đ$ = 1.10) were the second most potent with an MIC of 55 μg/mL. The other samples tested, 377 nm PFTMC$_{16}$-*b*-PDMAEMA$_{131}$ nanofibers ($Đ$ = 1.04), 15 nm nanospheres ($Đ$ = 1.05), PDMAEMA$_{91}$, and 114 nm PFTMC$_{18}$-*b*-PEG$_{530}$ ($Đ$ = 1.06) all displayed lower antibacterial activity with MIC values in excess of 100 μg/mL. The high antibacterial activity observed for the unquaternized 593 nm PFTMC$_{16}$-*b*-PDMAEMA$_{131}$ nanofibers (MIC = 17 μg/mL) implies that the 1D nanofiber shape and specific length can enhance antibacterial activity.

Our results show interesting similarities and differences to those from the aforementioned recent study of the antibacterial properties of triBCP nanofibers with a PCL core.[58] In the latter case the p$K_a$ of the protonated t-butylamino-functionalized corona was higher (9.12 vs 7.5 for PDMAEMA) and a higher cationic charge on the nanofibers in aqueous media would be anticipated. As with our study, the MIC value associated with the PCL-based nanofibers versus *E. Coli* strains was also found to be length dependent, with lengths ca. 750 nm having the lowest reported MICs (62.5 - 125 μg/mL) compared to shorter and longer examples, and also to analogous spherical micelles. In contrast, our results show that it is possible to employ a diBCP rather than a triBCP to afford

length controlled antibacterial nanofibers. In our studies, the cationic charge increased with increasing fiber length (a trend not followed by the PCL-based nanofibers), which may be due to the differing $pK_a$s of the coronas. Interestingly, the lower overall positive charge found for the PDMAEMA corona-containing nanofibers may be advantageous in targeting the anionic bacterial cell membrane as it may hinder aggregation of the nanofibers and thereby increase antibacterial activity.

Investigations into the mechanism of action and antibacterial resistance will be conducted in order to better understand how these materials act upon the bacterial membrane. Future work will also focus on loading[60] uniform length-controlled nanofibers with antimicrobial reagents which should further potential applications in surface treatment and composites. These studies should provide insight into how to further design materials for enhanced antibacterial activity.

## 2.6 Supporting Information

### 2.6.1 Supplementary Materials and Methods

**General considerations**

Methoxy-$PEG_{530}$ homopolymer was purchased from Polymer Source and used without purification, after drying via vacuum desiccation over phosphorous pentoxide. The synthesis and characterization of $PFTMC_{16}$-*b*-$PDMAEMA_{131}$ has been previously reported by Street et al.,[62] and the synthesis and characterization of $PFTMC_{18}$-*b*-$PEG_{530}$ has been reported by Garcia-Hernandez et al.[60,65] PFTMC Homopolymer degrees of polymerization ($DP_n$) were determined by matrix-assisted laser desorption/ionization (MALDI) mass spectrometry and block-copolymer $DP_n$ were determined by integrations of coronal block peaks in $^1H$ NMR relative to peaks of the PFTMC block. RAFT-CTA was dried via vacuum desiccation over phosphorus pentoxide prior to use. All other reagents and solvents were purchased from Sigma-Aldrich (Canada), Combi-Blocks (USA), VWR (Canada), or Fisher Scientific (Canada) and used without further purification. Solvents for

self-assembly were HPLC grade and were filtered through polytetrafluorethylene (PTFE) or nylon filters with a pore size of 200 nm before use.

### 2.6.2 Instrumentation

**Gel permeation chromatography (GPC)**

Gel permeation chromatograms were acquired on a Malvern OMNISEC triple-detector (refractive index, UV-Vis photodiode detector, light scattering detector and viscometer) chromatograph. Prepared samples were of 1 mg/mL concentration in HPLC grade THF, and were filtered through a PTFE filter with a 200 nm pore size prior to measurement. The eluent used was triethylamine/THF (1 % *v/v*) at a flow rate of 1 mL/min. Two columns were employed, the first of grade T3000 and the second of grade T5000, operated at 35 °C. Universal calibration was constructed using a polystyrene standard.

**Ultrasonication**

Micelle sonication was carried out using either a Fisherbrand 112xx series advanced ultrasonic cleaner (FB-11203), operated in sweep mode at 80 % power and 37 MHz at 15 °C, or using a Hielschur UP100H sonication probe (100 W total output power) at 80% power.

**Transmission electron microscopy (TEM)**

TEM images were obtained on a JEOL 1011 microscope equipped with an 11 megapixel CCD camera, operated at 80 kV. Nanoparticle solutions (3.5 µL, 1 – 4 mg/mL) were drop-casted onto a carbon-coated copper grid. Uranyl acetate solution (8 µL) in EtOH (3 wt %) was subsequently drop-casted on top, and the grids were left to dry overnight. Copper grids (400 mesh) were purchased from Ted Pella. Carbon films (ca. 6 nm) were prepared by carbon sputtering mica sheets with a Leica ACE 600 carbon coater. The carbon films were deposited onto copper grids via floatation on water and the grids were allowed air dry.

For micelle length analysis, a minimum of 200 nanofibers were traced manually using the FIJI software package. The number average micelle length ($L_n$) or width ($W_n$) and weight average micelle length ($L_w$) were calculated using eq. S1-2 from the individual contour lengths ($L_i$) of the micelles. Here, $N_i$ is the number of micelles of length $L_i$, and $n$ is the number of micelles examined in each sample. The distribution of micelle lengths is characterized by $Đ = L_w/L_n$.

$$L_n = \frac{\sum_{i=1}^{n} N_i L_i}{\sum_{i=1}^{n} Ni} \qquad L_w = \frac{\sum_{i=1}^{n} N_i L_i^2}{\sum_{i=1}^{n} NiLi} \qquad \text{(eq. S1-2)}$$

**Dynamic Light Scattering (DLS) and ζ-Potential Measurements**

Dynamic light scattering (DLS) and ζ-potential experiments were carried out using a Malvern Zetasizer Pro. Aqueous sample of nanofibers (100 ug/mL, 700 uL, 25 °C) were prepared in 5 mM NaCl and added into a folded capillary cell (DTS1070 type). For DLS, the correlation function was acquired in real time and analysed by Cumulant analysis. This process allowed the diffusion coefficients for the nanoparticles to be determined, and these were expressed as the effective hydrodynamic radius ($R_h$) using the Stokes-Einstein relationship for coated spheres in water (Refractive Index = 1.33, Dispersant Viscosity = 0.887, Dispersant Dielectric Constant = 78.5) with core properties of polystyrene latex (Refractive Index = 1.590, Absorption = 0.010). For ζ-potential measurements, the Smoluchowski approximation was used. A minimum of five measurements per sample were taken, consisting of between 10 and 100 cycles per run. The average ζ-potential was calculated from the individual measurements taken, with error represented as σ.

### 2.6.2 Self-Assembly Procedures

The composition of all solvent mixtures is given as *v:v*. Low dispersity nanofibers and nanospheres of PFTMC$_{16}$-*b*-PDMAEMA$_{131}$ were prepared by the procedures outlined below, which are based on those developed by Street et. al.,[62] while low dispersity nanofibers of PFTMC$_{18}$-*b*-PEG$_{530}$ were prepared according to the procedure by Garcia-Hernandez et. al.[60,65] All nanofibers were ultimately transferred into distilled water via dialysis or the preformed-nanoparticle solvent-switch loading (PNSL) method as reported by Garcia-Hernandez et. al.[60]

**General self-nucleation procedure**

A solution of diBCP dissolved in THF (unimer) (20 mg/mL – 200 mg/mL) was diluted with an appropriate amount of THF. Subsequently, unimer solution was slowly added via a micropipette into a selective solvent (MeOH) to yield solutions which had final diBCP concentrations between 1 mg/mL – 10 mg/mL with 10:90 THF:MeOH solvent ratios. Each solution was manually shaken for ~10 s, agitated using a vortex mixer for ~10 s, and left to age at 22 °C for 24 h for PFTMC-*b*-PDMAEMA$_{131}$ or heated to 70 °C for 3 h for PFTMC$_{18}$-*b*-PEG$_{530}$. The resulting length-disperse nanofibers were analyzed via TEM.

**General preparation of seed nanofibers**

Length disperse nanofibers (1 mg/mL – 10 mg/mL, 10:90 THF:MeOH) were sonicated for at least 3 h using a Hielschur UP100H sonication probe at a temperature between 0 °C and 22 °C or using

a Fisherbrand 112xx series advanced ultrasonic cleaner (FB-11203) for 3 h at 10 °C in sweep mode at 37 mHz and 80 % power. The resulting seed nanofibers were analyzed by TEM.

**General procedure for the preparation of low dispersity, controlled length nanofibers via seeded growth (living CDSA)**

For seeded growth assemblies with $m_{unimer}/m_{seed} \leq 10$: aliquots of unimer (20 mg/mL in THF) were added to diluted identical composition seed nanofiber solutions (0.1 mg/mL – 1 mg/mL) in MeOH. The self-assembly solutions (THF content: 10 – 20% in MeOH) were manually shaken for ~15 s and aged for 24 h at 22 °C.

For seeded growth assemblies with $m_{unimer}/m_{seed} > 10$: aliquots of unimer (20 mg/mL) were added in intervals of 10 $m_{unimer}/m_{seed}$ every 24 h. The self-assembly solutions were manually shaken for ~15 s and aged for 24 h at 22 °C.

**General procedure for the preparation of nanospheres**

Nanospheres of PFTMC$_{16}$-*b*-PDMAEMA$_{131}$ were prepared via dialysis of a unimer solution of BCP in THF into deionized water over 24 h. Dialysis membranes were purchased from Sigma Aldrich with a molecular weight cutoff of 12,000 – 14,000 Da. Dialysis clips were purchased from Spectrum Chemical. The dialysate was exchanged a minimum of three times, ensuring that all of the organic solvent had been removed. The resulting nanospheres were left overnight and analyzed via TEM.

### 2.6.3 Antibacterial assays

All bacteria work was performed in a biological safety cabinet (BSC) using sterile technique. All materials were autoclaved and disinfected with 70 % ethanol prior to being placed in the BSC. Clear, sterile, 96-well plates were purchased from Corning. Lysogeny broth (LB) was used for streak plates and liquid culturing. *Escherichia coli* (*E. coli*) W3110 was used for all experiments. The buffer was prepared by weighing out (4-(2-hydroxyethyl)-1-piperazineethanesulfonic acid) (HEPES) into a glass bottle, filling with distilled water, autoclaving, and balancing to pH 7.4. Kinetic growth curves were fitted using GraphPad Prism and the logistic growth model. Minimum inhibitory concentration curves were fitted using GraphPad Prism and the Lambert and Pearson method.[66] All bacterial experiments were repeated in triplicate on a minimum of three separate occasions, and the results were combined for analysis.

**Preparation of bacteria for assays**

From a stock solution of *E. coli* W3110 that was kept at -80 °C, a single loop was used to make a streak plate (LB agar). This was repeated. These plates were placed in an incubator at 37 °C for 24 h. From these two initial streak plates, a second propagation was performed. A disposable loop was used to select one colony from each, and streaked onto another plate, respectively. The new plates were incubated at 37 °C for 24 h. Subsequently, they were moved into a 4 °C fridge. To grow a liquid culture, a single colony was selected from a plate using a disposable loop. This was placed in 5 mL of LB broth contained in a 15 mL Falcon tube. The loop was swirled in the broth until the colony was visibly deposited in the broth. The falcon tube was placed in an incubator at 37 °C with orbital shaking at 200 rpm. The culture was allowed to grow for 24 h. From the initial culture, 25 µL of solution was taken and added to a second 15 mL falcon tube containing 5 mL of LB broth. This new culture was placed in an incubator at 37 °C with orbital shaking at 200 rpm for 24 h.

**Plating of bacteria and nanofibers for kinetic growth assays**

Liquid bacterial cultures were diluted in LB to a maximum volume of 3 mL and to an absorbance of 0.600 using an OD meter and a polystyrene cuvette. Once the appropriate dilutions were determined, they were performed on a larger scale to give at least 5 mL of *E. coli* and LB in a sterile reservoir. 10 mL of 40 mM HEPES buffer was added to a separate sterile reservoir. Using a multichannel pipette, 50 µL of buffer was added to each well, excluding the third column. The first row (A1-12) and the last row (H1-12) were topped up to 100 µL of buffer to be used as blanks and to prevent evaporation. The first column was also used as a buffer blank. To three wells in the third column (B3, C3, D3) 20 µL of 1 mg/mL material to be tested was added, and 20 µL of 1 mg/mL of a second material to be tested was added to the next three (E3, F3, G3). Each of these wells was then diluted with 80 µL of buffer solution. From the third column, 50 µL was taken from each well using a multichannel pipette and placed into the next column in order to dilute the material in half. This was repeated until the full plate was diluted. Each time, the material was pipetted up and down three times to ensure proper mixing. Subsequently, 50 µL of HEPES buffer was added to the second column (B-G2). Diluted *E. coli* in LB (50 µL) was added into each well, including the second column as a control (HEPES, broth, and bacteria). Therefore, the final volume in each well was 100 µL.

**Cytation 5 plate reading for kinetic assays**

Absorbance measurements (100 µL of sample) were obtained with the Biotek Cytation 5 multimode plate reader and were conducted at 37 °C in a Corning 96-well plate (clear plates, with the lid). The samples were excited at 600 nm and the absorbance values were recorded. Two readings were taken, 10 minutes apart. The reading at 10 minutes was used over the reading at 0 minutes as the blanks were consistent at this time point. After the 10-minute reading, the 96-well plate was placed back in an incubator at 37 °C with orbital shaking at 200 rpm.

### 2.6.4 Supplementary Tables

**Table S2.1.** Summary of molar mass data for PDMAEMA$_{91}$-CTA, PFTMC$_{16}$-*b*-PDMAEMA$_{131}$, and PFTMC$_{18}$-*b*-PEG$_{530}$ polymers.[60,62] Data for PFTMC$_{18}$-*b*-PEG$_{530}$ is reproduced with permission from the American Chemical Society.[60]

| Polymer | $M_n$ (g/mol) GPC | $M_w$ (g/mol) GPC | $Đ_M$ GPC | $DP_n$ NMR | $M_n$ (g/mol) NMR | $DP_n$ MALDI-TOF |
|---|---|---|---|---|---|---|
| PDMAEMA$_o$ | 49,500 | 59,400 | 1.20 | o = 91 | 14,710 | - |
| PFTMC$_m$-*b*-PDMAEMA$_q$ | 9,700 | 15,000 | 1.55 | m = 20<br>q = 131 | 24,881 | m = 16 |
| PFTMC$_n$-*b*-PEG$_s$ | 26,600 | 30,300 | 1.14 | n = 18<br>s = 530 | 27,921 | n = 18 |

**Table S2.2.** Hydrodynamic radius ($R_h$) and ζ-potential of $PFTMC_{16}$-*b*-$PDMAEMA_{131}$ nanofibers of different lengths, and nanospheres, recorded in 5 mM NaCl.

| Morphology | Length in THF/MeOH (nm) via TEM | Length in Water (nm) via TEM | Diameter in Water (nm) via TEM | $L_w/L_n$ in Water via TEM | $R_h$ in 5 mM NaCl (nm) via DLS | ζ-potential in 5 mM NaCl (mv) |
|---|---|---|---|---|---|---|
| Nanofiber | 112 ± 35 | 107 ± 34 | - | 1.10 | 39 ± 0.6 | +13.4 ± 0.7 |
| Nanofiber | 351 ± 69 | 377 ± 78 | - | 1.04 | 59.5 ± 0.8 | +15.7 ± 0.4 |
| Nanofiber | 701 ± 153 | 593 ± 222 | - | 1.14 | 77.5 ± 1.5 | +16.1 ± 0.2 |
| Nanosphere | - | - | 15 ± 3 | 1.05 | 65 ± 0.85 | +7.4 ± 0.2 |

### 2.6.5 Supplementary Figures

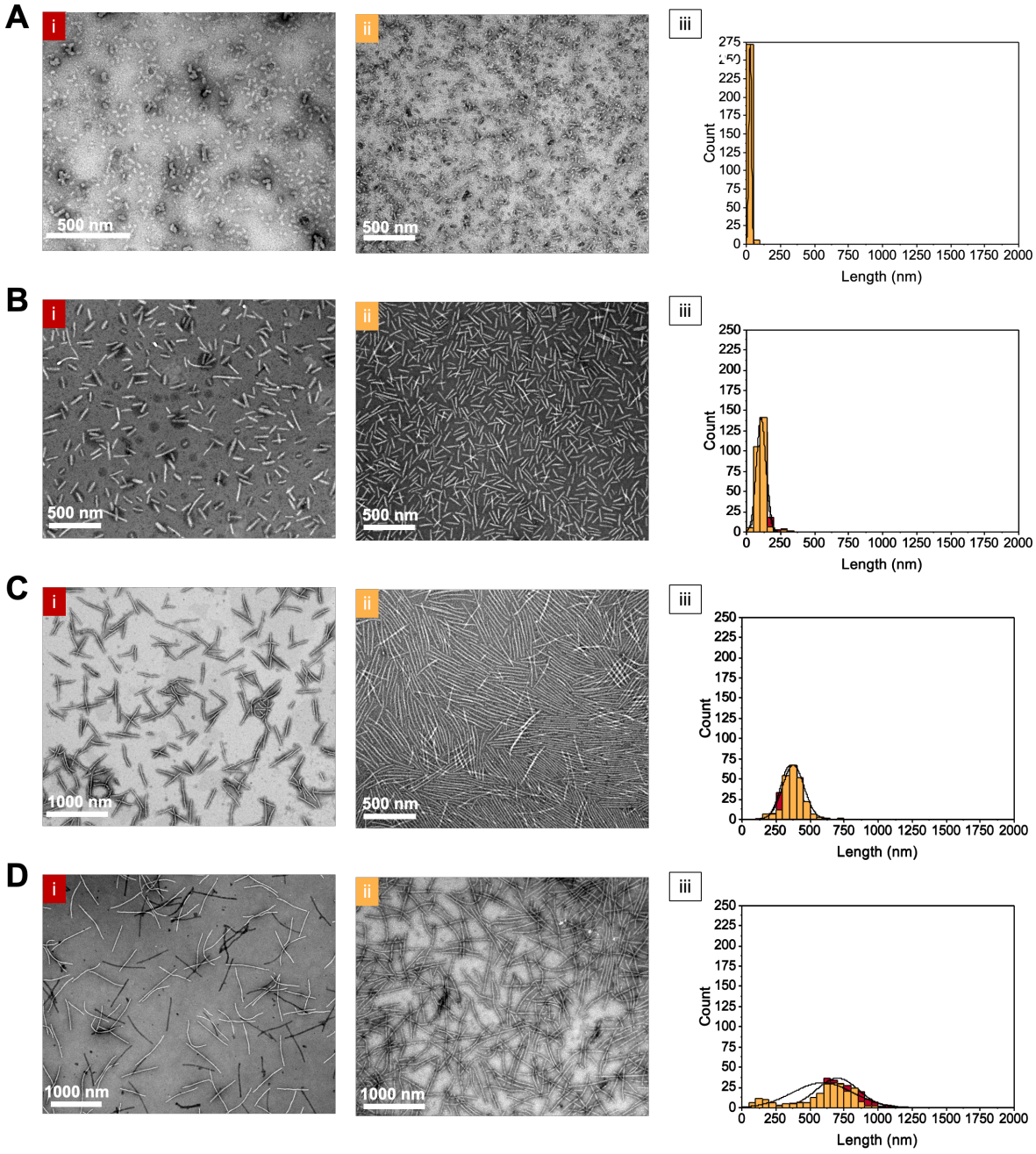


**Figure S2.1.** TEM micrographs of PFTMC$_{16}$-*b*-PDMAEMA$_{131}$ nanofibers. All samples were stained using a 3 wt % uranyl acetate solution in EtOH. Figures are colour coded where red represents the sample in organic solvents and yellow represents the sample after transfer into water for both the TEM micrographs and the corresponding histograms. (A) i) Seed nanoparticles after sonication using a Hielschur UP100H sonication probe (100W total output power) at 80% power ($L_n$ = 28 nm, $Đ$ = 1.20) in THF:MeOH (9:1) and ii) after dialysis into water ($L_n$ = 27 nm, $Đ$ = 1.12).

iii) Representative histogram of seed dispersity as measured in organic solvents (red) and water (yellow). (B) i) Length controlled PFTMC$_{16}$-*b*-PDMAEMA$_{131}$ nanofibers ($L_n$ = 112 nm, $Đ$ = 1.09) in THF:MeOH and ii) after dialysis into water ($L_n$ = 107 nm, $Đ$ = 1.10) iii) Representative histogram of the nanofiber sample dispersity. (C) i) PFTMC$_{16}$-*b*-PDMAEMA$_{131}$ nanofibers ($L_n$ = 351 nm, $Đ$ = 1.04) in THF:MeOH and ii) after transfer into water ($L_n$ = 377 nm, $Đ$ = 1.04) iii) Representative histogram of the sample dispersity. (D) i) PFTMC$_{16}$-*b*-PDMAEMA$_{131}$ nanofibers ($L_n$ = 701 nm, $Đ$ = 1.05) in THF:MeOH and ii) after transfer into water ($L_n$ = 593 nm, $Đ$ = 1.14). iii) Representative histogram of sample dispersity before and after dialysis. A small population of nanofibers centred around 200 nm was observed after dialysis due to small amounts of fragmentation occurring.

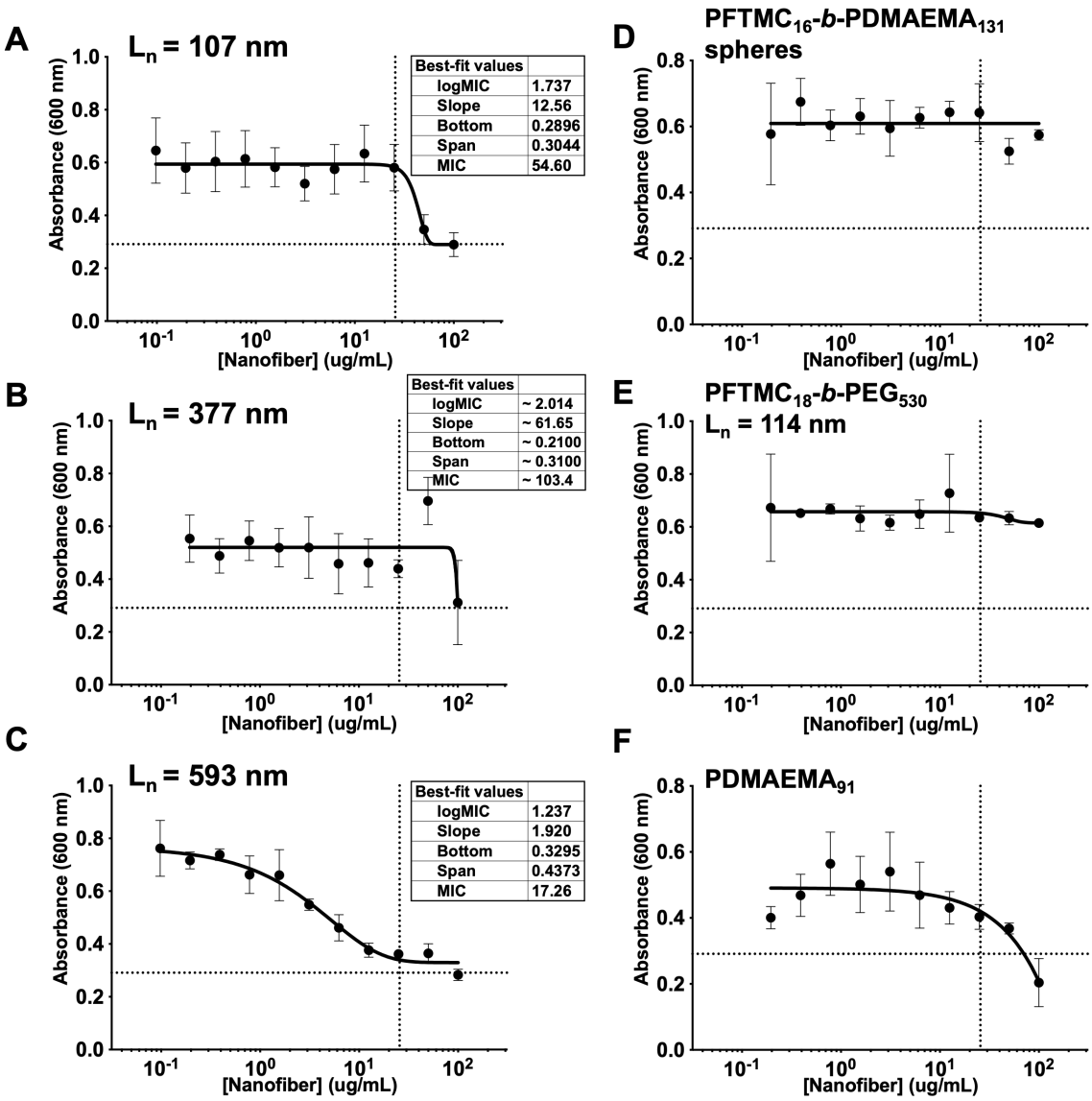


**Figure S2.2.** MIC curves as determined by the Lambert Pearson method using GraphPad Prism of nanofibers and materials tested against *E. coli* W3110. (A) Varying concentrations of $PFTMC_{16}$-*b*-$PDMAEMA_{131}$ nanofibers of $L_n$ = 107 nm fibers ($Đ$ = 1.10) (B) $L_n$ = 377 nm fibers ($Đ$ = 1.04) (C) $L_n$ = 593 nm fibers ($Đ$ = 1.14) (D) $PFTMC_{16}$-*b*-$PDMAEMA_{131}$ nanospheres of $R_H$ = 130 nm ($Đ$ = 1.05) (E) $PFTMC_{18}$-*b*-$PEG_{530}$ nanofibers of $L_n$ = 114 nm ($Đ$ = 1.06) (F) $PDMAEMA_{91}$ homopolymer

## 2.7 References


1. Frieri, M.; Kumar, K.; Boutin, A. Antibiotic Resistance. *J. Infect. Public Health* **2017**, *10*, 369–378. DOI: 10.1016/j.jiph.2016.08.007
2. Murray, C. J. L.; et al. Global Burden of Bacterial Antimicrobial Resistance in 2019: A Systematic Analysis. *Lancet* **2022**, *399* (10325), 629–655. DOI: 10.1016/S0140-6736(21)02724-0
3. Neu, H. C. The Crisis in Antibiotic Resistance. *Science* **1992**, *257*, 1064–1073. DOI: 10.1126/science.257.5073.1064
4. D'Costa, V. M.; King, C. E.; Kalan, L.; Morar, M.; Sung, W. W.; Schwarz, C.; Froese, D.; Zazula, G.; Calmels, F.; Debruyne, R.; Golding, G. B.; Poinar, H. N.; Wright, G. D. Antibiotic Resistance is Ancient. *Nature* **2011**, *477*, 457–461. DOI: 10.1038/nature10388
5. Blair, J. M.; Webber, M. A.; Baylay, A. J.; Ogbolu, D. O.; Piddock, L. J. Molecular Mechanisms of Antibiotic Resistance. *Nat. Rev. Microbiol.* **2014**, *13*, 42–51. DOI: 10.1038/nrmicro3380
6. Yocum, R. R.; Waxman, D. J.; Strominger, J. L. Interaction of Penicillin with its Receptors in Bacterial Membranes. *Trends Biochem. Sci.* **1980**, *5* (4), 97–101. DOI: 10.1016/0968-0004(80)90258-3
7. Davies, J.; Davies, D. Origins and Evolution of Antibiotic Resistance. *Microbiol. Mol. Biol. Rev.* **2010**, *74* (3), 417–433. DOI: 10.1128/MMBR.00016-10
8. Hancock, R. E. W.; Sahl, H.-G. Antimicrobial and Host-Defense Peptides as Infective Therapeutic Strategies. *Nat. Biotechnol*. **2006**, *24*, 1551–1557. DOI: 10.1038/nbt1267

9. Engler, A. C.; Shukla, A.; Puranam, S.; Buss, H. G.; Jreige, N.; Hammond, P. T. Effect of Side Group Functionality and Molecular Weight on the Activity of Synthetic Antimicrobial Peptides. *Biomacromolecules* **2011**, *12* (5), 1666–1674. DOI: 10.1021/bm2000583
10. Zhou, C.; Qi, X.; Li, P.; Chen, W. N.; Mouad, L.; Chang, M. W.; Leong, S. S.; Chan-Park, M. B. High Potency and Broad-Spectrum Antimicrobial Peptides Synthesized via Ring-Opening Polymerization of α-Aminoacid-N-carboxyanhydride. *Biomacromolecules* **2009**, *11*, 60–67. DOI: 10.1021/bm900896h
11. Huang, F.; Gao, Y.; Zhang, Y.; Cheng, T.; Ou, H.; Yang, L.; Liu, J.; Shi, L.; Liu, J. Silver-Decorated Polymeric Micelles Combined with Curcumin for Enhanced Antibacterial Activity. *ACS Appl. Mater. Interfaces* **2017**, *9* (20), 16880–16889. DOI: 10.1021/acsami.7b03347
12. Liu, L.; Zhang, Y.; Li, C.; Cao, J.; He, E.; Wu, X.; Wang, F.; Wang, L. Facile Preparation PCL/Modified Nano ZnO Organic-Inorganic Composite and its Application in Antibacterial Materials. *J. Polym. Res.* **2020**, *27*, 78. DOI: 10.1007/s10965-020-02046-z
13. Wu, V. M.; Tang, S.; Uskoković, V. Calcium Phosphate Nanoparticles as Intrinsic Inorganic Antimicrobials: The Antibacterial Effect. *ACS Appl. Mater. Interfaces* **2018**, *10* (40), 34013–34028. DOI: 10.1021/acsami.8b12784
14. Joo, Y. T.; Jung, K. H.; Kim, M. J.; Kim, Y. Preparation of Antibacterial PDMAEMA-Functionalized Multiwalled Carbon Nanotube via Atom Transfer Radical Polymerization. *J. Appl. Polym. Sci*. **2012**, *127* (3), 1508–1518. DOI: 10.1002/app.37571
15. Kang, S.; Herzberg, M.; Rodrigues, D. F.; Elimelech, M. Antibacterial Effects of Carbon Nanotubes: Size Does Matter. *Langmuir* **2008**, *24* (13), 6409–6413. DOI: 10.1021/la800951v

16. Chen, H.; Wang, B.; Gao, D.; Guan, M.; Zheng, L.; Ouyang, H.; Chai, Z.; Zhao, Y.; Feng, W. Broad-Spectrum Antibacterial Activity of Carbon Nanotubes to Human Gut Bacteria. *Small* **2013**, *9* (16), 2735–2746. DOI: 10.1002/smll.201202792
17. Nthunya, L. N.; Masheane, M. L.; Malinga, S. P.; Nxumalo, E. N.; Barnard, T. G.; Kao, M.; Tetana, Z. N.; Mhlanga, S. D. A Greener Approach to Prepare Electrospun Antibacterial β-Cyclodextrin/Cellulose Acetate Nanofibres for Removal of Bacteria from Water. *ACS Sustainable Chem. Eng.* **2016**, *5*, 153–160. DOI: 10.1021/acssuschemeng.6b01809
18. Kuntzler, S. G.; Costa, J. A.; Morais, M. G. Development of Electrospun Nanofibers Containing Chitosan/PEO Blend and Phenolic Compounds with Antibacterial Activity. *Int. J. Biol. Macromol.* **2018**, *117*, 800–806. DOI: 10.1016/j.ijbiomac.2018.05.224
19. Gao, Y.; Truong, Y. B.; Zhu, Y.; Kyratzis, I. L. Electrospun Antibacterial Nanofibers: Production, Activity, and *in vivo* Applications. *J. Appl. Polym. Sci.* **2014**, *131*, 40797. DOI: 10.1002/app.40797
20. Lam, S. J.; O'Brien-Simpson, N. M.; Pantarat, N.; Sulistio, A.; Wong, E. H. H.; Chen, Y.-Y.; Lenzo, J. C.; Holden, J. A.; Blencowe, A.; Reynolds, E. C.; Qiao, G. G. Combating Multidrug-Resistant Gram-Negative Bacteria with Structurally Nanoengineered Antimicrobial Peptide Polymers. *Nat. Microbiol.* **2016**, *1*, 16162. DOI: 10.1038/nmicrobiol.2016.162
21. Koufakis, E.; Manouras, T.; Anastasiadis, S. H.; Vamvakaki, M. Film Properties and Antimicrobial Efficacy of Quaternized PDMAEMA Brushes: Short vs Long Alkyl Chain Length. *Langmuir* **2020**, *36* (13), 3482–3493. DOI: 10.1021/acs.langmuir.9b03266
22. Jung, K.; Corrigan, N.; Wong, E. H.; Boyer, C. Bioactive Synthetic Polymers. *Adv. Mater.* **2021**, *34* (2), e2105063. DOI: 10.1002/adma.202105063

23. Liu, Y.; Busscher, H. J.; Zhao, B.; Li, Y.; Zhang, Z.; van der Mei, H. C.; Ren, Y.; Shi, L. Surface-Adaptive, Antimicrobially Loaded, Micellar Nanocarriers with Enhanced Penetration and Killing Efficiency in Staphylococcal Biofilms. *ACS Nano* **2016**, *10* (4), 4779–4789. DOI: 10.1021/acsnano.6b01370

24. Guo, L.; Wang, H.; Wang, Y.; Liu, F.; Feng, L. Organic Polymer Nanoparticles with Primary Ammonium Salt as Potent Antibacterial Nanomaterials. *ACS Appl. Mater. Interfaces* **2020**, *12* (19), 21254–21262. DOI: 10.1021/acsami.9b19921

25. Inam, M.; Foster, J. C.; Gao, J.; Hong, Y.; Du, J.; Dove, A. P.; O'Reilly, R. K. Size and shape Affects the Antimicrobial Activity of Quaternized Nanoparticles. *J. Polym. Sci. Part A: Polym. Chem*. **2018**, *57* (3), 255–259. DOI: 10.1002/pola.29195

26. Kuroki, A.; Kengmo Tchoupa, A.; Hartlieb, M.; Peltier, R.; Locock, K. E. S.; Unnikrishnan, M.; Perrier, S. Targeting Intracellular, Multi-Drug Resistant *Staphylococcus aureus* with Guanidinium Polymers by Elucidating the Structure-Activity Relationship. *Biomaterials* **2019**, *217*, 119249. DOI: 10.1016/j.biomaterials.2019.119249

27. Liu, L.; Xu, K.; Wang, H.; Tan, P. K. J.; Fan, W.; Venkatraman, S. S.; Li, L.; Yang, Y.-Y. Self-Assembled Cationic Peptide Nanoparticles as an Efficient Antimicrobial Agent. *Nat. Nanotechnol*. **2009**, *4*, 457–463. DOI: 10.1038/nnano.2009.153

28. Roy, D.; Knapp, J. S.; Guthrie, J. T.; Perrier, S. Antibacterial Cellulose Fiber via RAFT Surface Graft Polymerization. *Biomacromolecules* **2007**, *9* (1), 91–99. DOI: 10.1021/bm700849j

29. Carmona-Ribeiro, A.; de Melo Carrasco, L. Cationic Antimicrobial Polymers and Their Assemblies. *Int. J. Mol. Sci.* **2013***, 14* (5)*,* 9906–9946. DOI: 10.3390/ijms14059906

30. Choi, H. S.; Liu, W.; Misra, P.; Tanaka, E.; Zimmer, J. P.; Ipe, B. I.; Bawendi, M. G.; Frangioni, J. V. Renal Clearance of Quantum Dots. *Nat. Biotechnol*. **2007**, 25, 1165–1170. DOI: 10.1038/nbt1340

31. Liu, F.; He, X.; Chen, H.; Zhang, J.; Zhang, H.; Wang, Z. Gram-Scale Synthesis of Coordination Polymer Nanodots with Renal Clearance Properties for Cancer Theranostic Applications. *Nat. Commun*. **2015**, *6*, 8003. DOI: 10.1038/ncomms9003

32. Huang, H.; Hernandez, R.; Geng, J.; Sun, H.; Song, W.; Chen, F.; Graves, S. A.; Nickles, R. J.; Cheng, C.; Cai, W.; Lovell, J. F. A Porphyrin-PEG Polymer with Rapid Renal Clearance. *Biomaterials* **2016**, *76*, 25–32. DOI: 10.1016/j.biomaterials.2015.10.049

33. Williford, J.-M.; Santos, J. L.; Shyam, R.; Mao, H.-Q. Shape Control in Engineering of Polymeric Nanoparticles for Therapeutic Delivery. *Biomaterials Sci.* **2015***, 3*, 894–907. DOI: 10.1039/C5BM00006H

34. Zhao, Y.; Wang, Y.; Ran, F.; Cui, Y.; Liu, C.; Zhao, Q.; Gao, Y.; Wang, D.; Wang, S. A Comparison Between Sphere and Rod Nanoparticles Regarding Their *in vivo* Biological Behavior and Pharmacokinetics. *Sci. Rep.* **2017**, *7*, 4131. DOI: 10.1038/s41598-017-03834-2

35. Chen, J.; Wang, F.; Liu, Q.; Du, J. Antibacterial Polymeric Nanostructures for Biomedical Applications. *Chem. Commun.* **2014***, 50*, 14482–14493. DOI: 10.1039/C4CC03001J

36. Mai, Y.; Eisenberg, A. Self-Assembly of Block Copolymers. *Chem. Soc. Rev.* **2012***, 41*, 5969–5985. DOI: 10.1039/C2CS35115C

37. Blanazs, A.; Ryan, A. J.; Armes, S. P. Predictive Phase Diagrams for RAFT Aqueous Dispersion Polymerization: Effect of Block Copolymer Composition, Molecular Weight, and Copolymer Concentration. *Macromolecules* **2012***, 45 (12)*, 5099–5107. DOI: 10.1021/ma301059r

38. Tritschler, U.; Pearce, S.; Gwyther, J.; Whittell, G. R.; Manners, I. *50th Anniversary Perspective*: Functional Nanoparticles from the Solution Self-Assembly of Block Copolymers. *Macromolecules* **2017***, 50* (9), 3439–3463. DOI: 10.1021/acs.macromol.6b02767

39. Massey, J. A.; Temple, K.; Cao, L.; Rharbi, Y.; Raez, J.; Winnik, M. A.; Manners, I. Self-Assembly of Organometallic Block Copolymers: The Role of Crystallinity of the Core-Forming Polyferrocene Block in the Micellar Morphologies Formed by Poly(ferrocenylsilane-b-dimethylsiloxane) in n-Alkane Solvent. *J. Am. Chem. Soc.* **2000***, 122* (47), 11577–11584. DOI: 10.1021/ja002205d

40. Inam, M.; Cambridge, G.; Pitto-Barry, A.; Laker, Z. P.; Wilson, N. R.; Mathers, R. T.; Dove, A. P.; O'Reilly, R. K. 1D vs. 2D Shape Selectivity in the Crystallization-Driven Self-Assembly of Polylactide Block Copolymers. *Chem. Sci.* **2017***, 8*, 4223–4230. DOI: 10.1039/C7SC00641A

41. MacFarlane, L.; Zhao, C.; Cai, J.; Qiu, H.; Manners, I. Emerging Applications for Living Crystallization-Driven Self-Assembly. *Chem. Sci.* **2021***, 12*, 4661–4682. DOI: 10.1039/D0SC06878K

42. Karayianni, M.; Pispas, S. Block Copolymer Solution Self-Assembly: Recent Advances, Emerging Trends, and Applications. *J. Polym. Sci.* **2021***, 59* (17), 1874–1898. DOI: 10.1002/pol.20210430

43. Wang, X.; Guerin, G.; Wang, H.; Wang, Y.; Manners, I.; Winnik, M. A. Cylindrical Block Copolymer Micelles and Co-Micelles of Controlled Length and Architecture. *Science* **2007***, 317* (5838), 644–647. DOI: 10.1126/science.1141382

44. Ma, J.; Lu, G.; Huang, X.; Feng, C. π-Conjugated-Polymer-Based Nanofibers Through Living Crystallization-Driven Self-Assembly: Preparation, Properties and Applications. *Chem. Commun.* **2021**, *57*, 13259–13274. DOI: 10.1039/D1CC04825B

45. Ganda, S.; Stenzel, M. H. Concepts, Fabrication Methods and Applications of Living Crystallization-Driven Self-Assembly of Block Copolymers. *Prog. Polym. Sci.* **2020**, *101*, 101195. DOI: 10.1016/j.progpolymsci.2019.101195

46. Foster, J. C.; Varlas, S.; Couturaud, B.; Coe, Z.; O'Reilly, R. K. Getting into Shape: Reflections on a New Generation of Cylindrical Nanostructures' Self-Assembly Using Polymer Building Blocks. *J. Am. Chem. Soc.* **2019**, *141* (7), 2742–2753. DOI: 10.1021/jacs.8b08648

47. Sun, H.; Wang, Y.; Song, J. Polymer Vesicles for Antimicrobial Applications. *Polymers* **2021**, *13* (17), 2903. DOI: 10.3390/polym13172903

48. Zhang, C.; Zhu, Y.; Zhou, C.; Yuan, W.; Du, J. Antibacterial Vesicles by Direct Dissolution of a Block Copolymer in Water. *Polym. Chem.* **2013**, *4*, 255–259. DOI: 10.1039/C2PY20719B

49. Hisey, B.; Ragogna, P. J.; Gillies, E. R. Phosphonium-Functionalized Polymer Micelles with Intrinsic Antibacterial Activity. *Biomacromolecules* **2017**, *18* (3), 914–923. DOI: 10.1021/acs.biomac.6b01785

50. Zhou, C.; Zhou, X.; Su, X. Noncytotoxic Polycaprolactone-Polyethyleneglycol-3-Poly(L-lysine) Triblock Copolymer Synthesized and Self-Assembled as an Antibacterial Drug Carrier. *RSC Adv.* **2017**, *7*, 39718–39725. DOI: 10.1039/C7RA07102G

51. Yao, D.; Guo, Y.; Chen, S.; Tang, J.; Chen, Y. Shaped Core/Shell Polymer Nanoobjects with High Antibacterial Activities via Block Copolymer Microphase Separation. *Polymers* **2013**, *54* (14), 3485–3491. DOI: 10.1016/j.polymer.2013.05.005

52. Yang, K.; Ma, Y.-Q. Computer Simulation of the Translocation of Nanoparticles With Different Shapes Across a Lipid Bilayer. *Nat. Nanotechnol.* **2010***, 5*, 579–583. DOI: 10.1038/nnano.2010.141

53. Li, Z.; Sun, L.; Zhang, Y.; Dove, A. P.; O'Reilly, R. K.; Chen, G. Shape Effect of Glyco-Nanoparticles on Macrophage Cellular Uptake and Immune Response. *ACS Macro Lett.* **2016***, 5* (9), 1059–1064. DOI: 10.1021/acsmacrolett.6b00419

54. Champion, J. A.; Mitragotri, S. Shape Induced Inhibition of Phagocytosis of Polymer Particles. *Pharm. Res.* **2008***, 26* (1), 244–249. DOI: 10.1007/s11095-008-9626-z

55. Geng, Y.; Dalhaimer, P.; Cai, S.; Tsai, R.; Tewari, M.; Minko, T.; Discher, D. E. Shape Effects of Filaments versus Spherical Particles in Flow and Drug Delivery. *Nat. Nanotechnol.* **2007***, 2*, 249–255. DOI: 10.1038/nnano.2007.70

56. Xu, D.; Chen, W.; Tobin-Miyaji, Y. J.; Sturge, C. R.; Yang, S.; Elmore, B.; Singh, A.; Pybus, C.; Greenberg, D. E.; Sellati, T. J.; Qiang, W.; Dong, H. Fabrication and Microscopic and Spectroscopic Characterization of Cytocompatible Self-Assembling Antimicrobial Nanofibers. *ACS Infect. Dis.* **2018***, 4* (9), 1327–1335. DOI: 10.1021/acsinfecdis.8b00069

57. Song, Y.; Elsabahy, M.; Collins, C. A.; Khan, S.; Li, R.; Hreha, T. N.; Shen, Y.; Lin, Y.-N.; Letteri, R. A.; Su, L.; Dong, M.; Zhang, F.; Hunstad, D. A.; Wooley, K. L. Morphologic Design of Silver-Bearing Sugar-Based Polymer Nanoparticles for Uroepithelial Cell Binding and Antimicrobial Delivery. *Nano Lett.* **2021***, 21* (12), 4990–4998. DOI: 10.1021/acs.nanolett.1c00776

58. Li, Z.; Pearce, A. K.; Du, J.; Dove, A. P.; O'Reilly, R. K. Uniform Antibacterial Cylindrical Nanoparticles for Enhancing the Strength of Nanocomposite Hydrogels. *J. Polym. Sci.* **2022**, *61* (1), 44–55**.** DOI: 10.1002/pol.20210853

59. Finnegan, J. R.; He, X.; Street, S. T.; Garcia-Hernandez, J. D.; Hayward, D. W.; Harniman, R. L.; Richardson, R. M.; Whittell, G. R.; Manners, I. Extending the Scope of "Living" Crystallization-Driven Self-Assembly: Well-Defined 1D Micelles and Block Comicelles from Crystallizable Polycarbonate Block Copolymers. *J. Am. Chem. Soc.* **2018***, 140* (49), 17127–17140. DOI: 10.1021/jacs.8b09861

60. Garcia-Hernandez, J. D.; Street, S. T. G.; He, Y.; Harniman, R. L.; Manners, I. Cargo Encapsulation in Uniform, Length-Tunable Aqueous Nanofibers with a Coaxial Crystalline and Amorphous Core. *Macromolecules* **2021***, 54* (12), 5784–5796. DOI: 10.1021/acs.macromol.1c00672

61. He, X.; Finnegan, J. R.; Hayward, D. W.; MacFarlane, L. R.; Harniman, R. L.; Manners, I. Living Crystallization-Driven Self-Assembly of Polymeric Amphiphiles: Low-Dispersity Fiber-like Micelles from Crystallizable Phosphonium-Capped Polycarbonate Homopolymers. *Macromolecules* **2020***, 53* (23), 10591–10600. DOI: 10.1021/acs.macromol.0c02075

62. Street, S. T. G.; He, Y.; Harniman, R. L.; Garcia-Hernandez, J. D.; Manners, I. Precision Polymer Nanofibers with a Responsive Polyelectrolyte Corona Designed as a Modular, Functionalizable Nanomedicine Platform. *Polym. Chem.* **2022**, *13*, 3009–3025. DOI: 10.1039/D2PY00152G

63. Venkataraman, S.; Hedrick, J. L.; Yang, Y. Y. Fluorene-Functionalized Aliphatic Polycarbonates: Design, Synthesis and Aqueous Self-Assembly of Amphiphilic Block Copolymers. *Polym. Chem.* **2014***, 5*, 2035–2040. DOI: 10.1039/C3PY01207G

64. Alconcel, S. N.; Baas, A. S.; Maynard, H. D. FDA-Approved Poly(ethylene glycol)–Protein Conjugate Drugs. *Polym. Chem.* **2011***, 2*, 1442–1444. DOI: 10.1039/C1PY00034A

65. Garcia-Hernandez, J. D.; Parkin, H. C.; Manners, I. Hydrophobic Cargo Loading at the Core–Corona Interface of Uniform, Length-Tunable Aqueous Diblock Copolymer Nanofibers with a Crystalline Polycarbonate Core. *Polym. Chem.* **2022**, *13*, 4100–4110. Submitted. DOI: 10.1039/D2PY00395C

66. Lambert, R. J. W.; Pearson, J. Susceptibility Testing: Accurate and Reproducible Minimum Inhibitory Concentration (MIC) and Non-Inhibitory Concentration (NIC) Values. *J. Appl. Microbiol.* **2000***, 88* (5), 784–790. DOI: 10.1046/j.1365-2672.2000.01017.x

67. Yamamoto, O. Influence of Particle Size on the Antibacterial Activity of Zinc Oxide. *Int. J. Inorg. Mater.* **2001***, 3* (7), 643–646. DOI: 10.1016/S1466-6049(01)00197-0

68. Mori, N.; Ishii, Y.; Tateda, K.; Kimura, S.; Kouyama, Y.; Inoko, H.; Mitsunaga, S.; Yamaguchi, K.; Yoshihara, E. A Peptide Based on Homologous Sequences of the ß-Barrel Assembly Machinery Component Bamd Potentiates Antibiotic Susceptibility of *Pseudomonas aeruginosa*. *J. Antimicrob. Chemother.* **2012***, 67* (9), 2173–2181. DOI: 10.1093/jac/dks174

69. Sulavik, M. C.; Houseweart, C.; Cramer, C.; Jiwani, N.; Murgolo, N.; Greene, J.; DiDomenico, B.; Shaw, K. J.; Miller, G. H.; Hare, R.; Shimer, G. Antibiotic Susceptibility Profiles of *Escherichia coli* Strains Lacking Multidrug Efflux Pump Genes. *Antimicrob. Agents Chemother.* **2001***, 45* (4), 1126–1136. DOI: 10.1128/AAC.45.4.1126-1136.2001

70. Rawlinson, L.-A. B.; Ryan, S. M.; Mantovani, G.; Syrett, J. A.; Haddleton, D. M.; Brayden, D. J. Antibacterial Effects of Poly(2-(dimethylamino ethyl)methacrylate) against Selected Gram-Positive and Gram-Negative Bacteria. *Biomacromolecules* **2009***, 11* (2), 443–453. DOI: 10.1021/bm901166y

71. Lam, S. J.; Wong, E. H. H.; Boyer, C.; Qiao, G. G. Antimicrobial Polymeric Nanoparticles. *Prog. Polym. Sci.* **2018***, 76*, 40–64. DOI: 10.1016/j.progpolymsci.2017.07.007

72. Ma, J.; Ma, C.; Huang, X.; de Araujo, P. H.; Goyal, A. K.; Lu, G.; Feng, C. Preparation and Cellular Uptake Behaviors of Uniform Fiber-Like Micelles with Length Controllability and High Colloidal Stability in Aqueous Media. *Fundam. Res.* **2022**, *3* (1), 93–101. DOI: 10.1016/j.fmre.2022.01.020

# Chapter 3

## Mechanism of Action and Design of Potent Antibacterial Block Copolymer Nanoparticles

*This chapter is adapted from:*

Parkin, H. C., Street S. T. G., Gowen, B., Da-Silva-Correa, L. H., Hof, R., Buckley, H. L., Manners, I. *J. Am. Chem. Soc.* **2024**, *146* (8), 5128-5141.

*Contributions:*

*Hayley Parkin and Prof. Ian Manners conceived the project. Dr. Steven Street provided the BODIPY-labelled PFTMC-b-PDMAEMA materials and aided with experimental design. Hayley Parkin performed the synthesis, characterization, and self-assembly of the non-fluorescent PFTMC-b-PDMAEMA materials. Hayley Parkin carried out the experiments, and TEM and CLSM microscopy, analyzed and interpreted the data, and wrote the manuscript, with editing provided by Dr. Steven Street and Prof. Ian Manners. Brent Gowen prepared the cross-sections for TEM analysis. Luiz H. Da-Silva-Correa imaged the prepared SEM samples. R. Hof aided with experimental design and training. Prof. Heather L. Buckley provided supervision of L. H. Da-Silva-Correa.*

## 3.1 Abstract

Self-assembled polymer nanoparticles are promising antibacterials, with non-spherical morphologies of particular interest as recent work has demonstrated enhanced antibacterial activity relative to spherical counterparts. However, the reasons for this enhancement are currently unclear. We have performed a multifaceted analysis of the antibacterial mechanism of action of 1D nanofibers relative to nanospheres by the use of flow cytometry, high-resolution microscopy, and evaluations of the antibacterial activity of pristine and tetracycline-loaded nanoparticles. Low length dispersity, fluorescent diblock copolymer nanofibers with a crystalline poly(fluorenetrimethylenecarbonate) (PFTMC) core (length = 104 nm and 472 nm, height = 7 nm, width = 10 – 13 nm) and a partially protonated poly(dimethylaminoethylmethacrylate) (PDMAEMA) corona (length = 12 nm) were prepared via seeded growth living crystallization-driven self-assembly. Their behavior was compared to that of analogous nanospheres containing an amorphous PFTMC core (diameter = 12 nm). While all nanoparticles were uptaken into *Escherichia coli* W3110, crystalline-core nanofibers were observed to cause significant bacterial damage. Drug loading studies indicated that while all nanoparticle antibacterial activity was enhanced in combination with tetracycline, the enhancement was especially prominent when small nanoparticles (ca. 15 – 25 nm) were employed. Therefore, the identified differences in the mechanism of action and the demonstrated consequences for nanoparticle size and morphology control on antibacterial activity may inform the design of potent antibacterial agents. This study also reinforces the requirement of morphological control over polymer nanoparticles for biomedical applications, as differences in activity are observed depending on their size, shape, and core-crystallinity.

## 3.2 Introduction

Current antibiotics are powerful tools to combat many significant infectious diseases, but it is predicted that the number of infections caused by resistant bacteria will increase each year, resulting in an estimated 10 million deaths per annum by 2050.[1,2] Bacteria are capable of transferring antibiotic resistance genes between one another, and in addition, antibiotics can provide a selective pressure for resistant organisms when they are not present in a high enough concentration to kill the entire bacteria population.[3–5] The resistant organisms then fully flourish upon extinction of susceptible bacteria.[6–8] Once the resistance is established, these organisms can be readily transferred from patient to patient, especially in a nosocomial setting.[9] Therefore, the development of alternatives to traditional antibiotics, and vehicles that can decrease the required dose of antibiotics,[10–12] is of considerable interest for overcoming antibacterial resistance.[13–15]

Many of these alternatives have been explored, especially antimicrobial peptides and nanoparticles.[16–21] This is due to their more general mechanism of action, which usually involves targeting of the anionic bacterial cell membrane with cationic functional groups.[18,22,23] However, antimicrobial peptides can be susceptible to degradation by proteases and can have a high cost associated with their synthesis.[23] Different types of nanoparticles have therefore been explored, including organic,[24–26] inorganic,[27,28] and polymer-based materials.[29–31] Polymer-based materials are of interest due to their ease of modification and their ability to undergo self-assembly and load cargos. A wide range have been reported,[31–33] however, these particles can suffer from a trade-off between potency and toxicity,[34,35] and the lack of shape and size control of polymer assemblies can cause discrepancies between the predicted and observed *in vivo* effects.[36–38]

Amphiphilic diblock copolymers (BCPs) with core-forming solvophobic blocks and solvophilic corona-forming segments are able to self-assemble into core-shell nanoparticles in

block-selective solvents.[39] The biodistribution of these particles can be advantageously altered through tuning of the size and shape of the assemblies.[40–42] However, BCPs with an amorphous core-forming block generally self-assemble into spheres or vesicles whereas other morphologies are challenging to target.[43,44] Any variation in the characteristics of the BCP nanoparticles can alter the resulting properties, impacting their cellular interactions, targeting abilities, and accumulation sites.[41,45] Therefore, obtaining morphologically pure BCP nanoparticles with low size dispersity is of utmost importance for biological applications and non-spherical morphologies have been shown to be advantageous in many cases.[17,40,42,46–49]

Recent work has demonstrated that the use of a crystalline rather than an amorphous core-forming block directs the self-assembly predictably to yield either 1D nanofibers or 2D nanoplatelets.[50–53] Moreover, size control can then be achieved via the living crystallization-driven self-assembly (CDSA) seeded growth approach[54–56] which has been successfully applied to BCPs with a variety of biodegradable core-forming blocks.[57–62] In the case of nanofibers, a BCP containing a short crystallizable core-forming block and a long solvophilic corona-forming block is self-assembled to form length disperse nanofibers in a selective solvent for the corona.[50,54,55,63] Mechanical fragmentation (usually via sonication) results in a Gaussian-type distribution of short (typically ca. 15-40 nm), relatively low-length-dispersity nanofibers that function as seeds.[62,64] The seeds retain active termini to further epitaxial growth in the presence of added molecularly dissolved BCP (termed ‘unimer’). The result is a final nanofiber length that is directly dependent on the unimer to seed mass ratio.[55,64,65] Given the seeds have a relatively low length dispersity, the resulting nanofibers are substantially longer, and the rate of elongation is approximately equal for all seeds, the final lengths of the nanofibers are uniform with low length dispersities.[43,65] The uniformity of the final assembly, granted by their preparation via living CDSA, is crucial not only

for reducing off-target effects due to size variability, but also can be exploited to design pure nanoparticles of interesting morphologies that can enhance their innate performance in biological applications.

Self-assembled nanoparticles with antibacterial activity have been previously reported, and a dependence on particle shape and size on activity has been determined.[46,47,66,67] In our previous work, we reported that low length-dispersity nanofibers with a crystalline, biocompatible poly(fluorenetrimethylenecarbonate) (PFTMC) core and a hydrophilic poly(dimethylaminoethylmethacrylate) (PDMAEMA) corona can be prepared from a $PFTMC_{16}$-*b*-$PDMAEMA_{131}$ BCP (block ratio = 1:10, subscripts refer to the number average degree of polymerization, $DP_n$) via living CDSA.[68] At physiological pH the PDMAEMA corona is partially protonated,[69] which was proposed to drive electrostatic interactions with the anionic cell membrane of bacteria. We explored the antibacterial activity of the pristine nanofibers against *Escherichia coli* W3110 (*E. coli*) and found enhanced activity relative to nanospheres at every length studied. We also discovered that the behavior was length-dependant; longer nanofibers exhibited enhanced activity relative to intermediate length and short nanofibers.[68] As the reasons for the observed trends in antibacterial activity were unclear, an investigation into the mechanism of action of these antibacterial nanofibers was of considerable interest.

Studies directed at understanding the mechanism of action of antimicrobial nanoparticles have been reported, with many focusing on cationic antimicrobial peptides or polymer nanospheres.[18,70–75] The major results from these studies implicate cell membrane damage as the major mechanism of antibacterial action. This is largely determined using microscopy to observe cell contents leakage and osmotic balance changes caused by the nanoparticles.[76–79] In one report, self-assembled $\beta$-sheet antimicrobial peptides could be directly observed crossing the bacterial

membrane by transmission electron microscopy (TEM).[74] Another recent report utilized fluorescence microscopy to identify that short 1D cylindrical micelles formed by π-stacking amphiphiles were the most potent antibacterials relative to nanospheres or 2D nanoribbons.[80] Furthermore, by probing the energy of interactions of the nanoparticles with bacterial cell membrane mimics, this behavior was attributed to fast rupture of the bacterial membrane. In contrast, studies on the mechanism of action for kinetically stable 1D block copolymer nanoparticles with rigid, crystalline cores do not exist, and comparisons with nanospheres containing an amorphous core derived from the same material are particularly desirable. Elucidating how the differing properties of the nanoparticles affect their interactions with bacteria would truly demonstrate how the function of the nanoparticle follows its form.

In this work, we elucidate the mechanism of action of PFTMC-*b*-PDMAEMA block copolymer nanoparticles and demonstrate that the resultant antibacterial properties are dependent on their size and shape. We utilize this information to demonstrate that nanoparticle antibacterial activity can be enhanced by loading a small molecule antibiotic, decreasing the concentration required to induce a significant bacterial response. These results provide a framework for designing potent antibacterial systems that use nanoparticle size and shape to tune antibacterial activity and antibiotic delivery, rendering existing antibiotics more effective and providing multiple mechanisms of action. Together, these results have important implications for preventing antibiotic resistance.[4,12,14]

## 3.3 Results

### 3.3.1 Synthesis of PFTMC$_{16}$-*b*-PDMAEMA$_{131}$ and the preparation of dye-functionalised block comicelle length-controlled nanofibers and nanospheres

PFTMC$_{16}$-*b*-PDMAEMA$_{131}$ was prepared via ring-opening polymerization followed by reversible addition-fragmentation chain-transfer polymerization as previously reported (number-average molar mass $M_n$ = 18,300 g/mol, determined via $^1$H NMR; molar mass dispersity $Đ_M$ = 1.53, established via gel permeation chromatography, Figure S3.1, Figure S3.2, Table S3.1).[68,81,82] This diBCP has been previously demonstrated to form length-tunable colloidally stable nanofibers in mixtures of THF and MeOH (2:8 *v/v*) via the living CDSA method (Figure 3.1A) and to remain colloidally stable upon transfer into water.[68,81,82]

To aid with investigations into the mechanism of action, fluorescent nanofibers were desired to enable analysis via techniques such as flow cytometry and confocal laser scanning microscopy (CLSM). Previous studies have utilized a BODIPY$^{630/650\text{-X}}$ (BD) fluorescent dye that exhibits emission in the red region of the visible spectrum, where background cellular autofluorescence is minimal.[81,83] The BD dye was covalently attached to the terminal primary alcohol of PFTMC$_{16}$-*b*-PDMAEMA$_{131}$ via *N*-hydroxysuccinimide ester coupling, yielding BD-PFTMC$_{16}$-*b*-PDMAEMA$_{112}$ (Scheme S3.1, Figure S3.1B, Figure S3.2). A small change in the DP$_n$ of the PDMAEMA block was observed due to purification of the polymer via precipitation (Figure S3.3-Figure S3.5).

The self-assembly of BD-PFTMC$_{16}$-*b*-PDMAEMA$_{112}$ into nanofibers was attempted, however nanoplatelet impurities were also observed under a range of conditions, which indicated the desired morphological purity was lacking (Figure S3.6, Figure S3.7). To circumvent this issue, low dispersity fluorescent nanofibers were prepared directly by the addition of BD-

PFTMC$_{16}$-*b*-PDMAEMA$_{112}$ unimer to non-fluorescent PFTMC$_{16}$-*b*-PDMAEMA$_{131}$ seed nanofibers, followed by the addition of further non-fluorescent PFTMC$_{16}$-*b*-PDMAEMA$_{131}$ to the termini. This formed (PFTMC$_{16}$-*b*-PDMAEMA$_{131}$)-*m*-(BD-PFTMC$_{16}$-*b*-PDMAEMA$_{112}$)-*m*-(PFTMC$_{16}$-*b*-PDMAEMA$_{131}$)-*m*-(BD-PFTMC$_{16}$-*b*-PDMAEMA$_{112}$)-*m*-(PFTMC$_{16}$-*b*-PDMAEMA$_{131}$) (m = micelle) ABABA pentablock comicelles with fluorescent B segments that flanked non-fluorescent terminal and central A segments. This structure ensured that the dye would not affect any potential biological interactions (Figure 3.1). The ratio of BD-PFTMC$_{16}$-*b*-PDMAEMA$_{112}$ to PFTMC$_{16}$-*b*-PDMAEMA$_{131}$ was 1:1 for each nanofiber length prepared, resulting in pentablock comicelle nanofibers with lengths of 104 nm and 456 nm (length dispersity ($Đ_L$) = 1.09 and 1.04, respectively, core height = 7 nm, core width = 10 – 13 nm,[81] Table **S3.2**). Attachment of the BD dye to the core-segment facilitated solvation and an emission spectrum was observed in water with a maximum at 655 nm (Figure S3.8). This method highlights the utility of creating segmented nanostructures when morphological purity is inaccessible through the self-assembly of an individual BCP. After transfer of the nanofibers from THF:MeOH into water via syringe-pump infusion and evaporation, nanofibers with final lengths of 104 nm ($Đ_L$ = 1.11) and 472 nm ($Đ_L$ = 1.03) were obtained (Figure S3.9A-B, Table **S3.2**). To enable comparisons with nanospheres, random comicelle nanospheres with an amorphous PFTMC core were prepared via dialysis of a 1:1 mixture of PFTMC$_{16}$-*b*-PDMAEMA$_{131}$ and BD-PFTMC$_{16}$-*b*-PDMAEMA$_{112}$ unimers from DMSO directly into water ($d_{core}$ =12 nm, $Đ_L$ = 1.08, Figure S3.9C, Table **S3.2**). In this case the PFTMC core-forming block precipitates rapidly and has insufficient time to crystallize.[81] The two sets of fluorescent nanofibers and the sample of nanospheres were employed to explore the antibacterial mechanism of action.

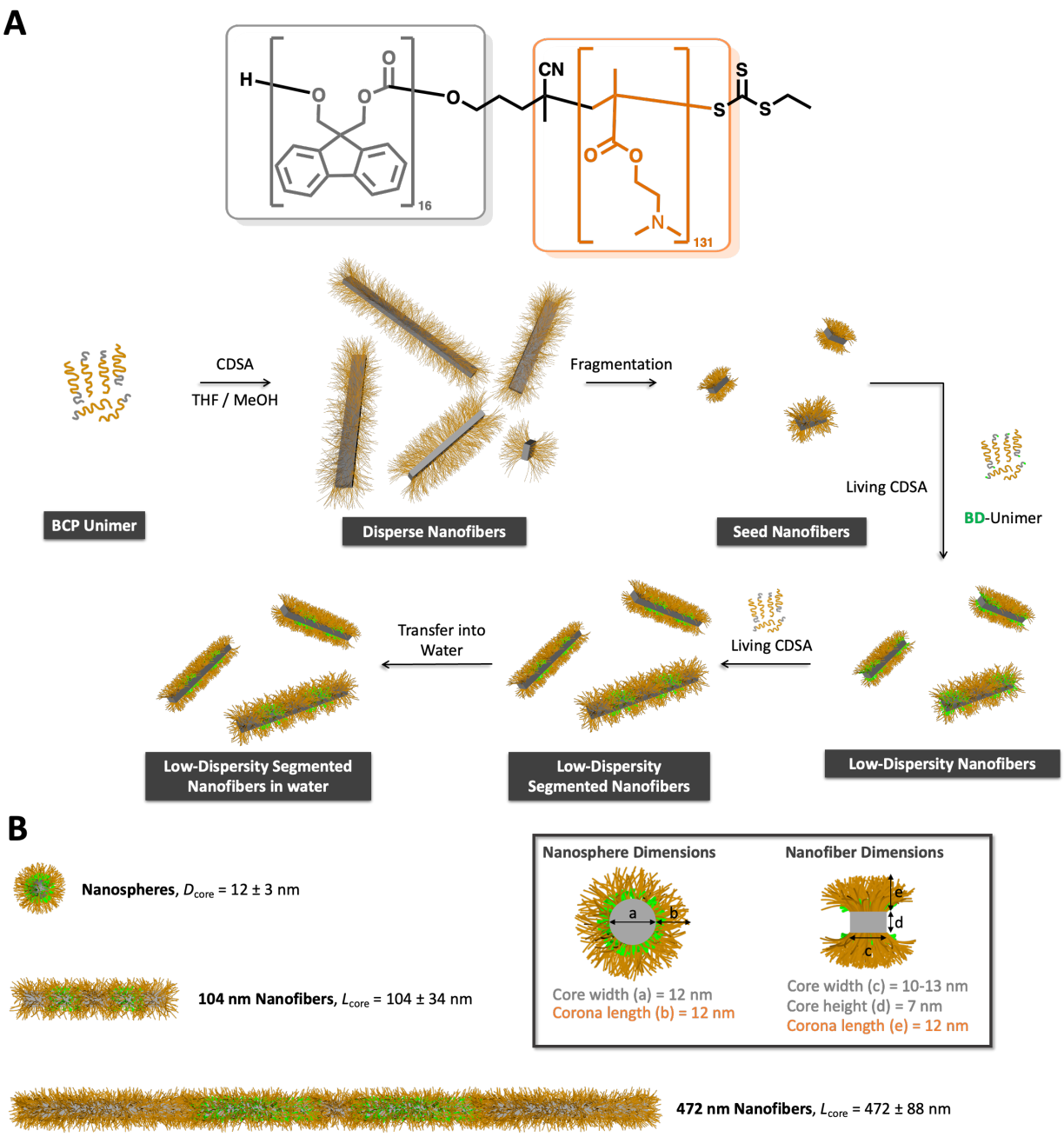


**Figure 3.1.** BCP Nanoparticles prepared by living CDSA in this work. (A) Chemical structure and schematic for the living CDSA and comicellization of pentablock ABABA fluorescent nanofibers where the A blocks are PFTMC$_{16}$-*b*-PDMAEMA$_{131}$ and the B blocks are BD-PFTMC$_{16}$-*b*-PDMAEMA$_{112}$. Adapted with permission from reference 81. Copyright 2020, Royal Society of Chemistry.[81] (B) Scale representations of the various nanofibers and nanospheres studied. The

length/diameter listed represents the core dimensions, not including the corona. The core height of the nanofibers was obtained by atomic force microscopy, and the core and corona widths were determined by contour analysis via TEM.[82] Full polymer and nanoparticle characterization is listed in Tables S3.1 and S3.2. Adapted from *J. Am. Chem. Soc*. **2022**, *144* (43), 19799–19812. DOI: 10.1021/jacs.2c06695. Copyright 2022, American Chemical Society.

### 3.3.2 Sample preparation for nanofibers and nanospheres with bacteria

Through investigation of the antibacterial mechanism of action, we sought to understand how the size and shape of crystalline-core 1D nanofibers and amorphous-core nanospheres can dictate the antibacterial activity, as well as why certain nanofiber lengths may outperform others. Sample preparation was identical for each analysis method. Controls consisted of *E. coli* (50 $\mu$L) diluted to an optical density at 600 nm of 0.6 in Lysogeny broth and mixed 1:1 with 2-(4-(2-hydroxyethyl)piperazin-1-yl)ethanesulfonic acid (HEPES) buffer (40 mM, 50 $\mu$L). The nanoparticle populations trialed were BD-labelled PFTMC$_{16}$-*b*-PDMAEMA$_{131}$-based nanofibers of length 104 nm ($Đ_L$ = 1.11) and 472 nm ($Đ_L$ = 1.03), as well as BD-labelled nanospheres 12 nm in core diameter ($Đ_L$ = 1.08), as measured by TEM (Figure S3.9D-F). These samples were diluted to 25 $\mu$g/mL in HEPES buffer and added 1:1 to a bacterial suspension in broth, giving a final concentration of 12.5 $\mu$g/mL of nanoparticles. These conditions were utilized to replicate previous antibacterial assays, at sub-inhibitory concentrations.[68] For a positive control of cell death, 100 $\mu$g/mL of 472 nm nanofibers was also prepared. All analyses involved these three nanoparticle samples, with the exception of scanning electron microscopy (SEM) where only bacteria controls, nanofibers of length 472 nm, and nanospheres were investigated. Any modifications to this procedure are noted in the specific subsections. To determine if the phenomena demonstrated against gram-negative *E. coli* are universal, the TEM and SEM experiments were also performed

against gram-positive *Staphylococcus epidermidis* 12228 (*S. epi*). However, a more in-depth study of the scope of the antibacterial activity of nanoparticles against additional bacterial strains is currently underway.

### 3.3.3 Flow cytometry studies to investigate nanoparticle-bacteria interactions

Our initial investigations involved an examination of how the nanofibers and nanospheres interact with bacteria via flow cytometry. Full sample preparation and analysis conditions can be found in the supporting information. The plot of forward-scatter vs side-scatter in the *E. coli* control was used for gating purposes. The entire population of the bacterial control was gated as "single bacteria" as minimal aggregation was expected. This population was then gated for BD fluorescence; no BD fluorescence was observable as expected (median = 10, 96% BD negative, Figure 3.2A, Figure S3.10A, Figure S3.11). The same process was applied to samples containing BD-labelled nanoparticles, however, in each an additional population of larger species was present outside of the region gated as "single bacteria" and thus was termed "aggregated bacteria" (Figure S3.10B-E). In the single bacteria population, all nanoparticle samples were BD positive. No significant difference in BD fluorescence intensity was observed between samples containing bacteria and either nanospheres or 104 nm nanofibers (median = 3,500 and 3,300; 90%, 87% BD positive respectively, Figure 3.2A, Figure S3.10B-C, Figure S3.11). There was an increased level of BD fluorescence when the 472 nm nanofibers were evaluated (median = 4,500; 91% BD positive, Figure 3.2A, Figure S3.10D, Figure S3.11). These results indicated that while approximately the same percentage of cells contained nanoparticles regardless of their shape or size, more 472 nm nanofibers were present with each cell than 104 nm nanofibers or 12 nm nanospheres. When the concentration of 472 nm nanofibers was increased from 12.5 $\mu$g/mL to 100 $\mu$g/mL, the median fluorescence increased from 4,500 to 16,000 (Figure 3.2A, Figure S3.10E,

Figure S3.11). Upon observation of the aggregated bacteria population in each nanoparticle sample, similar levels of BD fluorescence were found in each case (median = 36,000, 31,000 and 29,000 for 472 nm nanofibers, 104 nm nanofibers, and nanospheres respectively, Figure S3.12). As the concentration was increased to 100 $\mu$g/mL of 472 nm nanofibers, the median fluorescence levels increased considerably to 198,000 (Figure S3.12). Additionally, while the fluorescence levels in the aggregated bacteria population were not significantly different between samples at 12.5 $\mu$g/mL of nanoparticle, there was a higher count number of aggregated bacteria upon incubation with the 472 nm nanofibers (median = 670 events, Figure 3.2B) compared to the 104 nm nanofibers and nanospheres (median = 180 and 270 events respectively, Figure 3.2B). These studies demonstrate that longer nanofibers appear to show higher association with bacteria than shorter nanofibers or nanospheres, leading to increased bacteria aggregation.

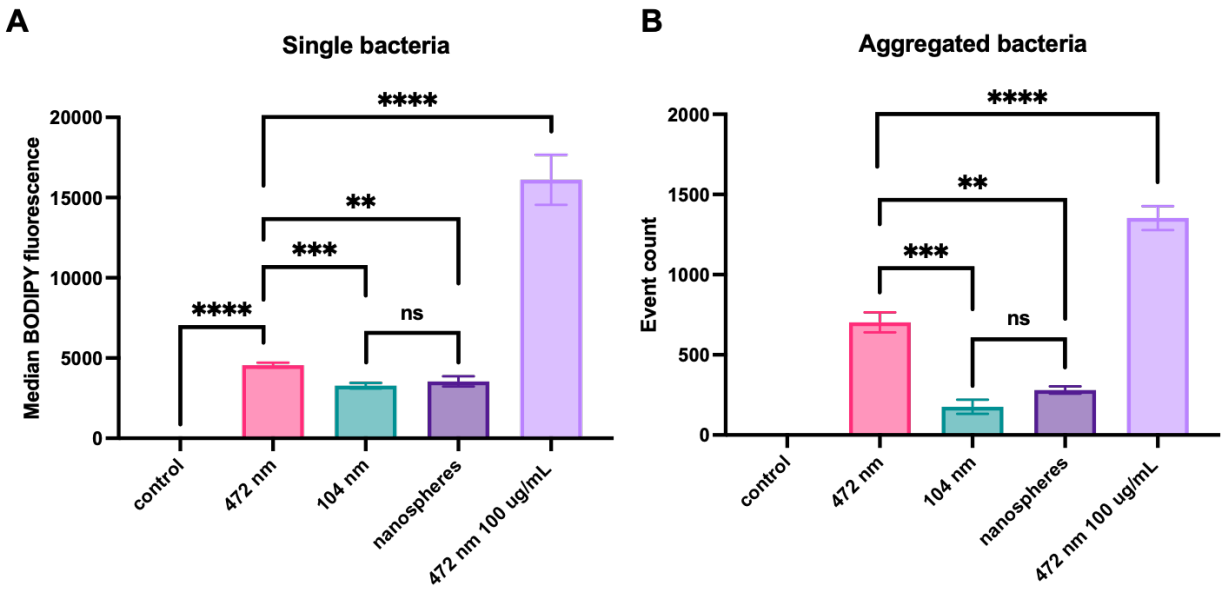


**Figure 3.2.** Flow cytometry data collected from incubation of BD-labelled nanoparticles with *E. coli* relative to bacteria incubated in the absence of nanoparticles. (A) Median BD expression of *E. coli* incubated with BD-labelled nanospheres (12.5 $\mu$g/mL, $d_{core}$ = 12 nm), 104 nm nanofibers (12.5 $\mu$g/mL), or 472 nm nanofibers (12.5 $\mu$g/mL and 100 $\mu$g/mL). (B) Median count of events in

the aggregated bacteria population via flow cytometry. A higher count is observed for the bacteria incubated with 12.5 μg/mL and 100 μg/mL of 472 nm nanofibers, in comparison to those incubated with 104 nm nanofibers and nanospheres. 95 % confidence interval of the median shown as error bars. **, ***, **** and ns indicate significance of $p < 0.01$, $p < 0.001$, $p < 0.0001$ and no significance respectively as determined by unpaired t-test between each respective group (Welch correction).

Additional flow cytometry experiments were conducted to determine the uptake of a small molecule fluorescent probe. Samples were prepared in an identical manner to the previously outlined experiments, however 1 $\mu$L of 1 $\mu$g/mL of carboxyfluorescein diacetate succinimidyl ester (CFDA-SE) was added into the mixture. CFDA-SE is a live-cell stain which becomes fluorescent upon cleavage by active intracellular esterases.[84] However, it has been well documented that this molecule is not significantly internalized by *E. coli*.[84,85] Therefore, we wished to determine the level of uptake of this dye in the presence and absence of the nanoparticles, and if this was shape- or length-dependent. The two cell populations (single bacteria and aggregated bacteria) were examined. No CFDA-SE expression was present in the control *E. coli* sample. In the single cell population, no significant difference in the level of CFDA-SE expression was observed when 12.5 $\mu$g/mL of nanoparticles were present (Figure S3.13A). Observation of the aggregated bacteria population demonstrated that there was significantly more CFDA-SE fluorescence when *E. coli* was incubated with 12.5 $\mu$g/mL of 472 nm nanofibers, relative to 12.5 $\mu$g/mL of 104 nm nanofibers, or nanospheres (Figure S3.13B). Upon incubation with 100 $\mu$g/mL of 472 nm nanofibers, a large increase was observed in CFDA-SE fluorescence in both single and aggregated bacteria (Figure S3.13A-B). Therefore, it appears that all nanoparticles allow entry of the small

molecule into the bacteria. Upon bacterial death, which is assumed to have occurred in the "aggregated bacteria" population, this small molecule entry is increased when 472 nm nanofibers are utilized.

### 3.3.4 CLSM studies to identify nanoparticle internalization into bacteria

CLSM was performed to investigate whether the BD-nanoparticles were internalized into the bacteria or merely adhered to the cell membrane. In order to visualize the *E. coli*, 4′,6-diamidino-2-phenylindole (DAPI) was added to the prepared samples (1 $\mu$L of 1 $\mu$g/mL). The DAPI fluorescence afforded facile visualization of the bacterial culture. Upon incubation with 472 nm nanofibers (12.5 $\mu$g/mL), larger aggregates of cells could be observed that colocalized with both DAPI and BD fluorescence (Figure S3.14). These aggregates were also observed via brightfield and fluorescence-filter microscopy (Figure S3.15). In each sample containing either 472 nm nanofibers, 104 nm nanofibers, or 12 nm nanospheres, a section of the field with fewer bacteria was selected for further magnification. A Z-stack was performed through the entirety of the bacteria. Uniform DAPI and BD fluorescence could be found throughout the entire cell with no discernable difference between samples (Figure 3.3, Figure S3.16, Figure S3.18). These results are indicative of nanoparticles being found uniformly throughout and surrounding the cells. Therefore, the ability of nanoparticles to cross the bacterial membrane is not critically affected by the nanoparticle shape and size. Thus, differences in cellular localization do not explain the observed antibacterial activity, however cellular uptake may contribute to the mechanism of action.

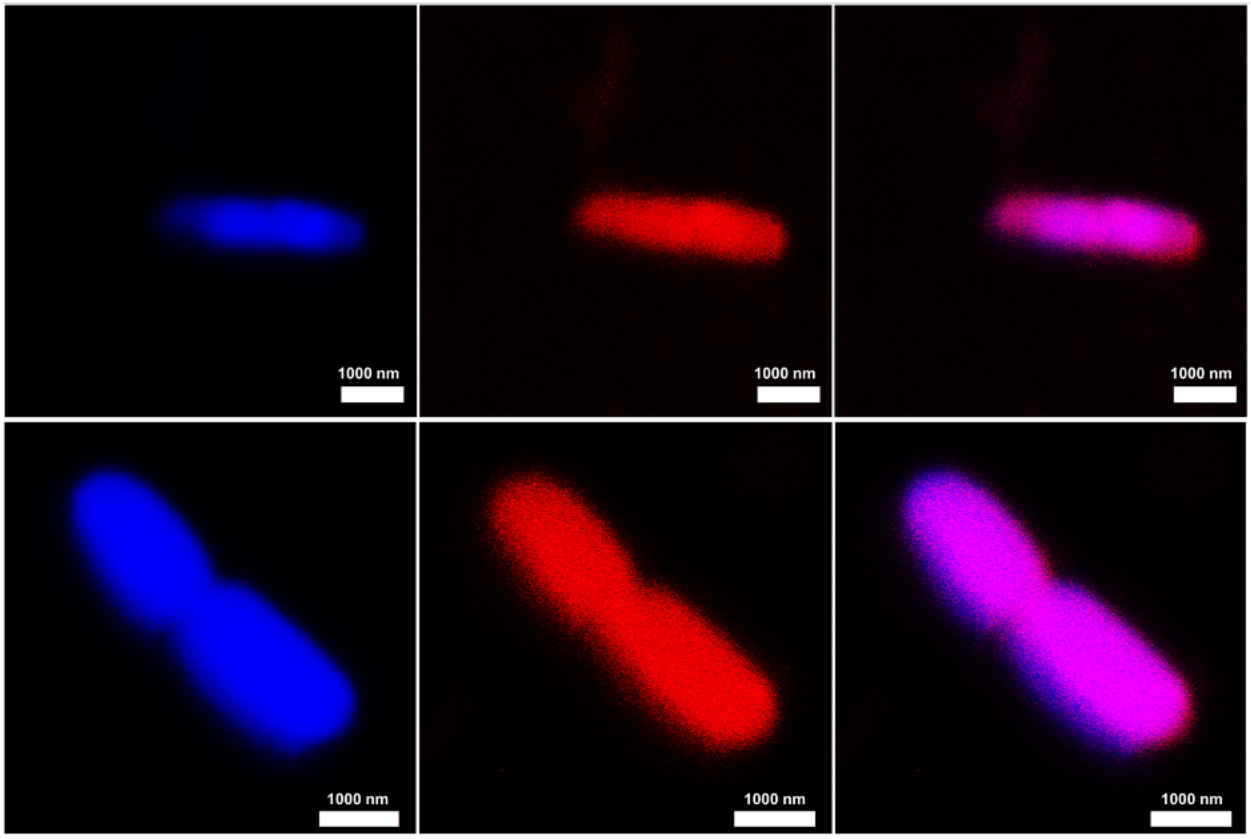


**Figure 3.3.** CLSM images of *E. coli* stained with DAPI (1 $\mu$L of 1.0 $\mu$g/mL), incubated with BD-labelled fluorescent 472 nm nanofibers (top images) or nanospheres at 12.5 $\mu$g/mL (bottom images). All images are taken from the middle of a Z-stack and the combined images are the result of overlaying the DAPI channel (blue) and BODIPY$^{630/650\text{-X}}$ channel (red).

### 3.3.5 TEM studies of nanoparticle interactions with the bacterial membrane

To gain further higher-resolution insights into whether the BD-nanoparticles were localized within bacteria or at the cell membrane, their interactions with bacteria were studied via TEM. Cells were centrifuged and collected, redispersed in a fixative, cross-sectioned, and the entirety was embedded in an Epon matrix. This was microtomed to create thin cross-sections which allowed for visualization of *E. coli* in multiple orientations (Figure 3.4). The control sample of *E. coli* showed

a high population density (Figure 3.4A). The bacterial membranes, which appear as dark edges around the bacteria, were largely intact (circled, Figure 3.4B). The bacterial size of 1.5 $\mu$m matched the expected length of *E. coli* when the bacteria were cross-sectioned along their length. Notably, upon incubation of the bacteria with 12.5 $\mu$g/mL of 472 nm nanofibers, the overall number of bacteria was considerably reduced in the sample, as shown in Figure 3.4C. Additionally, dark regions were observed around the bacterial membrane and appeared to represent fusion of the bacteria. Upon magnification of these regions, individual nanofibers were discernable (Figure 3.4D). In most cases, these nanofibers could be observed physically crossing the bacterial cell membrane (circled, Figure 3.4D). This phenomenon was observed for both the 104 nm and 472 nm samples of nanofibers (Figure S3.19). Similar aggregates of nanospheres could be observed around the bacterial cell membrane, but the TEM images showed no comparable evidence for these nanoparticles crossing the membrane in a similar fashion to the nanofibers, likely due to their smaller core dimensions (circled, Figure 3.4E). Upon incubation with 100 $\mu$g/mL of 472 nm nanofibers, TEM clearly showed that these nanofibers are capable of crossing multiple membranes simultaneously (circled, Figure 3.4F). Similar results were obtained against *S. epi* (Figure S3.20). Therefore, the 1D nanofibers are able to penetrate and remain embedded within the bacterial membrane, likely due to their length. The nanospheres appear to cross the membrane but are not visible remaining within it, likely due to their smaller dimensions.

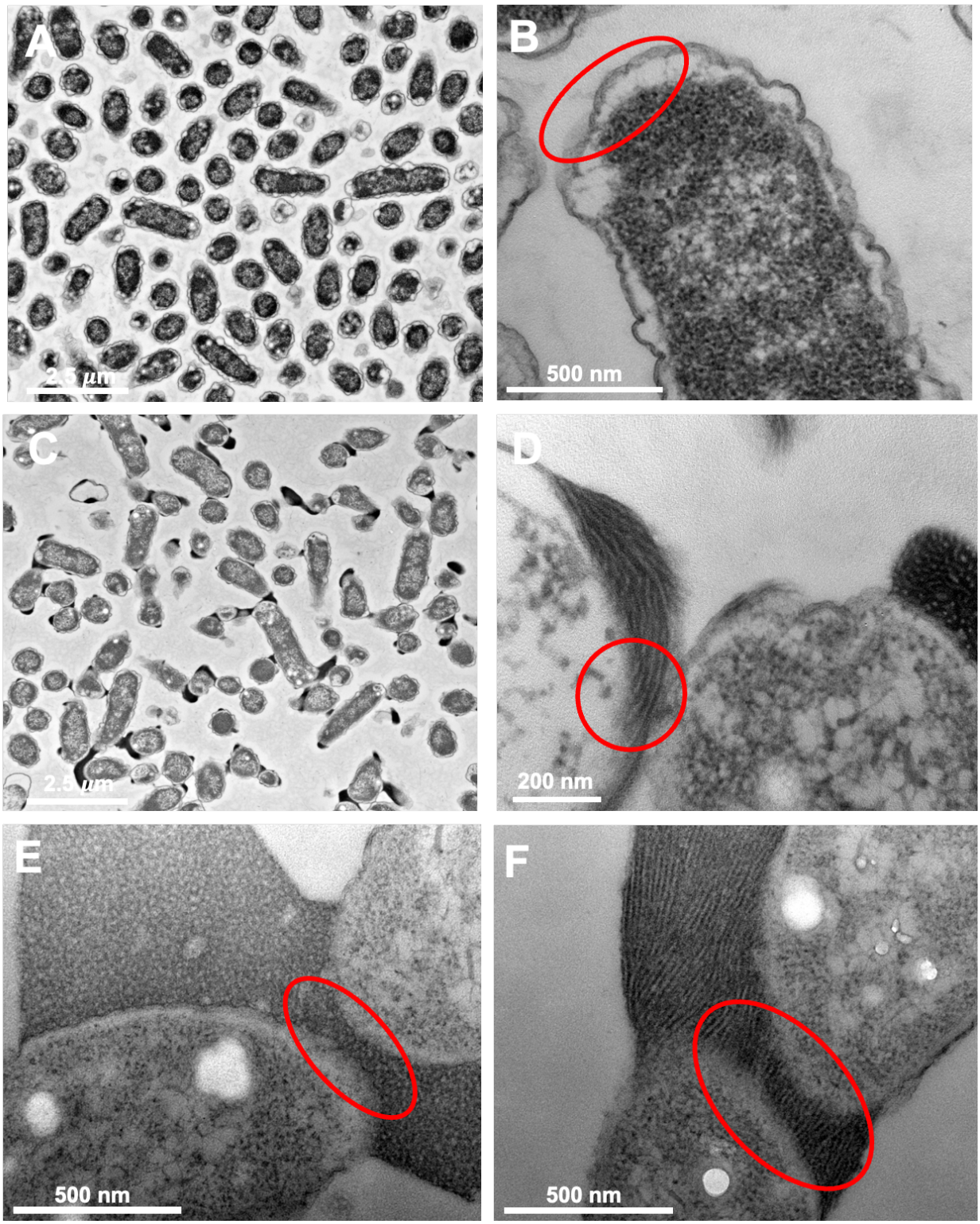


**Figure 3.4.** TEM micrographs of cross-sectioned *E. coli* before and after incubation with BD-labelled nanoparticles. (A) Low magnification TEM micrograph of control *E. coli*. They are in

high number and well dispersed. (B) Higher magnification TEM micrograph of *E. coli* found in the control sample. The appearance of the normal, intact bacterial cell membrane is highlighted in the circle. (C) Low magnification TEM micrograph of *E. coli* in the presence of 12.5 $\mu$g/mL of 472 nm nanofibers. A lower number of bacteria is observed. (D) Higher magnification TEM micrograph of *E. coli* incubated with 12.5 $\mu$g/mL of 472 nm nanofibers. The dark regions around the bacteria that correspond to long nanofibers surrounding and crossing the bacterial cell membrane are circled. (E) TEM micrograph of *E. coli* incubated with 12.5 $\mu$g/mL nanospheres ($d_{core}$ = 12 nm). The circle emphasizes the presence of nanoparticles around, but not clearly crossing the membrane. (F) *E. coli* upon incubation with 100 $\mu$g/mL of 472 nm nanofibers, where circled are the nanofibers crossing the membrane of two bacteria simultaneously, as observed by TEM. Data for 104 nm nanofibers can be found in Figure S3.19.

### 3.3.6 SEM studies of bacterial membrane integrity

To confirm that BD-nanofibers compromise the physical integrity of the bacterial membrane, SEM studies were performed. Each sample was prepared under the conditions as previously described, but an adherent polyamide coupon was added into the cell culture mixture which allowed for bacterial attachment onto a solid support for analysis. Each coupon was sputter-coated with gold to enhance contrast (full details of the procedure for sample fixation are provided in the supporting information). The control *E. coli* were well dispersed and uniformly shaped (Figure 3.5A-B). The membrane showed consistent texture and no obvious defects. Bacteria incubated with BD-nanospheres behaved similarly to the control with few defects observed (Figure 3.5C-D). Bacteria were also well-dispersed and of normal shape, corroborating the results found via TEM and CLSM. No nanospheres were apparent on the bacterial surface, but this may be due to their smaller size. To investigate this effect, bacteria were incubated with 100 $\mu$g/mL of nanospheres, upon

which point what appeared to be aggregated nanospheres could be visualized on the bacterial surface (Figure S3.21). In contrast, upon analysis of the sample containing 12.5 $\mu$g/mL of 472 nm nanofibers, the presence of deformed bacteria was common (circled, Figure 3.5E-F). Dark regions that appeared to be impressions in the membrane were apparent (circled, Figure 3.5F). In a similar manner to the samples studied by TEM and CLSM, the bacteria present were found in aggregates, confirming that the nanofibers can trigger this clustering to occur. It appeared that nanofibers were also discernable along the bacteria surface (arrows, Figure 3.5F). *E. coli* was also incubated with 100 $\mu$g/mL of 472 nm nanofibers, however a large precipitate formed instantaneously. Upon observation of the polyamide coupon, few bacteria were visible. Those present appeared to be extensively deformed (Figure S3.22). Through this data, it becomes clear that the crystalline-core of the nanofibers causes more membrane damage than analogous amorphous-core nanospheres, and this damage is enhanced by the increased length of the nanofibers. SEM data obtained upon incubation of *S. epi* with 12.5 $\mu$g/mL of nanoparticles demonstrated that both nanospheres and 472 nm nanofibers cause increased clustering of the bacteria, with nanoparticle aggregates also observable on the bacterial surface (Figure S3.23).

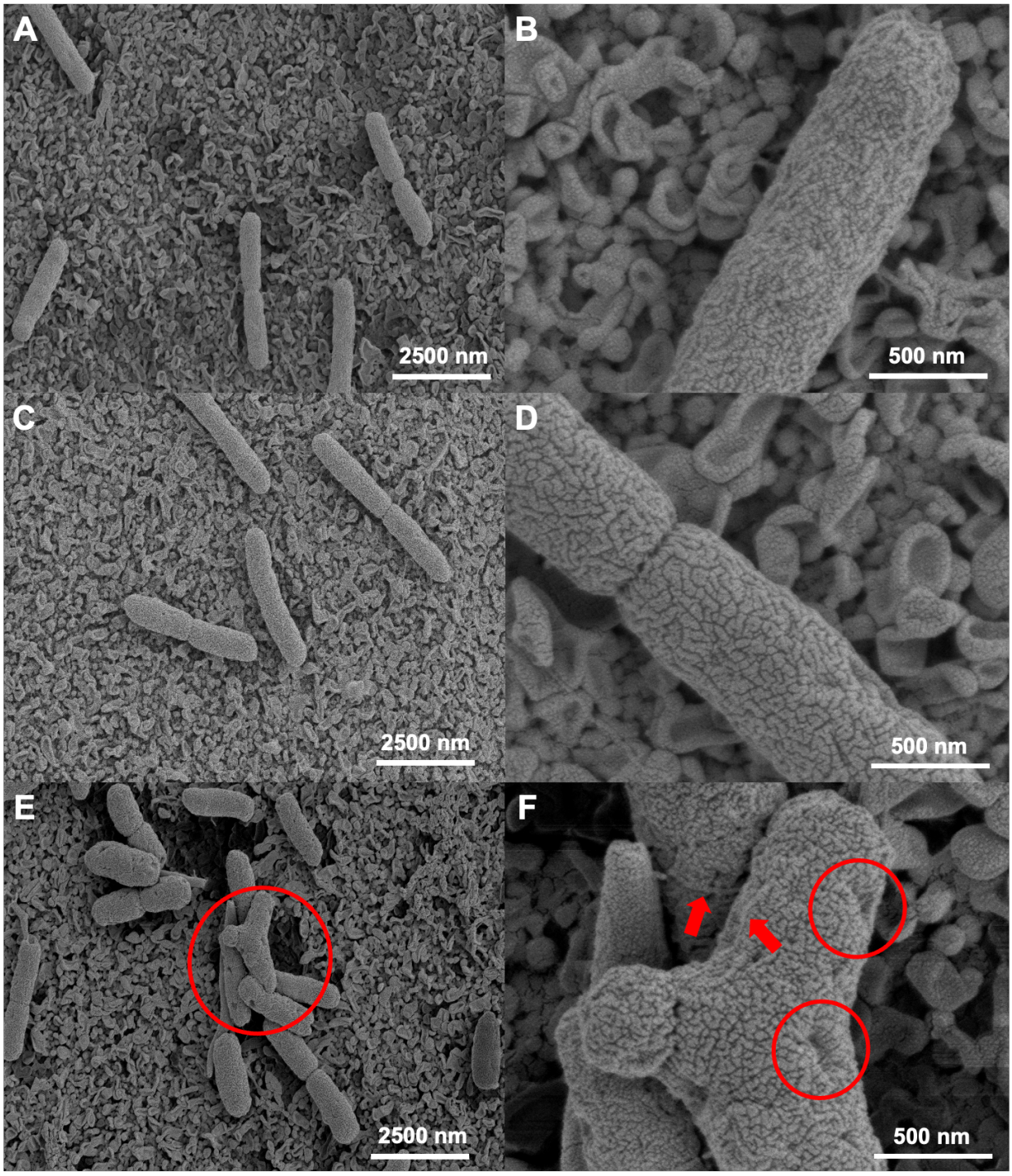


**Figure 3.5.** SEM images of *E. coli* and magnification of membrane characteristics upon incubation with BD-labelled nanoparticles, relative to the control sample. (A, B) SEM micrographs of control *E. coli* sputter coated in gold and adhered to a membrane coupon. (C, D) *E. coli* after incubation

with nanospheres (12.5 $\mu$g/mL, $d_{core}$ = 12 nm). (E, F) *E. coli* after incubation with 472 nm nanofibers (12.5 $\mu$g/mL). Circled regions highlight deformed bacterium with dark hole-like regions found throughout. Arrows indicate what appear to be nanofibers observable along the surface of the bacteria.

### 3.3.7 Studies of loaded nanofibers and nanospheres

#### 3.3.7.1 Loading molecular cargo into PFTMC$_{26}$-*b*-PDMAEMA$_{424}$ length controlled nanofibers

Next, we investigated if co-delivery of antibiotics with nanofibers could provide synergistic enhancement of antibacterial activity,[86] while providing further insights into the mechanism of action.[87,88] To this end, the dye-free BCP PFTMC$_{26}$-*b*-PDMAEMA$_{424}$ was synthesized and non-fluorescent nanofibers were prepared via living CDSA (see supporting information for full details).[89] The newly composed nanofibers were of comparable length ($L_n$ = 109 nm, $Đ_L$ = 1.07, core height = 7 nm, core width = 10 – 13 nm, Figure 3.6, Figure S3.24A, Table S3.3) to the shorter nanofibers used for investigating the mechanism of action microscopically ($L_n$ = 104 nm). Despite longer nanofibers having higher antibacterial activity, shorter nanofibers have been proven to be of more biological relevance as their size (ca. 100 nm) is critical for persistence in circulation by providing resistance to renal clearance whilst also being able to cross biological barriers.[40,41,90] Furthermore, short nanofibers have been demonstrated to most effectively load and deliver both nucleic acid and hydrophobic therapeutic cargos.[82,90,91] Thus, shorter nanofibers were selected for co-delivery studies. Dye-free nanospheres of a similar core diameter (16 nm, $Đ_L$ = 1.03) to those utilized for the mechanistic work (12 nm) were prepared via direct addition of a PFTMC$_{26}$-*b*-PDMAEMA$_{424}$ THF unimer solution into water (Figure 3.6, Figure S3.24B, Table S3.3) for comparisons to the activity of nanofibers. Lastly, to enable comparisons between similarly sized

nanoparticles which only differ in core shape and crystallinity, short seed nanofibers were prepared ($L_n$ = 23 nm, $Đ_L$ = 1.05) (Figure 3.6, Figure S3.24C, Table S3.3). These samples would allow us to determine if nanoparticle uptake and drug delivery is dependent on size, core crystallinity, or both.

To deliver antibiotics to the bacteria simultaneously with nanofibers, cargo-loading at the core-corona interface was investigated. Previous reports by our group illustrate this ability using the model compound nile red via a solvent-switch method that involves transferring the nanofibers and cargo from organic solvent into aqueous solution through the slow addition of water.[91,92] Full details of the drug loading procedure can be found in the supporting information. Tetracycline was selected as the candidate for drug loading as it is hydrophobic and active against gram-negative *E. coli*. Tetracycline targets the internal 30S subunit of ribosomal ribonucleic acid allowing us to determine if co-delivery with nanofibers aids its entry into the cell.[93]

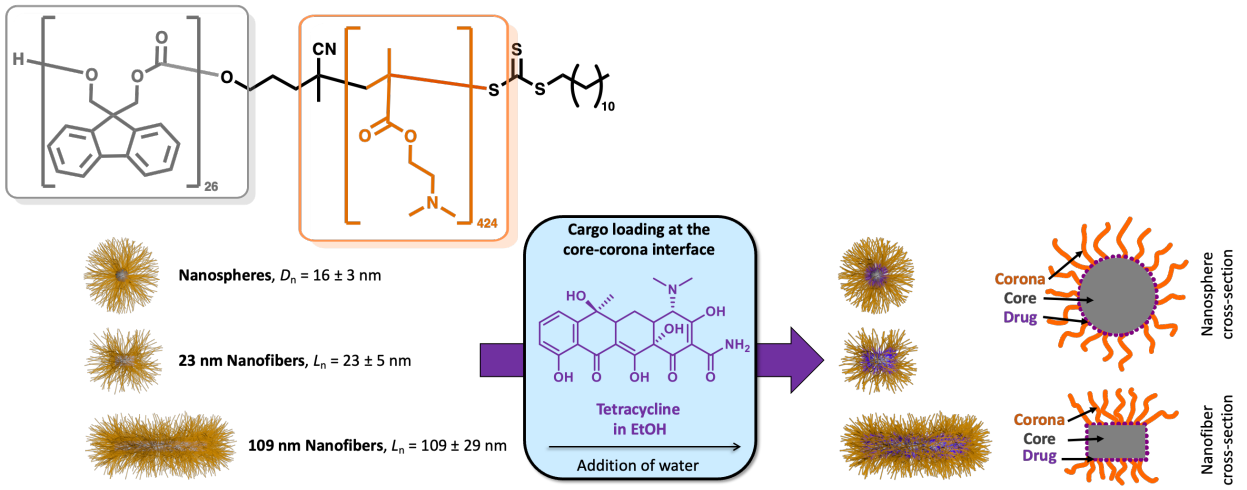


**Figure 3.6.** Nanoparticles evaluated for antibacterial activity against *E. coli* W3110. Nanoparticles are present in their respective self-assembly solvents. Tetracycline in EtOH, and water are then added at which point the organic solvents are allowed to evaporate, which is proposed to drive the hydrophobic cargo to the core-corona interface of the nanoparticles. Adapted from *J. Am. Chem.*

*Soc.* **2022**, *144* (43), 19799–19812. DOI: 10.1021/jacs.2c06695. 

Dynamic light scattering was employed to evaluate the maximum loading capacity of the nanofibers, as we envisaged that it was a versatile and time-efficient method that has been previously demonstrated to effectively characterize drug loading.[94] In addition, quantifying fluorescence emission as a means to determine drug loading was not viable due to the low intrinsic fluorescence of tetracycline. Tetracycline was loaded into 109 nm PFTMC$_{26}$-*b*-PDMAEMA$_{424}$ nanofibers in increments from 1 wt % to 50 wt % relative to nanofiber mass and the hydrodynamic radius ($R_h$) was measured. In the absence of nanofibers, tetracycline (equivalent to 1 wt % loading) exhibited an $R_h$ of 193 nm. Conversely, non-loaded nanofibers exhibited an $R_h$ of 115 nm. The $R_h$ of nanofibers loaded with 1 wt % to 20 wt % tetracycline matched that of the non-loaded nanofibers (Figure 3.7). At 50 wt %, the size distribution became much broader, and the $R_h$ was found to be in between that of the non-loaded nanofibers and the free drug control, indicating the tetracycline may be less closely associated with the nanofibers in solution (Figure 3.7). Similar results were obtained for both nanospheres and seed nanofibers upon loading of tetracycline at 20 wt % (Figure S3.25A-B). TEM investigations were performed to verify that there were no changes to the nanoparticle size or morphology upon addition of tetracycline (Figure S3.26). No major structures of pure tetracycline were visible by TEM (Figure S3.26). This is likely due to TEM being a solid-state technique and thus aggregation is not observable. Therefore, 20 wt % was selected as the optimal drug loading concentration.

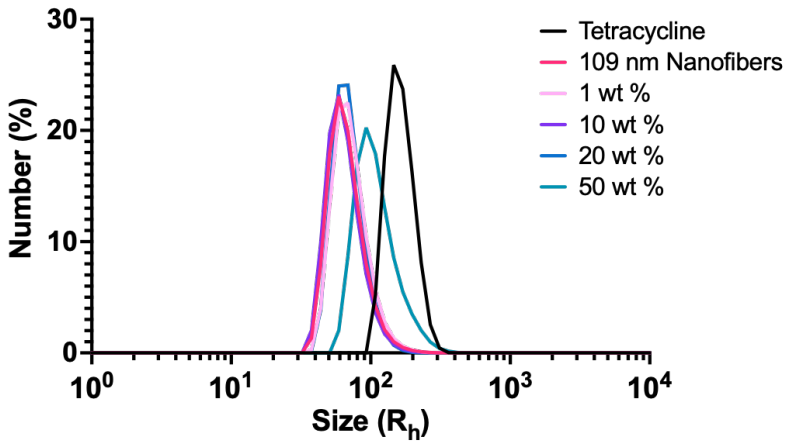


**Figure 3.7.** DLS traces given as $R_h$ vs. number of: 1 wt % free tetracycline ($R_h$ = 193 nm, $Đ$ = 0.093, black trace), non-loaded 109 nm nanofibers ($R_h$ = 115 nm, $Đ$ = 0.17, dark pink trace) and nanofibers loaded with 1 wt % ($R_h$ = 111 nm, $Đ$ = 0.14), 10 wt % ($R_h$ = 103 nm, $Đ$ = 0.13), 20 wt % ($R_h$ = 96 nm, $Đ$ = 0.22) and 50 wt % ($R_h$ = 154 nm, $Đ$ = 0.15) tetracycline. Traces are the mean of 5 replicates of 5 runs of each sample. Dispersities given are those reported by the DLS instrument.

As DLS is a relatively low-resolution method of determining drug loading, we wished to utilize a secondary method to confirm that the tetracycline was fully loaded onto the nanofibers at 20 wt %. The experimentally determined limit of detection of our nanofibers via flow cytometry is ca. 500 nm. Therefore, 483 nm ($Đ_L$ = 1.10, Figure S3.27A) nanofibers were loaded with 20 wt % tetracycline (Figure S3.27B), and compared to an equivalent amount of pristine nanofibers, along with free tetracycline, via flow cytometry. The results were normalized to the number of events detected for nanopure water. By assuming that each event represents either a nanofiber or a drug particle, we were able to determine that the number of events between drug-loaded (median = 265,300) and non-loaded nanofibers (245,600) did not significantly differ. The median number

of events for an equivalent amount of free tetracycline was found to be 51,950. Thus, we presume that the majority of the tetracycline is loaded at this percentage (Figure S3.28). While DLS, TEM, and flow cytometry data indicate that the tetracycline is associated with the nanoparticles, these techniques do not provide information about where on the nanoparticle it is located. Previous assessments performed by our group determined that hydrophobic small molecules localize to the core-corona interface of PFTMC nanofibers,[91] however, due to differences in the chemical composition of the corona and small molecules used, localization to the corona or inclusion within the crystalline core, though unlikely, cannot be discounted.

#### 3.3.7.2 Assessment of antibacterial activity

Optical density measurements were performed to determine the antibacterial activity of the nanofibers, nanospheres, and seed nanofibers as previously reported.[68] The $EC_{50}$ (half maximal effective concentration) of PFTMC-*b*-PDMAEMA materials have been previously measured against a variety of mammalian cell-types and range from 12 – 20 $\mu$g/mL.[81] No cytotoxicity was observed for $PFTMC_{26}$-*b*-$PDMAEMA_{424}$ against U-87 MG glioblastoma cells at 6.25 $\mu$g/mL.[89] *E. coli* W3110 was selected as a model gram-negative organism and because it allows for direct comparison to our previously reported results and microscopic studies. The minimum inhibitory concentration (MIC), or the concentration required to inhibit bacterial growth, was first determined for the non-loaded nanofibers. Minimum bactericidal concentrations (MBCs) were also determined for the non-loaded samples. Our previous report involved unloaded nanofibers composed of $PFTMC_{16}$-*b*-$PDMAEMA_{131}$ with lengths 107 nm and 593 nm ($Đ_L$ = 1.10, 1.14) that displayed MICs of 55 and 17 $\mu$g/mL, respectively. In agreement with these results, we observed a similar activity for 109 nm $PFTMC_{26}$-*b*-$PDMAEMA_{424}$ nanofibers with a longer PDMAEMA coronal block against *E. coli* (MIC = 37 $\mu$g/mL, MBC = 100 $\mu$g/mL, Figure 3.8). Upon addition

of 20 wt % tetracycline at the core-corona interface, the antibacterial activity of 109 nm nanofibers was substantially improved, exhibiting an MIC of 15 $\mu$g/mL indicative of potent antibacterial behavior (Figure 3.8A-B). Importantly, an amount of tetracycline equivalent to 20 wt % was also evaluated, and the antibiotic showed no inhibition of *E. coli* growth (Figure S3.29). Nanospheres and seed nanofibers alone exhibited no significant antibacterial activity (MIC > 100 $\mu$g/mL, $MBC_{spheres}$ > 250 $\mu$g/mL, $MBC_{seeds}$ = 150 $\mu$g/mL), in the former case in agreement with our previously published results on similar materials (Figure S3.30A-B).[68] However, upon incubation of *E. coli* with $PFTMC_{26}$-*b*-$PDMAEMA_{424}$ nanospheres loaded with 20 wt % tetracycline, the antibacterial activity was dramatically improved and a MIC of 3 $\mu$g/mL was determined (Figure S3.30C). A similar result was observed for $PFTMC_{26}$-*b*-$PDMAEMA_{424}$ seed nanofibers, with an MIC obtained of 4 $\mu$g/mL (Figure S3.30D). Upon visualization of the bacterial cultures via brightfield microscopy, stark differences were observed. In the samples containing loaded nanospheres, the bacteria were well dispersed and motile at all concentrations of loaded nanospheres, with the exception of 100 $\mu$g/mL where small clusters of cells were present (Figure S3.31). Upon investigation of the samples containing $PFTMC_{26}$-*b*-$PDMAEMA_{424}$ seed nanofibers and 109 nm nanofibers (both non-loaded and loaded with tetracycline), clear clustering and cell death were observed (Figure S3.31). This occurred only at higher concentrations of seed nanofibers (100 $\mu$g/mL – 25 $\mu$g/mL), below which point the bacteria began to behave more similarly to the samples containing nanospheres (Figure S3.31). Therefore, the small size afforded by the assembly of nanospheres or seed nanofibers is advantageous for drug delivery, while the crystalline-core of the seed nanofibers is crucial for imparting membrane damage to the bacteria.

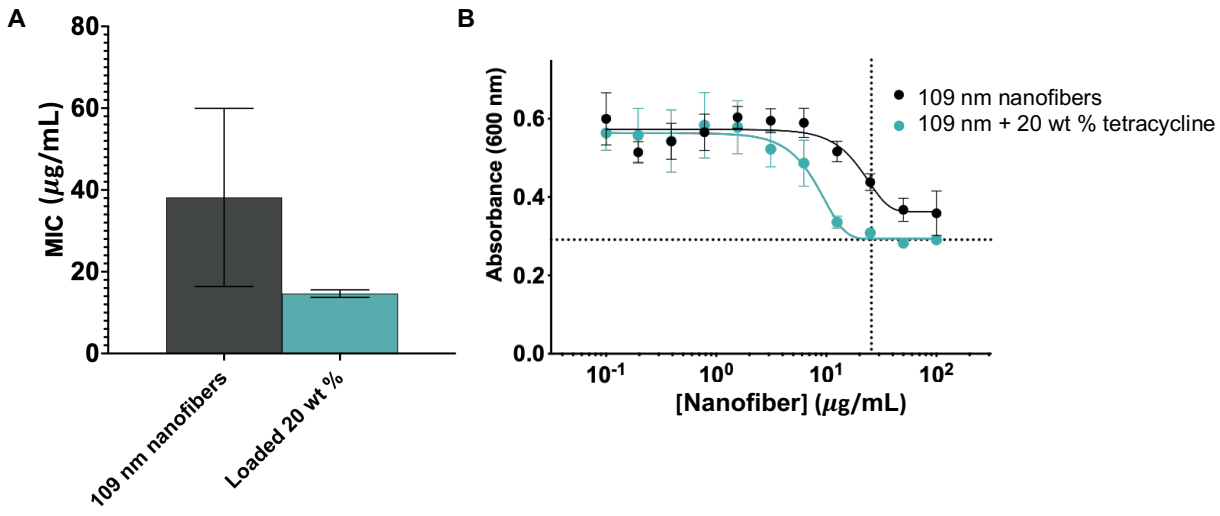


**Figure 3.8.** Antibacterial activity of 109 nm PFTMC$_{26}$-*b*-PDMAEMA$_{424}$ nanofibers compared to identical nanofibers loaded with 20 wt % tetracycline. (A) Minimum inhibitory concentrations against *E. coli* W3110 for nanofibers of $L_n$ = 109 nm ($Đ_L$ = 1.07) both non-loaded and loaded with 20 wt % tetracycline. The mean of 3 replicates, evaluated in triplicate is plotted, with error shown as σ. (B) Bacterial growth curves plotted as *E. coli* absorbance at 600 nm versus the concentration of 109 nm nanofibers. No effect was observed for the antibiotic alone (Figure S3.29).

## 3.4 Discussion

The goal of the aforementioned work was to elucidate the mechanism of action of antibacterial polymer nanofibers. Previous publications hypothesize that cationic nanoparticles largely disrupt bacteria through electrostatic interactions with the anionic cell membrane, however it is not well understood why there may be a length and shape dependence on the activity.[76,77,79,95,96] We attempted to address this knowledge gap by conducting multiple experiments involving flow cytometry and different forms of microscopy. The former method demonstrated that longer 472 nm nanofibers associate better with bacteria than shorter 104 nm nanofibers or 12 nm nanospheres.

This may be because of the increased length and thus higher availability of charged groups in a single nanoparticle to interact with the bacteria in a side-on manner. One could imagine that wrapping around the bacteria would be favourable as opposed to interacting end-on, as has been postulated previously.[97] Thus, the higher antibacterial activity associated with the longer nanofibers could be in part due to increased association with the bacteria.[67,68] Through flow cytometry we also demonstrated that while all nanoparticles enabled CFDA-SE uptake, CFDA-SE levels were higher in aggregated bacteria populations when 472 nm nanofibers are present in solution. This indicates that upon interaction of the bacteria with the long nanofibers, permeabilization occurs to a greater extent relative to 104 nm nanofibers or 12 nm nanospheres, allowing small molecule entry into the cell. In order to distinguish between any internal or external effects on the bacteria, CLSM was performed. Upon analysis of both DAPI and BODIPY$^{630/650\text{-}X}$ fluorescence in the bacterial culture, it became clear that the nanospheres, the 104 nm nanofibers, and the 472 nm nanofibers are all localized throughout the bacteria, indicating that each of these nanoparticles can cross the bacterial cell membrane. This led to an evaluation of the physical interactions with the bacteria using higher resolution microscopy. TEM of bacterial cross-sections allowed for further insight into differing interactions occurring with bacteria depending on the nanoparticle shape or size. Importantly, it was directly observed that both long and short nanofibers are capable of penetrating the bacterial cell membrane. It was also discovered that long nanofibers especially could adhere neighbouring bacteria together and disrupt multiple organisms simultaneously. Furthermore, nanofibers of increased length could likely outperform shorter counterparts due to their ability to better intercalate the membrane of a single bacterium. It was not possible to visualize nanospheres crossing the membrane in a similar fashion, however by CLSM, it is clear this also occurs as other mechanisms of particle uptake in bacteria are unlikely

due to their size (> 10 nm).[98] Lastly, using SEM analysis it was possible to corroborate the results obtained via TEM. In the presence of long nanofibers, the bacteria were misshapen and contained dark regions assumed to represent damage from the nanofibers, contributing to a decrease in membrane integrity. Upon incubation with nanospheres, bacteria contained far fewer of these defects and their shapes matched those found in the control. Therefore, while nanospheres are able to cross the cell membrane, it appears that this process does not cause sufficient stress to result in cell death or deformation. The 472 nm nanofibers conclusively cause severe clustering and deformation of bacteria. It can therefore be concluded that 1D nanofibers cause more membrane damage than analogous nanospheres, and thus nanoparticle shape is critical for obtaining optimum antibacterial activity. These results highlight that the mechanism of action of 1D nanofibers is largely physical, and thus antibacterial resistance should be difficult to acquire.[99,100]

The differing abilities of nanoparticles to deliver tetracycline to *E. coli* provides pertinent insight into the mechanism of action. Medium-length 109 nm nanofibers perform this task moderately. Significant bacterial damage is visualized via brightfield microscopy, and the MIC is improved, indicating successful delivery of the drug to the bacteria. The further results upon incubation of *E. coli* with drug-loaded seed nanofibers and nanospheres provide arguably more conclusive insight into the mechanism of action. It is clear that the antibacterial activity of the loaded nanospheres is solely attributable to the bacteriostatic action of the tetracycline, due to the lack of antibacterial activity and bactericidal damage caused by the nanospheres themselves. The antibiotic simply hinders bacterial replication and does not directly cause apoptosis of the bacteria, and therefore we observe what appear to be healthy bacteria but in low numbers relative to the controls. In contrast, the seed nanofibers impart significant cell damage at concentrations above 25 $\mu$g/mL, and below such concentrations effectively deliver the tetracycline which obstructs the

bacterial replication. The results of these studies demonstrate that the activity of nanofibers, nanospheres, and seed nanofibers is enhanced by co-delivery with antibiotics, and thus all nanoparticle morphologies and sizes are internalized to some extent, agreeing with our CLSM data (Table 3.1). It is clear however, that although the nanofibers possess higher inherent antibacterial activity, they are not able to enter the bacteria as readily and thus a less significant effect is observed upon antibiotic delivery. From the microscopic results, it is likely that the penetration of the membrane afforded by the 1D shape also impedes its full internalization into the cell. This process allows the nanofibers to cause significant cell damage in a pure state but hinders their abilities as delivery vehicles. In contrast, the smaller size of the nanospheres and seed nanofibers likely leads to facile crossing of the cell membrane without causing as significant damage, and thus higher internalization and stronger characteristics as delivery vehicles are observed. We can also conclude that the presence of the crystalline core found in the seed nanofibers facilitates the killing of the bacteria at higher concentrations. In other words, we witness bactericidal activity at high concentrations of seed nanofibers (Figure S3.31). In the case of nanospheres, bactericidal activity was not demonstrated, and only a bacteriostatic effect from the antibiotic is observed. Therefore, the crystalline core is crucial for imparting physical damage to the bacteria, with longer nanofibers exhibiting the highest inherent antibacterial activity, and shorter seed nanofibers proving to be superior for drug delivery (Table 3.1).

**Table 3.1.** Summary of the results for the antibacterial activity of trialed nanoparticles.

| **PFTMC$_{26}$-*b*-PDMAEMA$_{424}$ nanoparticle** | **MIC ($\mu$g/mL) in unloaded state** | **MIC ($\mu$g/mL) in Tetracycline-loaded state (20 wt. %)** | **Core composition** | **Degree of anisotropy** | **Membrane damage as observed via microscopy** |
|---|---|---|---|---|---|
| 109 nm nanofibers | 37 | 15 | crystalline | high | high[a] |
| 16 nm nanospheres | > 100 | 3 | amorphous | low | low[b] |
| 23 nm seed nanofibers | > 100 | 4 | crystalline | low | medium[c] |

[a, b, c] see Fig S31

Importantly, these results also showcase a synergy that occurs between the nanoparticles and the antibiotics. No effect was observed for the equivalent loaded amount of antibiotic alone, but in combination with the nanoparticles, the activity was enhanced to a value beyond that of the unloaded nanoparticles. The antibiotic is effectively solubilized and delivered to the cell. By taking advantage of the inherent antibacterial activity of the nanofibers and exploiting the mechanism of action of nanospheres and seed nanofibers we have been able to design potent antibacterial materials and render the bacteria more susceptible to antibiotic treatment, a step that is crucial for decreasing antibiotic resistance.[3] The MIC range for traditional antibiotics normally falls within 0.1 – 10 $\mu$g/mL and so the combination treatments reported here hold significant promise for treating bacterial infections.[101]

## 3.5 Conclusions

We have successfully determined the antibacterial mechanism of action of 1D nanofibers and nanospheres composed of the BCP PFTMC-*b*-PDMAEMA. Confirming previous hypotheses that the cationic corona was able to target bacteria,[46,67,68] we demonstrate that this occurs universally for 472 nm and 104 nm nanofibers and 12 nm nanospheres, but that the 1D shape of nanofibers prepared via living CDSA is solely able to significantly intercalate into the bacterial membrane, enhancing activity relative to nanospheres. In addition, 1D nanofibers, nanospheres, and seed nanofibers were loaded with 20 wt % of tetracycline and the antibacterial activity was measured. The enhanced inhibition exemplified by the combination treatments confirm that all nanoparticles trialed can facilitate entry of antibiotics into the cell, and that those smaller and less elongated are more useful for therapeutic delivery. The difference in uptake abilities and bactericidal activity between short nanofibers, nanospheres, and seed nanofibers highlights the importance of the presence of a rigid crystalline core in the 1D nanomaterials. Finally, the results presented here showcase how understanding the nuanced mechanisms of action governed by nanoparticle shape, size, and core-crystallinity is critical to create the most potent antibacterial materials.

## 3.6 Supporting Information

### 3.6.1 General considerations

The syntheses and characterizations of $PFTMC_{16}$-*b*-$PDMAEMA_{131}$ and $PFTMC_{26}$-*b*-$PDMAEMA_{424}$ have been previously reported by Street et al. and Parkin et al.[68,81,82,89] PFTMC homopolymer degrees of polymerization were determined by matrix-assisted laser desorption/ionization mass spectrometry and block-copolymer degrees of polymerization were determined by integrations of coronal block peaks in $^1H$ NMR relative to peaks of the PFTMC block. RAFT-CTA was dried via vacuum desiccation over phosphorus pentoxide prior to use. BODIPY$^{630/650\text{-}X}$ NHS ester (catalogue number: D10000) was purchased from ThermoFisher

Scientific (Canada). All other reagents and solvents were purchased from Sigma-Aldrich (Canada), Combi-Blocks (USA), VWR (Canada), or Fisher Scientific (Canada) and used without further purification. Solvents for self-assembly were HPLC grade and were filtered through PTFE, nylon, or cellulose filters with a pore size of 200 nm before use.

### 3.6.2 Instrumentation

**Gel permeation chromatography (GPC)**

GPC was conducted on a Malvern Viscotek RImax chromatograph equipped with a refractive index (RI) detector, a UV/Vis detector operating at 240 nm, and a viscometer. *n*-$Bu_4NBr$/THF (1% *v/v*) was used as the eluent, with the flow rate set at 1 mL/min. The columns used were T3000, followed by T5000 (Viscotek) at a constant temperature of 35 °C. The calibration of the RI detector was carried out using polystyrene standards (Viscotek). Samples were prepared at 1 mg/mL in eluent and filtered through a polytetrafluorethylene membrane filter, pore size = 0.2 μm. GPC chromatograms were processed using OMNISEC software (Malvern Panalytical, UK) and plotted using custom scripts (available on request) built using the open-source python modules NumPy, pandas and Matplotlib.

**NMR Spectroscopy**

$^{1}H$ and $^{13}C$ NMR spectra were obtained at 25 °C in the solvent specified with Bruker spectrometers, operating at the field strengths listed. Chemical shifts are quoted in parts per million with spectra referenced to the residual solvent peak. Multiplicities are abbreviated as: br (broad), s (singlet), d (doublet), t (triplet), q (quartet), p (pentet), m (multiplet) and *app.* (apparent) or combinations thereof. Assignments of $^{1}H$-NMR and $^{13}C$-NMR signals were made where possible, using COSY, HSQC and HMBC experiments. The $DP_n$ of PFTMC was determined via MALDI-TOF MS, whilst the $DP_n$ of PDMAEMA was determined via $^{1}H$-NMR spectrometry by comparing the integration of the PFTMC aromatic protons to the N-C$H_3$ protons of PDMAEMA.

**Ultrasonication**

Micelle sonication was carried out using either a Fisherbrand 112xx series advanced ultrasonic cleaner (FB-11203), operated in sweep mode for at 80 % power and 37 MHz at 15 °C, or using a Hielschur UP100H sonication probe (100W total output power) at 80% power.

**Transmission electron microscopy (TEM)**

TEM images were obtained on a JEOL 1011 microscope equipped with an 11 Megapixel CCD camera, operating at 80 kV. Nanoparticle solutions (1.5 μL, 1 – 4 mg/mL) were drop-casted onto

a carbon-coated copper grid. Uranyl acetate solution (8.5 µL) in EtOH (3 wt %) was subsequently drop-cast on top, and the grids were left to dry overnight. Copper grids (400 mesh) were purchased from Ted Pella. Carbon films (ca. 6 nm) were prepared by carbon sputtering mica sheets with a Leica ACE 600 carbon coater. The carbon films were deposited onto copper grids via floatation on water and the grids were allowed to air dry.

For micelle length analysis, a minimum of 150 nanofibers were traced manually using the FIJI software package (US National Institute of Health). The number average micelle length ($L_n$) or width ($W_n$) and weight average micelle length ($L_w$) were calculated using eq. S1-2 from the individual contour lengths ($L_i$) of the micelles. Here, $N_i$ is the number of micelles of length $L_i$, and $n$ is the number of micelles examined in each sample. The distribution of micelle lengths is characterized by $Đ_L = L_w/L_n$.

$$L_n = \frac{\sum_{i=1}^{n} N_i L_i}{\sum_{i=1}^{n} Ni} \qquad L_w = \frac{\sum_{i=1}^{n} N_i L_i^2}{\sum_{i=1}^{n} NiLi} \qquad \text{(eq. S1-2)}$$

**Sample preparation for bacteria-nanofiber analysis via TEM**

Samples were spun in an Eppendorf centrifuge. Supernatants were removed and replaced with 1.0 mL of fixative while disturbing the pellets to ensure even fixation. After 1 hr at 22 ℃, the sample were placed in a fridge overnight. The samples were again spun and the supernatants removed and replaced with low melt agarose, Type VII (Sigma, Cat # A9045, St Louis, MO, 63103 USA). The samples were spun and cooled to set in the agarose. The pellets were removed from their sample tubes and the excess agarose was cut off and discarded. The sample pellets were further fixed for 30 min at 22 ℃ and then in a fridge overnight. Once warmed to 22 ℃, the samples were washed in 0.1 M cacodylate buffer and then post-fixed in 1 % osmium tetroxide in cacodylate buffer for 1 h. After washing in cacodylate buffer, the samples were dehydrated in a graded ethanol series and embedded into an Epon replacement (EMBed-812, Cat # 14120, Electron Microscopy Sciences, Hatfield, PA 19440, USA) using propylene oxide as the transition liquid.[102] The Epon was polymerized at 60 ℃ for two days. Ultrathin TEM sections were cut and placed onto 150 mesh carbon-coated formvar grids and stained for 10 min in uranyl acetate and 4 min in lead citrate.[102]

**Dynamic Light Scattering (DLS)**

Dynamic light scattering (DLS) was carried out using a Malvern Zetasizer Pro. For DLS measurements to investigate drug-loaded samples, 10 µL of aqueous nanofiber solution was

diluted into 40 $\mu$L filtered 40 mM HEPES buffer (pH 7.4) (resulting in a 32 mM HEPES solution) and the size was recorded. The correlation function was acquired in real time and analyzed by Cumulant analysis. This process allowed the diffusion coefficients for the nanoparticles to be determined, and these were expressed as the effective hydrodynamic radius ($R_h$) using the Stokes-Einstein relationship for coated spheres in water (Refractive Index = 1.33, Dispersant Viscosity = 0.887, Dispersant Dielectric Constant = 78.5) with core properties of polystyrene latex (Refractive Index = 1.590, Absorption = 0.010).

**Flow Cytometry**

All experiments were performed on a Beckman Coulter CytoFLEX flow cytometer. The plate reader mode was utilized for analyzing bacterial samples. Optical filters were arranged according to instrument specifications to enable BODIPY$^{630/650\text{-}X}$ and DAPI monitoring. The gain and threshold for each channel was optimized using liquid broth as a control for bacterial experiments (Forward scatter gain = 300, Side-Scatter threshold = 40,000). Samples were prepared by incubating nanoparticles (12.5 $\mu$g/mL) with *E. coli* W3110 (0.6 absorbance at 600 nm) to a final volume of 100 $\mu$L. Each condition was prepared in triplicate. Samples were injected into the instrument and 10,000 events were recorded. Data collected included forward-scatter and side-scatter, count, and BODIPY$^{630/650\text{-}X}$ fluorescence.

**Cytation 5 plate reading for kinetic assays**

Absorbance measurements (100 µL of sample) were obtained with the Biotek Cytation 5 multimode plate reader and were conducted at 37 °C in a Corning 96-well plate (clear plates, with the lid). The samples were excited at 600 nm and the absorbance values were recorded. Two readings were taken, at time zero and 4 hours after. After the 0 hour reading, the 96-well plate was placed in an incubator at 37 °C with orbital shaking at 200 rpm.

**Confocal laser scanning microscopy (CLSM)**

CLSM images were obtained using a Zeiss LSM 880 microscope. Two channels were used for detecting fluorescence, one for DAPI using a 405 nm laser, and one for BODIPY$^{630/650\text{-}X}$ using a 633 nm laser. Filters for -405 nm and 488/543/633 were used. The pinhole was set to 1 Au. Each laser was operated at 2 % power and the gain was set to 650 for DAPI and 700 for BODIPY$^{630/650\text{-}X}$. Wavelengths observed were 411-510 nm and 641-754 nm. Images were acquired using the 63× oil objective and were processed using Zen software (Carl Zeiss AG, Germany).

**Scanning electron microscopy (SEM)**

SEM images were obtained on a Hitachi S-4800 SEM, operating at 1.0 kV and a working distance of 8 $\mu$m in high vacuum mode.[103] Three images were taken at 10,000× and 40,000× for each sample. Samples were coated in gold to 10 nm of thickness using an Anatech Hummer IV Au coater. Bacteria cultures were incubated with nanofibers in an eppie tube. Polyamide coupons (TriSep, YMACM34205) were placed in each eppie tube, and the samples were incubated for 1 h at 37 °C, at which point the coupons were removed and placed in individual polypropylene Petrie dishes. The coupons were rinsed with a solution of 2.5 % glutaraldehyde in phosphate buffered saline (PBS) at 4 °C for 4 h.[103] This solution was then removed, and each coupon was rinsed twice with sterile PBS for 5 min each time. The coupons were then rinsed twice with deionized water for 5 min each to remove the PBS. Samples were then dehydrated using a gradient of EtOH (30%, 50%, 70%, 80%, 96%, and 100%) by suspension in increasing concentrations of EtOH for 5 min each time.[103] Lastly, samples were dried using hexamethyldisilazane, first in a 50 % solution diluted in PBS for 30 min, followed by a 100 % solution for 30 min.[103] Coupons were left overnight in a desiccator to dry and imaged the following day.

### 3.6.3 Synthetic Procedures

**Synthesis of BD-PFTMC$_{16}$-*b*-PDMAEMA$_{112}$**

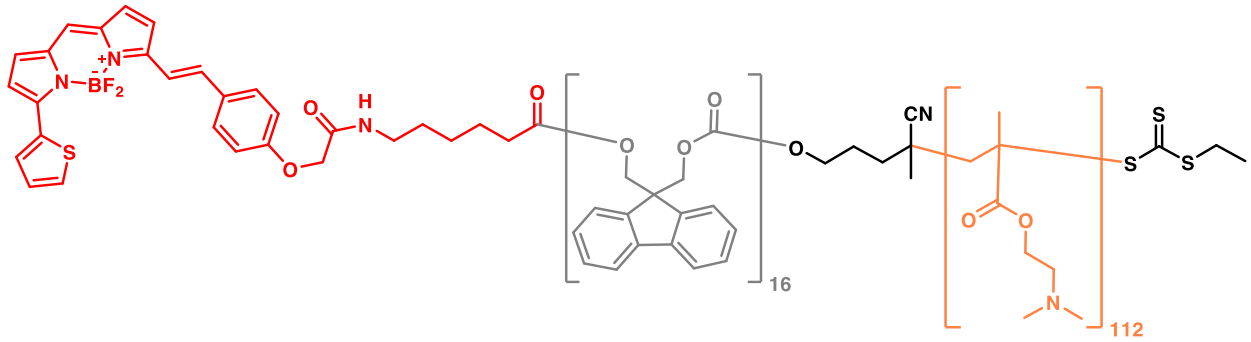


To a solution of PFTMC$_{16}$-*b*-PDMAEMA$_{131}$ (37.4 mg, 0.001 mmol, 1.0 eq) in anhydrous DMSO (5.0 mL), 4-dimethylaminopyridine (10 mg, 0.082 mmol, 55 eq), *N,N'*-Diisopropylcarbodiimide (2.0 µL, 0.013 mmol, 9 eq) and BODIPY$^{630/650\text{-X}}$ NHS ester (3.0 mg, 0.004 mg, 3 eq) was added and stirred at rt for 22 h until complete consumption of the starting material was observed via TLC and a blue spot which was fluorescent and UV active appeared (hexanes/EtOAc, 1:1, $R_f = 0.1$; $CH_2Cl_2$/MeOH, 8:2, $R_f = 0.9$). The crude reaction mixture was lyophilized to a solid, redissolved in $CH_2Cl_2$ (10 mL) and purified by precipitation into hexanes (note: this may be performed by

gently agitating the sample in a centrifuge tube). The precipitate was observed to be blue in colour and fluorescent, whilst the supernatant was slightly fluorescent. The supernatant was decanted off, the polymer dried, and precipitated from $CH_2Cl_2$ into hexanes twice more, at which point the supernatant was still slightly fluorescent. The polymer was dissolved in $CH_2Cl_2$ (2.0 mL) and dialysed into EtOH with four dialysate changes to remove any further unreacted BODIPY$^{630/650\text{-X}}$ dye, at which point it was observed that the dialysate was no longer fluorescent. The solution was dried *in vacuo* to yield BD-PFTMC$_{16}$-*b*-PDMAEMA$_{112}$ as a blue solid (32 mg, 77 %). Analysis of the $^1$H-NMR integrals of Hp, Ho, and Hg revealed a ca. 50 % end-capping with BODIPY$^{630/650\text{-X}}$. **$^1$H-NMR** (500 MHz, DMSO-$d_6$) δ 8.16 – 8.07 (1H, m, Hp), 8.04 (1H, d, $J$ = 3.6 Hz, Ho), 7.80 (32H, s, Hg), 7.65 – 7.55 (3H, m, Hn & Hk), 7.44 – 7.10 (96H, m, Hg), 7.08 (2H, d, $J$ = 8.6 Hz, Hl), 6.95 (1H, d, $J$ = 4.1 Hz, Hm), 4.54 (2H, s, Hj), 4.46 – 4.15 (70H, m, Hf), 3.98 (176H, s, Hc), Hd is underneath the water peak and not observable, 3.14 (2H, app. s, Hi), 2.64 (2H, app. s, Hh), 2.19 (669H, s, He), 1.94 – 1.39 (228H, m, Ha), 1.29 – 0.50 (342H, m, Hb), DP$_n$ PFTMC = 16, DP$_n$ PDMAEMA = 112; **GPC** (NEt$_3$/THF, PS standard): $M_n$ = 20,400 g/mol, $Đ_M$ = 2.13.

**Scheme S3.1.** Synthetic route to BD-PFTMC$_{16}$-*b*-PDMAEMA$_{112}$ (BD = BODIPY$^{630/650\text{-X}}$) from PFTMC$_{16}$-*b*-PDMAEMA$_{131}$.

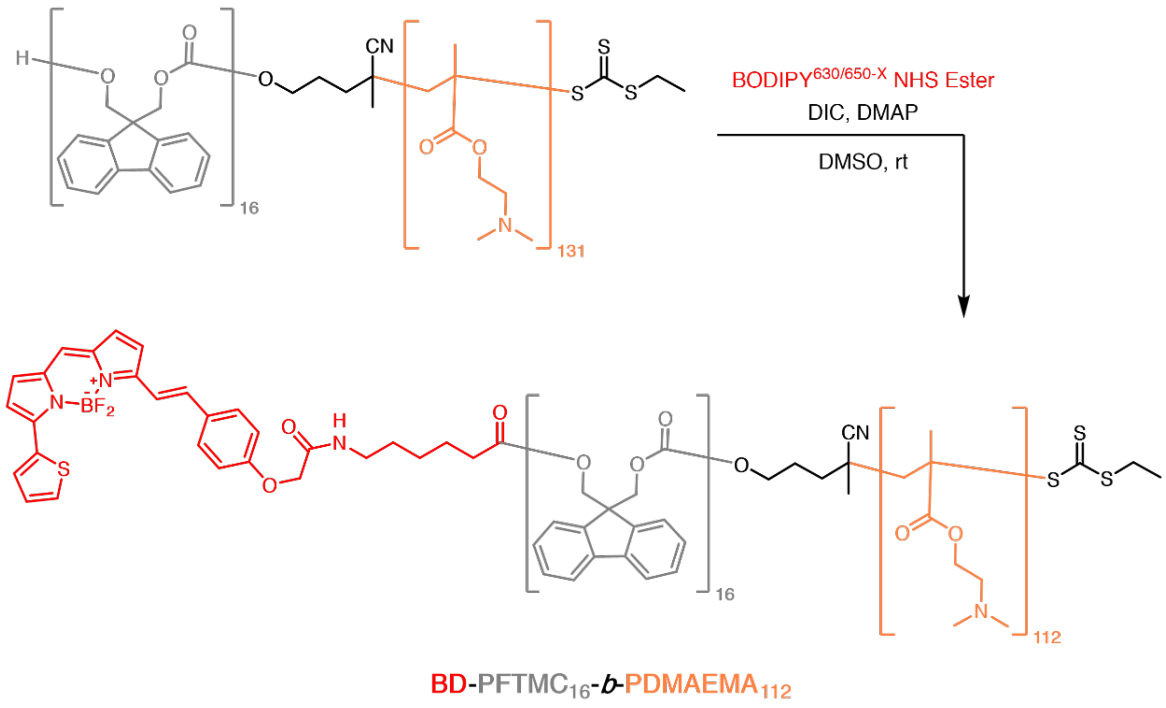

### 3.6.4 Self-Assembly Procedures

The composition of all solvents is given in *v:v*. Low dispersity nanofibers of BD-PFTMC$_{16}$-*b*-PDMAEMA$_{112}$/PFTMC$_{16}$-*b*-PDMAEMA$_{131}$ and PFTMC$_{26}$-*b*-PDMAEMA$_{424}$ were prepared according to the procedures reported by Street et. al.[68, 89] All nanofibers were ultimately transferred into distilled water via slow addition of water to the self-assembly solution, followed by evaporation of the organic solvent. The method is further outlined in the drug-loading section, and follows the same process as stated but excludes the addition of a therapeutic. The selective solvent for self-assembly of BD-PFTMC$_{16}$-*b*-PDMAEMA$_{112}$/PFTMC$_{16}$-*b*-PDMAEMA$_{131}$ was MeOH, while for PFTMC$_{26}$-*b*-PDMAEMA$_{424}$ EtOH was used. Nanospheres were prepared either by dialysis of DMSO unimer solution into water over the course of 3 days, or via direct addition of THF unimer solution into water followed by evaporation of the THF.

**General self-nucleation procedure**

A solution of diBCP dissolved in THF (unimer) (20 mg/mL) was diluted in THF. Unimer solution was slowly added via a micropipette into a selective solvent (e.g EtOH) to yield solutions with final solvent compositions of 20:80 THF:EtOH and 1 mg/mL of polymer. Each solution was manually shaken for ~10 s and aged at 23 °C for 24 h for PFTMC$_{16}$-*b*-PDMAEMA$_{131}$ or heated to 60 °C for 3 h and allowed to cool to 23 °C for PFTMC$_{26}$-*b*-PDMAEMA$_{424}$. The length-disperse nanofibers were analyzed via TEM.

**General preparation of seed nanofibers**

Disperse nanofibers were subjected to sonication using a using a Fisherbrand 112xx series advanced ultrasonic cleaner (FB-11203) at 10 °C in sweep mode at 37 mHz and 80 % power for at least 3 h, or using a Hielschur UP100H sonication probe (100W total output power) at 0 °C, 80% power for 3 h. The resulting seed nanofibers were analyzed via TEM.

**General procedure for the preparation of low dispersity, controlled length nanofibers via seeded growth (living CDSA)**

For seeded growth assemblies with $m_{unimer}/m_{seed} \leq 10$: aliquots of unimer (20 mg/mL in THF) were added to diluted identical composition seed nanofiber solutions (0.1 mg/mL – 1 mg/mL) in EtOH. The self-assembly solutions (THF content: 10 – 20% in EtOH) were manually shaken for ~15 s and aged for 24 h at 23 °C.

**General procedure for the preparation of segmented BODIPY$^{630/650\text{-}X}$ labelled nanofibers via living CDSA**

A solution of low dispersity PFTMC$_{16}$-*b*-PDMAEMA$_{131}$ seed nanofibers (between 0.1 and 5 mg/mL) were diluted in a volume of selective solvent appropriate to the final concentration of polymer and solvent composition. To this solution, an aliquot of BD-PFTMC$_{16}$-*b*-PDMAEMA$_{112}$ unimer solution in common solvent (THF, 20 mg/mL) appropriate to the desired $m_{\text{unimer}}$:$m_{\text{seed}}$ ratio was added, the sample was manually shaken for 10 s, then vortex mixed for 10 s, and aged at 23 °C for 24 h. The resulting triblock segmented nanofibers were then imaged via TEM, before a further aliquot of PFTMC$_{16}$-*b*-PDMAEMA$_{131}$ unimer solution in common solvent (THF, 20 mg/mL) appropriate to the desired $m_{\text{unimer}}$:$m_{\text{seed}}$ ratio was added, the sample was manually shaken for 10 s, then vortex mixed for 10 s, and aged at 23 °C for a further 24 h. The resulting pentablock segmented low dispersity nanofibers were then imaged via TEM before being transferred into water via the method outlined above.

**Example procedure for preparation of segmented BODIPY$^{630/650\text{-}X}$ labelled nanofibers via living CDSA**

28 nm PFTMC$_{16}$-*b*-PDMAEMA$_{131}$ nanofibers ($Đ_{\text{L}}$ = 1.20, $\sigma$ = 12 nm, 500 µL, THF/MeOH 1:99 *v/v*, 1 mg/mL) were diluted in MeOH (500 µL). To this solution, BD-PFTMC$_{16}$-*b*-PDMAEMA$_{112}$ unimer solution (50 µL, 20 mg/mL in THF, $m_{\text{unimer}}$:$m_{\text{seed}}$ = 2) was added, and the sample was manually shaken for 10 s, then vortex mixed for 10 s, and aged at 23 °C in the dark for 24 h. The resulting low dispersity nanofibers were characterized via TEM ($L_{\text{n}}$ = 66 nm, $Đ_{\text{L}}$ = 1.16, $\sigma$ = 27 nm). To a solution of these triblock segmented nanofibers, PFTMC$_{16}$-*b*-PDMAEMA$_{131}$ unimer (50 µL, 20 mg/mL in THF, $m_{\text{unimer}}$:$m_{\text{seed}}$ = 2, based on original seeds) was added, and the sample was manually shaken for 10 s, then vortex mixed for 10 s, and aged at 23 °C in the dark for 24 h. The resulting low dispersity pentablock segmented nanofibers were characterized via TEM ($L_{\text{n}}$ = 104 nm, $Đ_{\text{L}}$ = 1.09, $\sigma$ = 32 nm). To these pentablock segmented nanofibers (1mL, 2mg/mL), filtered deionized water was added (1mL) via syringe pump infusion (10 µL/min), then aged for 72 h at 23 °C until the mass of solution was less than 1 g. Filtered deionized water was added to make the sample up to 1 mg/mL gravimetrically (2 g). The resulting low dispersity nanofibers were characterized via TEM ($L_{\text{n}}$ = 104 nm, $Đ_{\text{L}}$ = 1.11, $\sigma$ = 34 nm) and stored in the dark.

**General preparation of nanospheres**

BD-nanospheres were prepared via 1:1 mixing of BD-PFTMC$_{16}$-*b*-PDMAEMA$_{112}$ unimer in DMSO with PFTMC$_{16}$-*b*-PDMAEMA$_{131}$ unimer also in DMSO. The resulting solution was placed in dialysis tubing and was dialyzed against water over 3 days. The final solution was collected and gravimetrically made up to 1 mg/mL. Nanospheres of PFTMC$_{26}$-*b*-PDMAEMA$_{424}$ were prepared via direct addition of 20 mg/mL THF unimer solution into water. The THF was allowed to evaporate, and the resulting solution was gravimetrically made up to 1 mg/mL.

### 3.6.5 Drug loading procedure

The solubility of the selected therapeutic was investigated. Tetracycline (5 mg) was added to a vial and 5 mL of solvent was added, to result in a 1 mg/mL solution. In water, a precipitate was visible to the eye. In ethanol, the compound readily dissolved. The loading capacity was investigated from 1 wt % to 50 wt % relative to nanofiber mass. For 1 wt % trials, a stock solution of 0.1 mg/mL drug was made in EtOH. For all other loading capacities, a 1 mg/mL solution was used. In each case, 100 µL of nanofibers or seed nanofibers in self-assembly solvent (THF:EtOH, 2:8 *v/v*) was added into a pre-weighed vial. The appropriate amount of therapeutic in EtOH was added for each respective loading quantity. $H_2O$ was filtered through a 0.3 $\mu$m cellulose acetate syringe filter and then added slowly to the mixture via micropipette in a volume 50 µL in excess of the organic solvent volume. The vial was left open to air overnight to promote organic solvent evaporation. The vial was re-weighed and a gentle stream of air was used to reduce the $H_2O$ volume to less than 100 µL. The vial was then topped up with $H_2O$ to reach 100 µL, at which point it was left open for a further 24 h to ensure total organic solvent evaporation. $H_2O$ was again added to reach a final volume of 100 µL. Loaded nanospheres were prepared in a similar manner, however due to the nature of the self-assembly process, the nanospheres were already present in water. Therefore, the tetracycline solution in EtOH was added directly into the water nanosphere solution, and the organic solvent was allowed to evaporate. No precipitate was observed during this process. As the organic solvent evaporated, $H_2O$ was added to reach the appropriate final volume and concentration. Each resulting drug-loaded solution (10 µL) was then diluted into 40 mM HEPES (40 µL) and the hydrodynamic radius was measured via DLS. For free drug controls, the same volume of drug stock solution (in EtOH) was added into blank EtOH and transferred into $H_2O$ following the same procedure. Nanofiber controls were performed similarly, but no drug was added. A 20 wt % loading was used for all antibacterial experiments.

### 3.6.6 Antibacterial assays

All bacteria work was performed in a biological safety cabinet using sterile technique. All materials were autoclaved and disinfected with 70 % ethanol prior to being placed in the biological safety cabinet. Clear, sterile, 96-well plates were purchased from Corning. Lysogeny broth (LB) was used for streak plates and liquid culturing of *Escherichia coli* (*E. coli*) W3110. The buffer was prepared by weighing out (4-(2-hydroxyethyl)-1-piperazineethanesulfonic acid) (HEPES) into a glass bottle, filling with distilled water, autoclaving, and balancing to pH 7.4. Minimum inhibitory concentration (MIC) curves were fitted using GraphPad Prism and the Lambert and Pearson method.[104] The procedure previously reported by Parkin et al.[68] was modified to observe the t = 0 min and t = 240 min timepoints, with a full 4 h of incubation at 37 °C at 200 rpm orbital shaking in between. Minimum bactericidal concentrations (MBCs) were determined by incubating *E. coli* with nanoparticles in concentrations from 50 µg/mL to 250 µg/mL for 24 h. The overnight cultures were visualized via brightfield microscopy and MBC values were taken as the concentrations where no motile bacteria were present within the culture.

**Preparation of bacteria for assays.**

From a stock solution of *E. coli* W3110 that was kept at -80 °C, a single loop was used to make a streak plate (LB agar). These plates were placed in an incubator at 37 °C for 24 h. This was repeated. From these initial streak plates, a second propagation was performed. A disposable loop was used to select one colony from each, and streaked onto another plate, respectively. The new plates were incubated at 37 °C for 24 h. Subsequently, they were moved into a 4 °C fridge. To grow a liquid culture, a single colony was selected from a plate using a disposable loop. This was placed in 5 mL of LB broth contained in a 15 mL Falcon tube. The loop was swirled in the broth until the colony was visibly deposited in the broth. The falcon tube was placed in an incubator at 37 °C with orbital shaking at 200 rpm. The culture was allowed to grow for 24 h. From the initial culture, 25 µL of solution was taken and added to a second 15 mL falcon tube containing 5 mL of broth. This new culture was placed in an incubator at 37 °C with orbital shaking at 200 rpm for 24 h.

**Plating of bacteria and nanofibers determining the minimum inhibitory concentration.** Liquid bacterial cultures were diluted in respective broth to a maximum volume of 3 mL and to an absorbance of 0.600 using an OD meter and a polystyrene cuvette. Once the appropriate dilutions were determined, they were performed on a larger scale to give at least 5 mL of bacterial

suspension in a sterile reservoir. 10 mL of 40 mM HEPES buffer was added to a separate sterile reservoir. Using a multichannel pipette, 50 µL of buffer was added to each well, excluding the third column. The first row (A1-12) and the last row (H1-12) were topped up to 100 µL of buffer to be used as blanks and to prevent evaporation. The first column was also used as a buffer blank. To three wells in the third column (B3, C3, D3) 20 µL of 1 mg/mL material to be tested was added, and 20 µL of 1 mg/mL of a second material to be tested was added to the next three (E3, F3, G3). Each of these wells was then diluted with 80 µL of buffer solution. From the third column, 50 µL was taken from each well using a multichannel pipette and placed into the next column in order to dilute the material in half. This was repeated until the full plate was serially diluted to 0.2 ug/mL. Each time, the material was pipetted up and down three times to ensure proper mixing. Diluted bacterial suspension (50 µL) was added into each well, including the second column as a control (HEPES, broth, and bacteria). Therefore, the final volume in each well was 100 µL.

### 3.6.7 Supplementary Tables

**Table S3.1.** Summary of molar mass data for, PFTMC$_{16}$-*b*-PDMAEMA$_{131}$, PFTMC$_{26}$-*b*-PDMAEMA$_{424}$ and BD-PFTMC$_{16}$-*b*-PDMAEMA$_{112}$ polymers. Data for PFTMC$_{16}$-*b*-PDMAEMA$_{131}$ and PFTMC$_{26}$-*b*-PDMAEMA$_{424}$ is reproduced with permission from the Royal Society of Chemistry.[68, 81] The large $M_n$ values observed with the universal calibration method is likely due to polymer aggregation and/or interaction with the column.

| Polymer | $M_n$ (g/mol) GPC | $M_w$ (g/mol) GPC | $Đ_M$ GPC | $DP_n$ NMR | $M_n$ (g/mol) NMR | $DP_n$ MALDI-TOF |
|---|---|---|---|---|---|---|
| PFTMC$_m$-*b*-PDMAEMA$_n$ | 9,700[a]<br>18,300[b] | 15,000[a]<br>28,000[b] | 1.55[a]<br>1.53[b] | m = 20<br>n = 131 | 24,900 | m = 16 |
| PFTMC$_o$-*b*-PDMAEMA$_p$ | 87,900[c] | 102,100[c] | 1.16[c] | o = 26<br>p = 424 | 73,500 | o = 26 |
| BD-PFTMC$_m$-*b*-PDMAEMA$_q$ | 20,400[b] | 43,600[b] | 2.13[b] | q = 112 | 22,400 | m = 16 |

[a] Previously reported GPC data, using polystyrene standards on a different instrument.

[b] GPC data from this publication, using polystyrene standards.

[c] Previously reported GPC data, using universal calibration.

**Table S3.2.** TEM length and dispersity data of ($PFTMC_{16}$-*b*-$PDMAEMA_{131}$)-m-(BD-$PFTMC_{16}$-*b*-$PDMAEMA_{112}$)-m-($PFTMC_{16}$-*b*-$PDMAEMA_{131}$)-m-(BD-$PFTMC_{16}$-*b*-$PDMAEMA_{112}$)-m-($PFTMC_{16}$-*b*-$PDMAEMA_{131}$) pentablock comicelle nanofibers and blend nanospheres.

| Morphology | Length in THF/MeOH (nm) | Length upon transfer into Water (nm) | $Đ_L$[+] from Water |
|---|---|---|---|
| Nanofibers | 104 ± 32 | 104 ± 34 | 1.11 |
| Nanofibers | 456 ± 94 | 472 ± 88 | 1.03 |
| Nanospheres | - | 12[*] ± 3 | 1.08 |

[*] diameter of the core,

[+] $Đ_L = L_w/L_n$

**Table S3.3.** TEM length and dispersity data in THF/EtOH mixtures, as well as hydrodynamic radius ($R_h$) of $PFTMC_{26}$-*b*-$PDMAEMA_{424}$ nanofibers, nanospheres, and seed nanofibers recorded in 32 mM HEPES via DLS.

| Morphology | Length from THF/EtOH (nm) | Length upon transfer into Water (nm) | $Đ_L$ from Water | $R_h$ in 32 mM HEPES (nm) |
|---|---|---|---|---|
| Nanofibers | 103 ± 28 | 109 ± 29 | 1.07 | 115 ± 2 |
| Nanospheres | - | 16 ± 3 | 1.03 | 110 ± 10 |
| Seed nanofibers | 24 ± 5 | 23 ± 5 | 1.05 | 94 ± 1 |

### 3.6.8 Supplementary Figures

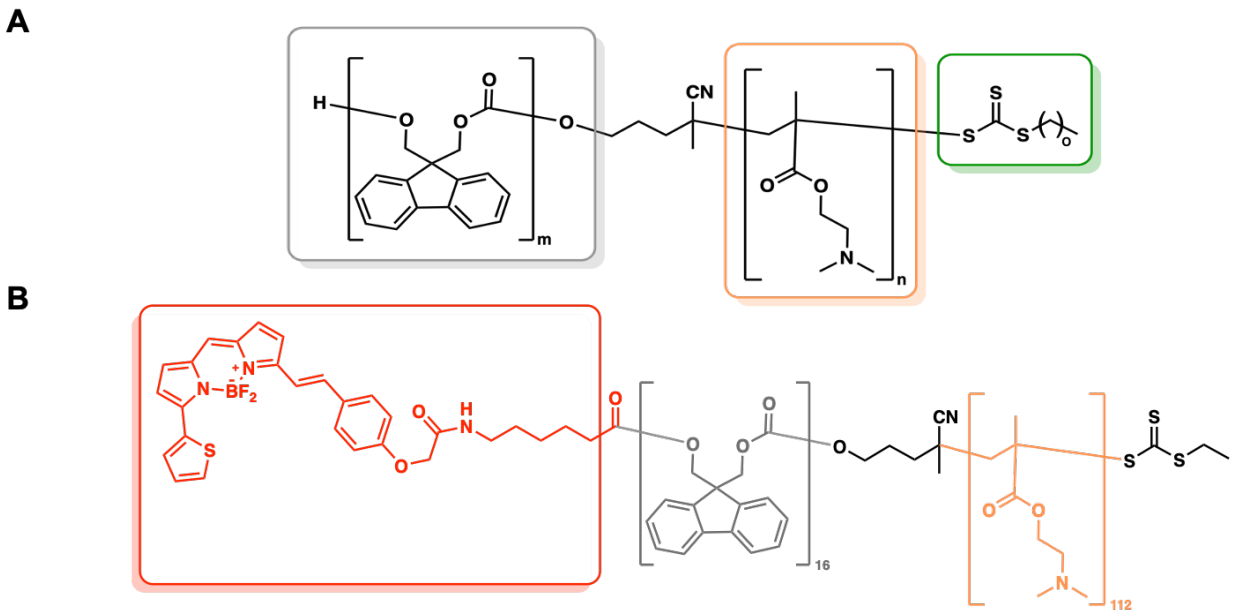

**Figure S3.1. (**A) General structure of the diblock copolymer PFTMC$_m$-*b*-PDMAEMA$_n$ used in this work, where m, and n, represent variable degrees of polymerization and o represents different numbers of multiple groups in the chain transfer agent. (B) Structure of the fluorescent BODIPY$^{630/650\text{-}X}$-capped diblock copolymer PFTMC$_{16}$-*b*-PDMAEMA$_{112}$ used to generate fluorescent blend nanospheres and controlled length block comicelle nanofibers through combination with non-fluorescent PFTMC$_{16}$-*b*-PDMAEMA$_{131}$ in a 1:1 ratio.

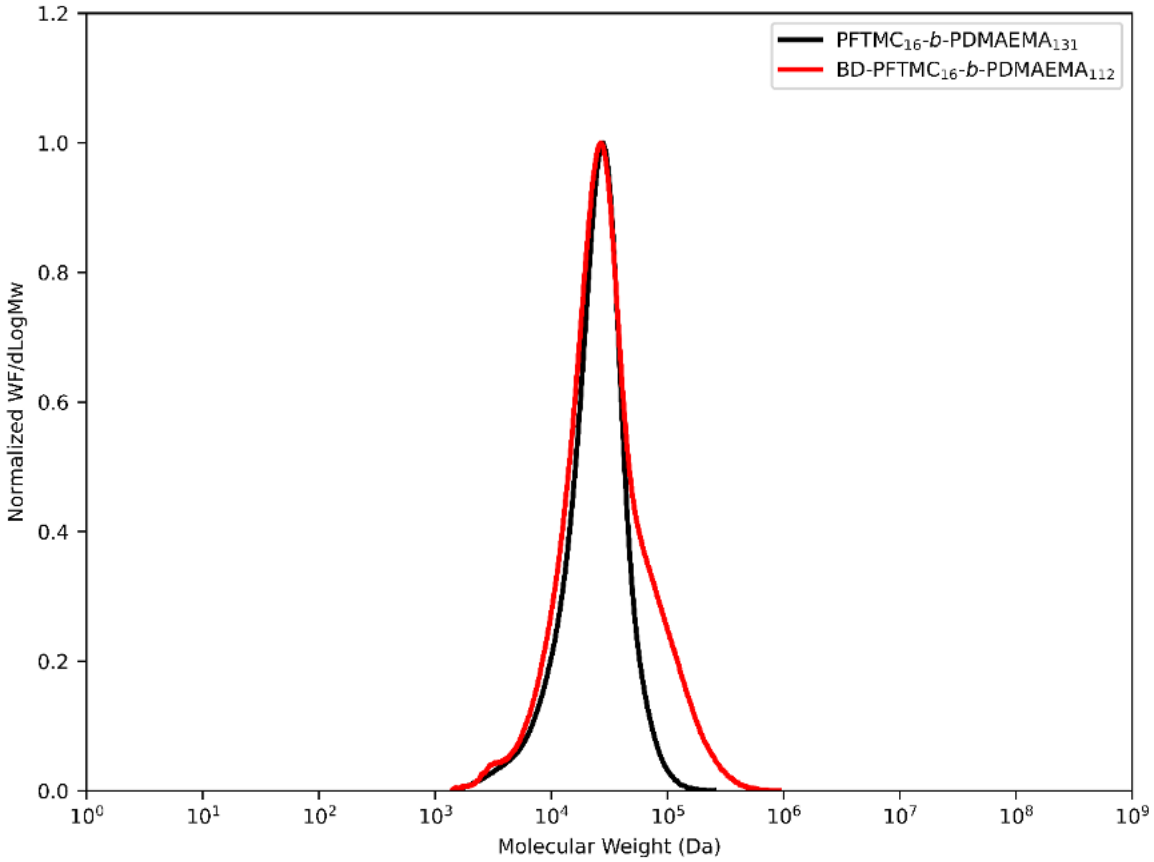


**Figure S3.2.** GPC Chromatograms in n-$Bu_4NBr$ (0.1 wt %)/THF of $PFTMC_{16}$-*b*-$PDMAEMA_{131}$ (black trace), and BD-$PFTMC_{16}$-*b*-$PDMAEMA_{112}$ (red trace). The "tailing" of the BD-$PFTMC_{16}$-*b*-$PDMAEMA_{112}$ polymer to the high molecular weight region is assumed to arise due to aggregation of the BD-capped polymer, which is present at 50 % capping efficiency.

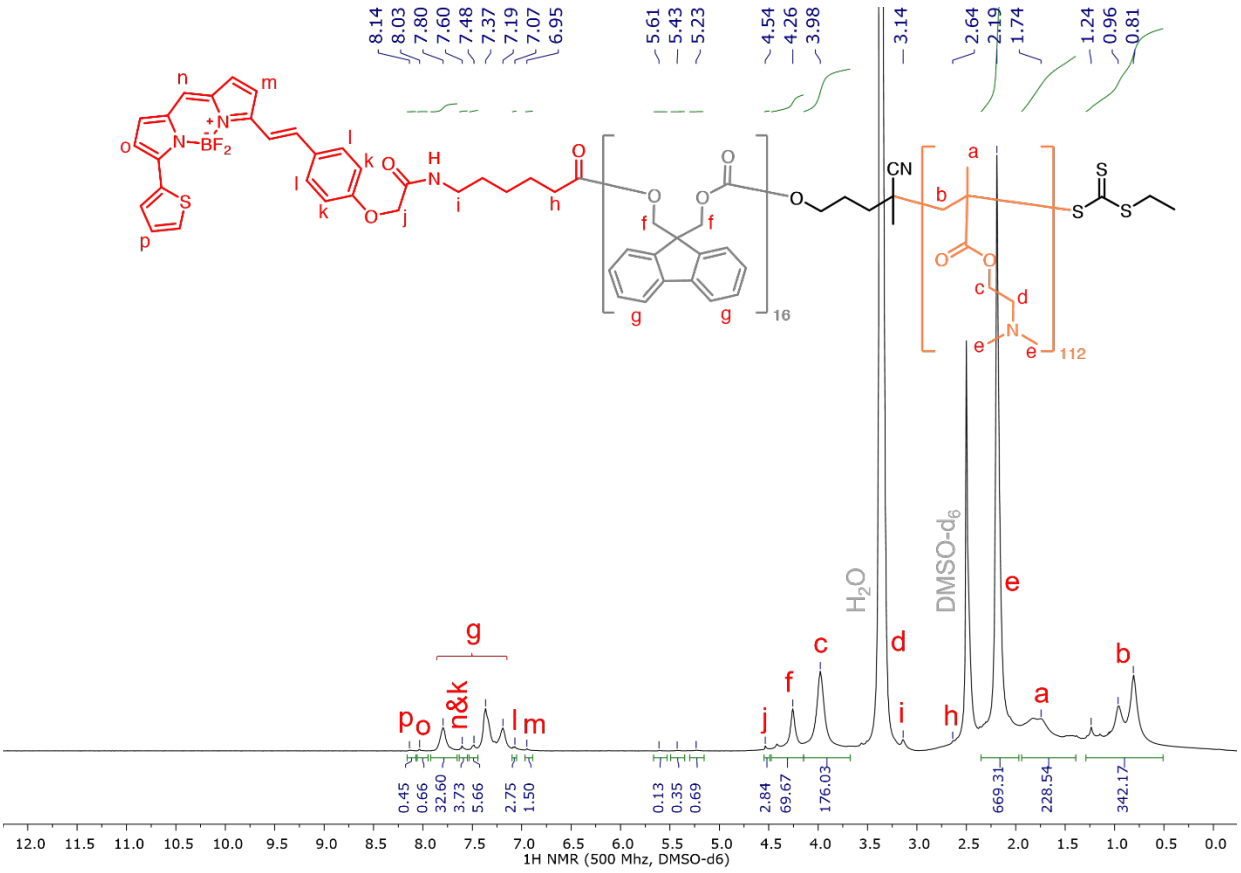


**Figure S3.3.** $^{1}$H-NMR spectrum of BD-PFTMC$_{16}$-*b*-PDMAEMA$_{112}$ in DMSO-d$_6$ (500 MHz). Expansion of the $^{1}$H-NMR region corresponding to the BODIPY$^{630/650\text{-}X}$ moiety is shown in Figure S3.5.

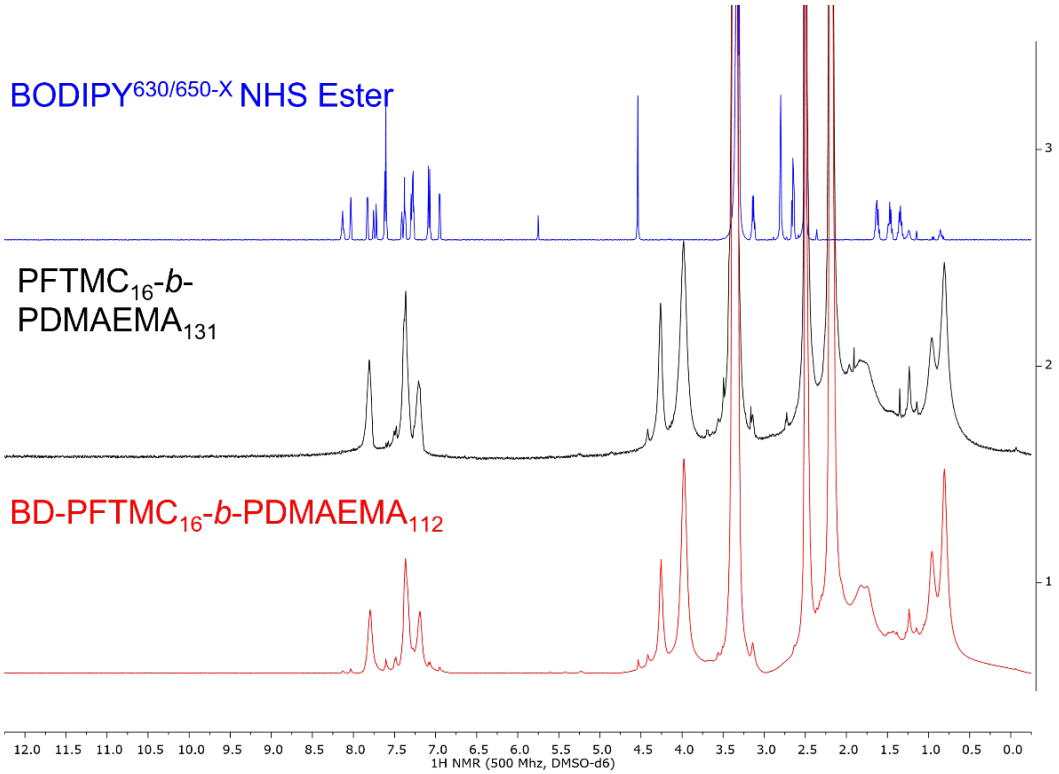


**Figure S3.4.** Stacked $^{1}$H-NMR spectra of BODIPY$^{630/650\text{-}X}$ NHS Ester (blue), PFTMC$_{16}$-*b*-PDMAEMA$_{131}$ (black), and BD-PFTMC$_{16}$-*b*-PDMAEMA$_{112}$ (red) in DMSO-d$_6$ (500 MHz).

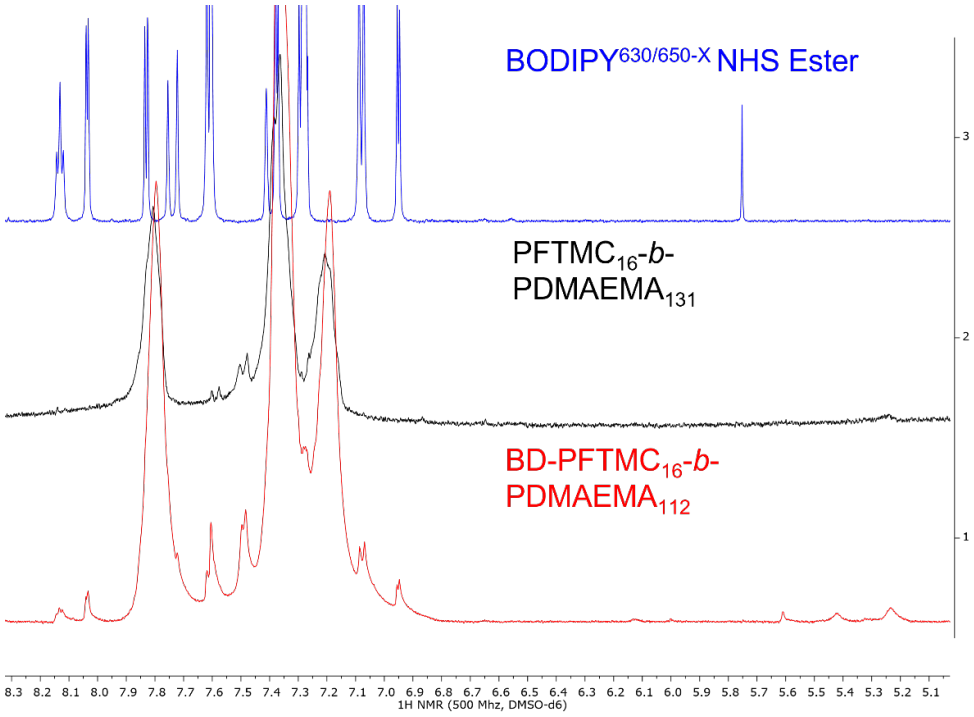


**Figure S3.5.** Expansion of the $^{1}$H-NMR region from 5.1 – 8.3 ppm in Figure S3.3.

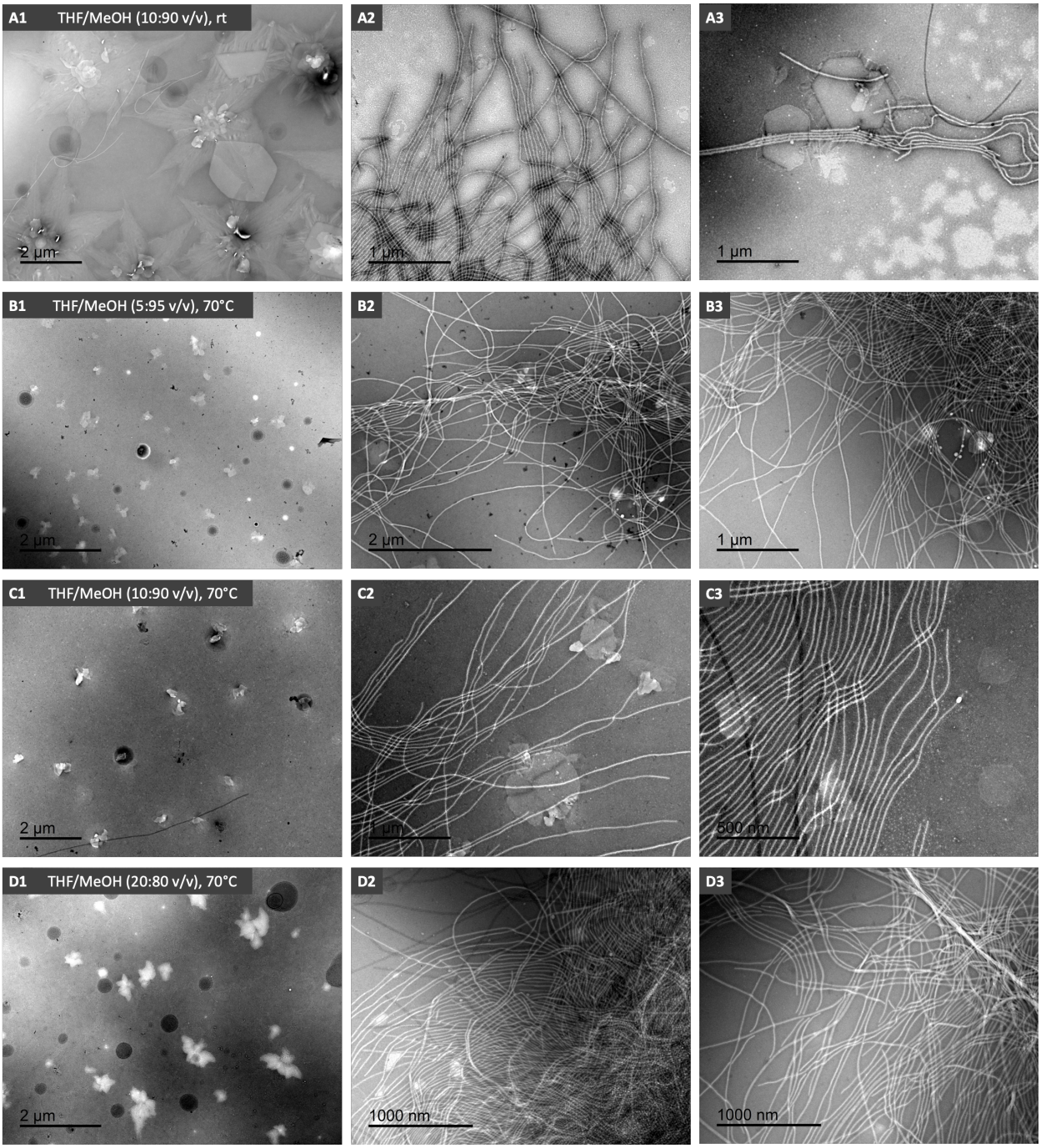


**Figure S3.6.** Conditions screened for the spontaneous (homogeneous) self-nucleation of BD-PFTMC$_{16}$-*b*-PDMAEMA$_{112}$. TEM micrographs of the assemblies formed after annealing at (A1-3) rt in THF/MeOH 10:90 (*v/v*) and annealing at 70°C for 30 min in (B1-3) THF/MeOH 5:95 (*v/v*), (C1-3) THF/MeOH 10:90 (*v/v*) and (D1-3) THF/MeOH 20:80 (*v/v*). All samples were stained with uranyl acetate (3 wt% in EtOH).

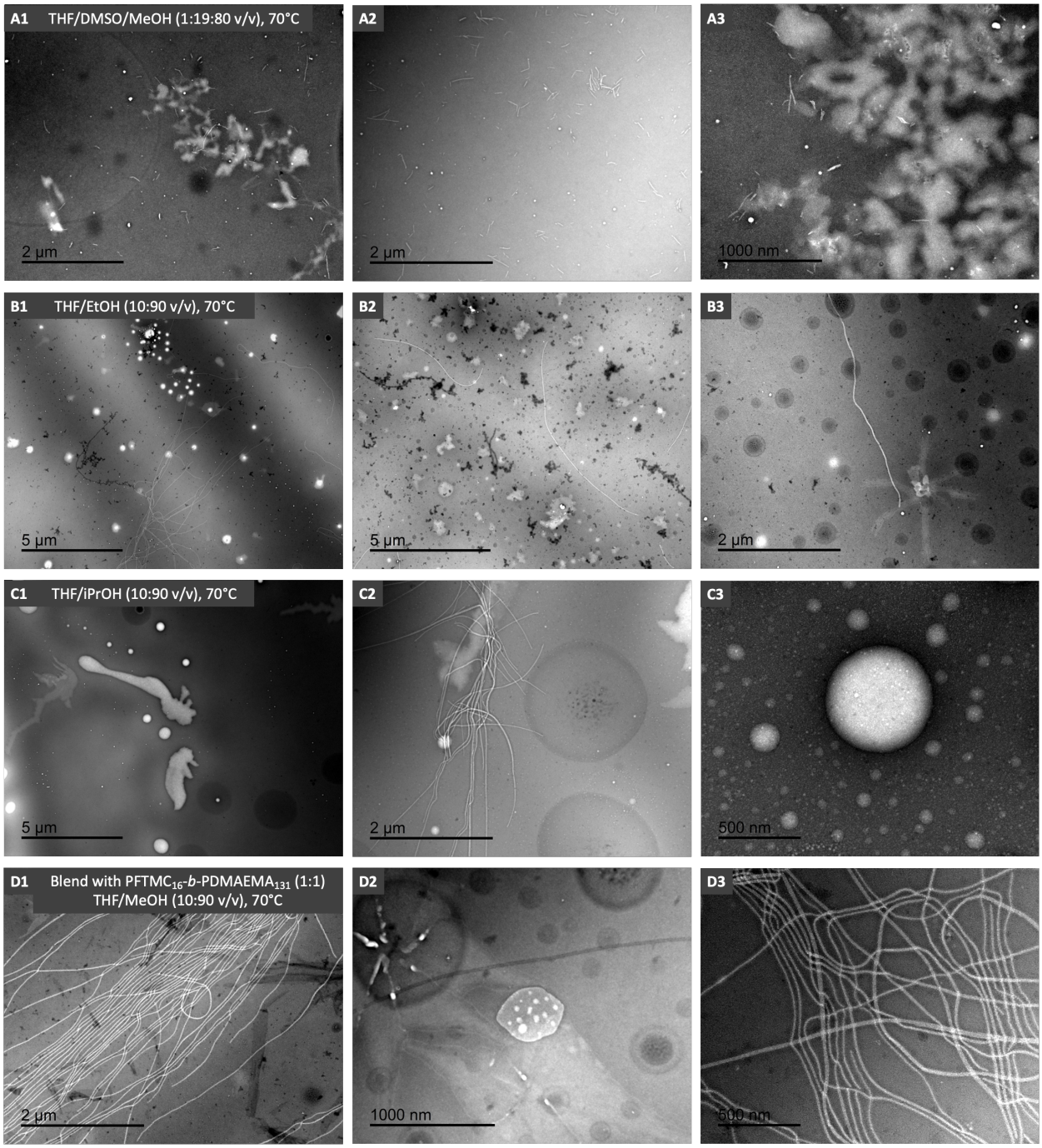


**Figure S3.7.** Further conditions screened for the spontaneous (homogeneous) self-nucleation of BD-PFTMC$_{16}$-*b*-PDMAEMA$_{112}$. TEM micrographs of the assemblies formed after annealing at 70°C for 30 min in (A1-3) THF/DMSO/MeOH 1:19:80 (*v/v*), (B1-3) THF/EtOH 10:90 (*v/v*), (C1-3) THF/iPrOH 10:90 (*v/v*) and (D1-3) a 1:1 bend with PFTMC$_{16}$-*b*-PDMAEMA$_{131}$ in THF/MeOH 10:90 (*v/v*). All samples were stained with uranyl acetate (3 wt % in EtOH).

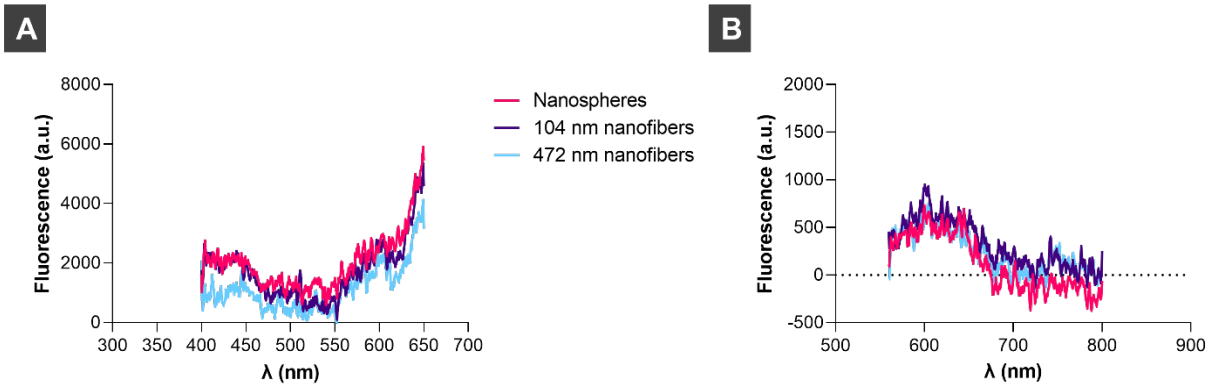


**Figure S3.8.** Overlay of (A) fluorescence excitation and (B) emission spectra of BD-labelled nanospheres (magenta), 104 nm nanofibers (purple) and 472 nm nanofibers (cyan) at 50 µg/mL in 10 mM HEPES, pH 7.4. (A) fluorescence excitation spectra ($\lambda_{ex}$ = 400 – 650 nm, $\lambda_{em}$ = 655 nm), and (B) fluorescence emission spectra ($\lambda_{ex}$ = 540 nm, $\lambda_{em}$ = 560 - 800 nm). The fluorescence excitation and emission profile and intensity is similar for all samples.

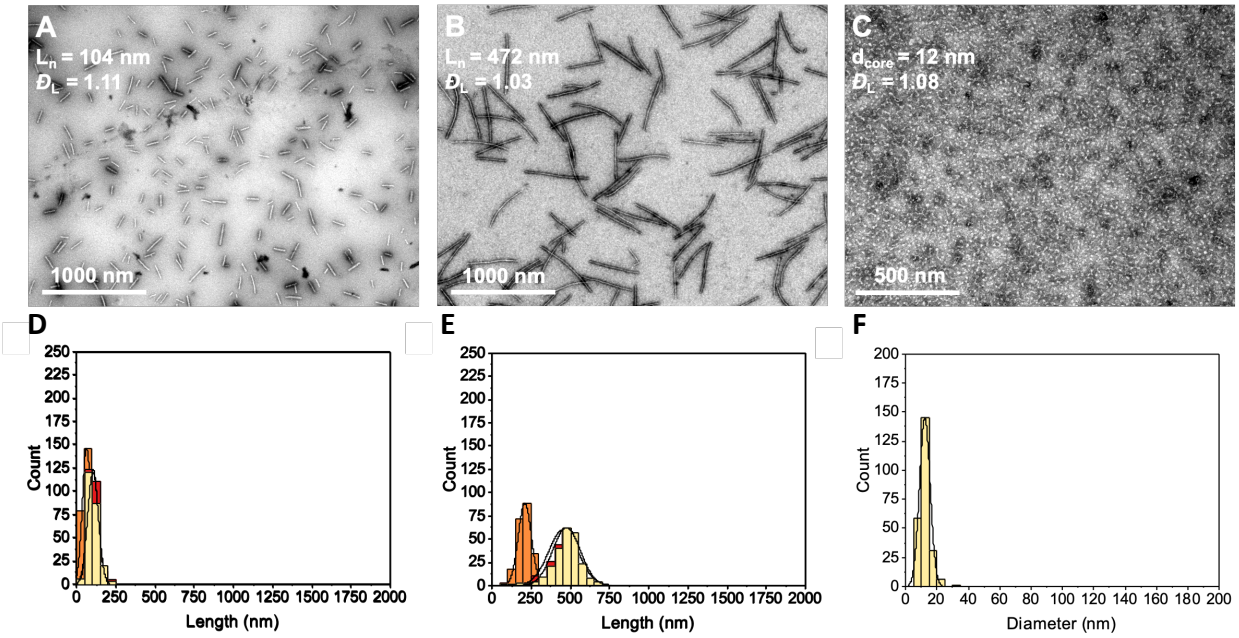


**Figure S3.9.** TEM micrographs and representative histograms below of self-assembly for BD-labelled nanoparticles. (A) 104 nm nanofibers (B) 472 nm nanofibers and (C) Nanospheres ($d_{core}$ = 12 nm). Each image is after transfer into water and stained with 3 wt % uranyl acetate in EtOH. Histogram colours represent the length contour analysis of intermediate triblock comicelle

nanofibers (orange), final pentablock comicelle nanofibers in THF/MeOH (10:90 *v/v*) (red) and after transfer into water (yellow).

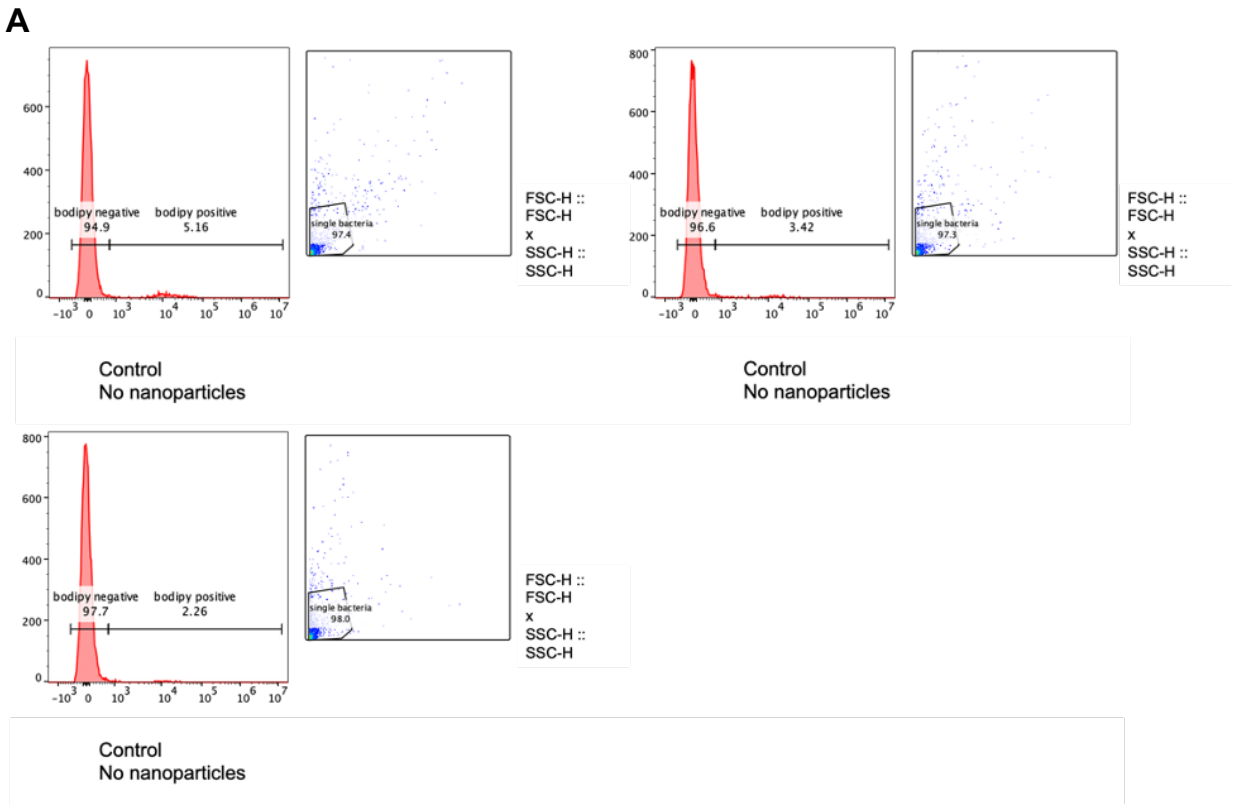

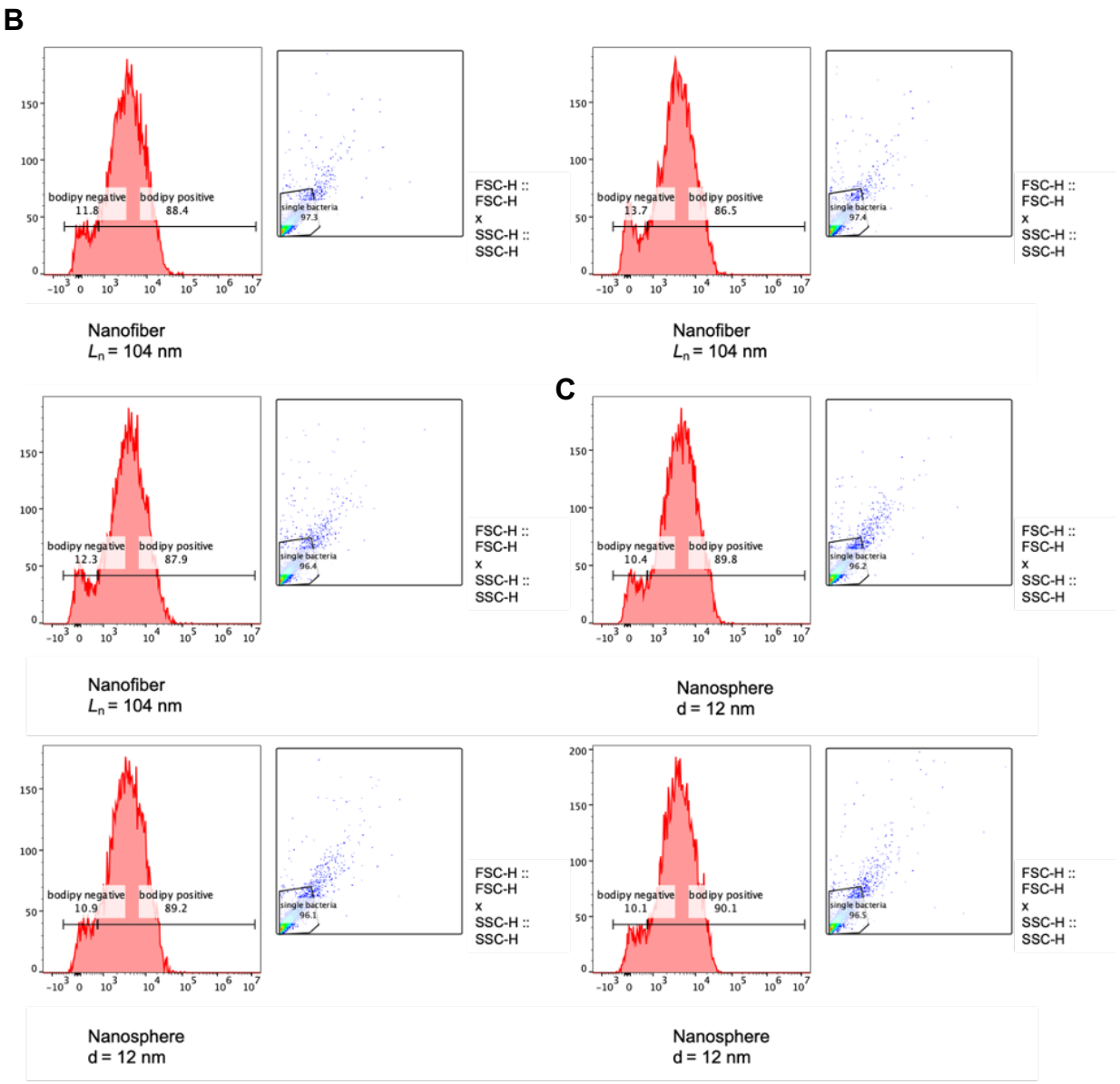
B
bodipy negative
11.8
bodipy positive
88.4
single bacteria
97.3
FSC-H :: FSC-H x SSC-H :: SSC-H
Nanofiber
$L_n$ = 104 nm
bodipy negative
13.7
bodipy positive
86.5
single bacteria
97.4
FSC-H :: FSC-H x SSC-H :: SSC-H
Nanofiber
$L_n$ = 104 nm
C
bodipy negative
12.3
bodipy positive
87.9
single bacteria
96.4
FSC-H :: FSC-H x SSC-H :: SSC-H
Nanofiber
$L_n$ = 104 nm
bodipy negative
10.4
bodipy positive
89.8
single bacteria
96.2
FSC-H :: FSC-H x SSC-H :: SSC-H
Nanosphere
d = 12 nm
bodipy negative
10.9
bodipy positive
89.2
single bacteria
96.1
FSC-H :: FSC-H x SSC-H :: SSC-H
Nanosphere
d = 12 nm
bodipy negative
10.1
bodipy positive
90.1
single bacteria
96.5
FSC-H :: FSC-H x SSC-H :: SSC-H
Nanosphere
d = 12 nm

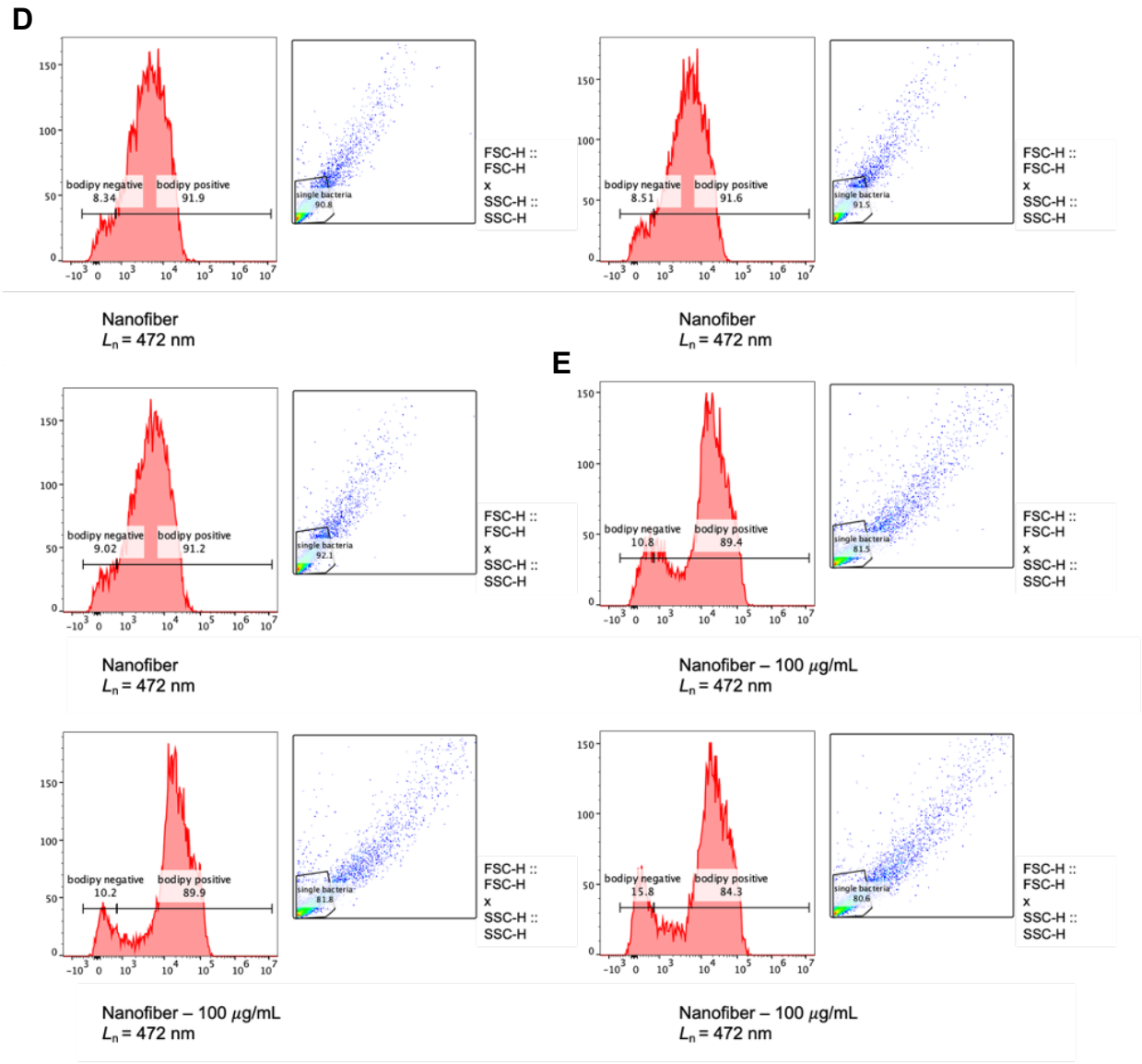


**Figure S3.10.** Flow cytometry data of BODIPY$^{630/650\text{-}X}$ fluorescence in BD-labelled nanofiber-bacteria samples and relevant controls, gated for "single bacteria" population in forward-scatter vs. side-scatter plots. Control samples of bacterial broth with no nanoparticles were utilized to gate for "bodipy negative", with the second population gated as "bodipy positive". Each sample was evaluated in triplicate. The x-axis is BODIPY$^{630/650\text{-}X}$ fluorescence and the y-axis is count.

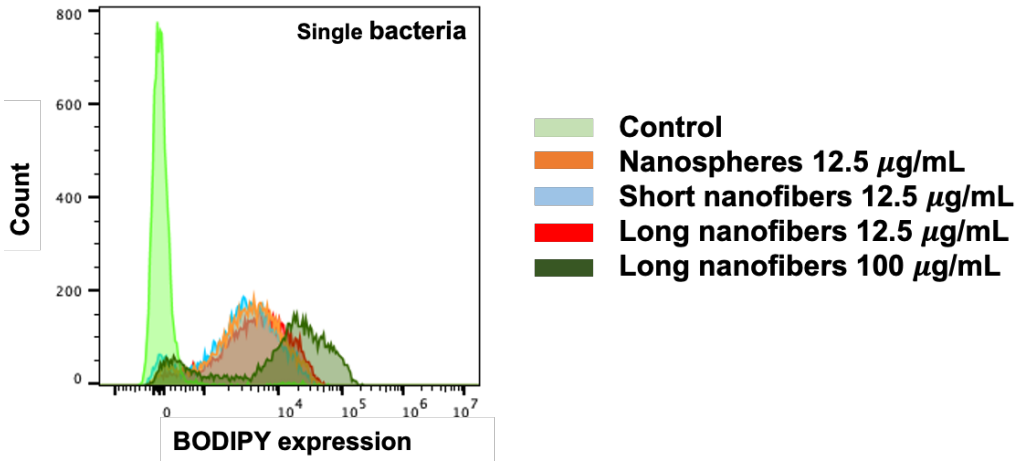


**Figure S3.11.** Median BD expression as a function of the count of E. coli incubated with 12.5 $\mu$g/mL of BD-labelled nanospheres ($d_{core}$ = 12 nm), 104 nm nanofibers, or 472 nm nanofibers, or 100 $\mu$g/mL of 472 nm nanofibers.

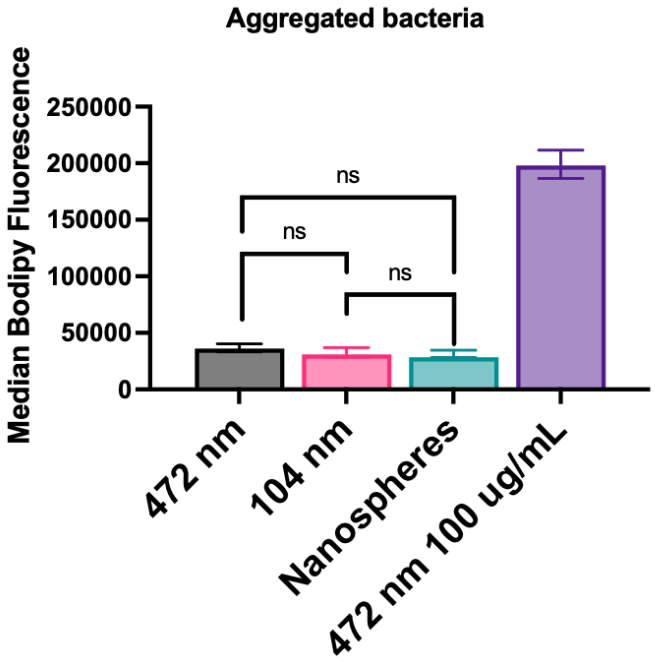


**Figure S3.12.** Median BODIPY$^{630/650\text{-}X}$ fluorescence in samples gated as "aggregated bacteria" in initial populations, as dependent on BD-labelled nanofiber length, nanoparticle shape, and nanofiber concentration. 12.5 $\mu$g/mL of nanoparticle was used for all samples aside from

100 $\mu$g/mL of 472 nm nanofibers (purple bar). No significant difference is observed between samples at 12.5 $\mu$g/mL.

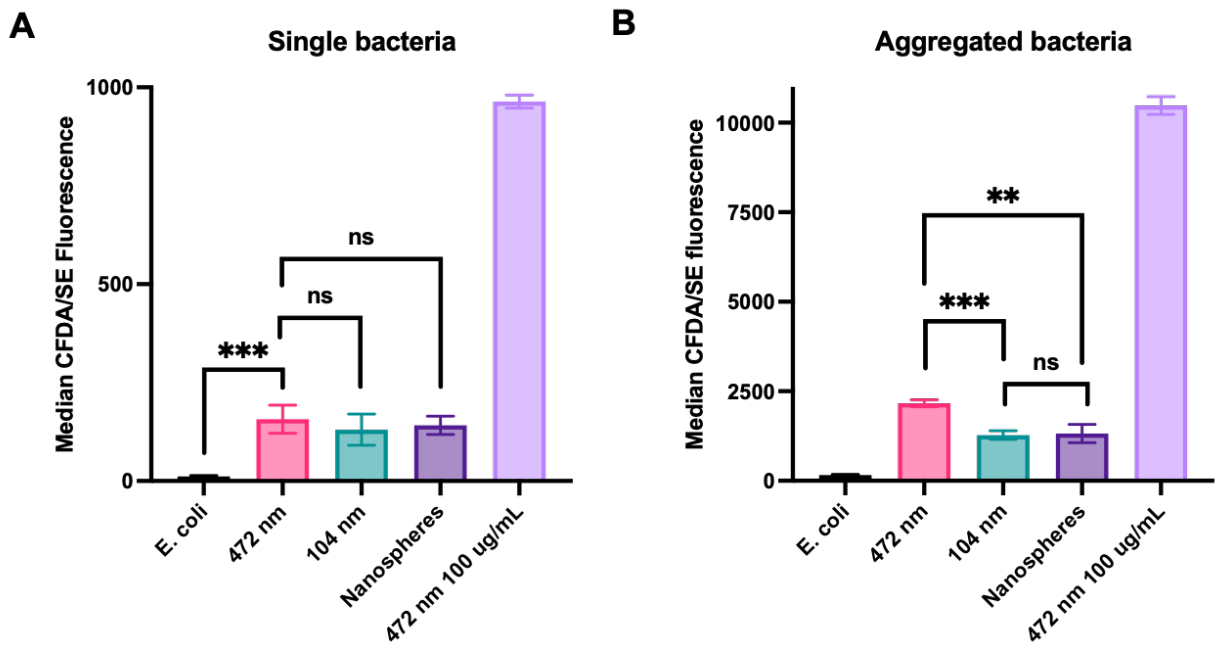


**Figure S3.13.** Median CFDA-SE fluorescence in "single bacteria" and "aggregated bacteria populations. (A) No significant difference in CFDA-SE expression is observed between nanoparticle samples at the same concentrations. Minimal CFDA-SE fluorescence is present in control *E. coli* populations in the absence of nanoparticles. A large increase in expression is observed when 100 $\mu$g/mL of 472 nm nanofibers is incubated with *E. coli*. (B) An increase in the median CFDA-SE fluorescence signal within the aggregated bacteria population is observed when 12.5 $\mu$g/mL of 472 nm nanofibers is present relative to 12.5 $\mu$g/mL of 104 nm nanofibers and 12 nm nanospheres. No difference is observed between the 104 nm nanofibers and nanospheres. A large increase in fluorescence is observed upon increasing the concentration of 472 nm nanofibers to 100 $\mu$g/mL.

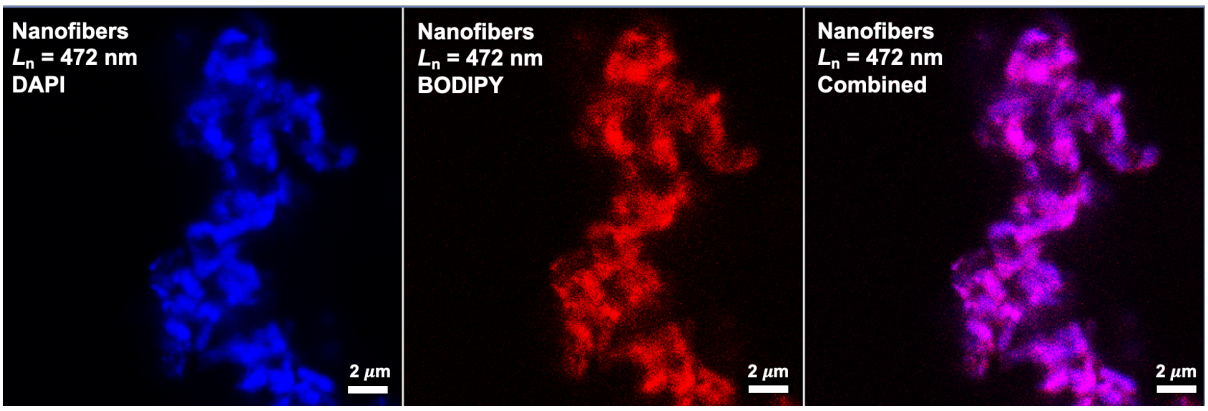


**Figure S3.14.** CLSM images of cell clusters observed upon incubation of bacteria with 12.5 $\mu$g/mL of 472 nm BD-labelled nanofibers. Images are taken from the center of a Z-stack performed through the entirety of the cluster, with the blue channel representing DAPI fluorescence, the red representing BODIPY$^{630/650\text{-X}}$ fluorescence and the final image showing the overlay of the two.

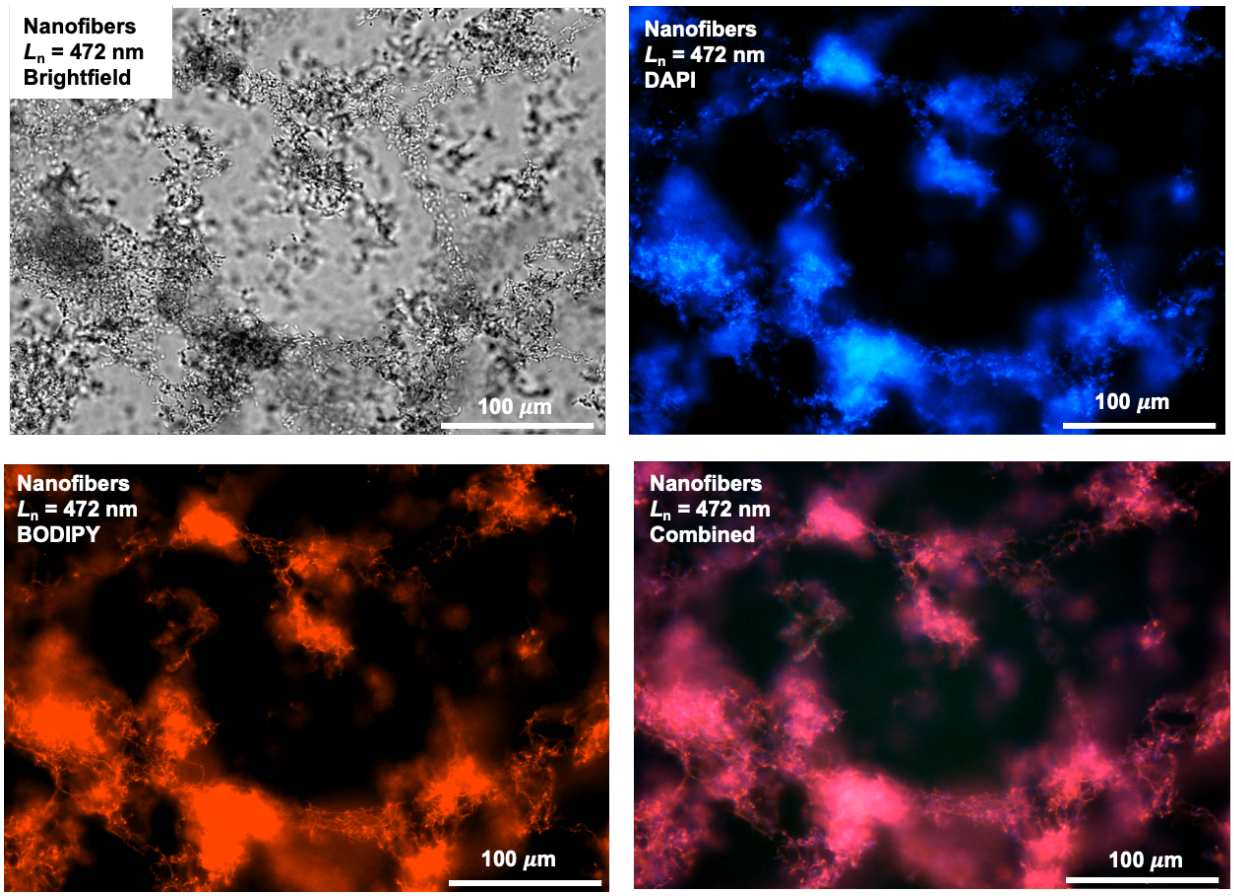


**Figure S3.15.** Clusters of cells visualized via brightfield microscopy followed by the corresponding fluorescence images acquired on a Cytation 5 plate reader of *E. coli* W3110 incubated in the presence of 472 nm BD-labelled nanofibers (100 μg/mL) for 4 h at 37 ℃. DAPI (1 μL, 1 μg/mL) was added to visualize the bacteria. The cell clusters align with the presence of DAPI and BODIPY$^{630/650\text{-X}}$ fluorescence and are assumed to be inactive.

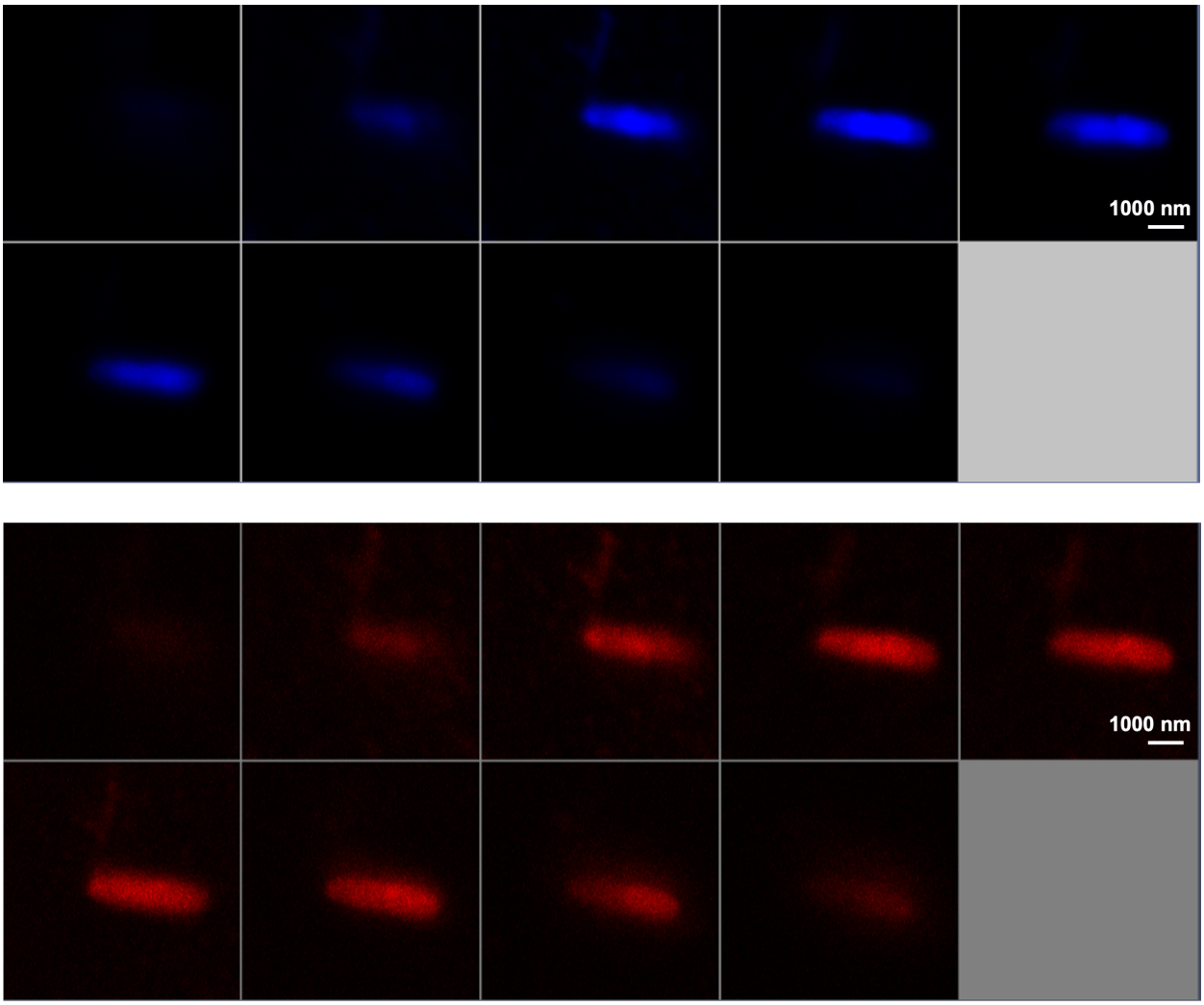


**Figure S3.16.** CLSM images of *E. coli* W3110 incubated with 12.5 $\mu$g/mL of BODIPY$^{630/650\text{-X}}$ labelled 472 nm nanofibers. The series of images arises from a Z-stack taken throughout the entirety of the bacterium, with the top image showing the DAPI channel and the bottom showing the BODIPY channel.

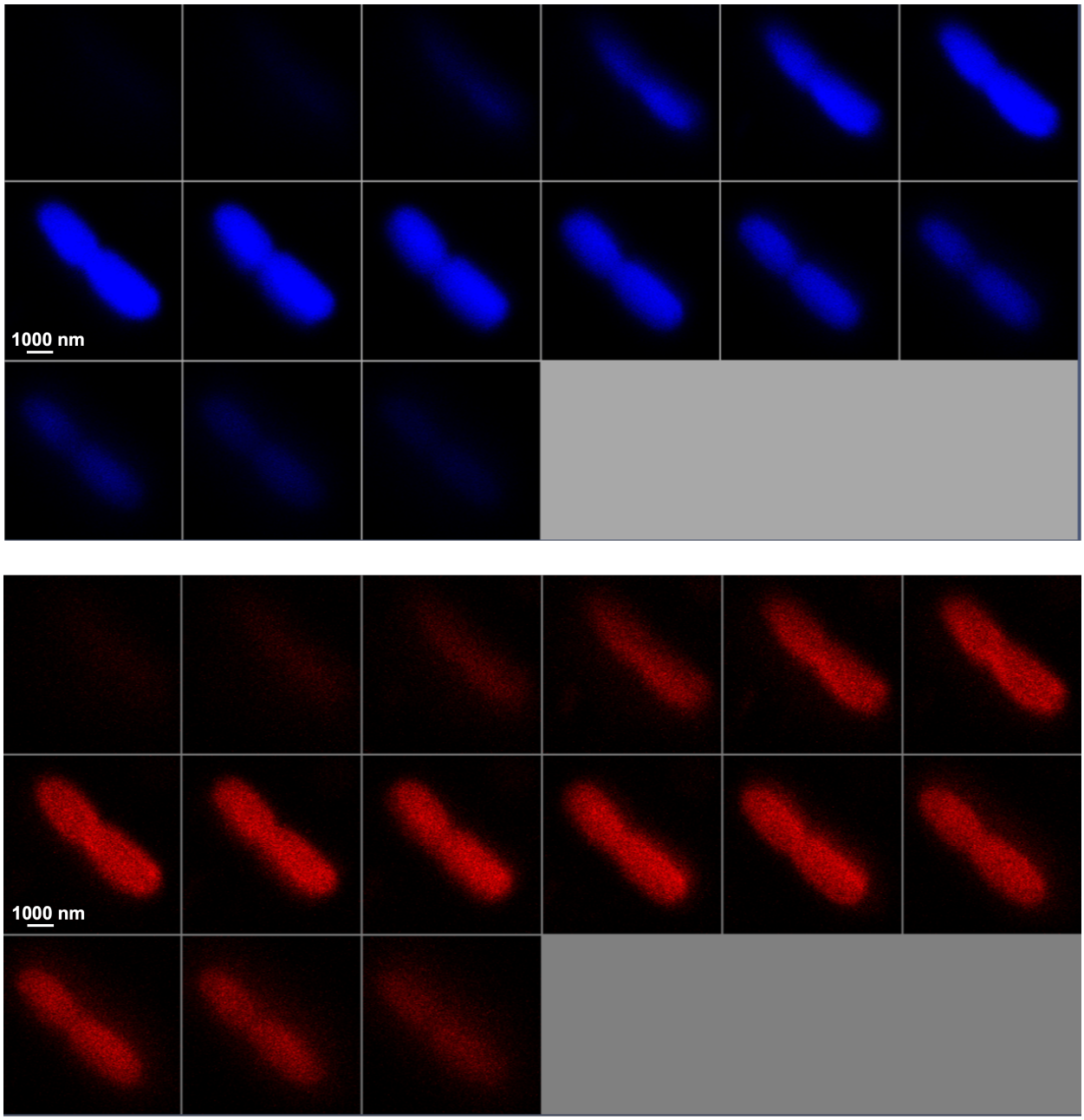


**Figure S3.17.** CLSM images of *E. coli* W3110 incubated with 12.5 $\mu$g/mL of BODIPY$^{630/650\text{-X}}$ labelled nanospheres. The series of images arises from a Z-stack taken throughout the entirety of the bacterium, with the top image showing the DAPI channel and the bottom showing the BODIPY channel.

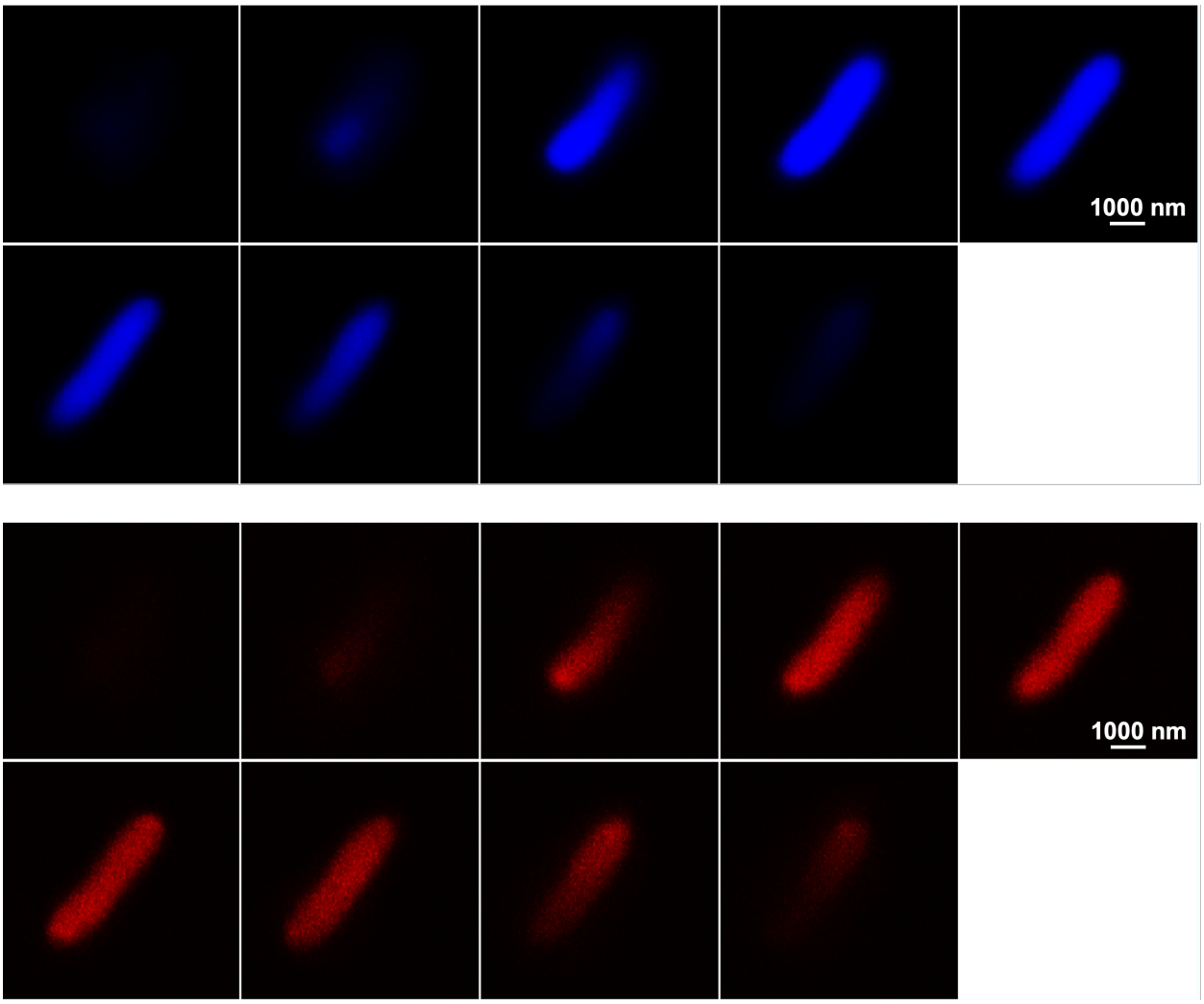


**Figure S3.18.** CLSM images of *E. coli* W3110 upon incubation with 104 nm BD-labelled nanofibers. The DAPI channel is shown in blue in the top image, and the BODIPY$^{630/650\text{-X}}$ channel is shown below in red. Uniform fluorescence is found throughout the cell as demonstrated by the Z-stack.

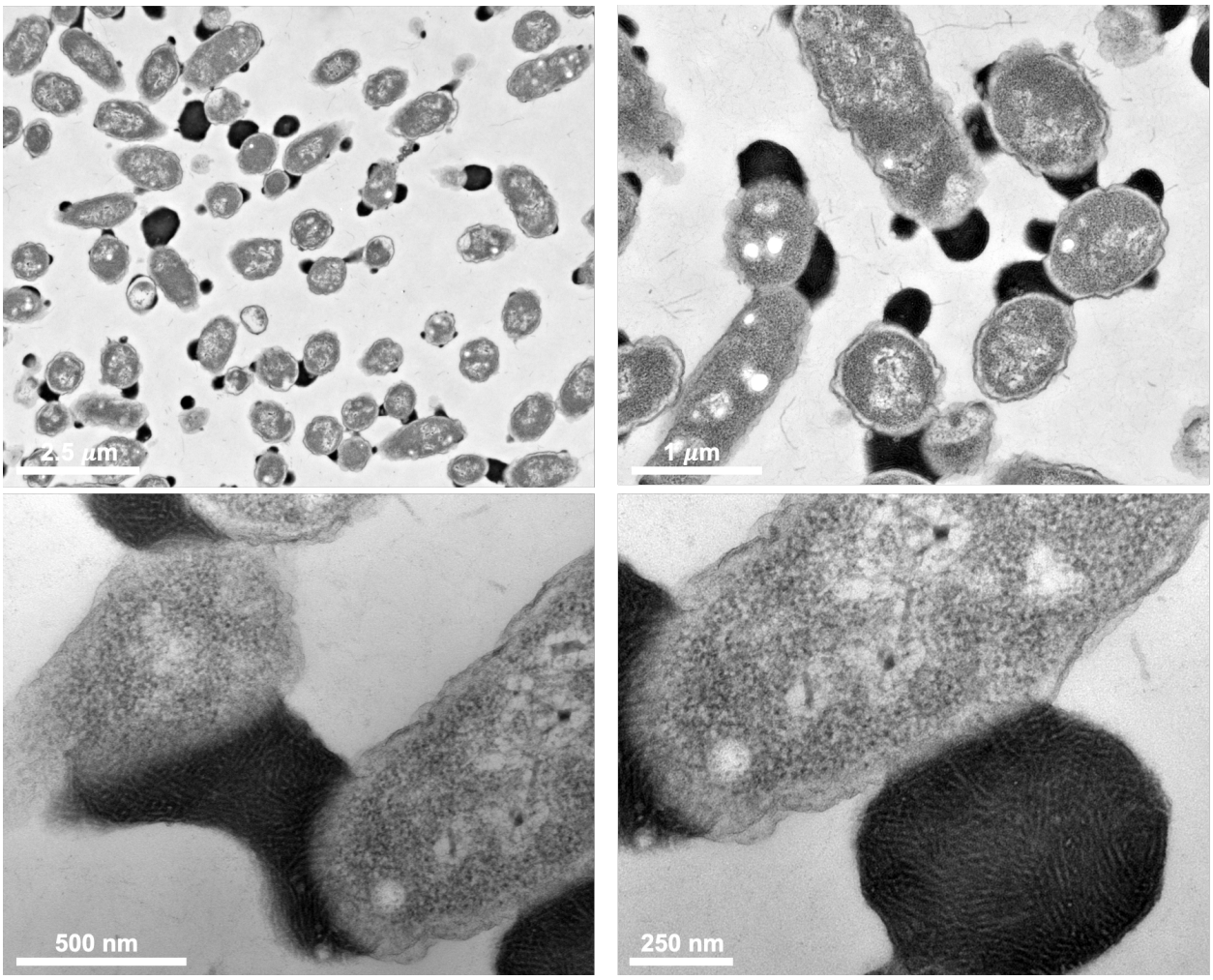


**Figure S3.19.** TEM micrographs of 104 nm BD-labelled nanofibers incubated with *E. coli* W3110. The dark clusters contain nanofibers, which can be observed crossing the bacterial membrane and fusing the bacteria together.

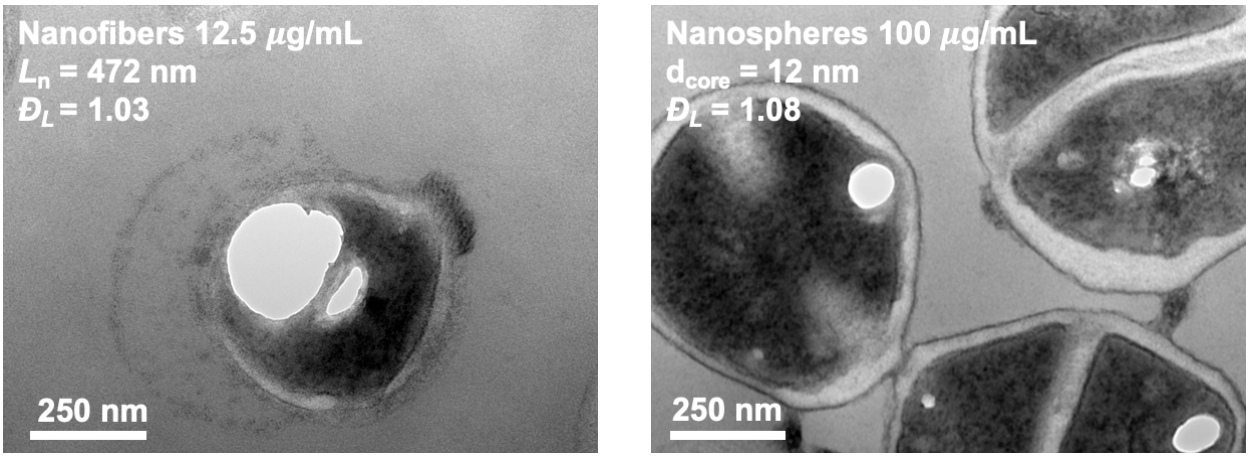


**Figure S3.20.** TEM micrographs of cross-sectioned *S. epi* upon incubation with 12.5 μg/mL of 472 nm nanofibers, or 12 nm nanospheres. 472 nm nanofibers can be observed penetrating the cell membrane, and what appears to be cell contents leakage is observed neighboring the bacterium. In contrast, relatively few 12 nm nanospheres are observed in contact with the cell membrane, and no cell contents leakage is observable.

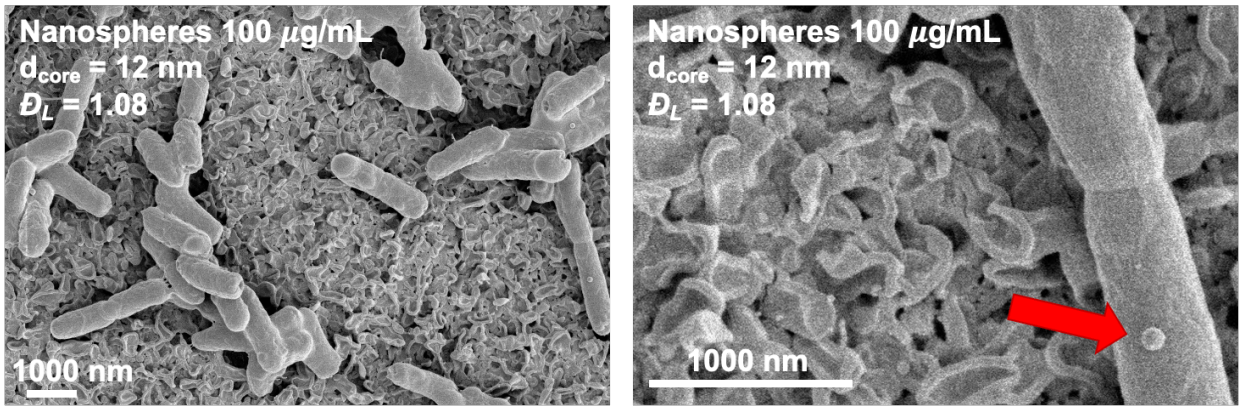


**Figure S3.21.** Representative SEM images of *E. coli* upon incubation with 100 μg/mL of 12 nm nanospheres. Clustering of the bacteria occurs, along with deformation of the bacteria and bulging of the bacterial membrane. Upon magnification, what appears to be larger spherical aggregates are discernable on the bacterial surface, as indicated by the red arrow.

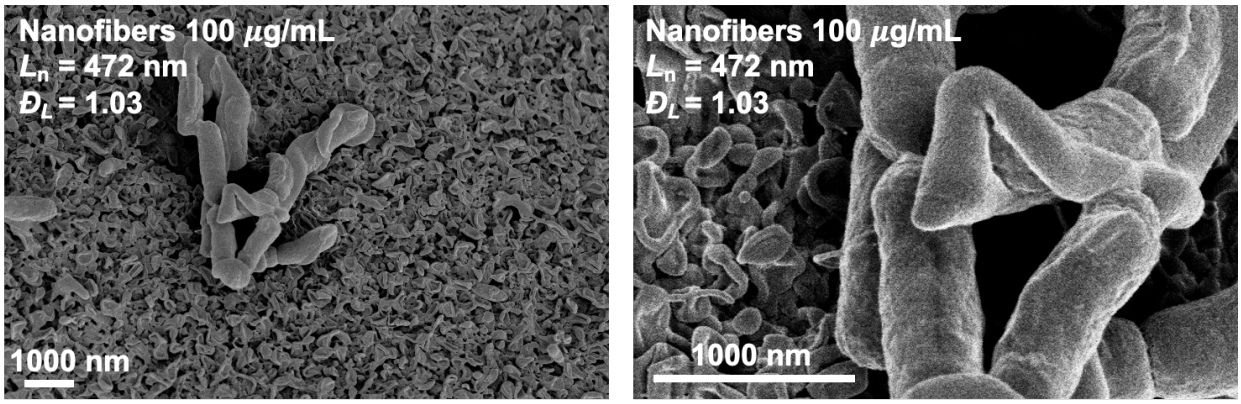


**Figure S3.22.** Representative SEM images of *E. coli* upon incubation with 100 $\mu$g/mL of 472 nm nanofibers. Clustering of the bacteria occurs, along with large deformation of the bacteria. Upon magnification, this deformation is visualized more clearly.

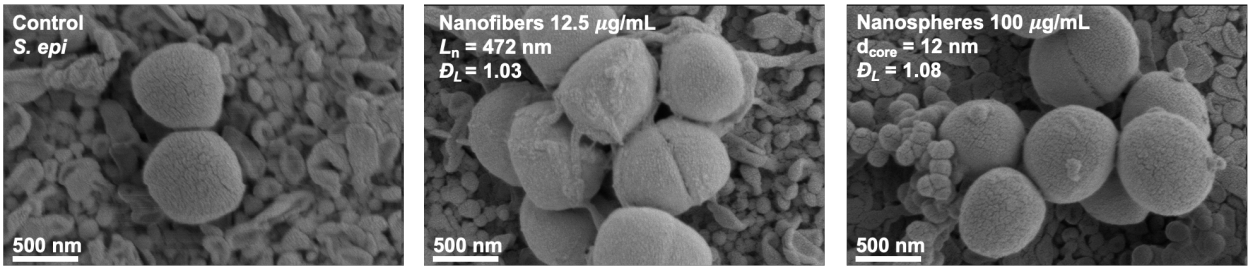


**Figure S3.23.** SEM images of *S. epi* in the presence and absence of polymer nanoparticles. Control bacteria are of normal shape and found in their expected diplococci state. Upon incubation with 12.5 $\mu$g/mL of 472 nm nanofibers, oblong clustered bacteria are visible and appear to be coated in nanofibers. Similarly, upon incubation with 12.5 $\mu$g/mL of 12 nm nanospheres, bacterial clustering is triggered, and spherical aggregates are present on the surface. The overall shape of the bacteria appears to be less affected relative to when they are in the presence of nanofibers.

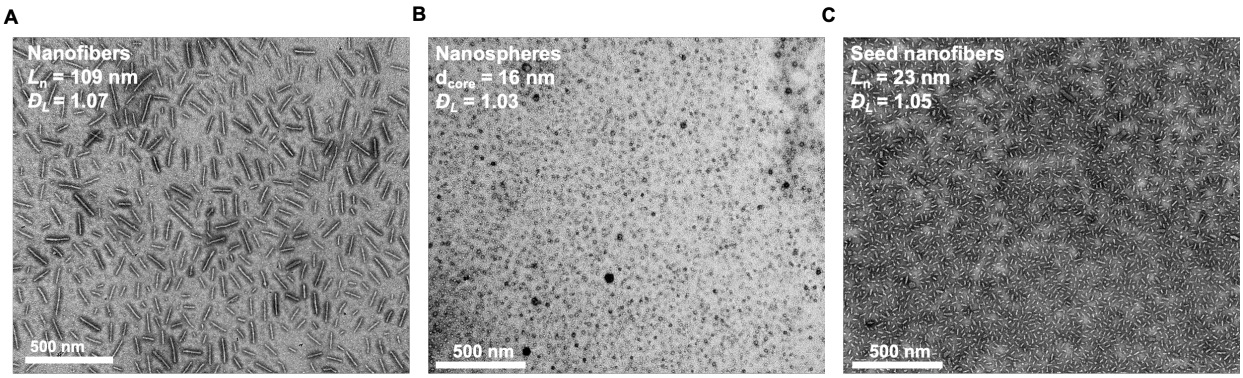


**Figure S3.24.** Nanofibers, nanospheres, and seed nanofibers of $PFTMC_{26}$-*b*-$PDMAEMA_{424}$ used in this work for delivering antibiotics. (A) TEM micrograph of 109 nm nanofibers upon transfer into $H_2O$ (B) TEM micrograph of nanospheres in water. Slight aggregation of the nanospheres is visible. (C) TEM micrograph of seed nanofibers upon transfer into water. All TEM grids are stained with a 3 wt % uranyl acetate solution in water.

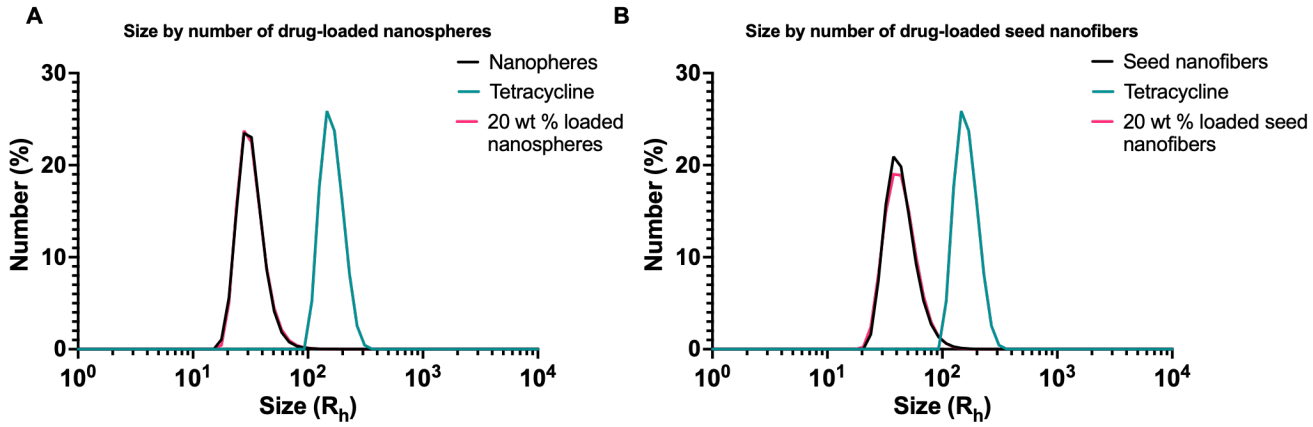


**Figure S3.25.** Data of the hydrodynamic radii of non-loaded and loaded nanospheres and seed nanofibers. (A) Overlayed distribution of size by number of nanospheres, nanospheres loaded with 20 wt % tetracycline, and the tetracycline control (1 wt %). The average hydrodynamic radius of nanospheres was 110 nm, and that for loaded nanospheres was 101 nm. (B) Overlayed distribution of size by number of non-loaded and loaded seed nanofibers relative to tetracycline control (1 wt %). The average hydrodynamic radius of pure seed nanofibers was 94 nm, and of loaded seed nanofibers was 92 nm.

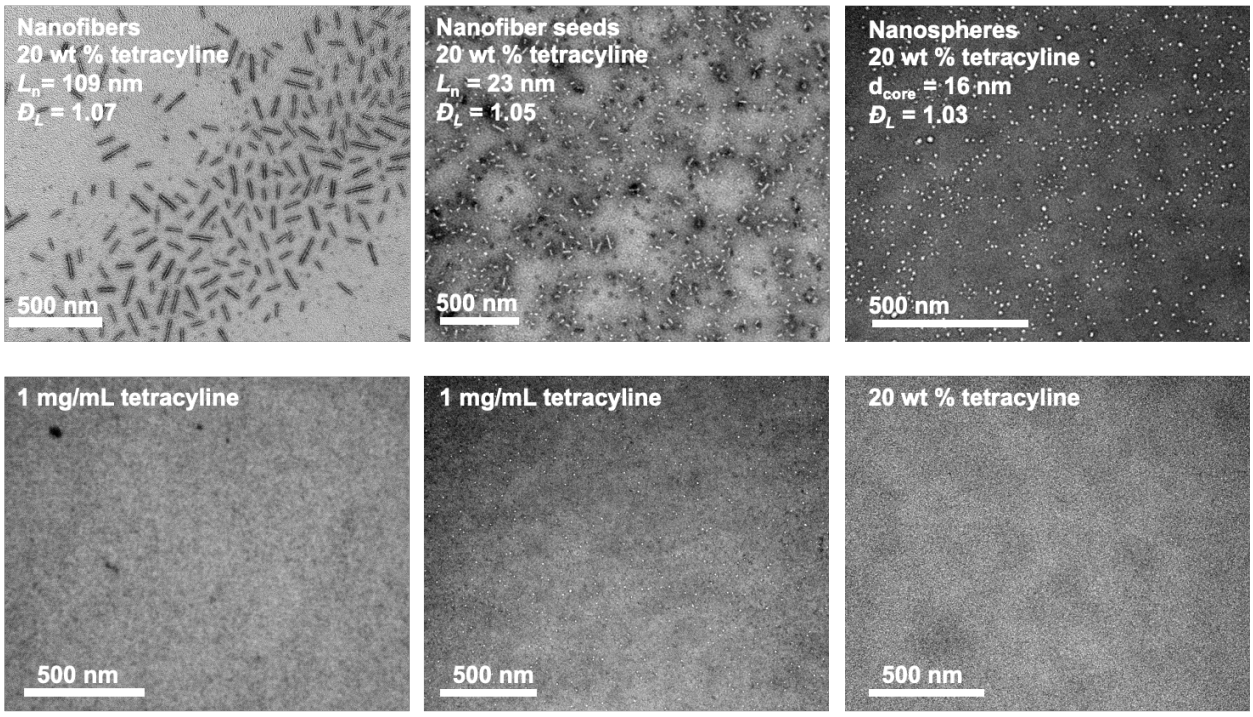


**Figure S3.26.** Representative TEM micrographs of drug-loaded nanofibers, as well as tetracycline. Nanoparticle morphology is conserved in all cases upon loading with 20 wt % tetracycline. At both high (1 mg/mL) and low (0.2 mg/mL) concentrations of tetracycline no major structures are visible by TEM.

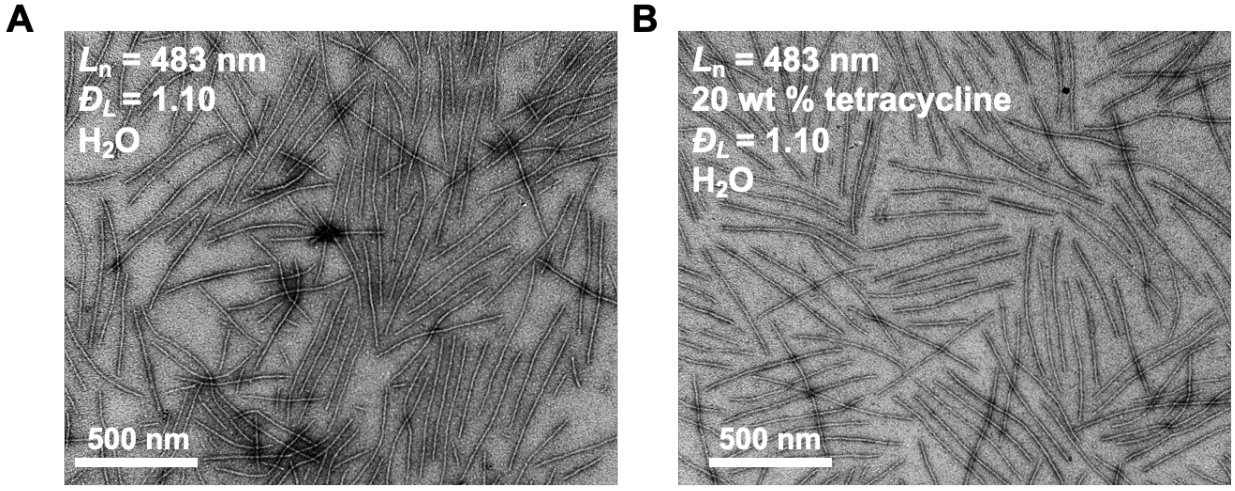


**Figure S3.27.** TEM micrographs of newly assembled 483 nm nanofibers composed of the block copolymer PFTMC$_{26}$-*b*-PDMAEMA$_{424}$ for the use of flow cytometry studies of drug-loading,

upon (A) transfer into $H_2O$ and (B) loading with 20 wt % tetracycline. No significant changes in morphology or dispersity are observed between the samples.

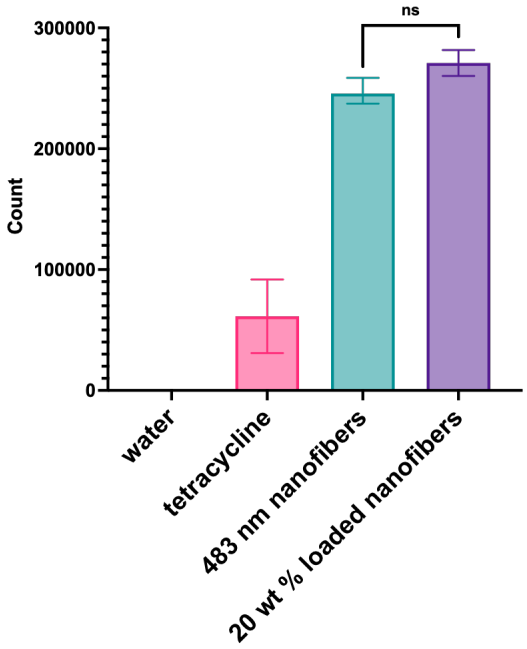


**Figure S3.28.** Flow cytometry data of the count number, normalized to ultrapure water, for tetracycline (equivalent to 20 wt %), 483 nm nanofibers, and 483 nm nanofibers loaded with 20 wt % tetracycline. No significant difference in count is observed between the non-loaded and loaded nanofiber samples.

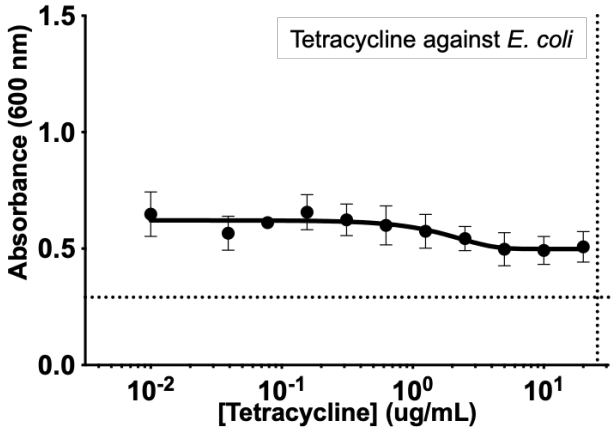


**Figure S3.29.** *E. coli* growth response curve upon incubation with tetracycline, from 0 $\mu$g/mL to 20 $\mu$g/mL, representing an amount equivalent to that loaded onto nanofibers. No MIC was

determinable for the above sample, showcasing an ineffective antibacterial activity upon incubation with the antibiotic alone.

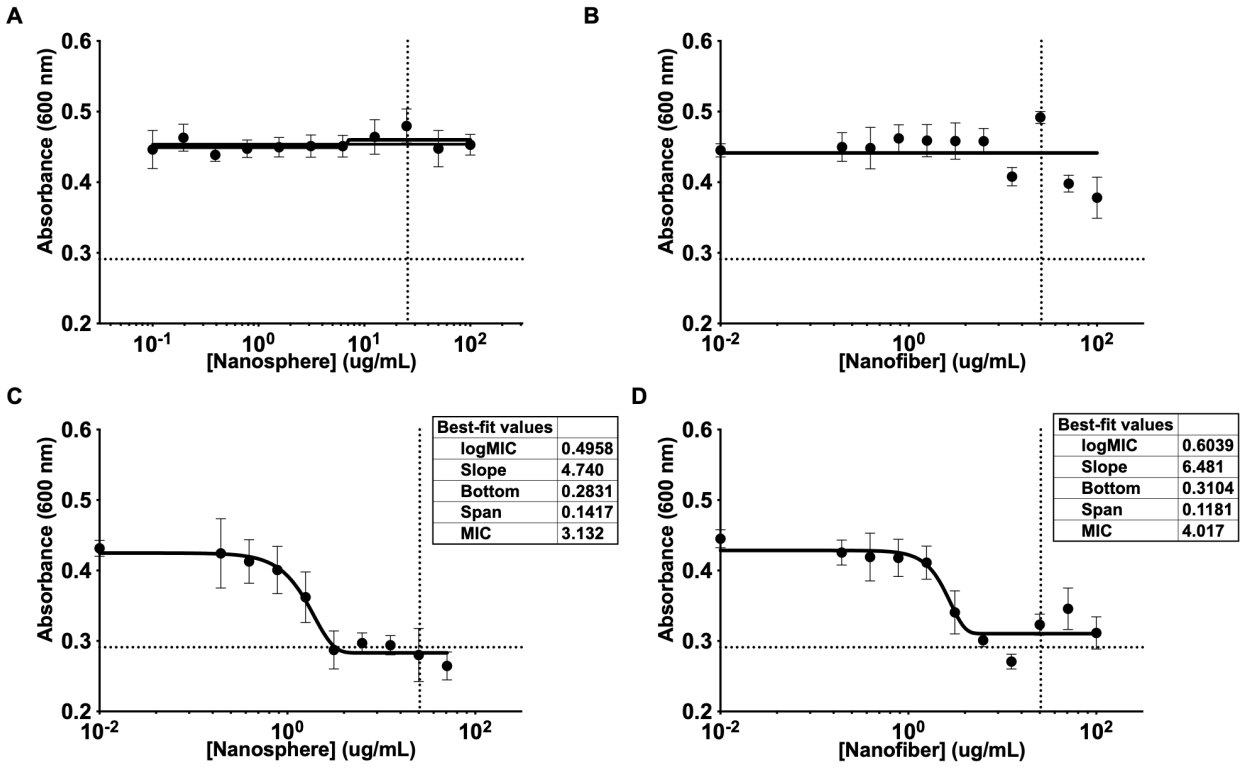


**Figure S3.30.** Curves to determine the MIC for each respective sample. (A) Non-loaded nanospheres against *E. coli*. No MIC is determinable, and no bacterial inhibition is observed. (B) Non-loaded seeds activity against *E. coli*. No MIC is determinable. Slight bacterial inhibition is observed at 100 $\mu$g/mL and 50 $\mu$g/mL, however it is not enough to significantly alter the bacterial growth. (C) Inhibition curve of nanospheres loaded with 20 wt % tetracycline. The data point from the 100 $\mu$g/mL concentration was excluded for the purpose of fitting the curve and determining an accurate MIC value. The average values obtained at this concentration were 0.198, 0.200, and 0.182, representing significant bacterial growth inhibition. Each value is the average of a triplicate. (D) Inhibition curve of seed nanofibers loaded with 20 wt % tetracycline.

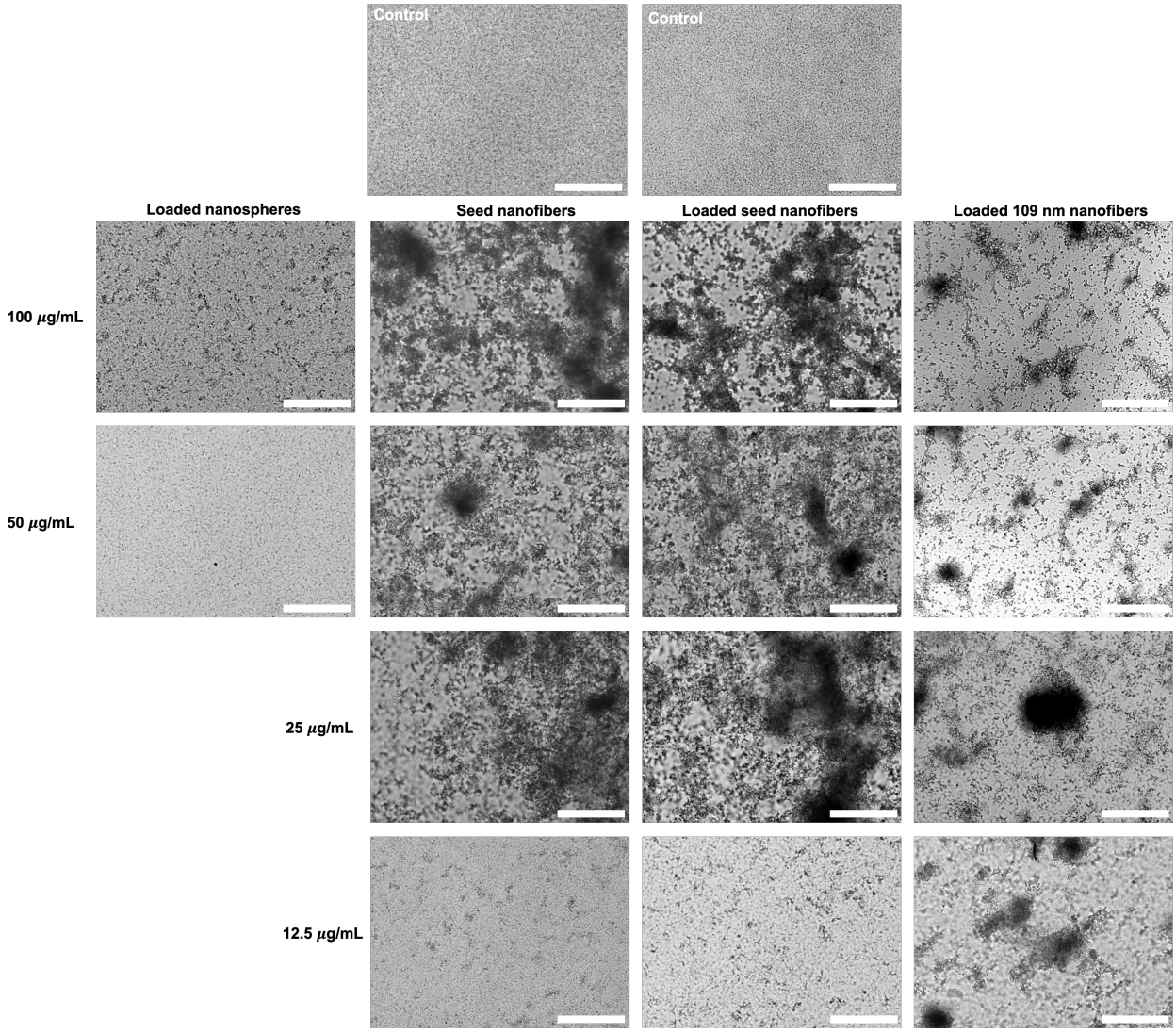


**Figure S3.31.** Brightfield microscopy images upon incubation with nanoparticle samples, relative to control bacterial cultures. Dark clusters are assumed to be dead or significantly damaged cells. From the images, we can determine that the seed nanofibers both pristine and loaded cause more cell damage than loaded nanospheres, which only appear to cause slight damage at 100 $\mu$g/mL and limit bacterial growth at concentrations below. All scale bars represent 100 $\mu$m.

## 3.7 References


1. Murray, C. J.; Ikuta, K. S.; Sharara, F.; Swetschinski, L.; Aguilar, G. R.; Gray, A.; Han, C.; Bisignano, C.; Rao, P.; Wool, E.; et al. Global Burden of Bacterial Antimicrobial Resistance in 2019: A Systematic Analysis. *Lancet* **2022**, *399* (10325), 629–655. DOI: 10.1016/s0140-6736(21)02724-0.
2. O'Neill, J. Tackling Drug-Resistance: Final Report and Recommendations. *Review on Antimicrobial Resistance*. https://apo.org.au/sites/default/files/resource-files/2016-05/apo-nid63983.pdf (accessed 2023-01-10).
3. Darby, E. M.; Trampari, E.; Siasat, P.; Gaya, M. S.; Alav, I.; Webber, M. A.; Blair, J. M. Molecular Mechanisms of Antibiotic Resistance Revisited. *Nat. Rev. Microbiol.* **2022**, 21, 280-295. DOI: 10.1038/s41579-022-00820-y.
4. Kolář, M.; Urbánek, K.; Látal, T. Antibiotic Selective Pressure and Development of Bacterial Resistance. *Int. J. Antimicrob. Agents* **2001**, *17* (5), 357–363. DOI: 10.1016/s0924-8579(01)00317-x.
5. Albrich, W. C.; Monnet, D. L.; Harbarth, S. Antibiotic Selection Pressure and Resistance in *Streptococcus Pneumoniae* and *Streptococcus Pyogenes*. *Emerg. Infect. Dis.* **2004**, *10* (3), 514–517. DOI:10.3201/eid1003.030252.
6. Reygaert, W. C. An Overview of the Antimicrobial Resistance Mechanisms of Bacteria. *AIMS Microbiol.* **2018**, *4* (3), 482–501. DOI: 10.3934/microbiol.2018.3.482.
7. Munita, J. M.; Arias, C. A. Mechanisms of Antibiotic Resistance. *Microbiol. Spectrum* **2016**, *4* (2), 482–490. DOI: 10.1128/microbiolspec.vmbf-0016-2015.

8. Davies, J.; Davies, D. Origins and Evolution of Antibiotic Resistance. *Microbiol. Mol. Bio. Rev.* **2010**, *74* (3), 417–433. DOI: 10.1128/mmbr.00016-10.
9. Sydnor, E. R.; Perl, T. M. Hospital Epidemiology and Infection Control in Acute-Care Settings. *Clin. Microbiol. Rev.* **2011**, *24* (1), 141–173. DOI: 10.1128/cmr.00027-10.
10. Gupta, A.; Mumtaz, S.; Li, C.; Hussain, I.; Rotello, V. M. Combatting Antibiotic-Resistant Bacteria Using Nanomaterials. *Chem. Soc. Rev.* **2019**, *48* (2), 415–427. DOI: 10.1039/c7cs00748e.
11. Ravensdale, J.; Wong, Z.; O'Brien, F.; Gregg, K. Efficacy of Antibacterial Peptides against Peptide-Resistant MRSA Is Restored by Permeabilization of Bacteria Membranes. *Front. Microbiol.* **2016**, *7*, 1745. DOI: 10.3389/fmicb.2016.01745.
12. Drusano, G. L. Prevention of Resistance: A Goal for Dose Selection for Antimicrobial Agents. *Clin. Infect. Dis.* **2003**, *36* (S1), S42–S50. DOI: 10.1086/344653.
13. Antibiotic Resistance. http://www.who.int/news-room/fact-sheets/detail/antibiotic-resistance (accessed 2023-01-10).
14. Lee, C.; Cho, I.; Jeong, B.; Lee, S. Strategies to Minimize Antibiotic Resistance. *Int. J. Environ. Res. Public Health* **2013**, *10* (9), 4274–4305. DOI:10.3390/ijerph10094274.
15. Khameneh, B.; Diab, R.; Ghazvini, K.; Fazly Bazzaz, B. S. Breakthroughs in Bacterial Resistance Mechanisms and the Potential Ways to Combat Them. *Microb. Pathog.* **2016**, *95*, 32–42. DOI: 10.1016/j.micpath.2016.02.009.
16. Sun, H.; Hong, Y.; Xi, Y.; Zou, Y.; Gao, J.; Du, J. Synthesis, Self-Assembly, and Biomedical Applications of Antimicrobial Peptide–Polymer Conjugates. *Biomacromolecules* **2018**, *19* (6), 1701–1720. DOI: 10.1021/acs.biomac.8b00208.

17. Sayed, F. A.; Eissa, N. G.; Shen, Y.; Hunstad, D. A.; Wooley, K. L.; Elsabahy, M. Morphologic Design of Nanostructures for Enhanced Antimicrobial Activity. *J. Nanobiotechnol.* **2022**, *20*, 536. DOI: 10.1186/s12951-022-01733-x.

18. Benfield, A. H.; Henriques, S. T. Mode-of-Action of Antimicrobial Peptides: Membrane Disruption vs. Intracellular Mechanisms. *Front. Med. Technol.* **2020**, *2*, 610997. DOI: 10.3389/fmedt.2020.610997.

19. Lin, W.; Huang, K.; Li, Y.; Qin, Y.; Xiong, D.; Ling, J.; Yi, G.; Tang, Z.; Lin, J.; Huang, Y.; et al. Facile in Situ Preparation and in Vitro Antibacterial Activity of PDMAEMA-Based Silver-Bearing Copolymer Micelles. *Nanoscale Res. Lett.* **2019**, *14*, 256. DOI: 10.1186/s11671-019-3074-z.

20. Zheng, W.; Anzaldua, M.; Arora, A.; Jiang, Y.; McIntyre, K.; Doerfert, M.; Winter, T.; Mishra, A.; Ma, H.; Liang, H. Environmentally Benign Nanoantibiotics with a Built-in Deactivation Switch Responsive to Natural Habitats. *Biomacromolecules* **2020**, *21* (6), 2187–2198. DOI: 10.1021/acs.biomac.0c00163.

21. Cebrián, R.; Lucas, R.; Fernández-Cantos, M. V.; Slot, K.; Peñalver, P.; Martínez-García, M.; Párraga-Leo, A.; de Paz, M. V.; García, F.; Kuipers, O. P.; et al. Synthesis and Antimicrobial Activity of Aminoalkyl Resveratrol Derivatives Inspired by Cationic Peptides. *J. Enzyme Inhib. Med. Chem.* **2023**, *38* (1), 267–281. DOI: 10.1080/14756366.2022.2146685.

22. Haney, E. F.; Straus, S. K.; Hancock, R. E. Reassessing the Host Defense Peptide Landscape. *Front. Chem.* **2019**, *7*, 43. DOI: 10.3389/fchem.2019.00043.

23. Fjell, C. D.; Hiss, J. A.; Hancock, R. E.; Schneider, G. Designing Antimicrobial Peptides: Form Follows Function. *Nat. Rev. Drug Discov.* **2011**, *11*, 37–51. DOI: 10.1038/nrd3591.

24. Joo, Y. T.; Jung, K. H.; Kim, M. J.; Kim, Y. Preparation of Antibacterial PDMAEMA-Functionalized Multiwalled Carbon Nanotube via Atom Transfer Radical Polymerization. *J. Appl. Polym. Sci.* **2012**, *127* (3), 1508–1518. DOI: 10.1002/app.37571.

25. Chen, H.; Wang, B.; Gao, D.; Guan, M.; Zheng, L.; Ouyang, H.; Chai, Z.; Zhao, Y.; Feng, W. Broad-Spectrum Antibacterial Activity of Carbon Nanotubes to Human Gut Bacteria. *Small* **2013**, *9* (16), 2735–2746. DOI: 10.1002/smll.201202792.

26. Roy, D.; Knapp, J. S.; Guthrie, J. T.; Perrier, S. Antibacterial Cellulose Fiber via Raft Surface Graft Polymerization. *Biomacromolecules* **2008**, *9* (1), 91–99. DOI: 10.1021/bm700849j.

27. Wu, V. M.; Tang, S.; Uskoković, V. Calcium Phosphate Nanoparticles as Intrinsic Inorganic Antimicrobials: The Antibacterial Effect. *ACS Appl. Mater. Interfaces* **2018**, *10* (40), 34013–34028. DOI: 10.1021/acsami.8b12784.

28. Liu, L.; Zhang, Y.; Li, C.; Cao, J.; He, E.; Wu, X.; Wang, F.; Wang, L. Facile Preparation PCL/ Modified Nano ZnO Organic-Inorganic Composite and Its Application in Antibacterial Materials. *J. Polym. Res.* **2020**, *27* (3), 78. DOI: 10.1007/s10965-020-02046-z.

29. Guo, L.; Wang, H.; Wang, Y.; Liu, F.; Feng, L. Organic Polymer Nanoparticles with Primary Ammonium Salt as Potent Antibacterial Nanomaterials. *ACS Appl. Mater. Interfaces* **2020**, *12* (19), 21254–21262. DOI: 10.1021/acsami.9b19921.

30. Kuntzler, S. G.; Costa, J. A.; Morais, M. G. Development of Electrospun Nanofibers Containing Chitosan/PEO Blend and Phenolic Compounds with Antibacterial Activity. *Int. J. Biol. Macromol.* **2018**, *117*, 800–806. DOI: 10.1016/j.ijbiomac.2018.05.224.

31. Kamaruzzaman, N. F.; Tan, L. P.; Hamdan, R. H.; Choong, S. S.; Wong, W. K.; Gibson, A. J.; Chivu, A.; de Pina, M. F. Antimicrobial Polymers: The Potential Replacement of Existing Antibiotics? *Int. J. Mol. Sci.* **2019**, *20* (11), 2747. DOI: 10.3390/ijms20112747.

32. Kuroki, A.; Kengmo Tchoupa, A.; Hartlieb, M.; Peltier, R.; Locock, K. E. S.; Unnikrishnan, M.; Perrier, S. Targeting Intracellular, Multi-Drug Resistant Staphylococcus Aureus with Guanidinium Polymers by Elucidating the Structure-Activity Relationship. *Biomaterials* **2019**, *217*, 119249. DOI: 10.1016/j.biomaterials.2019.119249.

33. Liu, H.; Zhang, X.; Zhao, Z.; Yang, F.; Xue, R.; Yin, L.; Song, Z.; Cheng, J.; Luan, S.; Tang, H. Efficient Synthesis and Excellent Antimicrobial Activity of Star-Shaped Cationic Polypeptides with Improved Biocompatibility. *Biomater. Sci.* **2021**, *9* (7), 2721–2731. DOI: 10.1039/d0bm02151b.

34. Ding, X.; Wang, A.; Tong, W.; Xu, F. Biodegradable Antibacterial Polymeric Nanosystems: A New Hope to Cope with Multidrug-resistant Bacteria. *Small* **2019**, *15* (20), 1900999. DOI: 10.1002/smll.201900999.

35. Garcia Maset, R.; Hapeshi, A.; Hall, S.; Dalgliesh, R. M.; Harrison, F.; Perrier, S. Evaluation of the Antimicrobial Activity in Host-Mimicking Media and *in Vivo* Toxicity of Antimicrobial Polymers as Functional Mimics of Amps. *ACS Appl. Mater. Interfaces* **2022**, *14* (29), 32855–32868. DOI: 10.1021/acsami.2c05979.

36. Chan, W. C. W. Principles of Nanoparticle Delivery to Solid Tumors. *BME Front.* **2023**, *4*, 0016. DOI: 10.34133/bmef.0016.

37. Champion, J. A.; Mitragotri, S. Role of Target Geometry in Phagocytosis. *Proc. Natl. Acad. Sci.* **2006**, *103* (13), 4930–4934. DOI: 10.1073/pnas.0600997103.

38. Tenzer, S.; Docter, D.; Rosfa, S.; Wlodarski, A.; Kuharev, J.; Rekik, A.; Knauer, S. K.; Bantz, C.; Nawroth, T.; Bier, C.; et al. Nanoparticle Size Is a Critical Physicochemical Determinant of the Human Blood Plasma Corona: A Comprehensive Quantitative Proteomic Analysis. *ACS Nano* **2011**, *5* (9), 7155–7167. DOI: 10.1021/nn201950e.

39. Mai, Y.; Eisenberg, A. Self-Assembly of Block Copolymers. *Chem. Soc. Rev.* **2012**, *41* (18), 5969. DOI: 10.1039/c2cs35115c.

40. Geng, Y.; Dalhaimer, P.; Cai, S.; Tsai, R.; Tewari, M.; Minko, T.; Discher, D. E. Shape Effects of Filaments versus Spherical Particles in Flow and Drug Delivery. *Nat. Nanotechnol.* **2007**, *2* (4), 249–255. DOI: 10.1038/nnano.2007.70.

41. Blanco, E.; Shen, H.; Ferrari, M. Principles of Nanoparticle Design for Overcoming Biological Barriers to Drug Delivery. *Nat. Biotechnol.* **2015**, *33* (9), 941–951. DOI: 10.1038/nbt.3330.

42. Li, Z.; Sun, L.; Zhang, Y.; Dove, A. P.; O'Reilly, R. K.; Chen, G. Shape Effect of Glyco-Nanoparticles on Macrophage Cellular Uptake and Immune Response. *ACS Macro Lett.* **2016**, *5* (9), 1059–1064. DOI: 10.1021/acsmacrolett.6b00419.

43. Tritschler, U.; Pearce, S.; Gwyther, J.; Whittell, G. R.; Manners, I. *50th Anniversary Perspective*: Functional Nanoparticles from the Solution Self-Assembly of Block Copolymers. *Macromolecules* **2017**, *50* (9), 3439–3463. DOI: 10.1021/acs.macromol.6b02767.

44. Canham, P. A.; Lally, T. P.; Price, C.; Stubbersfield, R. B. Formation of Worm-like Micelles from a Polystyrene–Polybutadiene–Polystyrene Block Copolymer in Ethyl Acetate. *J. Chem. Soc., Faraday Trans 1* **1980**, *76*, 1857–1867. DOI: 10.1039/f19807601857.

45. Chan, W. C. W. Nanomedicine 2.0. *Acc. Chem. Res.* **2017**, *50* (3), 627–632. DOI: 10.1021/acs.accounts.6b00629.

46. Inam, M.; Foster, J. C.; Gao, J.; Hong, Y.; Du, J.; Dove, A. P.; O'Reilly, R. K. Size and Shape Affects the Antimicrobial Activity of Quaternized Nanoparticles. *J. Polym. Sci., Part A: Polym. Chem.* **2018**, *57* (3), 255–259. DOI: 10.1002/pola.29195.

47. Song, Y.; Elsabahy, M.; Collins, C. A.; Khan, S.; Li, R.; Hreha, T. N.; Shen, Y.; Lin, Y.; Letteri, R. A.; Su, L.; et al. Morphologic Design of Silver-Bearing Sugar-Based Polymer

Nanoparticles for Uroepithelial Cell Binding and Antimicrobial Delivery. *Nano Lett.* **2021**, *21* (12), 4990–4998. DOI: 10.1021/acs.nanolett.1c00776.

48. Rabanel, J.; Mirbagheri, M.; Olszewski, M.; Xie, G.; Le Goas, M.; Latreille, P.; Counil, H.; Hervé, V.; Silva, R. O.; Zaouter, C.; et al. Deep Tissue Penetration of Bottle-Brush Polymers via Cell Capture Evasion and Fast Diffusion. *ACS Nano* **2022**, *16* (12), 21583–21599. DOI: 10.1021/acsnano.2c10554.
49. Zhang, K.; Rossin, R.; Hagooly, A.; Chen, Z.; Welch, M. J.; Wooley, K. L. Folate-Mediated Cell Uptake of Shell-Crosslinked Spheres and Cylinders. *J. Polym. Sci., Part A: Polym. Chem.* **2008**, *46* (22), 7578–7583. DOI: 10.1002/pola.23020.
50. Cao, L.; Manners, I.; Winnik, M. A. Influence of the Interplay of Crystallization and Chain Stretching on Micellar Morphologies: Solution Self-Assembly of Coil−crystalline Poly(Isoprene-*Block*-Ferrocenylsilane). *Macromolecules* **2002**, *35* (22), 8258–8260. DOI: 10.1021/ma021068x.
51. Petzetakis, N.; Walker, D.; Dove, A. P.; O'Reilly, R. K. Crystallization-Driven Sphere-to-Rod Transition of Poly(Lactide)-b-Poly(Acrylic Acid) Diblock Copolymers: Mechanism and Kinetics. *Soft Matter* **2012**, *8* (28), 7408–7414. DOI: 10.1039/c2sm25247c.
52. Li, Z.; Zhang, Y.; Wu, L.; Yu, W.; Wilks, T. R.; Dove, A. P.; Ding, H.; O'Reilly, R. K.; Chen, G.; Jiang, M. Glyco-Platelets with Controlled Morphologies via Crystallization-Driven Self-Assembly and Their Shape-Dependent Interplay with Macrophages. *ACS Macro Lett.* **2019**, *8* (5), 596–602. DOI: 10.1021/acsmacrolett.9b00221.
53. Massey, J. A.; Temple, K.; Cao, L.; Rharbi, Y.; Raez, J.; Winnik, M. A.; Manners, I. Self-Assembly of Organometallic Block Copolymers: The Role of Crystallinity of the Core-Forming Polyferrocene Block in the Micellar Morphologies Formed by Poly(Ferrocenylsilane-

*b*-Dimethylsiloxane) in *n*-Alkane Solvents. *J. Am. Chem. Soc.* **2000**, *122* (47), 11577–11584. DOI: 10.1021/ja002205d.

54. Wang, X.; Guerin, G.; Wang, H.; Wang, Y.; Manners, I.; Winnik, M. A. Cylindrical Block Copolymer Micelles and Co-Micelles of Controlled Length and Architecture. *Science* **2007**, *317* (5838), 644–647. DOI: 10.1126/science.1141382.
55. MacFarlane, L.; Zhao, C.; Cai, J.; Qiu, H.; Manners, I. Emerging Applications for Living Crystallization-Driven Self-Assembly. *Chem. Sci.* **2021**, *12* (13), 4661–4682. DOI: 10.1039/d0sc06878k.
56. Foster, J. C.; Varlas, S.; Couturaud, B.; Coe, Z.; O'Reilly, R. K. Getting into Shape: Reflections on a New Generation of Cylindrical Nanostructures' Self-Assembly Using Polymer Building Blocks. *J. Am. Chem. Soc.* **2019**, *141* (7), 2742–2753. DOI: 10.1021/jacs.8b08648.
57. Zhang, X.; Chen, G.; Liu, L.; Zhu, L.; Tong, Z. Precise Control of Two-Dimensional Platelet Micelles from Biodegradable Poly(*P*-Dioxanone) Block Copolymers by Crystallization-Driven Self-Assembly. *Macromolecules* **2022**, *55* (18), 8250–8261. DOI: 10.1021/acs.macromol.2c01158.
58. Merg, A. D.; van Genderen, E.; Bazrafshan, A.; Su, H.; Zuo, X.; Touponse, G.; Blum, T. B.; Salaita, K.; Abrahams, J. P.; Conticello, V. P. Seeded Heteroepitaxial Growth of Crystallizable Collagen Triple Helices: Engineering Multifunctional Two-Dimensional Core–Shell Nanostructures. *J. Am. Chem. Soc.* **2019**, *141* (51), 20107–20117. DOI: 10.1021/jacs.9b09335.
59. Finnegan, J. R.; Pilkington, E. H.; Alt, K.; Rahim, M. A.; Kent, S. J.; Davis, T. P.; Kempe, K. Stealth Nanorods *via* the Aqueous Living Crystallisation-Driven Self-Assembly of Poly(2-Oxazoline)s. *Chem. Sci.* **2021**, *12* (21), 7350–7360. DOI: 10.1039/d1sc00938a.

60. Ma, J.; Ma, C.; Huang, X.; de Araujo, P. H.; Goyal, A. K.; Lu, G.; Feng, C. Preparation and Cellular Uptake Behaviors of Uniform Fiber-like Micelles with Length Controllability and High Colloidal Stability in Aqueous Media. *Fundam. Res.* **2023**, *3* (1), 93–101. DOI: 10.1016/j.fmre.2022.01.020.

61. Tang, Z.; Gao, L.; Lin, J.; Cai, C.; Yao, Y.; Guerin, G.; Tian, X.; Lin, S. Anchorage-Dependent Living Supramolecular Self-Assembly of Polymeric Micelles. *J. Am. Chem. Soc.* **2021**, *143* (36), 14684–14693. DOI: 10.1021/jacs.1c06020.

62. Finnegan, J. R.; He, X.; Street, S. T. G.; Garcia-Hernandez, J. D.; Hayward, D. W.; Harniman, R. L.; Richardson, R. M.; Whittell, G. R.; Manners, I. Extending the Scope of "Living" Crystallization-Driven Self-Assembly: Well-Defined 1D Micelles and Block Comicelles from Crystallizable Polycarbonate Block Copolymers. *J. Am. Chem. Soc.* **2018**, *140* (49), 17127–17140. DOI: 10.1021/jacs.8b09861.

63. He, W.; Xu, J. Crystallization Assisted Self-Assembly of Semicrystalline Block Copolymers. *Prog. Polym. Sci.* **2012**, *37* (10), 1350–1400. DOI: 10.1016/j.progpolymsci.2012.05.002.

64. Gilroy, J. B.; Gädt, T.; Whittell, G. R.; Chabanne, L.; Mitchels, J. M.; Richardson, R. M.; Winnik, M. A.; Manners, I. Monodisperse Cylindrical Micelles by Crystallization-Driven Living Self-Assembly. *Nat. Chem.* **2010**, *2* (7), 566–570. DOI: 10.1038/nchem.664.

65. Ganda, S.; Stenzel, M. H. Concepts, Fabrication Methods and Applications of Living Crystallization-Driven Self-Assembly of Block Copolymers. *Prog. Polym. Sci.* **2020**, *101*, 101195. DOI: 10.1016/j.progpolymsci.2019.101195.

66. Lim, Y. H.; Tiemann, K. M.; Heo, G. S.; Wagers, P. O.; Rezenom, Y. H.; Zhang, S.; Zhang, F.; Youngs, W. J.; Hunstad, D. A.; Wooley, K. L. Preparation and *in Vitro* Antimicrobial

Activity of Silver-Bearing Degradable Polymeric Nanoparticles of Polyphosphoester-*Block*-Poly(L-Lactide). *ACS Nano* **2015**, *9* (2), 1995–2008. DOI: 10.1021/nn507046h.

67. Li, Z.; Pearce, A. K.; Du, J.; Dove, A. P.; O'Reilly, R. K. Uniform Antibacterial Cylindrical Nanoparticles for Enhancing the Strength of Nanocomposite Hydrogels. *J. Polym. Sci.* **2022**, *61* (1), 44–55. DOI: 10.1002/pol.20210853.
68. Parkin, H. C.; Garcia-Hernandez, J. D.; Street, S. T. G; Hof, R.; Manners, I. Uniform, Length-Tunable Antibacterial 1D Diblock Copolymer Nanofibers. *Polym. Chem.* **2022**, *13* (20), 2941–2949. DOI: 10.1039/d2py00262k.
69. van de Wetering, P.; Zuidam, N. J.; van Steenbergen, M. J.; van der Houwen, O. A.; Underberg, W. J.; Hennink, W. E. A Mechanistic Study of the Hydrolytic Stability of Poly(2-(Dimethylamino)Ethyl Methacrylate). *Macromolecules* **1998**, *31* (23), 8063–8068. DOI: 10.1021/ma980689g.
70. Hartmann, M.; Berditsch, M.; Hawecker, J.; Ardakani, M. F.; Gerthsen, D.; Ulrich, A. S. Damage of the Bacterial Cell Envelope by Antimicrobial Peptides Gramicidin S and PGLa as Revealed by Transmission and Scanning Electron Microscopy. *Antimicrob. Agents Chemother.* **2010**, *54* (8), 3132–3142. DOI: 10.1128/aac.00124-10.
71. Benincasa, M.; Pacor, S.; Gennaro, R.; Scocchi, M. Rapid and Reliable Detection of Antimicrobial Peptide Penetration into Gram-Negative Bacteria Based on Fluorescence Quenching. *Antimicrob. Agents Chemother.* **2009**, *53* (8), 3501–3504. DOI: 10.1128/aac.01620-08.
72. Chen, R.; Zhang, K.; Zhang, H.; Gao, C.; Li, C. Analysis of the Antimicrobial Mechanism of Porcine Beta Defensin 2 against E. coli by Electron Microscopy and Differentially Expressed Genes. *Sci. Rep.* **2018**, *8*, 14711. DOI: 10.1038/s41598-018-32822-3.

73. Schneider, V. A.; Coorens, M.; Ordonez, S. R.; Tjeerdsma-van Bokhoven, J. L. M.; Posthuma, G.; van Dijk, A.; Haagsman, H. P.; Veldhuizen, E. J. Imaging the Antimicrobial Mechanism(s) of Cathelicidin-2. *Sci. Rep.* **2016**, *6*, 32948. DOI: 10.1038/srep32948.

74. Xu, D.; Chen, W.; Tobin-Miyaji, Y. J.; Sturge, C. R.; Yang, S.; Elmore, B.; Singh, A.; Pybus, C.; Greenberg, D. E.; Sellati, T. J.; et al. Fabrication and Microscopic and Spectroscopic Characterization of Cytocompatible Self-Assembling Antimicrobial Nanofibers. *ACS Infect. Dis.* **2018**, *4* (9), 1327–1335. DOI: 10.1021/acsinfecdis.8b00069.

75. Xi, Y.; Song, T.; Tang, S.; Wang, N.; Du, J. Preparation and Antibacterial Mechanism Insight of Polypeptide-Based Micelles with Excellent Antibacterial Activities. *Biomacromolecules* **2016**, *17* (12), 3922–3930. DOI: 10.1021/acs.biomac.6b01285.

76. Zhao, R.; Wang, H.; Ji, T.; Anderson, G.; Nie, G.; Zhao, Y. Biodegradable Cationic ε-Poly-L-Lysine-Conjugated Polymeric Nanoparticles as a New Effective Antibacterial Agent. *Sci. Bull.* **2015**, *60* (2), 216–226. DOI: 10.1007/s11434-014-0704-9.

77. Fukushima, K.; Liu, S.; Wu, H.; Engler, A. C.; Coady, D. J.; Maune, H.; Pitera, J.; Nelson, A.; Wiradharma, N.; Venkataraman, S.; et al. Supramolecular High-Aspect Ratio Assemblies with Strong Antifungal Activity. *Nat. Commun.* **2013**, *4*, 2861. DOI: 10.1038/ncomms3861.

78. Liu, S.; Wei, L.; Hao, L.; Fang, N.; Chang, M. W.; Xu, R.; Yang, Y.; Chen, Y. Sharper and Faster "Nano Darts" Kill More Bacteria: A Study of Antibacterial Activity of Individually Dispersed Pristine Single-Walled Carbon Nanotube. *ACS Nano* **2009**, *3* (12), 3891–3902. DOI: 10.1021/nn901252r.

79. Nederberg, F.; Zhang, Y.; Tan, J. P.; Xu, K.; Wang, H.; Yang, C.; Gao, S.; Guo, X. D.; Fukushima, K.; Li, L.; et al. Biodegradable Nanostructures with Selective Lysis of Microbial Membranes. *Nat. Chem.* **2011**, *3* (5), 409–414. DOI: 10.1038/nchem.1012.

80. Sikder, A.; Pearce, A. K.; Kumar, C. M.; O'Reilly, R. K. Elucidating the Role of Multivalency, Shape, Size and Functional Group Density on Antibacterial Activity of Diversified Supramolecular Nanostructures Enabled by Templated Assembly. *Mater. Horiz.* **2023**, *10* (1), 171–178. DOI: 10.1039/d2mh01117d.

81. Street, S. T. G.; He, Y.; Harniman, R. L.; Garcia-Hernandez, J. D.; Manners, I. Precision Polymer Nanofibers with a Responsive Polyelectrolyte Corona Designed as a Modular, Functionalizable Nanomedicine Platform. *Polym. Chem.* **2022**, *13* (20), 3009–3025. DOI: 10.1039/d2py00152g.

82. Street, S. T. G.; Chrenek, J.; Harniman, R. L.; Letwin, K.; Mantell, J. M.; Borucu, U.; Willerth, S. M.; Manners, I. Length-Controlled Nanofiber Micelleplexes as Efficient Nucleic Acid Delivery Vehicles. *J. Am. Chem. Soc.* **2022**, *144* (43), 19799–19812. DOI: 10.1021/jacs.2c06695.

83. Street, S. T. G.; He, Y.; Jin, X.; Hodgson, L.; Verkade, P.; Manners, I. Cellular Uptake and Targeting of Low Dispersity, Dual Emissive, Segmented Block Copolymer Nanofibers. *Chem. Sci.* **2020**, *11* (32), 8394–8408. DOI: 10.1039/d0sc02593c.

84. Ananta, E.; Voigt, D.; Zenker, M.; Heinz, V.; Knorr, D. Cellular Injuries upon Exposure of Escherichia Coli and Lactobacillus Rhamnosus to High-Intensity Ultrasound. *J. Appl. Microbiol.* **2005**, *99* (2), 271–278. DOI: 10.1111/j.1365-2672.2005.02619.x.

85. Hoefel, D.; Grooby, W. L.; Monis, P. T.; Andrews, S.; Saint, C. P. A Comparative Study of Carboxyfluorescein Diacetate and Carboxyfluorescein Diacetate Succinimidyl Ester as Indicators of Bacterial Activity. *J. Microbiol. Methods* **2003**, *52* (3), 379–388. DOI: 10.1016/s0167-7012(02)00207-5.

86. Si, Z.; Pethe, K.; Chan-Park, M. B. Chemical Basis of Combination Therapy to Combat Antibiotic Resistance. *JACS Au* **2023**, *3* (2), 276–292. DOI: 10.1021/jacsau.2c00532.

87. Yeh, Y.; Huang, T.; Yang, S.; Chen, C.; Fang, J. Nano-Based Drug Delivery or Targeting to Eradicate Bacteria for Infection Mitigation: A Review of Recent Advances. *Front. Chem.* **2020**, *8,* 286. DOI: 10.3389/fchem.2020.00286.

88. Gao, W.; Chen, Y.; Zhang, Y.; Zhang, Q.; Zhang, L. Nanoparticle-Based Local Antimicrobial Drug Delivery. *Adv. Drug Deliv. Rev.* **2018**, *127*, 46–57. DOI: 10.1016/j.addr.2017.09.015.

89. Street, S. T. G.; Parkin, H. C.; Shopperly, L.; Chrenek, J.; Letwin, K.; Willerth, S. M.; Manners, I. Optimization of Precision Nanofiber Micelleplexes for DNA Delivery. *Biomater. Sci.* **2023**, *11* (10), 3512-3523. DOI: 10.1039/D2BM02014A

90. Elsabahy, M.; Wooley, K. L. Design of Polymeric Nanoparticles for Biomedical Delivery Applications. *Chem. Soc. Rev.* **2012**, *41* (7), 2545–2561. DOI: 10.1039/c2cs15327k.

91. Garcia-Hernandez, J. D.; Parkin, H. C.; Ren, Y.; Zhang, Y.; Manners, I. Hydrophobic Cargo Loading at the Core–Corona Interface of Uniform, Length-Tunable Aqueous Diblock Copolymer Nanofibers with a Crystalline Polycarbonate Core. *Polym. Chem.* **2022**, *13* (28), 4100–4110. DOI: 10.1039/d2py00395c.

92. Garcia-Hernandez, J. D.; Street, S. T. G.; Kang, Y.; Zhang, Y.; Manners, I. Cargo Encapsulation in Uniform, Length-Tunable Aqueous Nanofibers with a Coaxial Crystalline and Amorphous Core. *Macromolecules* **2021**, *54* (12), 5784–5796. DOI: 10.1021/acs.macromol.1c00672.

93. Chopra, I.; Roberts, M. Tetracycline Antibiotics: Mode of Action, Applications, Molecular Biology, and Epidemiology of Bacterial Resistance. *Microbiol. Mol. Biol. Rev.* **2001**, *65* (2), 232–260. DOI: 10.1128/mmbr.65.2.232-260.2001.

94. Lv, S.; Wu, Y.; Cai, K.; He, H.; Li, Y.; Lan, M.; Chen, X.; Cheng, J.; Yin, L. High Drug Loading and Sub-Quantitative Loading Efficiency of Polymeric Micelles Driven by Donor–Receptor Coordination Interactions. *J. Am. Chem. Soc.* **2018**, *140* (4), 1235–1238. DOI: 10.1021/jacs.7b12776.

95. Song, J.; Jang, J. Antimicrobial Polymer Nanostructures: Synthetic Route, Mechanism of Action and Perspective. *Adv. Colloid Interface Sci.* **2014**, *203*, 37–50. DOI: 10.1016/j.cis.2013.11.007.

96. Lam, S. J.; Wong, E. H. H.; Boyer, C.; Qiao, G. G. Antimicrobial Polymeric Nanoparticles. *Prog. Polym. Sci.* **2018**, *76*, 40–64. DOI: 10.1016/j.progpolymsci.2017.07.007.

97. Gao, J.; Wang, M.; Wang, F.; Du, J. Synthesis and Mechanism Insight of a Peptide-Grafted Hyperbranched Polymer Nanosheet with Weak Positive Charges but Excellent Intrinsically Antibacterial Efficacy. *Biomacromolecules* **2016**, *17* (6), 2080–2086. DOI: 10.1021/acs.biomac.6b00307.

98. Brock, T. D.; Madigan, M. T.; Dunlap, P. V.; Clark, D. P. *Brock Biology of Microorganisms*, 9th ed.; Pearson Higher Education: San Francisco, CA., 2008.

99. Magana, M.; Pushpanathan, M.; Santos, A. L.; Leanse, L.; Fernandez, M.; Ioannidis, A.; Giulianotti, M. A.; Apidianakis, Y.; Bradfute, S.; Ferguson, A. L.; et al. The Value of Antimicrobial Peptides in the Age of Resistance. *Lancet Infect. Dis.* **2020**, *20* (9), e216–e250. DOI: 10.1016/s1473-3099(20)30327-3.

100. MacNair, C. R.; Brown, E. D. Outer Membrane Disruption Overcomes Intrinsic, Acquired, and Spontaneous Antibiotic Resistance. *MBio* **2020**, *11* (5), e01615–20. DOI: 10.1128/mbio.01615-20.

101. Microbiology guide to interpreting minimum inhibitory concentration (MIC) https://www.idexx.com/files/microbiology-guide-interpreting-mic.pdf. (accessed 2023-01-10).

102. Hayat, M. A. Principles and Techniques of Electron Microscopy: Biological Applications **1989**, CRC Press, Boca Raton, FL, 3rd Ed, 469.

103. Da-Silva-Correa, L. H.; Aasen, K.; Gamm, N. E.; Godoy, R.; Rahmati, N.; Buckley, H. L. Efficacy Testing of Non-Oxidizing Biocides for Polyamide Membrane Biofouling Prevention Using a Modified CDC Biofilm Reactor. *AQUA - Water Infrastruc. Ecosyst. and Soc.* **2023**, *72* (3), 313. DOI: 10.2166/aqua.2023.217

104. Lambert, R. J. W.; Pearson, J. Susceptibility Testing: Accurate and Reproducible Minimum Inhibitory Concentration (MIC) and Non-Inhibitory Concentration (NIC) Values. *J. Appl. Microbiol.* **2000***, 88* (5), 784–790. DOI: 10.1046/j.1365-2672.2000.01017.x

# Chapter 4

## Uniform Block Copolymer Nanofibers for the Delivery of Paclitaxel in 2D and 3D Glioblastoma Tumor Models

*This chapter is adapted from:*

Parkin, H. C.[+], Shopperly, L. K.[+], Perez, M. R., Willerth, S. M., Manners, I. *Biomater. Sci.* **2024**, *Submitted.*

*Contributions:*

*The work in this chapter was jointly carried out by Hayley Parkin and Lennard Shopperly. Hayley Parkin conceived the project, performed the synthesis, characterization, and self-assembly of the 1D nanofibers, and performed the drug-loading experiments. Lennard Shopperly carried out the cell experiments. Data were analyzed jointly by Hayley Parkin and Lennard Shopperly. Milena Restan-Perez aided with 3D cell culture. The initial manuscript was written by Hayley Parkin, with editing provided by Prof. Ali Nazemi, Lennard Shopperly, and Prof. Stephanie Willerth.*

## 4.1 Abstract

Cancer treatment has transformed in recent years, with the introduction of immunotherapy providing substantial improvements in prognoses for certain cancers. However, traditional small molecule chemotherapeutics remain as the major frontline of defence, and improving their delivery to solid tumors is of utmost importance for improving potency and reducing side effects. Here, length-controlled one-dimensional seed nanofibers (ca. 25 nm, $Đ_L$ = 1.05) were generated from poly(fluorenetrimethylenecarbonate)-*b*-poly(dimethylaminoethylmethacrylate) via living crystallization-driven self-assembly. Paclitaxel, with an encapsulation content ranging from 1-100 wt%, was loaded onto the preformed nanoparticles by solvent addition and evaporation. Drug loading was quantified by dynamic light scattering and transmission electron microscopy. Drug-loaded vectors were then incubated with U87 MG glioblastoma cells in a 2D cell assay for up to 72 h, and their anticancer properties were determined. It was observed that seed nanofibers loaded with 20 wt% paclitaxel were the most advantageous combination ($IC_{50(nanofiber)}$ = 0.48 $\mu$g/mL wherein $IC_{50(paclitaxel)}$ = 0.11 $\mu$M), while pure seed nanofibers with no loaded drug displayed much lower cytotoxicity ($IC_{50(nanofiber)}$ = 11.52 $\mu$g/mL). The $IC_{50}$ of the loaded seed nanofibers rivaled that of free paclitaxel ($IC_{50(paclitaxel)}$ = 0.15 $\mu$M) as well as the commercially approved Abraxane® ($IC_{50(abraxane)}$ = 0.46 $\mu$g/mL wherein $IC_{50(paclitaxel)}$ = 0.06 $\mu$M). 3D tumor spheroids were then cultured and subjected to the same stresses. Live/dead cell staining revealed that once more, seed nanofibers with 20 wt% PTX, Abraxane®, and paclitaxel all exhibited similar levels of potency (55% viability), whereas control samples exhibited much higher cell viability (70%) after 3 days. These results demonstrate that nanofibers contain great potential as biocompatible drug delivery vehicles for cancer treatment as they exert a similar anticancer effect to the commercially available Abraxane®.

## 4.2 Introduction

It is well known that cancer has been, and remains, a major threat to health worldwide.[1–3] Research in this area has been of the highest priority in the last few decades and has realized some of the most significant scientific breakthroughs in recent years, with immunotherapy leading the way as a new gold standard of treatment.[4–6] The increased effectiveness and lower toxicity of these treatments make them an attractive alternative to traditional small molecule chemotherapeutics.[4] However, despite their obvious advantages, these newly discovered remedies can suffer from a lack of curative ability with tumor recurrences common,[7,8] as well as a high cost, which together currently impede universal implementation.[9] Thus, small molecule chemotherapeutics are still considered a frontline defense for cancer therapy, accounting for an estimated 63% of prescribed treatments.[10,11] While they are widely utilized, these drugs often suffer from poor solubility in aqueous media and non-specific action requiring large therapeutic doses to exert an effect, which leads to the recognizable and deleterious side effects habitually associated with chemotherapy.[12,13] Therefore, creating drug carriers that can improve the bioavailability, biodistribution, and anticancer efficacy of chemotherapeutics is required to ensure these become more tolerable and more effective treatment options.[10,14,15]

Some of the most notable research efforts in this area would be those made to deliver paclitaxel (PTX).[16,17] This drug suffers from extremely poor water solubility (~ 0.3 $\mu$g/mL), yet is effective at treating a broad range of cancer types including, but not limited to, Kaposi's sarcoma, breast, ovarian, prostate, gastric, and brain cancers.[14,18–20] The non-discriminatory mechanism of action, which involves the stabilization of mitotic spindles and thus prevention of cell division, favours apoptosis of cancer cells over quiescent healthy cells due to their more rapid rate of division.[14,18]

This makes PTX a potent cancer therapeutic, which is unfortunately associated with several severe side effects such as hypersensitivity, nephrotoxicity, and neurotoxicity originating from poor water-solubility and bioavailability of the drug.[16,21] Many carriers have been developed to enhance the solubility of PTX with the aim of reducing the administered dose and associated adverse side effects. The first of these newly developed systems was named Taxol®, which contains PTX solubilized in a mixture of polyoxyethylated castor oil and ethanol (Cremophor® EL).[16,18] While this formulation aids solubility, patients must undergo rigorous pre-medication to help reduce side effects. The second FDA-approved formulation was named Abraxane® (ABX), which consists of PTX encapsulated in an albumin shell, generating spherical particles approximately 130 nm in size.[18] This development significantly reduced the toxicity associated with PTX administration, where patients no longer needed pre-treatments.[18] It also helped increase the solubility of the drug, allowing for shorter infusion times. However, some clinical trials have demonstrated that a 50% higher dose of ABX is required to obtain a better anticancer response relative to Taxol®. In addition, some side effects such as neuropathy are still present in patients treated with ABX.[18]

While ABX is largely considered a success, efforts have not stopped to improve the anticancer activity and delivery of PTX to tumor sites through the creation of new delivery vehicles.[10,17] Recently, polymer nanoparticles have emerged as promising drug delivery systems due to their chemical modifiability, higher colloidal stability, and their ability to passively or actively target cancer cells.[22–24] The most successful of these is Genexol-PM®, which consists of a block copolymer (BCP) containing a poly($_{D,L}$-lactide) core-forming block and a poly(ethylene glycol) corona-forming block. This copolymer assembles to form spherical micelles that entrap PTX in their hydrophobic core.[18] This technology has been approved for clinical use in some countries;

however, it is still under development in others. Other approved formulations include Nanoxel® and Paclical®. Most carriers are spherical in shape and encapsulate the cargo in their hydrophobic core.[25–30] Alternative morphologies are also interesting to explore, as this parameter has been deemed critical for influencing nanoparticle biodistribution and blood circulation time.[31,32] Discher and coworkers reported the use of filomicelles containing a poly($\varepsilon$-caprolactone) core and poly(ethylene oxide) corona to deliver PTX.[33] They compared the activity relative to analogous nanospheres and discovered that the filomicelles were twice as effective at loading PTX.[33] Additionally, they demonstrated that both filomicelles and spherical nanoparticles were less toxic than Cremophore-EL® and had five times higher anticancer activity.[33] Despite these successes, relatively few polymer nanoparticles have reached clinical trials. This may be in part because most are prepared by methods that lack control over the resulting nanoparticle morphology and size distribution.[17,34,35] These differences can cause discrepancies in the observed biological effect, resulting in differential activity *in vivo* relative to *in vitro*.[31,36] Therefore, controlling the shape of nanomaterials is particularly important when designing effective and predictable drug-carriers.

Living crystallization-driven self-assembly (CDSA) has been proven to yield monodisperse polymer nanoparticles of controlled size and shape, allowing access to less commonly obtained morphologies such as one-dimensional (1D) nanofibers and two-dimensional (2D) nanoplatelets.[37–42] This morphological space is afforded by the use of a BCP consisting of a crystalline core-forming block and a hydrophilic corona-forming block.[38,43–45] The morphology of the final assembly can be controlled by tuning the relative block ratios between the core- and corona-forming blocks in the BCP. In these systems, ratios closer to 1:1 yield 2D nanoplatelets, and ratios approaching 1:10 (core:corona) form 1D nanofibers.[39,41] In the case of 1D nanofibers,

upon introduction of a poor solvent for the core, crystallization occurs to generate long and polydisperse nanofibers. These nanofibers are then susceptible to mechanical stress and can be sonicated to yield short nanofibers commonly termed "seeds" (ca. 25 nm in length).[46,47] The rate of fragmentation is proportional to the nanofiber length, with longer nanofibers undergoing scission more rapidly than shorter ones.[46] The end result is seeds that are relatively uniform in length, with dispersities regularly found between 1.1 and 1.2. An interesting feature of these seeds is that they contain crystalline termini which remain active to epitaxial growth upon the addition of further dissolved polymer, commonly known as "unimer". In this case, the rate of elongation is approximately equal for all seeds, resulting in nanofibers of a controlled length that is directly proportional to the unimer/seed mass ratio.[37,38,47] This method has been used to generate length-controlled and morphologically pure nanofibers using a diverse set of core- and corona-forming blocks finding applications in electronics, catalysis, and nanomedicine.[44,48–55]

Previous work in our group has explored a BCP consisting of a biodegradable poly(fluorenetrimethylenecarbonate) (PFTMC) core-forming block and a cationic poly(dimethylaminoethylmethacrylate) (PDMAEMA) water-soluble corona-forming block for biomedical applications.[49,56–58] This BCP has been demonstrated to undergo living CDSA in mixtures of tetrahydrofuran (THF) and methanol (MeOH) as well as THF and ethanol (EtOH) (both 1:4 *v/v*) depending on the relative block ratios. The resulting nanofibers demonstrate sufficient colloidal stability in water. The cationic PDMAEMA corona present in the micelles mediates electrostatic cellular interactions with both anionic mammalian and bacterial cell membranes.[49,56] We have demonstrated that the corona in these fibers can complex nucleic acid cargo and deliver it to cancer cells, resulting in high levels of protein expression. In addition, we

have shown that small nanoparticles exhibit higher levels of cell and tumor uptake.[49,59] In this work, we aim to demonstrate the application of these 1D nanofibers in cancer therapy when loaded with chemotherapeutics.

Herein, we report the non-covalent loading of PTX at the core-corona interface of nanofiber seeds, composed of PFTMC$_{26}$-*b*-PDMAEMA$_{424}$, approximately 26 nm in length. The loaded nanofibers were then evaluated for anticancer activity against U87 malignant glioma (MG) glioblastoma (GBM) cells relative to non-loaded seeds of identical composition and length, free PTX, and ABX in a 2D model over the course of 72 h. Different loading percentages were prepared to determine the maximum loading capacity of the seeds and the amount of loaded PTX corresponding to the highest anticancer activity. The best performing system (seeds + 20 wt% PTX) was carried through to the next stage of experiments which involved evaluating the anticancer activity in a patient-derived GBM 3D tumor spheroid model, allowing for more accurate results to be obtained for prediction of *in vivo* activity. In this context, the drug-loaded nanofibers were compared to pristine seeds, free PTX, and ABX to determine their potential as a PTX drug delivery system.

## 4.3 Results

### 4.3.1 – Synthesis of PFTMC$_{26}$-*b*-PDMAEMA$_{424}$ and generation of low dispersity, short nanofibers

PFTMC$_{26}$-*b*-PDMAEMA$_{424}$ (number-average molar mass $M_n$ = 87,900 g/mol, as determined via $^1$H NMR; molar mass dispersity $Đ_M$ = 1.16, as established by gel permeation chromatography, Figure S4.1, Table S4.1) was synthesized via ring-opening polymerization of spiro[fluorene-9,5′-[1,3]-dioxan]-2′-one monomer to yield the core-forming block, followed by reversible addition-

fragmentation chain transfer polymerization of 2-(dimethylamino)ethyl methacrylate to generate the corona-forming PDMAEMA block, as reported previously.[58] The PFTMC core-forming block degree of polymerization was determined via matrix-assisted laser desorption/ionization mass spectrometry as well as by $^{1}$H NMR integration of the chain-transfer agent signals relative to the PFTMC signals. The corona-forming PDMAEMA degree of polymerization in the resulting BCP was determined by $^{1}$H NMR integration of the PFTMC aromatic region relative to the coronal segment. This BCP has been previously demonstrated to undergo robust CDSA in THF:EtOH solvent mixtures (1:4 *v/v*).[58]

Previous studies examining the length-dependence of self-assembled PFTMC-*b*-PDMAEMA nanofibers on DNA complexation and delivery to cancer cells elucidated that short nanofibers (ca. 25 nm), often referred to as "seeds", are superior to longer nanofibers at delivering cargo to cells.[49,58] Therefore, in this work, $PFTMC_{26}$-*b*-$PDMAEMA_{424}$ was first dissolved in THF at a concentration of 20 mg/mL. An aliquot of this solution was then added to EtOH as the selective solvent, driving the self-assembly into length-disperse nanofibers (1 mg/mL) as visualized by transmission electron microscopy (TEM) (Figure 4.1). These polydisperse nanofibers were then sonicated for 3 h, resulting in the formation of seed nanofibers 25 nm in length (length dispersity ($Đ_L$) = 1.10, Table S4.2). The seed nanofibers were transferred into water by solvent addition-evaporation, resulting in final seed nanofibers of 26 nm in length ($Đ_L$ = 1.05) as determined by TEM (Figure 4.1, Table S4.2).

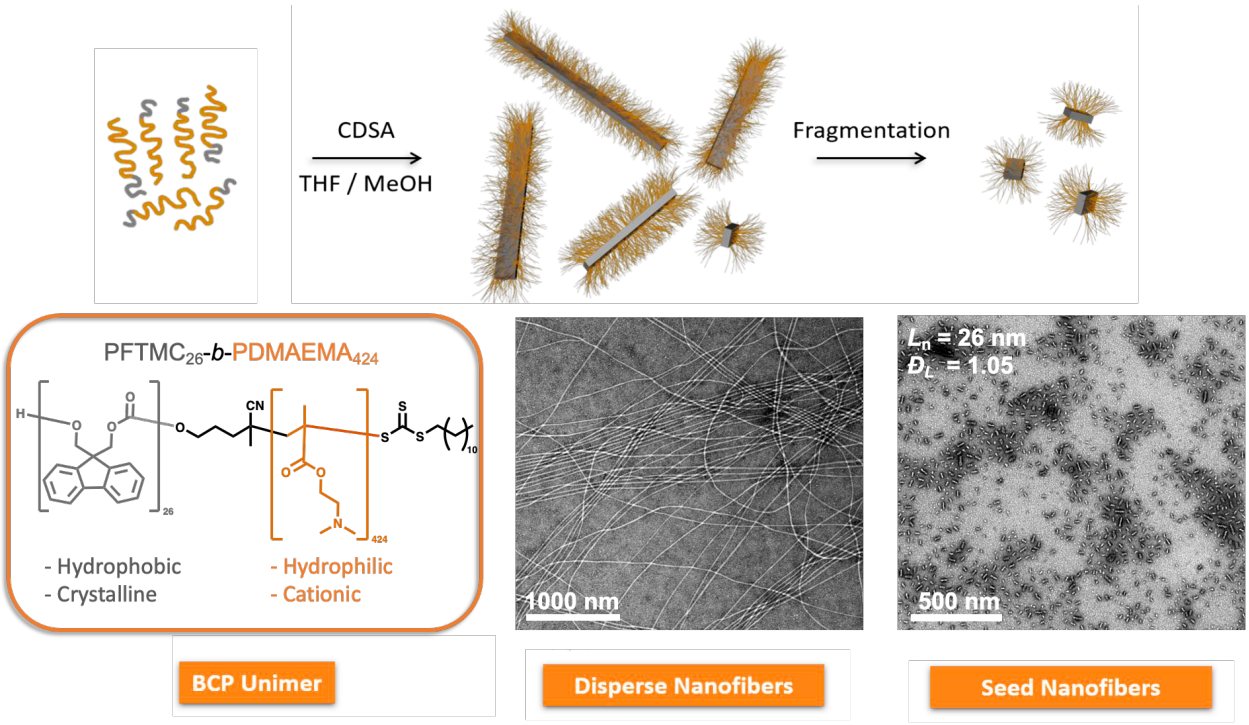


**Figure 4.1.** General schematic for the formation of $PFTMC_{26}$-*b*-$PDMAEMA_{424}$ nanofibers in THF/MeOH and representative TEM micrographs of the long polydisperse fibers as well as their corresponding seed fibers. Each sample is stained with 3 wt% uranyl acetate in EtOH.

### 4.3.2 – Loading of PTX at the core-corona interface of seed nanofibers

#### 4.3.2.1 – Evaluation of maximum drug loading by DLS

Achieving adequate drug-loading in crystalline-core nanoparticles is a key challenge these types of systems face. Traditionally, cargo is covalently attached to the coronal chains, which can create issues with drug release and modification of cell-binding properties.[60] Conversely, non-covalent cargo loading strategies have yielded lower-than-desirable loading capacities relative to cargo encapsulation in nanomaterials with an amorphous core.[61] Previous reports by our group describe a non-covalent loading procedure based on cargo addition to preformed nanoparticles followed by solvent evaporation.[61,62] This process relies on cargo that is soluble in organic solvents and

insoluble in water. The cargo is solubilized in the selective solvent for the corona (EtOH) of the nanofibers and is added to preformed nanofibers in THF/EtOH. As water is added and the organic solvent is allowed to evaporate, the hydrophobic cargo is driven to the interface between the hydrophobic core and the hydrophilic corona of the nanofibers due to the hydrophobic effect. Recently, we were able to increase the maximum loading capacity from 1 wt% of Nile Red to 20 wt% of tetracycline on ca. 100 nm nanofibers.[63] This was largely possible through the use of dynamic light scattering (DLS) which is emerging as a powerful tool to quantify drug-loading.[64] Quantification of drug loading can be laborious, requiring either fluorescence detection or complicated removal of the nanoparticles from the drug solution which can give inaccurate results of the loading capacity. In contrast, DLS does not require removal of nanoparticles from the solution or the use of dialysis, ensuring that the concentration of nanoparticles present remains constant. Therefore, to investigate the maximum loading capacity of seed nanofibers for PTX delivery, the water addition/solvent evaporation procedure was utilized to load PTX at percentages from 10 – 80 wt%, and the results were monitored by DLS. Briefly, the nanofibers were kept in their organic self-assembly solvent (in this case, THF:EtOH 1:4 *v/v*) while the PTX was solubilized in EtOH at a concentration of 1 mg/mL. The drug solution (10 - 80 $\mu$L) was then added to the nanofibers (100 $\mu$L, 1 mg/mL). Finally, an excess amount of water (150 – 200 $\mu$L) was added to the combination and the organic solvents were allowed to completely evaporate (Figure 4.2). In this method, if excess therapeutic is present in the solution and is not loaded, it will aggregate and be detectable by DLS allowing for determination of the maximum loading capacity.

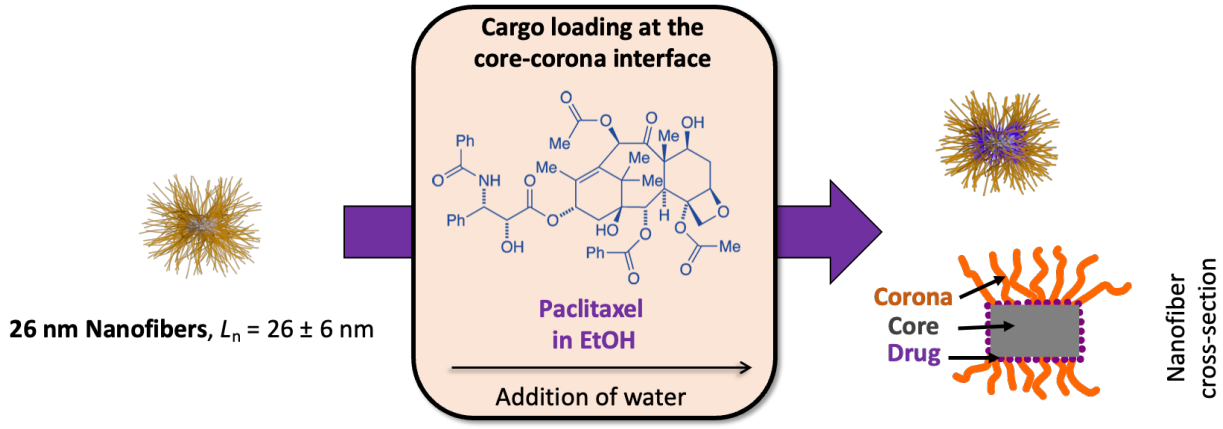


**Figure 4.2.** General schematic of drug loading procedure employed. PTX is dissolved in EtOH and is added to the nanofiber self-assembly solvent mixture. Water is then slowly added, and the organic solvent is allowed to evaporate. This results in localization of the drug at the core-corona interface of the fibers, as shown by the representative cross-section.

Measurements were taken by the addition of 10 $\mu$L of the loaded nanofiber solution into 40 $\mu$L of 40 mM (4-(2-hydroxyethyl)-1-piperazineethanesulfonic acid) (HEPES) buffer (pH 7.4). Pristine 26 nm nanofibers displayed a hydrodynamic radius ($R_h$) of 126 nm, whereas the $R_h$ of free drug equivalent to 20 wt% loading (200 $\mu$g/mL) was determined to be 1439 nm, indicating the presence of large drug aggregates in solution (Figure 4.3). This is unsurprising, as PTX is poorly soluble in water (0.3 $\mu$g/mL).[18] At 10, 20, and 30 wt% drug loading, the $R_h$ largely matched that of the non-loaded nanofibers (117 nm, 124 nm, and 126 nm, respectively) (Figure 4.3A,B). As the loading amount was increased to 40, 60, and 80 wt%, the size began to deviate ($R_h$ = 156 nm, 243 nm, 1039 nm respectively), and the distribution broadened (Figure 4.3B, S4.2). These results indicated that at 40 wt%, the PTX likely begins to unload from the nanofibers.

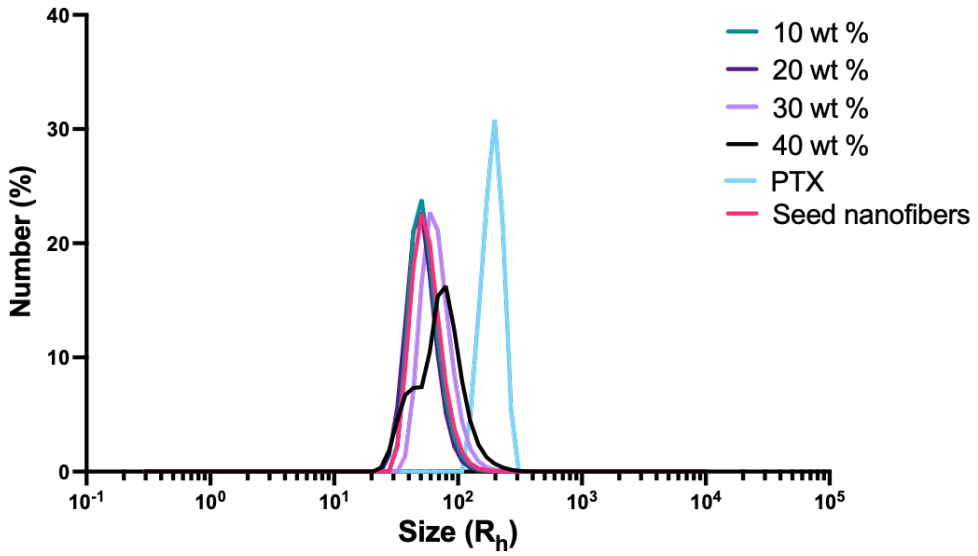


**Figure 4.3.** Hydrodynamic radius of the drug-loaded nanoparticles relative to non-loaded seed nanofibers and free PTX (blue trace). PTX loadings of 10 (teal trace) and 20 wt% (dark purple trace) overlap well with that of non-loaded nanofibers (pink trace). The hydrodynamic radius of assemblies with 30 (light purple trace) and 40 wt% (black trace) PTX loading, where the size begins to deviate from that of the nanofibers themselves. This indicates less close association between the nanofibers and the drug molecules.

#### 4.3.2.2 – Investigation of drug loading by TEM

We were also interested in determining if TEM is a viable method to evaluate drug loading. To do so, a sample of pure PTX in water was prepared at a concentration of 200 $\mu$g/mL, as well as a pure seed solution at 1 mg/mL and PTX-loaded seeds from 1 wt% to 100 wt% at a seed concentration of 1 mg/mL (Figure S4.3). Each sample was stained using a 3 wt% uranyl acetate solution in EtOH to provide sufficient contrast. As PTX is highly insoluble in water, large platelet-like needles were observed throughout the entire sample, as visualized by TEM (Figure 4.4A). Interestingly, these structures never reappeared regardless of PTX loading content even at 100 wt% loading on the

nanofibers (Figure 4.4B,C, S4.3). The seeds retained their shape and no PTX was evident either on the seeds or surrounding them. Therefore, the presence of seed nanofibers appears to sufficiently disrupt the assembly of the pure drug structures into very large aggregates. We postulate that the nanofibers may partially solubilize the drug through association, leading to the larger hydrodynamic radius visible via DLS, yet no structures large enough to be visible by TEM.

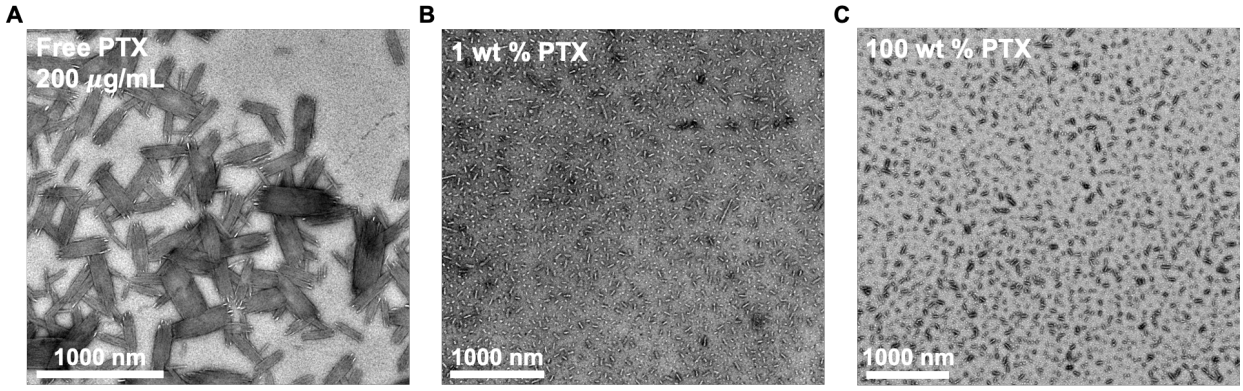


**Figure 4.4.** TEM micrographs to monitor drug loading in the nanofiber seeds. Large platelet-type structures are observed when PTX is in the absence of seed nanofibers at a concentration of 200 ug/mL (A). In contrast, at 1 wt% loading (B) and even 100 wt% (C), these PTX structures are not found in the samples when nanofibers are present.

### 4.3.3 – PTX delivery to U87 MG GBM cells over 72 h in a 2D cell model

While we were quite confident that 20 wt% was the highest loading capacity possible for PTX in our nanofibers, we also wished to investigate if the entire drug amount was required to be loaded to exert a high anticancer effect. Therefore, samples were prepared of non-loaded seeds as well as PTX-loaded seeds at 1, 10, 20, 30, 40, 60, 80, and 100 wt% PTX. GBM cells were utilized as a cell type that is susceptible to the action of PTX[30,65,66] and is also capable of forming 3D tumor spheroids, which would allow for comparisons between 2D and 3D cancer cell models.[67–69] 2D cell culture experiments are the standard method for evaluating a primary level of activity for any

nanoparticular system. However, it is becoming widely understood that 2D models do not accurately represent the tumor micro-environment and do not allow cell-cell interactions to occur or represent realistic particle penetration into the body of a tumor. This results in many developed nanoparticle-based drug delivery vehicles not reaching their clinical potential, and thus comparisons to 3D models are particularly desirable.[70] Cells were seeded at 10,000 cells/well and allowed to adhere to microwell plates overnight, at which point the cell media was replaced and the samples were applied. Drug-loaded and non-loaded seeds were applied at concentrations ranging from 0.1 – 25 µg/ml. Each sample was evaluated in triplicate, with cell viability determined via an alamarBlue™ metabolic assay. The $IC_{50}$ for each loading was assessed after 24 h, 48 h, and 72 h.

Upon analysis of cell viability after 24 h of incubation with PTX-loaded nanofibers, those containing no PTX did not demonstrate noticeable toxicity at concentrations below 4 µg/ml, with an $IC_{50}$ of 9.52 $\mu$g/mL obtained. The $IC_{50}$ of the nanofibers gradually decreased as the loading % increased to 20 wt%, which exhibited the lowest $IC_{50}$ (2.06 $\mu$g/mL, Figure 4.5, Table ***4.1.***). At all drug loadings higher than 20 wt% of PTX, the $IC_{50}$ increased to values between 2.69 - 3.86 $\mu$g/mL (Figure 4.5, Table 4.1). Upon observation after 72 h of incubation, the $IC_{50}$ of nanofibers with no PTX increased further to 11.52 $\mu$g/mL. The $IC_{50}$ of 20 wt% loaded seeds was again the lowest at 0.48 $\mu$g/mL, with all other loading contents showcasing higher $IC_{50}$ values (Figure 4.5, S4.4, Table 4.1, S4.3). Upon comparison of the relative amounts of PTX present in each sample, it becomes clear that full loading of the drug is necessary to exert the desired effect. The 30 - 80 wt% drug-loaded samples, after 72 h incubation, exhibit the highest $IC_{50}$ values yet contain the greatest amount of PTX (Figure S4.4, Table S4.3). In contrast, samples that contain 20

wt% PTX and below demonstrate the most potent specific anticancer activity (Figure 4.5). Interestingly, the 1 wt% drug-loaded sample exhibits an extremely low $IC_{50}$ of PTX (0.04 $\mu$M), indicating very effective delivery of the chemotherapeutic drug. However, large amounts of seed nanofibers would be required to exert the desired anticancer efficacy, as indicated by the much higher overall $IC_{50}$ of 3.12 $\mu$g/mL. Similarly, the nanofibers containing 10 wt% PTX demonstrate an $IC_{50}$ of 0.07 $\mu$M (on the basis of PTX), similar to that recorded for nanofibers with 20 wt% PTX (0.11 $\mu$M). The $IC_{50}$ values were also identified for free PTX solubilized in DMSO, as well as ABX. After 24 h of incubation, both ABX and PTX exhibited high $IC_{50}$ values, with the value for ABX being incalculable, and that of PTX being 13.21 $\mu$M (Figure 4.5,

Table ***4.1.***). The potency improved over the course of 72 h, with $IC_{50}$ values of 0.06 $\mu$M and 0.15 $\mu$M for ABX and PTX, respectively. These correspond to $IC_{50}$ values of PTX and Abraxane® that have been previously reported for PTX/ABX treatment of U87 MG GBM cells (Figure 4.5, Table 4.1).[65,71–73] These experiments demonstrate that the 20 wt% drug-loaded sample could deliver the most PTX while requiring the least amount of carrier to exert a reasonable anticancer efficacy. As a result, this drug delivery composition was carried forward for the 3D cell culture experiments. Furthermore, these results indicated that observation after 3 days of incubation is necessary to visualize the full effect of the drug delivery system.

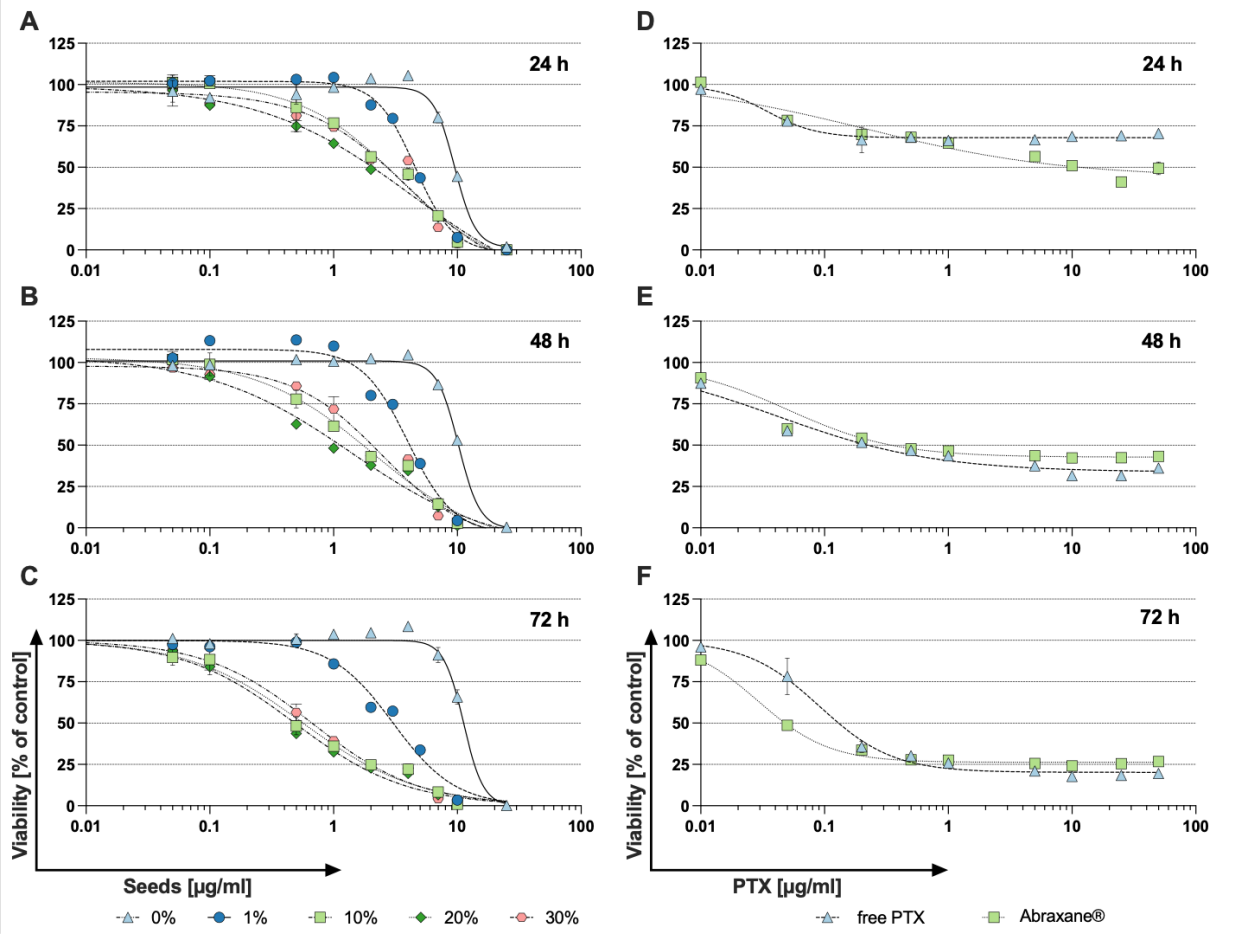


**Figure 4.5.** Cell viability curves utilized to calculate $IC_{50}$ values for each evaluated sample. Cell viability after incubation with drug-loaded nanofibers after (A) 24 h (B) 48 h and (C) 72 h. Charts D, E, and F indicate cell viability upon incubation with ABX or free PTX after (D) 24 h, (E) 48 h, and (F) 72 h. Each experiment was performed in triplicate. Standard deviations for all $IC_{50}$ values can be found in Table S4.4.

**Table 4.1.** $IC_{50}$ values calculated for samples at a given concentration of PTX, recorded over 72 h. PTX $IC_{50}$ values represent the equivalent amount of PTX to which the nanofiber $IC_{50}$ corresponds. Standard deviations for all $IC_{50}$ values can be found in Table S4.4.

| | Nanofiber $IC_{50}$ [$\mu$g/mL] | | | PTX $IC_{50}$ [$\mu$M] | | |
|---|---|---|---|---|---|---|
| **Sample (wt % PTX)** | **24 h** | **48 h** | **72 h** | **24 h** | **48 h** | **72 h** |
| 0 | 9.52 | 10.22 | 11.37 | - | - | - |
| 1 | 4.56 | 4.12 | 3.12 | 0.05 | 0.05 | 0.04 |
| 10 | 2.72 | 1.72 | 0.57 | 0.32 | 0.20 | 0.07 |
| 20 | 2.06 | 1.13 | 0.48 | 0.48 | 0.26 | 0.11 |
| 30 | 2.70 | 2.05 | 0.69 | 0.95 | 0.72 | 0.24 |
| Free PTX | - | - | - | 13.21 | 0.26 | 0.15 |
| Abraxane | - | 1.78 | 0.46 | undefined | 0.23 | 0.06 |

### 4.3.4 – PTX delivery to 3D patient-derived GBM cell spheroids over 3 days

A 3D tumor spheroid model was used to enable more accurate quantification of PTX delivery and anticancer activity relative to the 2D models. Primary GBM cells have been previously demonstrated to form 3D tumor spheroids consistently[74–77] and thus, were selected for inoculation with each sample. Cell culture flasks were seeded with primary patient-derived GBM single cells in DMEM/F12 media at 100k cells/mL. After 3 days, Aggrewell™ plates (STEMCELL Technologies) were seeded at a cell concentration of 900k cells/well, or 3000 cells/microwell, to promote the formation of well-defined tumor spheroids. The well plates were then incubated for 3 days to enable all the cells to integrate properly into spheroids. On day 3 of incubation, the spheroids were exposed to the samples of interest. Finally, after 3 further days of incubation, the cell culture media was replaced with live/dead stain (Invitrogen), and the samples were imaged after a 30-minute incubation at 22 ℃.

Images were taken of a minimum of 3 different spheroids using brightfield microscopy and fluorescence filter microscopy to visualize the calcein-AM (live) and ethidium homodimer-1 (dead) fluorescence. Fluorescence intensities were measured in FIJI software and the corrected total cell fluorescence was calculated by subtracting the background fluorescence according to equation S3. The total calcein-AM and ethidium homodimer-1 fluorescence was summed for each individual spheroid, and the percentage of live cells and dead cells was calculated. This ensures that any discrepancies in the relative amounts of live/dead stain between wells are accounted for. Each sample's mean percentage of live and dead cells was then compared.

The evaluated samples included spheroids incubated only in the presence of cell culture media, pristine nanofiber seeds, nanofiber seeds loaded with 20 wt% PTX, free PTX solubilized in DMSO, and ABX. For these experiments, the concentration of PTX was kept constant to enable conclusions to be drawn about the capabilities of the drug delivery vectors themselves. The application of samples did not disrupt the tumor spheroid formation or their overall shape, with all spheroids retaining their normal appearance. Control cells grown in the presence of solely DMEM/F12 media exhibited 70% viability after incubation for 3 days (Figure 4.6, S4.5). Those incubated with non-loaded seed nanofibers (4 μg/mL) displayed identical levels of viability at 70% (Figure 4.6, S4.6). In contrast, all samples containing PTX exhibited much lower levels of cell viability with PTX at 56% (Figure 4.6, S4.7) and ABX (Figure 4.6, S4.8) as well as 20 wt% PTX-loaded seed nanofibers (Figure 4.6, and S4.9) at 55% cell viability after 3 days. These results demonstrate that seed nanofibers alone do not display high toxicity in a 3D model at the concentrations tested. However, upon encapsulation of seed nanofibers with 20 wt% PTX at their core-corona interface, much higher potency that rivals that of a commercially approved treatment

is observed. The nanofibers can deliver the same amount of PTX as ABX while requiring a smaller amount of carrier (10 wt% *vs.* 20 wt% loading for ABX and nanofibers, respectively).[78] This can potentially reduce the side effects of administered PTX or enable higher contents of PTX to be delivered using the same amount of carrier.

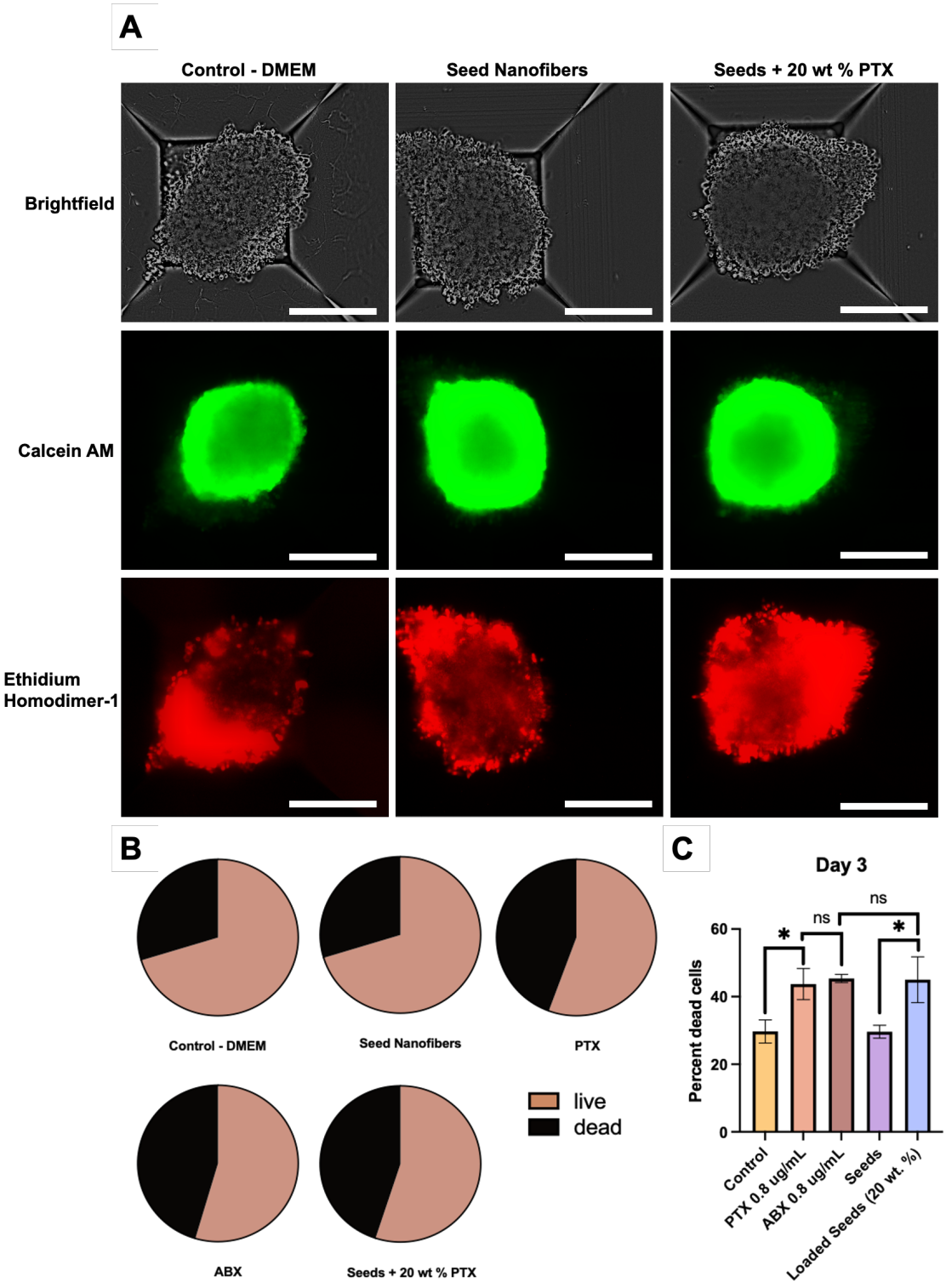


**Figure 4.6.** Representative images of 3D tumor spheroids captured on a Cellcyte imager at 10 x magnification. Spheroids shown are those incubated in DMEM, with pristine seeds, and with seeds

loaded with 20 wt% PTX. Green fluorescence represents live cells, whereas red fluorescence represents dead cells. All scale bars represent 200 μm.

## 4.4 Discussion

In this work, we have reported the application of PFTMC$_{26}$-*b*-PDMAEMA$_{424}$ seed nanofibers for use as cancer therapeutic drug delivery vehicles. Investigation of the maximum drug loading capacity of these nanofibers was performed by DLS and TEM measurements. By examining the average hydrodynamic radius, it was determined that 20 wt% is the highest amount of PTX that can be loaded onto the nanofibers, with amounts higher than 20 wt% exhibiting a shift away from the natural size of the nanofibers. TEM analysis revealed that as long as some nanofibers are present in solution, the PTX is solubilized enough to prevent the formation of large crystalline aggregates observed in the control PTX TEM images. This is confirmed in the DLS data where, even at 80 wt% PTX loading, a second size population that would correspond to the free PTX hydrodynamic radius was never observed.

Toxicity studies on 2D monolayer cell cultures were performed to verify this proposed maximum loading capacity and to investigate if the entirety of the drug must be loaded to exert a potent anticancer effect. The best performing system matched the maximum loading capacity, i.e. seed nanofibers loaded with 20 wt% of PTX. While systems with higher PTX loadings also displayed relatively low $IC_{50}$ values, the $IC_{50}$ of the equivalent PTX was much higher indicating ineffective delivery of PTX. In contrast, while lower PTX loadings did not display very potent overall $IC_{50}$ values, the $IC_{50}$ value for the PTX contained in the drug-nanofiber conjugate was much lower, even more so than that measured at 20 wt% of PTX. While these appear to deliver PTX incredibly

effectively, this is offset by the requirement of a larger amount of carrier to be used. A few important differences are noted upon comparing the loaded seed nanofiber samples with PTX and ABX. Primarily, after 24 h of incubation, the nanofiber $IC_{50}$ values are all relatively low and experience a gradual further decrease over the subsequent 48 h. In stark contrast, both the PTX and ABX exhibit high $IC_{50}$ values after 24 h with no $IC_{50}$ defined for ABX after 24 h. These then become much more active over the next 48 h and exhibit $IC_{50}$ values similar to those of our drug-loaded nanofibers. These results demonstrate that the seed nanofibers deliver PTX more efficiently than ABX and that the anticancer activity persists over a period of at least 3 days.

Finally, the anticancer properties of 1D seed nanofibers relative to ABX and PTX were evaluated in a more biologically relevant patient-derived GBM 3D cell model. Spheroids formed well over the span of 3 days after which they were exposed to PTX-containing samples and non-loaded nanofiber seeds. As PTX requires time to exert its anticancer effect (prevention of cell division), and all treatments were active after 72 h, spheroids were imaged three days post-inoculation. Spheroids incubated in DMEM/F12 media were used as a baseline level of viability, which was found to be 70%. Pristine seed nanofibers exhibited almost the same level of viability (70%) indicating that no adverse effects are present due to the seeds themselves at the concentrations of interest. Spheroids incubated with seeds loaded with 20 wt% PTX, ABX, and free PTX were then evaluated. The spheroids were exposed to the same concentration of PTX in each case, and thus, only the amount of carrier (or DMSO in the case of free PTX) was effectively varied. All the PTX-containing samples exhibited the same level of viability (~55%), a reduction of approximately 15% from control samples. Notably, we demonstrate that the 1D seed nanofibers exhibit an advantage over the traditional ABX carrier. As the loading capacity of the seed nanofibers is

approximately double that of ABX (20 wt% *vs.* 10 wt%), we delivered the same amount of PTX using half the amount of the carrier. As no cytotoxicity is observed for the seeds alone at these concentrations, this may be promising for lowering PTX-associated side effects. In turn, 1D seed nanofibers could deliver twice the amount of PTX for a given amount of ABX. This should increase the anticancer efficacy of PTX delivered by seed nanofibers compared to ABX. Additionally, upon comparisons between the performance of each treatment in 2D and 3D models, important differences are observed. After 72 h of incubation with ABX in a 2D cell model, the $IC_{50(paclitaxel)}$ was found to be 0.06 μM. In contrast, the $IC_{50(paclitaxel)}$ of 20 wt% loaded seed nanofibers was 0.11 μM. The overall $IC_{50}$ values of each carrier was approximately the same (0.46 μg/mL *vs* 0.48 μg/mL for ABX and loaded seed nanofibers, respectively). This means that in the 3D model when the concentration of PTX is kept constant (0.8 μg/mL), we would expect the ABX to possess a higher anticancer activity. This is not what is observed and instead the effect is identical. Thus, the 1D nanofibers more effectively deliver the PTX in 3D models over 2D models likely due to their small size and advantageous 1D shape, allowing for better penetration into the tumor. In summary, in the 2D cell model, more PTX was required in loaded seed nanofibers relative to ABX to exert the desired effect. In the 3D model, the same amount of PTX was utilized to obtain an identical anticancer effect, showcasing the advantageous properties of 1D nanofibers for obtaining desirable delivery properties in more complex cell environments. Therefore, 1D seed nanofibers are a promising alternative delivery vehicle for PTX as the anticancer properties demonstrated in this article rival that of the commercially available and widely employed treatment, ABX, with several promising advantages.

## 4.5 Conclusion

Herein, we describe PFTMC$_{26}$-*b*-PDMAEMA$_{424}$ seed nanofibers as cancer therapeutic drug delivery vehicles, with activity that rivals the commercially approved ABX. The maximum drug loading capacity of ca. 25 nm seed nanofibers was explored through DLS and TEM and was found to be 20 wt%. It was determined that full drug loading is required for optimum anticancer activity of drug-loaded seed nanofibers. In addition, seed nanofibers with no added therapeutic proved to be non-cytotoxic up to 4 $\mu$g/mL. PTX-loaded seed nanofibers were found to exert anticancer activity more quickly (beginning on day 1) than the traditional therapy ABX and free PTX (effect observed on day 2). Lastly, it was found that when PTX concentration was kept constant, 1D seed nanofibers were equally as effective as ABX at delivering PTX to the tumor. As the drug loading capacity for seed nanofibers is twice as much as ABX, we expect twice as much PTX to be deliverable to cancer cells using seed nanofibers compared to ABX. Therefore, the degradable and biocompatible drug-loaded polymer nanofibers presented herein should help lower the unwanted side effects normally associated with PTX treatment.

## 4.6 Supporting Information

### 4.6.1 General considerations

The synthesis and characterization of PFTMC$_{26}$-*b*-PDMAEMA$_{424}$ have been previously reported by Street et al. and Parkin et al.[58,63] The PFTMC homopolymer degree of polymerization was determined by matrix-assisted laser desorption/ionization mass spectrometry and the coronal-block degree of polymerization was determined by integrations of coronal block peaks in $^1$H NMR relative to peaks of the PFTMC block. RAFT-CTA was dried via vacuum desiccation over phosphorus pentoxide prior to use. Paclitaxel was purchased from Sigma-Aldrich (Canada). All other reagents and solvents were purchased from Sigma-Aldrich (Canada), Combi-Blocks (USA), VWR (Canada), or Fisher Scientific (Canada) and used without further purification. Solvents for

self-assembly were HPLC grade and were filtered through PTFE, nylon, or cellulose filters with a pore size of 200 nm before use.

### 4.6.2 Instrumentation

**Gel permeation chromatography (GPC)**

Gel permeation chromatograms were acquired on a Malvern OMNISEC triple-detector (refractive index, UV-Vis photodiode detector, light scattering detector and viscometer) chromatograph. Prepared samples were of 1 mg/mL concentration in HPLC grade THF, and were filtered through a PTFE filter with a 200 nm pore size prior to measurement. The eluent used was *n*-$Bu_4NBr$/THF (1 % *v/v*) at a flow rate of 1 mL/min. Two columns were employed, the first of grade T3000 and the second of grade T5000, operated at 35 °C. Universal calibration was constructed using a polystyrene standard.

**Preparatory Gel permeation chromatography (Prep GPC)**

Preparatory gel permeation chromatography was performed on a Shimadzu Prep GPC equipped with a CBM-20A communications bus module, LC-20AP solvent delivery unit, SIL-10AP autosampler, CTO-40C column oven, SPD-40 UV-Vis detector, RID-20A refractive index detector, and FRC-10A fraction collector. An initial injection of polymer in THF (1 mL, 10 mg/mL) at a flow rate of 3 mL/min using HPLC grade THF as eluent was used to gather the retention times of the species in solution. Using this data, the fraction collector was calibrated to separate the desired peaks into separate vials. Subsequent injections (3 mL, 10 mg/mL, 3 mL/min) were repeated until the desired volume was collected. The resulting solutions were concentrated in vacuo to yield the final polymer.

**Ultrasonication**

Micelle sonication was carried out using a Fisherbrand 112xx series advanced ultrasonic cleaner (FB-11203), operated in sweep mode at 80 % power and 37 MHz at 10 °C.

**Transmission electron microscopy (TEM)**

TEM images were obtained on a JEOL 1011 microscope equipped with an 11 Megapixel CCD camera, operated at 80 kV. Nanoparticle solutions (1.5 μL, 1 mg/mL) were drop-casted onto a carbon-coated copper grid. Uranyl acetate solution (8 μL) in EtOH (3 wt %) was subsequently drop-casted on top, and the grids were left to dry overnight. Copper grids (400 mesh) were

purchased from Ted Pella. Carbon films (ca. 6 nm) were prepared by carbon sputtering mica sheets with a Leica ACE 600 carbon coater. The carbon films were deposited onto copper grids via floatation on water and the grids were allowed air dry.

For micelle length analysis, a minimum of 200 nanofibers were traced manually using the FIJI software package. The number average micelle length ($L_n$) or width ($W_n$) and weight average micelle length ($L_w$) were calculated using eq. S1-2 from the individual contour lengths ($L_i$) of the micelles. Here, $N_i$ is the number of micelles of length $L_i$, and $n$ is the number of micelles examined in each sample. The distribution of micelle lengths is characterized by $Đ = L_w/L_n$.

$$L_n = \frac{\sum_{i=1}^{n} N_i L_i}{\sum_{i=1}^{n} Ni} \qquad L_w = \frac{\sum_{i=1}^{n} N_i L_i^2}{\sum_{i=1}^{n} NiLi} \qquad \text{(eq. S1-2)}$$

**Dynamic Light Scattering (DLS) Measurements**

Dynamic light scattering (DLS) experiments were carried out using a Malvern Zetasizer Pro. Aqueous samples for DLS were prepared at 50 $\mu$L of 1 mg/mL. The correlation function was acquired in real-time and analysed by Cumulant analysis. This process allowed the diffusion coefficients for the nanoparticles to be determined. These were expressed as the effective hydrodynamic radius ($R_h$) using the Stokes-Einstein relationship for coated spheres in water (Refractive Index = 1.33, Dispersant Viscosity = 0.887, Dispersant Dielectric Constant = 78.5) with core properties of polystyrene latex (Refractive Index = 1.590, Absorption = 0.010). For

### 4.6.3 Self-Assembly Procedures

The composition of all solvent mixtures is given as *v:v*. All nanofibers were ultimately transferred into Milli-Q® water *via* a modified procedure of the preformed-nanoparticle solvent-switch loading (PNSL) method as reported by Garcia-Hernandez et al.[64] Modifications include slow drop-wise addition of water from a micropipette, followed by organic solvent evaporation over the course of 2 days. No filtration through a syringe filter was performed.

**General self-nucleation procedure**

A solution of diBCP dissolved in THF (unimer) (20 mg/mL – 200 mg/mL) was diluted with an appropriate amount of THF. Subsequently, unimer solution was slowly added via a micropipette into a selective solvent (EtOH) to yield solutions which had final diBCP concentrations between 1 mg/mL – 10 mg/mL with 20:80 THF:EtOH solvent ratios. Each solution was manually shaken

for ~10 s, agitated using a vortex mixer for ~10 s, and heated to 70 °C for 3 h. The resulting length-disperse nanofibers were analyzed via TEM.

**General preparation of seed nanofibers**

Length disperse nanofibers (1 mg/mL – 10 mg/mL, 20:80 THF:EtOH) were sonicated for at least 3 h using a Fisherbrand 112xx series advanced ultrasonic cleaner (FB-11203) for 3 h at 10 °C in sweep mode at 37 MHz and 80% power. The resulting seed nanofibers were analyzed by TEM.

### 4.6.4 Cell culture assays

All cell work was performed in a biological safety cabinet (BSC) using sterile technique. All materials were autoclaved and disinfected with 70 % ethanol prior to being placed in the BSC. U87 MG human GBM cells (CRL-1573, ATCC) were cultured in Dulbecco's Modified Eagle Medium, high glucose (DMEM, Thermo Fisher), supplemented with 10% fetal bovine serum (FBS, Gibco) at 37 °C and 5% $CO_2$. Media changes were performed every two days. Cells were passaged at ~80% confluency using 0.25% Trypsin-EDTA (15400054, Thermo Fisher) diluted in PBS. Cell counting was performed using the dye exclusion method with Trypan blue on an automated cell counter (DeNovix CellDrop FL). Reseeding of cells was performed at a density of $1.5\times10^4$ cells/cm$^2$. Cryopreservation was performed at $1\times10^6$ cells/mL density in CryoStor® CS10 cell freezing medium (STEMCELL Technologies). Vials were first placed in a Freezing container (Nalgene) and stored at -80 °C overnight before being transferred to liquid nitrogen.

**2D cell culture**

Solutions of PTX-loaded nanofibers were made up at 10 – 40% w/w (PTX/nanofibers). U87 MG cells were seeded in a black-walled 96-well plate in culture medium containing 10% FBS at a density of 10,000 cells/well and left to adhere for 24 h. All media was then aspirated and replaced with 100 µl of sample or control solutions in FBS-free DMEM. Non-loaded nanofibers or PTX-loaded nanofibers were used at concentrations ranging from 0.1 – 25 µg/ml. Free PTX or albumin-NP bound PTX (Abraxane®, Celgene) were used as positive controls. After 24, 48, and 72 h, media were aspirated and replaced with 10% alamarBlue™ in DMEM. Plates were incubated for 2 h, after which fluorescence readings were taken directly from the plate using a microwell plate reader ($\lambda_{ex}$ = 560/9 nm; $\lambda_{em}$ = 590/20 nm). The absolute half maximal inhibitory concentration

($IC_{50}$) values were calculated for nanofibers and PTX content in the samples using GraphPad Prism 10 software by non-linear regression *via* fitting of a variable slope four-parameter function.

**3D cell culture**

Patient-derived GBM cells were generously provided by Dr. David Nathanson (UCLA, GS54). Single cells were expanded in suspension culture in DMEM/F12 media supplemented with 200 nM GlutaMAX™, 10 U/ml Penicillin/Streptomycin, B27 supplement w/o vitamin A (all Thermo Fisher) and 5 µg/ml heparin, 20 ng/ml FGFb and 20 ng/ml EGF (all Gibco). Cells were passaged every 7 days using 1x TrypLE (Life Technologies). Following passaging, single cells were seeded into 24-well AggreWell™ plates (STEMCELL Technologies), seeded at 900k cells/well, equivalent to 3000 cells/microwell, and a volume of 2 mL. Cells were distributed by gentle agitation, placed in an incubator at 37 °C, and left undisturbed for 72 h to induce spheroid formation. Exposure to PTX-loaded nanofibers, free PTX, or ABX was then performed by aspirating 1 mL from each well and gently adding 1 ml of sample solution at 2x concentration to achieve the desired final sample concentration. Samples analyzed 3 days after application.

**Live/Dead staining of spheroids**

GBM spheroids treated with nanofibers, PTX, or ABX were stained for live and dead cells using a 2 µM Calcein-AM and 3 µM Ethidium homodimer-1 (both Invitrogen) staining solution in PBS. 1 mL of cell culture medium was gently aspirated and replaced with the staining solution to achieve the final concentration.

**Cellcyte or Cytation 5 Imaging Procedure**

Brightfield and fluorescence images were taken either on a Cellcyte X™ or Biotek Cytation 5 multimode plate reader, 30 minutes post-addition of live/dead stain. The images were taken of the microwell plate directly, with the lid on. Imaging on the Cytation was performed at 4 x and 20 x magnification on a minimum of 12 separate spheroids at 4 x and 3 separate spheroids at 20 x. The green fluorescence protein filter ($\lambda_{ex}$ = 469/35 nm; $\lambda_{em}$ = 525/39 nm) was employed for measuring fluorescence intensity from calcein-AM, and the Texas Red fluorescence filter ($\lambda_{ex}$ = 586/15 nm, $\lambda_{em}$ = 647/57 nm) was utilized for measuring fluorescence from Ethidium Homodimer-1. All settings were kept constant between samples. Imaging on the Cellcyte was performed at 10 x magnification, and a minimum of 3 spheroids were imaged continuously over the course of 3 h.

Green fluorescence was measured at an excitation of 473/91 nm and emission of 502/61 nm, and red fluorescence was measured at an excitation of 580/98 nm and an emission of 612/80 nm. The first timepoint was selected for calculation of the corrected total fluorescence. All settings were kept constant between samples.

**Calculation of corrected total cell fluorescence (CTCF)**

Spheroid images were opened in FIJI software. The red and green fluorescence of 3 separate spheroids was measured, along with 3 separate areas of the background. To calculate the corrected total cell fluorescence, eq. S3 was utilized. From the integrated density (given by FIJI), the multiplication product of the cell area and the mean of the background readings was subtracted. The sum of the green and red fluorescence was calculated for each spheroid, and the percentage of each relative to the total fluorescence was computed. The standard deviation was then calculated for the three separate percentages, giving an average red:green ratio, which gave a value for percent alive, versus percent dead cells.

$$CTCF = Integrated\ density - (area\ of\ cell \times mean\ background\ fluorescence)$$

(eq. S3)

### 4.6.5 Supplementary Tables

**Table S4.1.** Summary of molar mass data for PFTMC$_{26}$-*b*-PDMAEMA$_{424}$ polymer.[58,63] Data is reproduced with permission from the Royal Society of Chemistry, and American Chemical Society.[63]

| Polymer | $M_n$ (g/mol) GPC | $M_w$ (g/mol) GPC | $Đ_M$ GPC | $DP_n$ NMR | $M_n$ (g/mol) NMR | $DP_n$ MALDI-TOF |
|---|---|---|---|---|---|---|
| PFTMC$_m$-*b*-PDMAEMA$_n$ | 87,900 | 102,100 | 1.16 | m = 26<br>n = 424 | 73,500 | m = 26 |

**Table S4.2.** Summary of self-assembly data for $PFTMC_{26}$-*b*-$PDMAEMA_{424}$ nanofibers.[58,63] Data is reproduced with permission from the Royal Society of Chemistry, and American Chemical Society.

| Morphology | Length in THF/EtOH (nm) via TEM | Length in Water (nm) via TEM | $L_w/L_n$ in water via TEM |
|---|---|---|---|
| **Nanofiber** | 25 ± 8 | 26 ± 6 | 1.05 |

**Table S4.3.** $IC_{50}$ values for nanofiber samples loaded with given amounts of PTX, over the course of 72 h, with measured relative PTX $IC_{50}$ values for each respective sample.

| | Nanofiber $IC_{50}$ [$\mu$g/mL] | | | PTX $IC_{50}$ [$\mu$M] | | |
|---|---|---|---|---|---|---|
| **Sample (wt % PTX)** | **24 h** | **48 h** | **72 h** | **24 h** | **48 h** | **72 h** |
| 40 | 2.92 | 2.10 | 0.78 | 1.37 | 0.98 | 0.37 |
| 60 | 2.69 | 1.06 | 0.86 | 1.89 | 0.74 | 0.60 |
| 80 | 2.96 | 1.85 | 0.76 | 2.77 | 1.73 | 0.71 |
| 100 | 3.86 | 2.06 | 0.60 | 4.52 | 2.41 | 0.70 |

**Table S4.4.** $IC_{50}$ values for all samples trialed, with their calculated standard deviation values included.

| | Nanofiber $IC_{50}$ [$\mu$g/mL] | | | PTX $IC_{50}$ [$\mu$M] | | |
|---|---|---|---|---|---|---|
| **Sample (wt % PTX)** | **24 h** | **48 h** | **72 h** | **24 h** | **48 h** | **72 h** |
| 0 | 9.52 ± 0.23 | 10.22 ± 0.25 | 11.37 ± 0.26 | - | - | - |
| 1 | 4.56 ± 0.21 | 4.12 ± 0.07 | 3.12 ± 0.06 | 0.05 ± 0.00 | 0.05 ± 0.00 | 0.04 ± 0.00 |
| 10 | 2.72 ± 0.18 | 1.72 ± 0.08 | 0.57 ± 0.02 | 0.32 ± 0.02 | 0.20 ± 0.01 | 0.07 ± 0.00 |
| 20 | 2.06 ± 0.28 | 1.13 ± 0.13 | 0.48 ± 0.02 | 0.48 ± 0.07 | 0.26 ± 0.03 | 0.11 ± 0.01 |
| 30 | 2.70 ± 0.08 | 2.05 ± 0.26 | 0.69 ± 0.13 | 0.95 ± 0.03 | 0.72 ± 0.09 | 0.24 ± 0.05 |
| 40 | 2.92 ± 0.11 | 2.10 ± 0.27 | 0.78 ± 0.14 | 1.37 ± 0.05 | 0.98 ± 0.12 | 0.37 ± 0.07 |
| 60 | 2.69 ± 0.39 | 1.06 ± 0.22 | 0.86 ± 0.04 | 1.89 ± 0.28 | 0.74 ± 0.15 | 0.60 ± 0.03 |
| 80 | 2.96 ± 0.12 | 1.85 ± 0.15 | 0.76 ± 0.09 | 2.77 ± 0.11 | 1.73 ± 0.14 | 0.71 ± 0.08 |
| 100 | 3.86 ± 0.21 | 2.06 ± 0.18 | 0.60 ± 0.18 | 4.52 ± 0.02 | 2.41 ± 0.02 | 0.70 ± 0.02 |
| Free PTX | - | - | - | 13.21 ± 5.27 | 0.26 ± 0.02 | 0.15 ± 0.07 |
| Abraxane | - | 1.78 ± 0.31 | 0.46 ± 0.03 | undefined | 0.23 ± 0.04 | 0.06 ± 0.00 |

### 4.6.6 Supplementary Figures

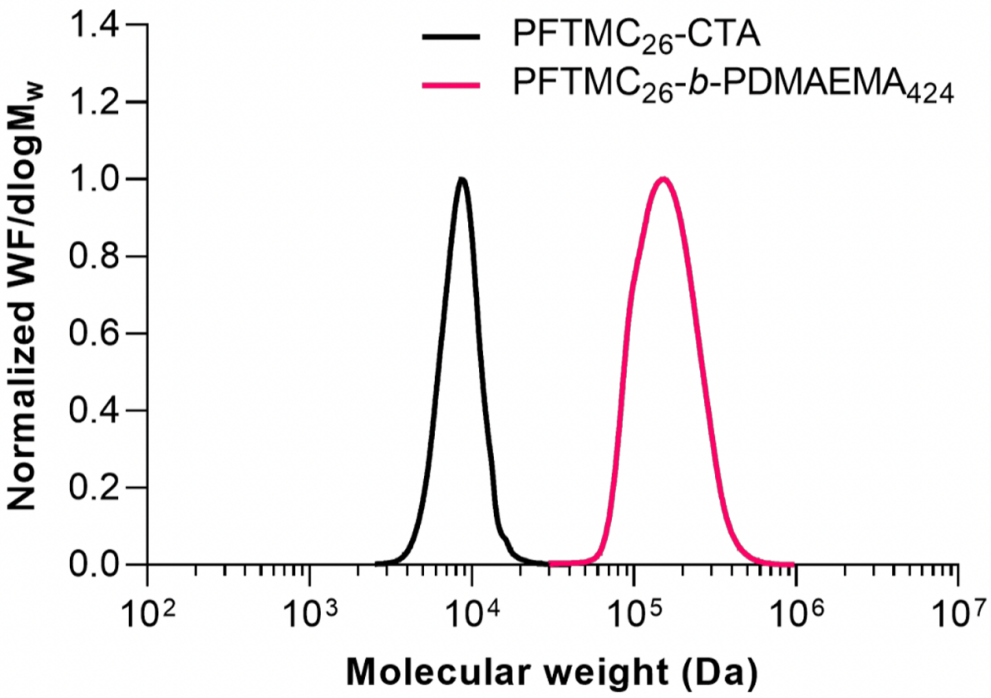


**Figure S4.1.** GPC chromatograms (refractive index detector) of $PFTMC_{26}$ homopolymer (black trace) and $PFTMC_{26}$-based block copolymer (pink trace), measured in n-$Bu_4NBr$/THF. Figure reproduced with permission from the Royal Society of Chemistry.[58]

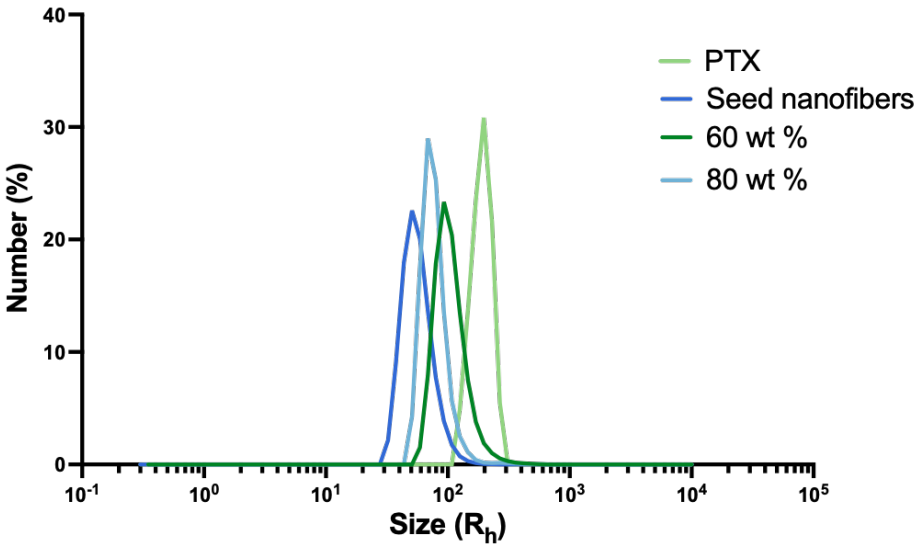


**Figure S4.2.** Average hydrodynamic radius by number (%) of drug-loaded seed nanofiber samples. At 60 and 80 wt % we observe deviations from the pure seed nanofiber size.

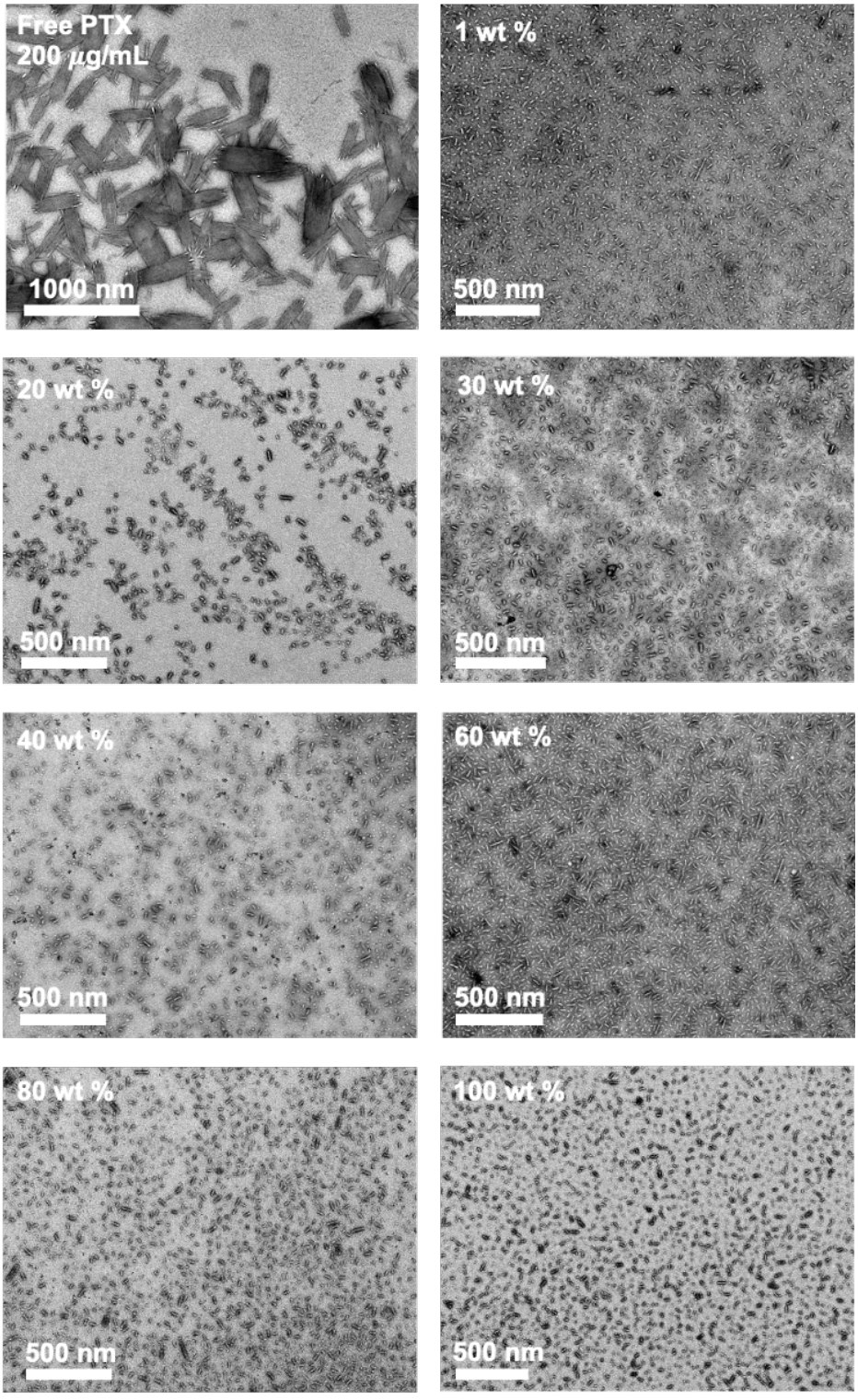


**Figure S4.3.** Representative TEM micrographs of free PTX (200 ug/mL) relative to loaded seed nanofiber samples from 1 wt % to 100 wt %. All samples are stained with 3 wt % uranyl acetate

in EtOH. Large crystalline aggregates of PTX are observed in the absence of seed nanofibers, which fail to reappear even at high loading percentages.

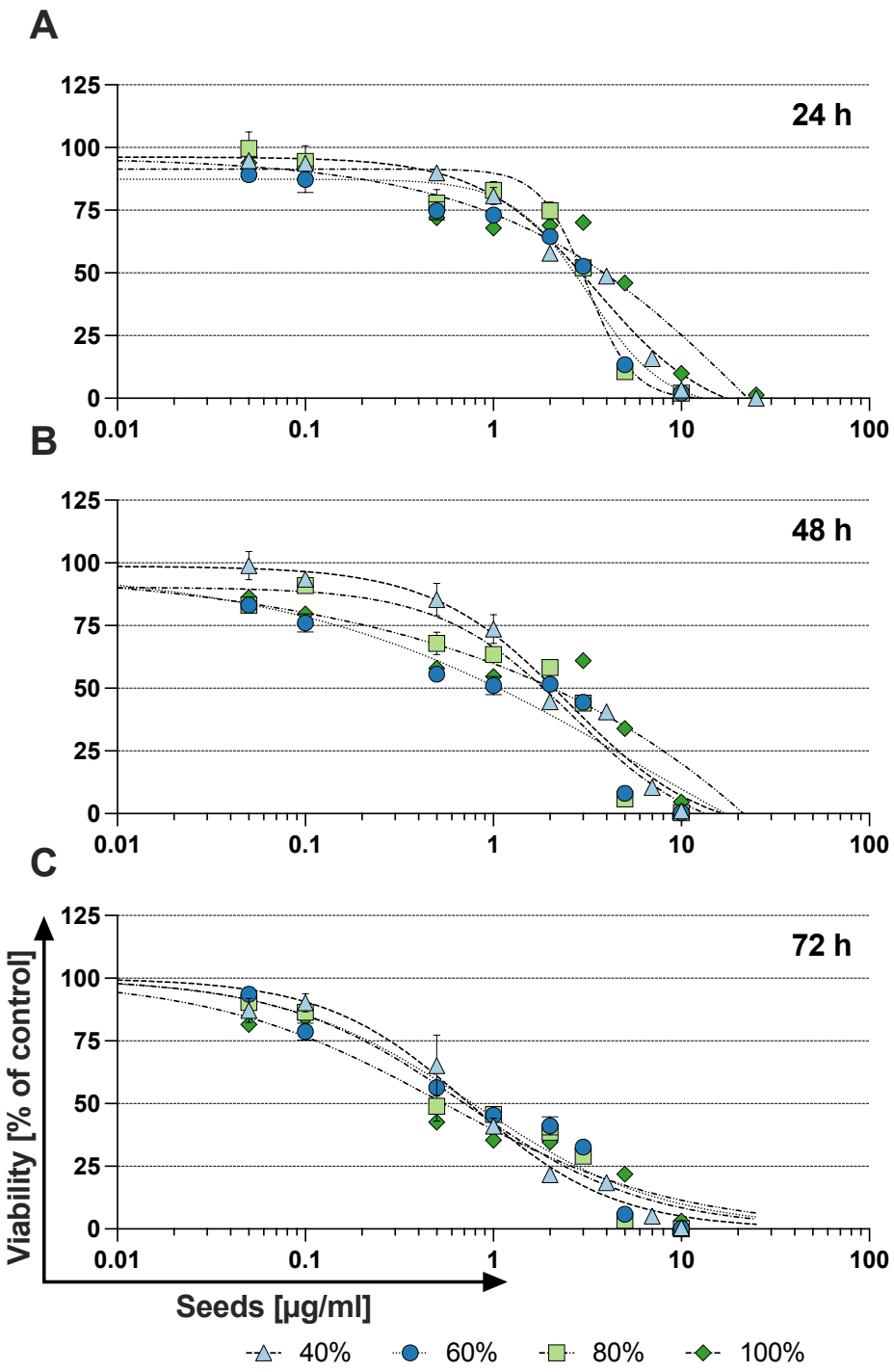


**Figure S4.4.** Cell viability curves utilized to calculate $IC_{50}$ values for seeds loaded with ≥ 40 wt % PTX over (A) 24 h, (B), 48 h, and (C) 72 h.

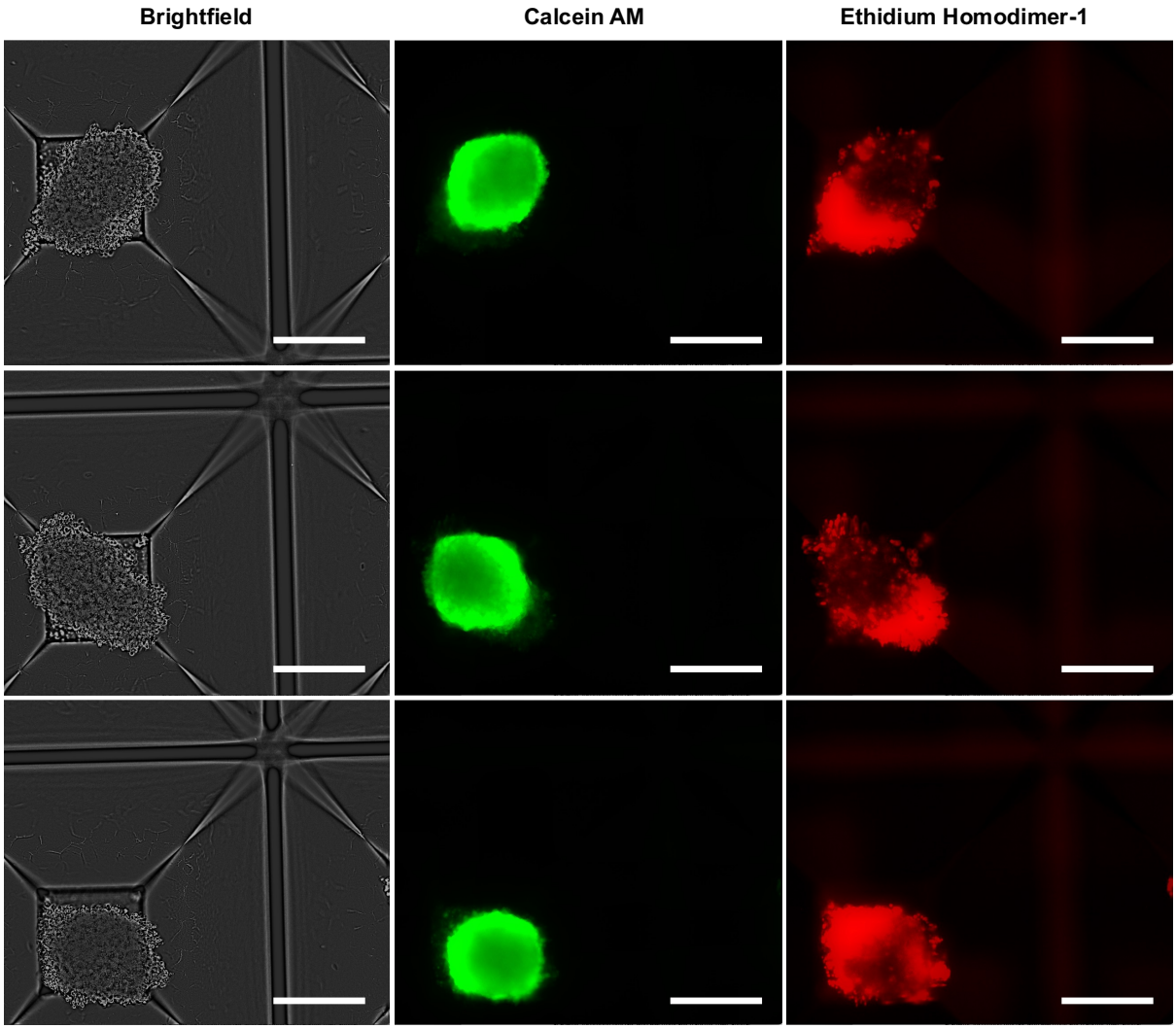


**Figure S4.5.** Three distinct GBM tumor spheroids with no treatment in DMEM/F12 cell culture media, stained with calcein-AM and ethidium homodimer-1. All scale bars represent 200 μm.

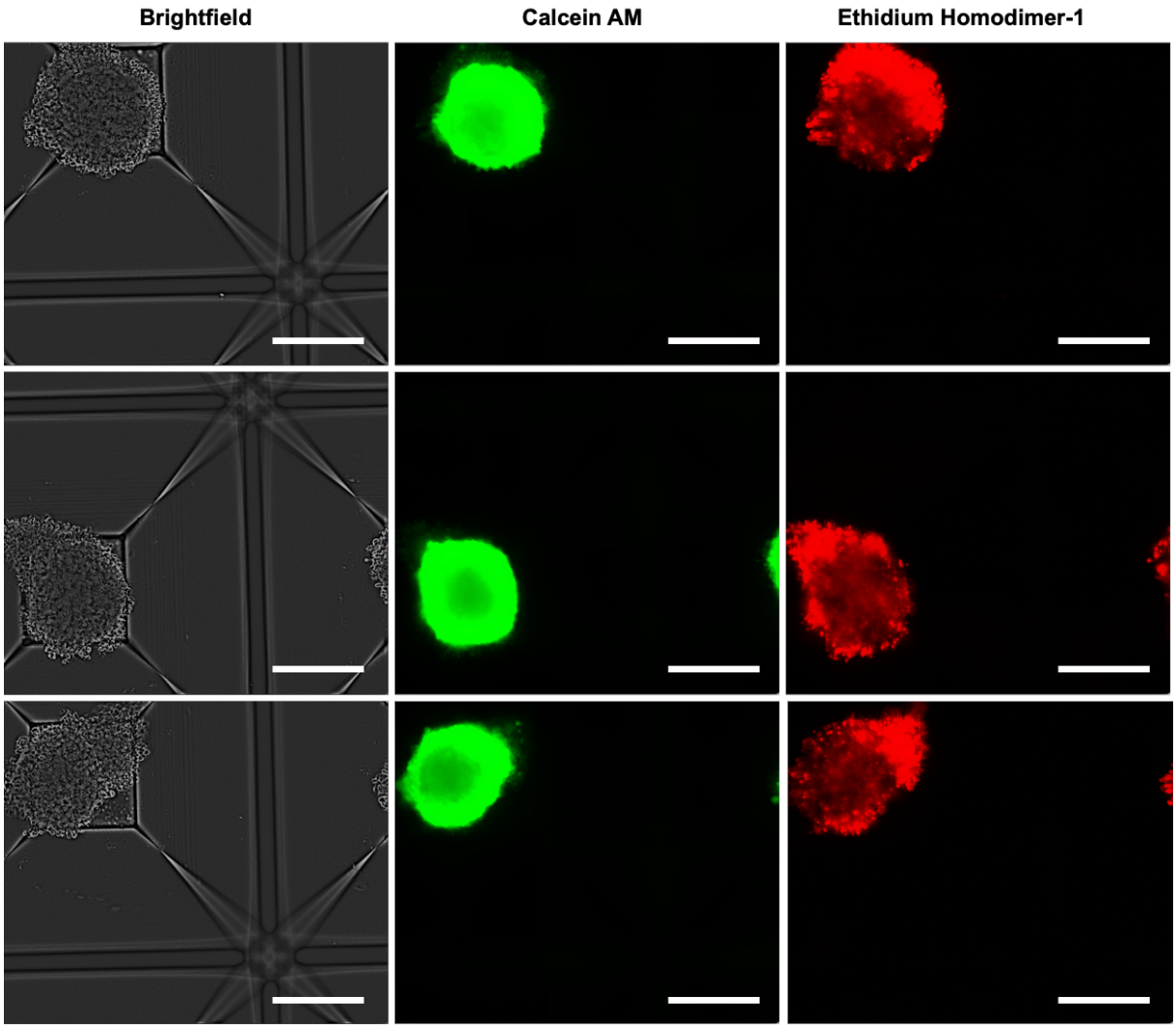


**Figure S4.6.** Tumor spheroids upon incubation with seed nanofibers (0 wt % PTX) and stained with calcein-AM and ethidium homodimer-1. All scale bars represent 200 µm

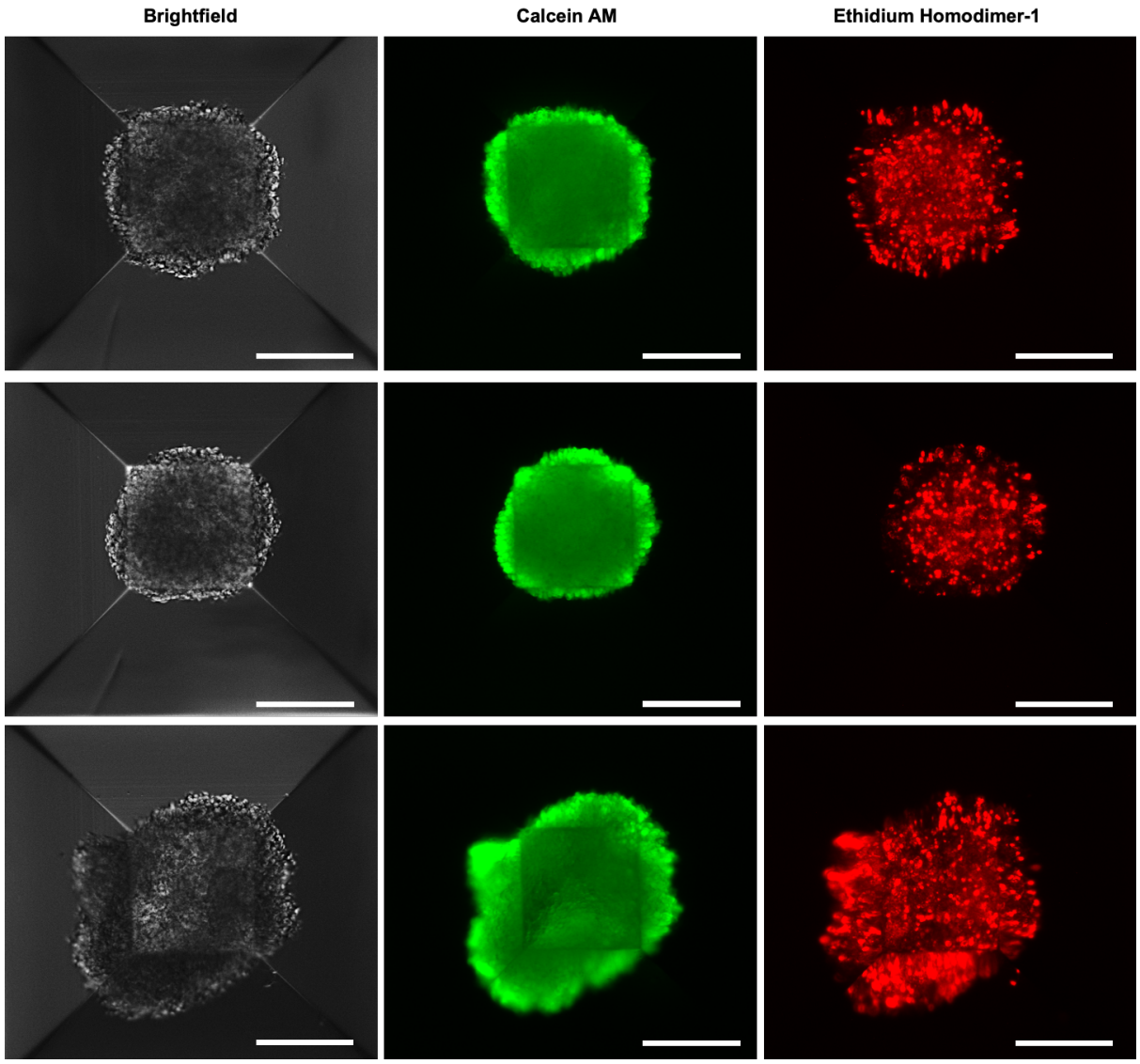


**Figure S4.7.** GBM tumor spheroids upon incubation with free PTX solubilized in $H_2O$/DMSO (5 %). Images were taken using a Cytation 5 plate reader at 4x magnification. Calcein-AM fluorescence was detected with a green fluorescence protein fluorescence filter, and ethidium homodimer-1 fluorescence was detected with a Texas Red fluorescence filter. All scale bars represent 200 $\mu$m.

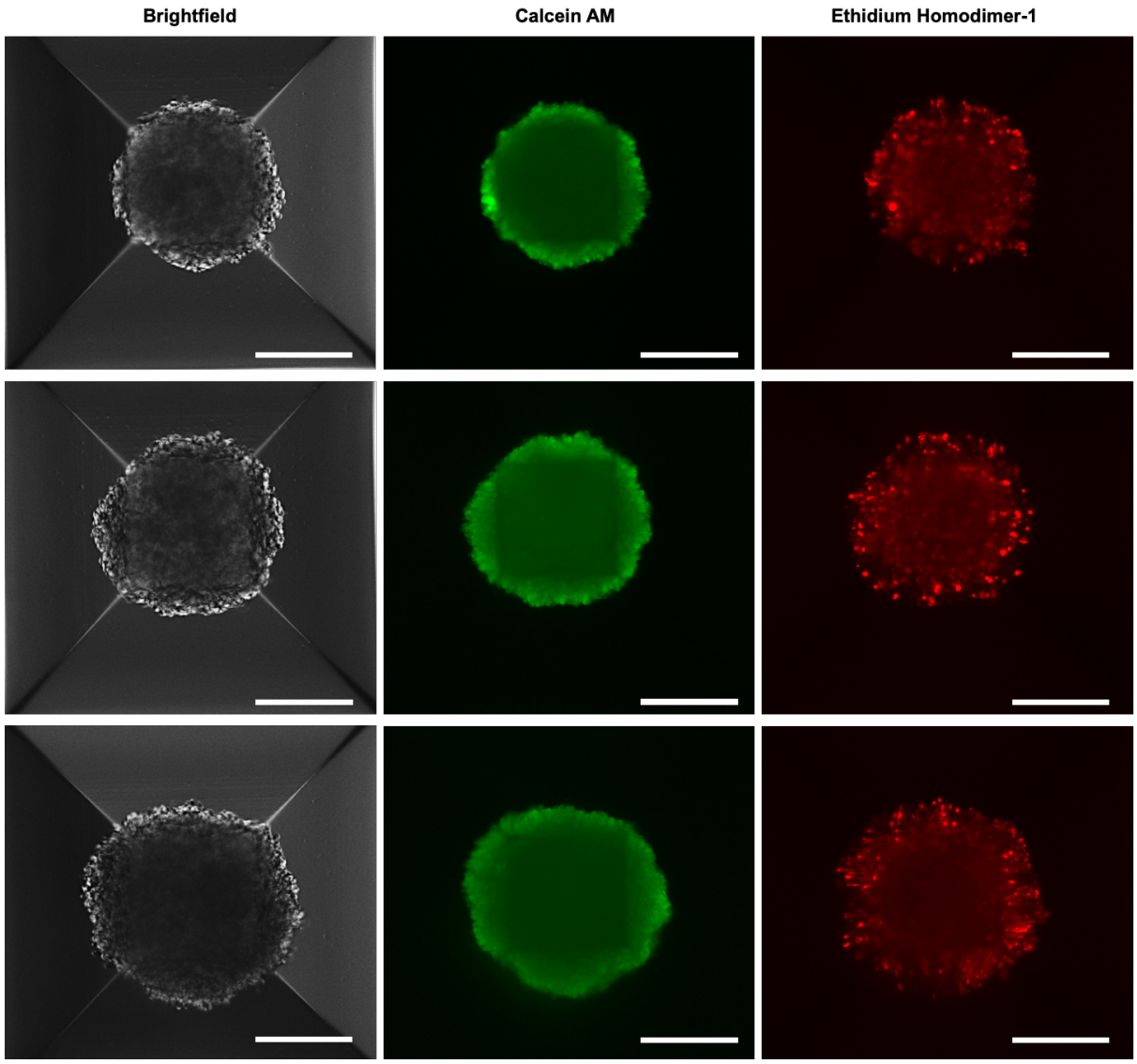


**Figure S4.8.** GBM tumor spheroids upon incubation with ABX. Images were taken using a Cytation 5 plate reader at 4x magnification. Calcein-AM fluorescence was detected with a green fluorescence protein fluorescence filter, and ethidium homodimer-1 fluorescence was detected with a Texas Red fluorescence filter. All scale bars represent 200 $\mu$m.

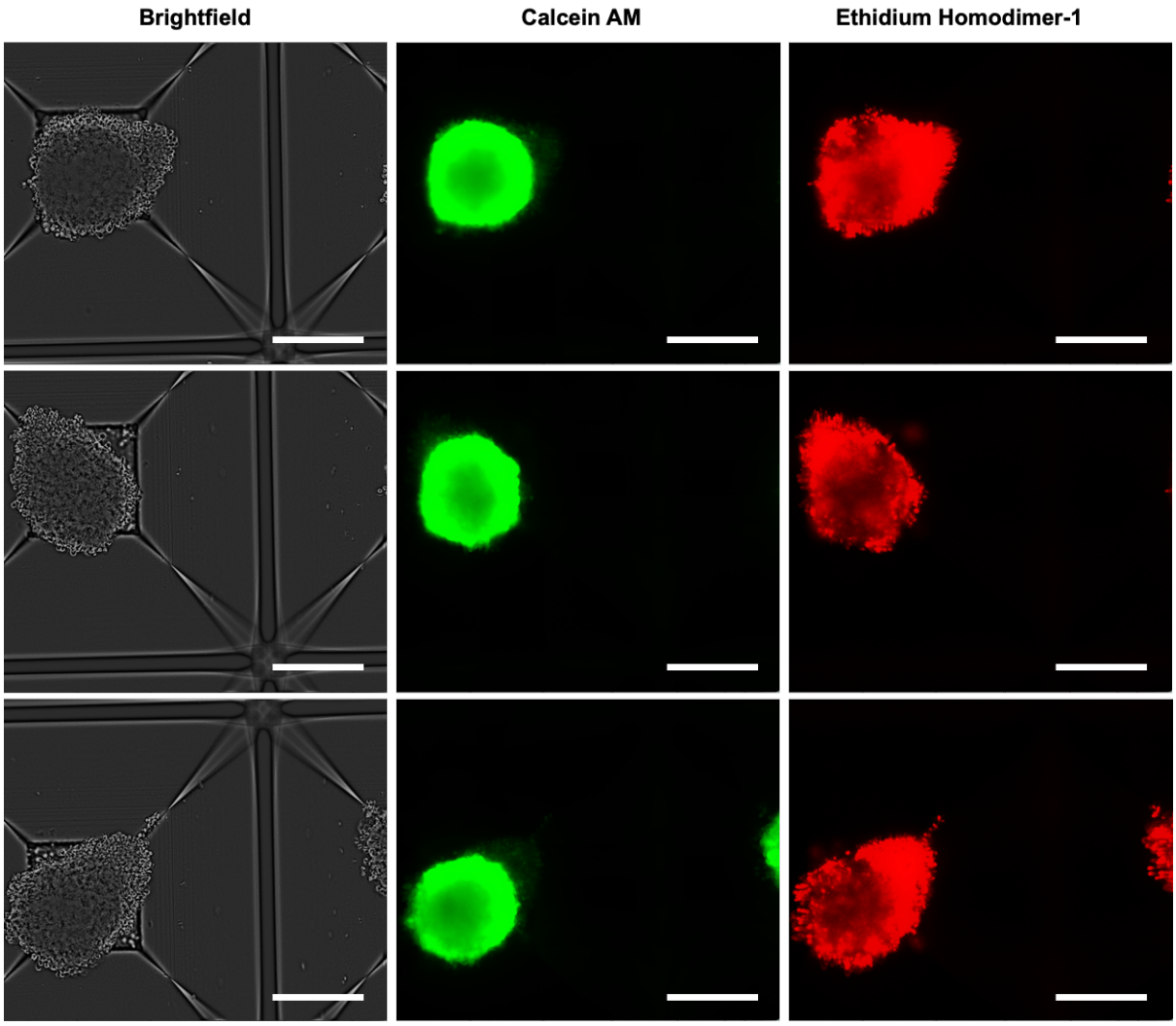


**Figure S4.9.** Tumor spheroids post-incubation with seed nanofibers loaded with 20 wt % PTX. Green fluorescence from calcein-AM measures live cells, and red fluorescence from ethidium homodimer-1 measures dead cells. All scale bars represent 200 μm.

## 4.7 References


1. Bray, F.; Ferlay, J.; Soerjomataram, I.; Siegel, R. L.; Torre, L. A.; Jemal, A. Global Cancer Statistics 2018: Globocan Estimates of Incidence and Mortality Worldwide for 36 Cancers in 185 Countries. *CA Cancer J. Clin.* **2018**, *68* (6), 394–424. DOI:10.3322/caac.21492.
2. Ames, B. N.; Gold, L. S.; Willett, W. C. The Causes and Prevention of Cancer. *Proc. Natl. Acad. Sci.* **1995**, *92* (12), 5258–5265. DOI:10.1073/pnas.92.12.5258.
3. de Martel, C.; Georges, D.; Bray, F.; Ferlay, J.; Clifford, G. M. Global Burden of Cancer Attributable to Infections in 2018: A Worldwide Incidence Analysis. *Lancet Glob. Health* **2020**, *8* (2), e180-e190. DOI:10.1016/s2214-109x(19)30488-7.
4. Zugazagoitia, J.; Guedes, C.; Ponce, S.; Ferrer, I.; Molina-Pinelo, S.; Paz-Ares, L. Current Challenges in Cancer Treatment. *Clin. Ther.* **2016**, *38* (7), 1551–1566. DOI:10.1016/j.clinthera.2016.03.026.
5. Kciuk, M.; Yahya, E. B.; Mohamed Ibrahim Mohamed, M.; Rashid, S.; Iqbal, M. O.; Kontek, R.; Abdulsamad, M. A.; Allaq, A. A. Recent Advances in Molecular Mechanisms of Cancer Immunotherapy. *Cancers* **2023**, *15* (10), 2721. DOI:10.3390/cancers15102721.
6. Kruger, S.; Ilmer, M.; Kobold, S.; Cadilha, B. L.; Endres, S.; Ormanns, S.; Schuebbe, G.; Renz, B. W.; D'Haese, J. G.; Schloesser, H.; Heinemann, V.; Subklewe, M.; Boeck, S.; Werner, J.; von Bergwelt-Baildon, M. Advances in Cancer Immunotherapy 2019 – Latest Trends. *J. Exp. Clin. Cancer Res.* **2019**, *38*, 268. DOI:10.1186/s13046-019-1266-0.
7. Chakraborty, S.; Rahman, T. The Difficulties in Cancer Treatment. *ecancer* **2012**, *6* (16), 1–5. DOI:10.3332/ecancer.2012.ed16.

8. Chen, Z.; Yue, Z.; Yang, K.; Shen, C.; Cheng, Z.; Zhou, X.; Li, S. Four Ounces Can Move a Thousand Pounds: The Enormous Value of Nanomaterials in Tumor Immunotherapy. *Adv. Healthc. Mater.* **2023**, *12* (26), 2300882. DOI:10.1002/adhm.202300882.
9. Verma, V.; Sprave, T.; Haque, W.; Simone, C. B.; Chang, J. Y.; Welsh, J. W.; Thomas, C. R. A Systematic Review of the Cost and Cost-Effectiveness Studies of Immune Checkpoint Inhibitors. *J. ImmunoTher. Cancer* **2018**, *6*, 128. DOI:10.1186/s40425-018-0442-7.
10. Lorscheider, M.; Gaudin, A.; Nakhlé, J.; Veiman, K.-L.; Richard, J.; Chassaing, C. Challenges and Opportunities in the Delivery of Cancer Therapeutics: Update on Recent Progress. *Ther. Deliv.* **2021**, *12*, 55–76. DOI:10.4155/tde-2020-0079.
11. Debela, D. T.; Muzazu, S. G.; Heraro, K. D.; Ndalama, M. T.; Mesele, B. W.; Haile, D. C.; Kitui, S. K.; Manyazewal, T. New Approaches and Procedures for Cancer Treatment: Current Perspectives. *SAGE Open Med.* **2021**, *9*, 205031212110343. DOI:10.1177/20503121211034366.
12. De Souza, R.; Zahedi, P.; Allen, C. J.; Piquette-Miller, M. Polymeric Drug Delivery Systems for Localized Cancer Chemotherapy. *Drug Deliv.* **2010**, *17* (6), 365–375. DOI:10.3109/10717541003762854.
13. Shewach, D. S.; Kuchta, R. D. Introduction to Cancer Chemotherapeutics. *Chem. Rev.* **2009**, *109* (7), 2859–2861. DOI:10.1021/cr900208x.
14. Sharifi-Rad, J.; Quispe, C.; Patra, J. K.; Singh, Y. D.; Panda, M. K.; Das, G.; Adetunji, C. O.; Michael, O. S.; Sytar, O.; Polito, L.; Živković, J.; Cruz-Martins, N.; Klimek-Szczykutowicz, M.; Ekiert, H.; Choudhary, M. I.; Ayatollahi, S. A.; Tynybekov, B.; Kobarfard, F.; Muntean, A. C.; Grozea, I.; Daştan, S. D.; Butnariu, M.; Szopa, A.; Calina, D. Paclitaxel: Application in

Modern Oncology and Nanomedicine-Based Cancer Therapy. *Oxid. Med. Cell. Longev.* **2021**, *2021*, 1–24. DOI:10.1155/2021/3687700.

15. Steichen, S. D.; Caldorera-Moore, M.; Peppas, N. A. A Review of Current Nanoparticle and Targeting Moieties for the Delivery of Cancer Therapeutics. *Eur. J. Pharm. Sci.* **2013**, *48* (3), 416–427. DOI:10.1016/j.ejps.2012.12.006.
16. Singla, A. K.; Garg, A.; Aggarwal, D. Paclitaxel and Its Formulations. *Int. J. Pharm.* **2002**, *235* (1–2), 179–192. DOI:10.1016/s0378-5173(01)00986-3.
17. Ma, P. Paclitaxel Nano-Delivery Systems: A Comprehensive Review. *J. Nanomed. Nanotechnol.* **2013**, *04* (02), 1000164. DOI:10.4172/2157-7439.1000164.
18. Bernabeu, E.; Cagel, M.; Lagomarsino, E.; Moretton, M.; Chiappetta, D. A. Paclitaxel: What Has Been Done and the Challenges Remain Ahead. *Int. J. Pharm.* **2017**, *526* (1–2), 474–495. DOI:10.1016/j.ijpharm.2017.05.016.
19. Dan, V. M.; Raveendran, R. S.; Baby, S. Resistance to Intervention: Paclitaxel in Breast Cancer. *Mini-Reviews Med. Chem.* **2021**, *21* (10), 1237–1268. DOI:10.2174/1389557520999201214234421.
20. Sgadari, C.; Toschi, E.; Palladino, C.; Barillari, G.; Carlei, D.; Cereseto, A.; Ciccolella, C.; Yarchoan, R.; Monini, P.; Stürzl, M.; Ensoli, B. Mechanism of Paclitaxel Activity in Kaposi's Sarcoma. *J. Immunol.* **2000**, *165*, 509–517. DOI:10.4049/jimmunol.165.1.509.
21. Xu, Y.; Jiang, Z.; Chen, X. Mechanisms Underlying Paclitaxel-Induced Neuropathic Pain: Channels, Inflammation and Immune Regulations. *Eur. J. Pharmacol.* **2022**, *933*, 175288. DOI:10.1016/j.ejphar.2022.175288.
22. Zhang, Z.; Mei, L.; Feng, S.-S. Paclitaxel Drug Delivery Systems. *Expert Opin. Drug Deliv.* **2013**, *10* (3), 325–340. DOI:10.1517/17425247.2013.752354.

23. Pillai, O.; Panchagnula, R. Polymers in Drug Delivery. *Curr. Opin. Chem. Biol.* **2001**, *5* (4), 447–451. DOI:10.1016/s1367-5931(00)00227-1.

24. Grund, S.; Bauer, M.; Fischer, D. Polymers in Drug Delivery—State of the Art and Future Trends. *Adv. Eng. Mater.* **2011**, *13* (3), B67-B87. DOI:10.1002/adem.201080088.

25. Wang, J.; Liu, W.; Tu, Q.; Wang, J.; Song, N.; Zhang, Y.; Nie, N.; Wang, J. Folate-Decorated Hybrid Polymeric Nanoparticles for Chemically and Physically Combined Paclitaxel Loading and Targeted Delivery. *Biomacromolecules* **2010**, *12*, 228–234. DOI:10.1021/bm101206g.

26. Sakhi, M.; Khan, A.; Iqbal, Z.; Khan, I.; Raza, A.; Ullah, A.; Nasir, F.; Khan, S. A. Design and Characterization of Paclitaxel-Loaded Polymeric Nanoparticles Decorated with Trastuzumab for the Effective Treatment of Breast Cancer. *Front. Pharmacol.* **2022**, *13*, 855294. DOI:10.3389/fphar.2022.855294.

27. Trickler, W. J.; Nagvekar, A. A.; Dash, A. K. A Novel Nanoparticle Formulation for Sustained Paclitaxel Delivery. *AAPS PharmSciTech* **2008**, *9* (2), 486–493. DOI:10.1208/s12249-008-9063-7.

28. Kawasaki, R.; Kawamura, S.; Hino, S.; Yamana, K.; Ikeda, A. Water Solubilization of Paclitaxel Using Polypeptides for Cancer Therapy. *Mater. Adv.* **2022**, *3*, 467–473. DOI:10.1039/d1ma00800e.

29. Xiao, K.; Luo, J.; Fowler, W. L.; Li, Y.; Lee, J. S.; Xing, L.; Cheng, R. H.; Wang, L.; Lam, K. S. A Self-Assembling Nanoparticle for Paclitaxel Delivery in Ovarian Cancer. *Biomaterials* **2009**, *30* (30), 6006–6016. DOI:10.1016/j.biomaterials.2009.07.015.

30. Malinovskaya, Y.; Melnikov, P.; Baklaushev, V.; Gabashvili, A.; Osipova, N.; Mantrov, S.; Ermolenko, Y.; Maksimenko, O.; Gorshkova, M.; Balabanyan, V.; Kreuter, J.; Gelperina, S.

Delivery of Doxorubicin-Loaded Plga Nanoparticles into U87 Human Glioblastoma Cells. *Int. J. Pharm.* **2017**, *524* (1–2), 77–90. DOI:10.1016/j.ijpharm.2017.03.049.

31. Blanco, E.; Shen, H.; Ferrari, M. Principles of Nanoparticle Design for Overcoming Biological Barriers to Drug Delivery. *Nat. Biotechnol.* **2015**, *33* (9), 941–951. DOI:10.1038/nbt.3330.
32. Petros, R. A.; DeSimone, J. M. Strategies in the Design of Nanoparticles for Therapeutic Applications. *Nat. Rev. Drug Discov.* **2010**, *9* (8), 615–627. DOI:10.1038/nrd2591.
33. Cai, S.; Vijayan, K.; Cheng, D.; Lima, E. M.; Discher, D. E. Micelles of Different Morphologies—Advantages of Worm-like Filomicelles of Peo-PCL in Paclitaxel Delivery. *Pharm. Res.* **2007**, *24* (11), 2099–2109. DOI:10.1007/s11095-007-9335-z.
34. Song, N.; Liu, W.; Tu, Q.; Liu, R.; Zhang, Y.; Wang, J. Preparation and in Vitro Properties of Redox-Responsive Polymeric Nanoparticles for Paclitaxel Delivery. *Colloids Surf. B: Biointerfaces* **2011**, *87* (2), 454–463. DOI:10.1016/j.colsurfb.2011.06.009.
35. Luo, J.; Xiao, K.; Li, Y.; Lee, J. S.; Shi, L.; Tan, Y.-H.; Xing, L.; Holland Cheng, R.; Liu, G.-Y.; Lam, K. S. Well-Defined, Size-Tunable, Multifunctional Micelles for Efficient Paclitaxel Delivery for Cancer Treatment. *Bioconjug. Chem.* **2010**, *21* (7), 1216–1224. DOI:10.1021/bc1000033.
36. Chan, W. C. W. Principles of Nanoparticle Delivery to Solid Tumors. *BME Front.* **2023**, *4*, 0016. DOI:10.34133/bmef.0016.
37. MacFarlane, L.; Zhao, C.; Cai, J.; Qiu, H.; Manners, I. Emerging Applications for Living Crystallization-Driven Self-Assembly. *Chem. Sci.* **2021**, *12* (13), 4661–4682. DOI:10.1039/d0sc06878k.

38. Wang, X.; Guerin, G.; Wang, H.; Wang, Y.; Manners, I.; Winnik, M. A. Cylindrical Block Copolymer Micelles and Co-Micelles of Controlled Length and Architecture. *Science* **2007**, *317* (5838), 644–647. DOI:10.1126/science.1141382.

39. Arno, M. C.; Inam, M.; Coe, Z.; Cambridge, G.; Macdougall, L. J.; Keogh, R.; Dove, A. P.; O'Reilly, R. K. Precision Epitaxy for Aqueous 1D and 2D Poly(ε-caprolactone) Assemblies. *J. Am. Chem. Soc.* **2017**, *139* (46), 16980–16985. DOI:10.1021/jacs.7b10199.

40. Ellis, C. E.; Fukui, T.; Cordoba, C.; Blackburn, A.; Manners, I. Towards Scalable, Low Dispersity, and Dimensionally Tunable 2D Platelets Using Living Crystallization-Driven Self-Assembly. *Polym. Chem.* **2021**, *12* (25), 3650–3660. DOI:10.1039/d1py00571e.

41. Inam, M.; Cambridge, G.; Pitto-Barry, A.; Laker, Z. P.; Wilson, N. R.; Mathers, R. T.; Dove, A. P.; O'Reilly, R. K. 1D vs. 2D Shape Selectivity in the Crystallization-Driven Self-Assembly of Polylactide Block Copolymers. *Chem. Sci.* **2017**, *8* (6), 4223–4230. DOI:10.1039/c7sc00641a.

42. Gilroy, J. B.; Gädt, T.; Whittell, G. R.; Chabanne, L.; Mitchels, J. M.; Richardson, R. M.; Winnik, M. A.; Manners, I. Monodisperse Cylindrical Micelles by Crystallization-Driven Living Self-Assembly. *Nat. Chem.* **2010**, *2*, 566–570. DOI: 10.1038/nchem.664

43. Cao, L.; Manners, I.; Winnik, M. A. Influence of the Interplay of Crystallization and Chain Stretching on Micellar Morphologies: Solution Self-Assembly of Coil−crystalline Poly(Isoprene-*Block*-Ferrocenylsilane). *Macromolecules* **2002**, *35* (22), 8258–8260. DOI:10.1021/ma021068x.

44. Finnegan, J. R.; He, X.; Street, S. T.; Garcia-Hernandez, J. D.; Hayward, D. W.; Harniman, R. L.; Richardson, R. M.; Whittell, G. R.; Manners, I. Extending the Scope of "Living" Crystallization-Driven Self-Assembly: Well-Defined 1D Micelles and Block Comicelles from

Crystallizable Polycarbonate Block Copolymers. *J. Am. Chem. Soc.* **2018**, *140* (49), 17127–17140. DOI:10.1021/jacs.8b09861.

45. Ganda, S.; Stenzel, M. H. Concepts, Fabrication Methods and Applications of Living Crystallization-Driven Self-Assembly of Block Copolymers. *Prog. Polym. Sci.* **2020**, *101*, 101195. DOI:10.1016/j.progpolymsci.2019.101195
46. Guérin, G.; Wang, H.; Manners, I.; Winnik, M. A. Fragmentation of Fiberlike Structures: Sonication Studies of Cylindrical Block Copolymer Micelles and Behavioral Comparisons to Biological Fibrils. *J. Am. Chem. Soc.* **2008**, *130* (44), 14763–14771. DOI:10.1021/ja805262v.
47. Tritschler, U.; Pearce, S.; Gwyther, J.; Whittell, G. R.; Manners, I. *50th Anniversary Perspective*: Functional Nanoparticles from the Solution Self-Assembly of Block Copolymers. *Macromolecules* **2017**, *50* (9), 3439–3463. DOI:10.1021/acs.macromol.6b02767.
48. Street, S. T. G.; He, Y.; Jin, X.-H.; Hodgson, L.; Verkade, P.; Manners, I. Cellular Uptake and Targeting of Low Dispersity, Dual Emissive, Segmented Block Copolymer Nanofibers. *Chem. Sci.* **2020**, *11* (32), 8394–8408. DOI:10.1039/d0sc02593c.
49. Street, S. T. G.; Chrenek, J.; Harniman, R. L.; Letwin, K.; Mantell, J. M.; Borucu, U.; Willerth, S. M.; Manners, I. Length-Controlled Nanofiber Micelleplexes as Efficient Nucleic Acid Delivery Vehicles. *J. Am. Chem. Soc.* **2022**, *144* (43), 19799–19812. DOI:10.1021/jacs.2c06695.
50. Jin, X.; Price, M. B.; Finnegan, J. R.; Boott, C. E.; Richter, J. M.; Rao, A.; Menke, S. M.; Friend, R. H.; Whittell, G. R.; Manners, I. Long-Range Exciton Transport in Conjugated Polymer Nanofibers Prepared by Seeded Growth. *Science* **2018**, *360* (6391), 897–900. DOI:10.1126/science.aar8104.

51. Tian, J.; Zhang, Y.; Du, L.; He, Y.; Jin, X.-H.; Pearce, S.; Eloi, J.-C.; Harniman, R. L.; Alibhai, D.; Ye, R.; Phillips, D. L.; Manners, I. Tailored Self-Assembled Photocatalytic Nanofibres for Visible-Light-Driven Hydrogen Production. *Nat. Chem.* **2020**, *12* (12), 1150–1156. DOI:10.1038/s41557-020-00580-3.

52. Lei, S.; Tian, J.; Kang, Y.; Zhang, Y.; Manners, I. AIE-Active, Stimuli-Responsive Fluorescent 2D Block Copolymer Nanoplatelets Based on Corona Chain Compression. *J. Am. Chem. Soc.* **2022**, *144* (38), 17630–17641. DOI:10.1021/jacs.2c07133.

53. Cai, J.; Li, C.; Kong, N.; Lu, Y.; Lin, G.; Wang, X.; Yao, Y.; Manners, I.; Qiu, H. Tailored Multifunctional Micellar Brushes via Crystallization-Driven Growth from a Surface. *Science* **2019**, *366* (6469), 1095–1098. DOI:10.1126/science.aax9075.

54. Finnegan, J. R.; Pilkington, E. H.; Alt, K.; Rahim, Md. A.; Kent, S. J.; Davis, T. P.; Kempe, K. Stealth Nanorods via the Aqueous Living Crystallisation-Driven Self-Assembly of Poly(2-oxazoline)s. *Chem. Sci.* **2021**, *12* (21), 7350–7360. DOI: 10.1039/D1SC00938A

55. Ma, J.; Lu, G.; Huang, X.; Feng, C. π-Conjugated-Polymer-Based Nanofibers through Living Crystallization-Driven Self-Assembly: Preparation, Properties and Applications. *Chem. Commun.* **2021**, *57* (98), 13259–13274. DOI:10.1039/D1CC04825B

56. Parkin, H. C.; Garcia-Hernandez, J. D.; Street, S. T. G.; Hof, R.; Manners, I. Uniform, Length-Tunable Antibacterial 1D Diblock Copolymer Nanofibers. *Polym. Chem.* **2022**, *13* (20), 2941–2949. DOI:10.1039/d2py00262k.

57. Street, S. T. G.; He, Y.; Harniman, R. L.; Garcia-Hernandez, J. D.; Manners, I. Precision Polymer Nanofibers with a Responsive Polyelectrolyte Corona Designed as a Modular, Functionalizable Nanomedicine Platform. *Polym. Chem.* **2022**, *13* (20), 3009–3025. DOI:10.1039/d2py00152g.

58. Street, S. T. G.; Parkin, H. C.; Shopperly, L.; Chrenek, J.; Letwin, K.; Willerth, S. M.; Manners, I. Optimization of Precision Nanofiber Micelleplexes for DNA Delivery. *Biomater. Sci.* **2023**, *11* (10), 3512–3523. DOI:10.1039/d2bm02014a.

59. Yu, Q.; Roberts, M. G.; Houdaihed, L.; Liu, Y.; Ho, K.; Walker, G.; Allen, C.; Reilly, R. M.; Manners, I.; Winnik, M. A. Investigating the Influence of Block Copolymer Micelle Length on Cellular Uptake and Penetration in a Multicellular Tumor Spheroid Model. *Nanoscale* **2021**, *13*, 280–291. DOI:10.1039/d0nr08076d.

60. Ganda, S.; Wong, C. K.; Stenzel, M. H. Corona-Loading Strategies for Crystalline Particles Made by Living Crystallization-Driven Self-Assembly. *Macromolecules* **2021**, *54* (14), 6662–6669. DOI:10.1021/acs.macromol.1c00643.

61. Garcia-Hernandez, J. D.; Parkin, H. C.; Ren, Y.; Zhang, Y.; Manners, I. Hydrophobic Cargo Loading at the Core–Corona Interface of Uniform, Length-Tunable Aqueous Diblock Copolymer Nanofibers with a Crystalline Polycarbonate Core. *Polym. Chem.* **2022**, *13* (28), 4100–4110. DOI:10.1039/d2py00395c.

62. Garcia-Hernandez, J. D.; Street, S. T.; Kang, Y.; Zhang, Y.; Manners, I. Cargo Encapsulation in Uniform, Length-Tunable Aqueous Nanofibers with a Coaxial Crystalline and Amorphous Core. *Macromolecules* **2021**, *54* (12), 5784–5796. DOI:10.1021/acs.macromol.1c00672.

63. Parkin, H. C.; Street, S. T. G.; Gowen, B.; Da-Silva-Correa, L. H.; Hof, R.; Buckley, H. L.; Manners, I. Mechanism of Action and Design of Potent Antibacterial Block Copolymer Nanoparticles. *J. Am. Chem. Soc.* **2024**, *146* (8), 5128–5141. DOI:doi.org/10.1021/JACS.3C09033.

64. Lv, S.; Wu, Y.; Cai, K.; He, H.; Li, Y.; Lan, M.; Chen, X.; Cheng, J.; Yin, L. High Drug Loading and Sub-Quantitative Loading Efficiency of Polymeric Micelles Driven by Donor–

Receptor Coordination Interactions. *J. Am. Chem. Soc.* **2018**, *140* (4), 1235–1238. DOI:10.1021/jacs.7b12776.

65. Najlah, M.; Kadam, A.; Wan, K.; Ahmed, W.; Taylor, K. M. G.; Elhissi, A. M. A. Novel Paclitaxel Formulations Solubilized by Parenteral Nutrition Nanoemulsions for Application against Glioma Cell Lines. *Int. J. Pharm.* **2016**, *506* (1–2), 102–109. DOI:10.1016/j.ijpharm.2016.04.027.
66. Bonomi, A.; Lisini, D.; Navone, S. E.; Frigerio, S.; Dossena, M.; Ciusani, E.; Rampini, P.; Marfia, G.; Coccè, V.; Cavicchini, L.; Sisto, F.; Parati, E.; Mantegazza, R.; Rimoldi, M.; Rizzetto, M.; Alessandri, G.; Pessina, A. Human CD14+ Cells Loaded with Paclitaxel Inhibit in Vitro Cell Proliferation of Glioblastoma. *Cytotherapy* **2015**, *17* (3), 310–319. DOI:10.1016/j.jcyt.2014.09.009.
67. Smits, I. P. M.; Blaschuk, O. W.; Willerth, S. M. Novel N-Cadherin Antagonist Causes Glioblastoma Cell Death in a 3D Bioprinted Co-Culture Model. *Biochem. Biophys. Res. Commun.* **2020**, *529* (2), 162–168. DOI:10.1016/j.bbrc.2020.06.001.
68. Bruns, J.; Egan, T.; Mercier, P.; Zustiak, S. P. Glioblastoma Spheroid Growth and Chemotherapeutic Responses in Single and Dual-Stiffness Hydrogels. *Acta Biomater.* **2023**, *163*, 400–414. DOI:10.1016/j.actbio.2022.05.048.
69. Pevná, V.; Huntošová, V. Imaging of Heterogeneity in 3D Spheroids of U87MG Glioblastoma Cells and Its Implications for Photodynamic Therapy. *Photodiagnosis Photodyn. Ther.* **2023**, *44*, 103821. DOI:10.1016/j.pdpdt.2023.103821.
70. Yang, J.; Wang, X.; Wang, B.; Park, K.; Wooley, K.; Zhang, S. Challenging the Fundamental Conjectures in Nanoparticle Drug Delivery for Chemotherapy Treatment of Solid Cancers. *Adv. Drug Deliv. Rev.* **2022**, *190*, 114525. DOI:10.1016/j.addr.2022.114525.

71. Joyceline, P.; Sushruta S., H.; Bharath Raja, G. Synergistic Effect of Paclitaxel and Curcumin in Nano-Formulations on U87 and A549 Cancer Cell Lines. *J. Appl. Pharm. Sci.* **2022**, *12*, 031-047. DOI:10.7324/japs.2021.120204.

72. He, Z.; Schulz, A.; Wan, X.; Seitz, J.; Bludau, H.; Alakhova, D. Y.; Darr, D. B.; Perou, C. M.; Jordan, R.; Ojima, I.; Kabanov, A. V.; Luxenhofer, R. Poly(2-Oxazoline) Based Micelles with High Capacity for 3rd Generation Taxoids: Preparation, in Vitro and in Vivo Evaluation. *J. Control. Release* **2015**, *208*, 67–75. DOI:10.1016/j.jconrel.2015.02.024.

73. Hassanin, I. A.; Elzoghby, A. O. Self-Assembled Non-Covalent Protein-Drug Nanoparticles: An Emerging Delivery Platform for Anti-Cancer Drugs. *Expert Opin. Drug Deliv.* **2020**, *17* (10), 1437–1458. DOI:10.1080/17425247.2020.1813713.

74. Xiao, W.; Wang, S.; Zhang, R.; Sohrabi, A.; Yu, Q.; Liu, S.; Ehsanipour, A.; Liang, J.; Bierman, R. D.; Nathanson, D. A.; Seidlits, S. K. Bioengineered Scaffolds for 3D Culture Demonstrate Extracellular Matrix-Mediated Mechanisms of Chemotherapy Resistance in Glioblastoma. *Matrix Biol*. **2020**, *85–86*, 128–146. DOI: 10.1016/j.matbio.2019.04.003

75. Mai, W. X.; Gosa, L.; Daniels, V. W.; Ta, L.; Tsang, J. E.; Higgins, B.; Gilmore, W. B.; Bayley, N. A.; Harati, M. D.; Lee, J. T.; Yong, W. H.; Kornblum, H. I.; Bensinger, S. J.; Mischel, P. S.; Rao, P. N.; Clark, P. M.; Cloughesy, T. F.; Letai, A.; Nathanson, D. A. Cytoplasmic p53 Couples Oncogene-Driven Glucose Metabolism to Apoptosis and as a Therapeutic Target in Glioblastoma. *Nat. Med*. **2017**, *23*, 1342–1351. DOI: 10.1038/nm.4418

76. Garcia, G.; Chakravarty, N.; Paiola, S.; Urena, E.; Gyani, P.; Tse, C.; French, S. W.; Danielpour, M.; Breunig, J. J.; Nathanson, D. A.; Arumugaswami, V. Differential Susceptibility of Ex Vivo Primary Glioblastoma Tumors to Oncolytic Effect of Modified Zika Virus. *Cells* **2023**, *12* (19), 2384. DOI: 10.3390/cells12192384

77. Safarians, G.; Sohrabi, A.; Solomon, I.; Xiao, W.; Bastola, S.; Rajput, B. W.; Epperson, M.; Rosenzweig, I.; Tamura, K.; Singer, B.; Huang, J.; Harrison, M. J.; Sanazzaro, T.; Condro, M. C.; Kornblum, H. I.; Seidlits, S. K. Glioblastoma Spheroid Invasion through Soft, Brain-Like Matrices Depends on Hyaluronic Acid–CD44 Interactions. *Adv. Healthc. Mater.* **2023**, *12* (14), 2203143. DOI:10.1002/adhm.202203143

78. Gao, Y.; Nai, J.; Yang, Z.; Zhang, J.; Ma, S.; Zhao, Y.; Li, H.; Li, J.; Yang, Y.; Yang, M.; Wang, Y.; Gong, W.; Yu, F.; Gao, C.; Li, Z.; Mei, X. A Novel Preparative Method for Nanoparticle Albumin-Bound Paclitaxel with High Drug Loading and its Evaluation both *in vitro* and *in vivo*. *PLOS ONE* **2021**, *16* (4), e0250670. DOI:10.1371/journal.pone.0250670

# Chapter 5

## Extending the Scope of Antibacterial Activity of One-dimensional Crystalline-core Nanofibers for Overcoming Antibacterial Resistance

*This chapter contains as of yet unpublished results.*

*Contributions:*

*Hayley Parkin conceived the project and carried out the experiments. Dr. Juan Diego Garcia-Hernandez provided the PFTMC-b-PEG and PFTMC-b-PNIPAM unimer solutions. Hayley Parkin wrote and edited the manuscript.*

## 5.1 Abstract

The need for new antibacterial materials with general mechanisms of action is increasing year over year, as antibiotic resistance continues to rise. Self-assembled polymer nanoparticles have recently been demonstrated as promising alternatives to antibiotics due to possessing both intrinsic antibacterial activity, as well as strong capabilities as drug-delivery vehicles. In this work, we explore 1-dimensional nanofibers prepared via living crystallization-driven self-assembly, derived from the block copolymer poly(fluorenetrimethylenecarbonate)-block-poly(dimethylaminomethacrylate), as antibacterial agents and a drug-delivery system against *Staphylococcus epidermidis* 12228. The demonstrated antibacterial activity is high, with minimum inhibitory concentrations obtained between 13 - 6 μg/mL. Upon loading with 20wt% erythromycin, the MIC decreased from 13 μg/mL to 3 μg/mL. Furthermore, we investigate the growth inhibition of *Burkholderia vietnamiensis* BAA-248, a bacterial strain which possesses resistance against cationic antimicrobial peptides, upon incubation with nanofibers containing both cationic and neutral coronal blocks. We demonstrate that those containing cationic coronas are more effective at inhibiting bacterial growth, and that a synergy occurs upon co-incubation with the antimicrobial peptide polymyxin B. This study demonstrates that block copolymer nanofibers containing a crystalline core-forming block and a cationic corona-forming block possess antibacterial activity against multiple strains of bacteria, and have the potential to be potent against gram positive bacteria. Furthermore, the results demonstrate that nanofibers are promising treatments for permeabilizing the bacterial membrane, allowing the entry of additional therapeutics into the bacterium, and an enhanced effect to be obtained.

## 5.2 Introduction

Infectious diseases caused by pathogenic strains of bacteria are a major cause of death worldwide. Soon after the discovery of penicillin in 1928, it was noted that certain organisms were able to survive despite living in high concentrations of the therapeutic.[1,2] This phenomenon is now recognized as antibiotic resistance. It has since been discovered that many bacteria contain inherent resistance to many common antibacterial treatments due to constitutive exposure to the compounds in their natural habitat.[3–5] Furthermore, the genes that grant the resistance of one bacterium to an antibacterial mechanism of action can be transferred to other organisms through horizontal gene transfer.[6] Finally, due to the high replication rate of many bacterial strains, opportunistic mutations that grant resistance quickly take hold in the genome of the bacteria, allowing favourable survival of resistant organisms, otherwise known as natural selection.[7,8] Treatments with more general mechanisms of action that target an unmodifiable feature of bacteria are thus highly desirable, as resistance should be much more difficult to acquire.

Antimicrobial peptides (AMPs) fill this need. AMPs are naturally produced by microorganisms for their own protection and can be isolated and employed as novel antibacterial treatments.[9,10] More potent AMPs have also been synthesized through careful modification of the active-site residues.[11–13] Importantly, AMPs commonly show synergy (activity higher than the sum of the individual components) with more specific antibiotics, and this is largely due to their mechanism of action.[9,14] Pioneering work in the field has demonstrated several mechanisms of action of AMPs exist, but most commonly cationic residues within the AMP allow for general targeting of the anionic bacterial cell membrane.[15–17] Upon successful adherence to the membrane, hydrophobic residues then insert themselves into the membrane, causing physical disruption of the membrane

integrity. This process is known as self-promoted uptake.[18–20] Other mechanisms of action include the "carpet model" and the "aggregate channel model".[15] Overall, AMPs represent a major step-forward in the discovery of a new-generation of treatments for fighting significant bacterial infections that cannot be targeted with small-molecule antibiotics. However, issues in their employment still remain. As they are naturally produced by microorganisms, they can also be naturally degraded by proteases found in mammalian cells.[21,22] These enzymes will cleave the peptide backbone, degrading the AMP to a state where it is no longer functional. Additionally, the production of new AMPs is costly, as the synthesis and modification of sequence defined peptides is laborious and challenging. Therefore, the development of materials that possess a similar broad-spectrum mechanism of action to that of AMPs but avoid deleterious enzymatic degradation is of utmost importance.[4] Additionally, if these treatments can showcase a synergy with small-molecule antibiotics or AMPs that allows for increased potency in a reduced concentration of therapeutic, the multi-mode mechanisms of action should be exceptionally difficult for bacteria to overcome.[4]

Several organisms have been discovered that are not susceptible to the action of AMPs, especially when they contain more neutral and more rigid membranes.[23–28] One major class of resistant organisms is a group known as the *Burkholderia cepacia complex*. Normally, these organisms are found in the soil where they are constitutively exposed to small amounts of AMPs excreted by surrounding bacteria and fungi.[26] These bacteria, known for causing opportunistic infections in patients with cystic fibrosis, possess incredibly rigid and more neutral membranes which hinders targeting by cationic AMPs.[58–61] Additionally, their over expression of efflux pumps results in efficient transport of antibiotics out of the cell. Together, these characteristics result in incredible challenges in treatment. For example, their growth has been observed using penicillin as the sole

carbon source. Furthermore, these bacteria are able to survive in solutions of pure chlorohexidine, a commonly employed disinfectant. Thus, identification of materials which can overcome these barriers is also of great interest, as these would be truly beneficial for overcoming even the severest forms of antibiotic resistance.

Polymer nanomaterials are garnering intense attention as novel antibacterial treatments for these reasons. Commonly, polymer materials are synthesized to contain quaternized or partially protonated pendant amines which are hypothesized to target the anionic bacterial membrane, similarly to AMPs.[29–40] These targeting groups are easily installed along the polymer backbone and allow for general targeting of several strains of bacteria. Recently, the benefits of employing self-assembled block copolymer (BCP) nanoparticles for antibacterial activity have been elucidated. In particular, it has been identified that anisotropic nanoparticles possess higher inherent antibacterial activity than isotropic nanospheres.[39–43] These nanoparticle morphologies are traditionally more difficult to access through self-assembly, but a process known as living crystallization-driven self-assembly (CDSA) helps overcome this challenge. The distinguishing feature of this process is the use of a crystallizable solvophobic core-forming block in the BCP.[44,45] Upon the introduction of a solvent selective for the solvophilic corona-forming block, random crystallization of the core-forming block occurs, generating disperse yet morphologically pure nanoparticles.[44,45] This crystallization favours the formation of low interfacial-curvature structures such as 1D nanofibers and 2D nanoplatelets.[46,47] As these nanoparticles possess crystalline cores, they can be fractured under physical stress, such as sonication.[48] If the solution is sonicated for a sufficient period of time, very small nanoparticles (ca. 25 – 40 nm) are generated, known as seeds.[48] These seeds retain termini that behave as nuclei for further epitaxial growth upon the

addition of further dissolved polymer (unimer).[44,45] As the rate of elongation is roughly equal for all seeds, the result is length or size-controlled 1D nanofibers or 2D nanoplatelets, where the size is directly dependent on unimer to seed mass ratio. Thus, the generation of highly size-controlled and morphologically pure nanoparticles is possible.[49–55]

A key feature of the nanoparticles fabricated from living CDSA is the presence of a crystalline core. Recently, it has been elucidated that the presence of the rigid core is crucial for mediating antibacterial activity. For example, our group was able to determine that long 1D nanofibers (ca. 500 nm), derived from the BCP poly(fluorenetrimethylenecarbonate)-*block*-poly(dimethylamino methacrylate) (PFTMC-*b*-PDMAEMA) are able to intercalate the bacterial membrane of gram-negative *Escherichia coli* (*E. coli*), and that in addition, long nanofibers can penetrate the membrane of multiple bacteria simultaneously.[42] This correlated to increased membrane damage and bacterial cell death upon incubation with long nanofibers over amorphous-core nanospheres of identical composition. Interestingly, enhanced membrane damage was demonstrated for all other nanofiber lengths tested (ca. 25 nm seeds and 100 nm nanofibers), showcasing that the crystalline-core is crucial for imparting membrane damage. Additionally, we demonstrated that both the 1D nanofibers and amorphous-core nanospheres displayed synergy with tetracycline, but that this synergy was particularly enhanced when nanoparticles with smaller dimensions were employed.[42] Therefore, 1D nanofibers containing a rigid crystalline core are very promising alternatives to traditional small-molecule antibiotics which possess a similar mechanism of action to AMPs and display antibiotic synergy, yet are more resistant to degradation. However, this mechanism was only elucidated against gram-negative *E. coli* and thus information about the

spectrum of activity is currently unknown. Furthermore, the ability of 1D nanofibers to target bacteria that are resistant to the activity of AMPs was of great interest for exploration.

Herein, we expand the spectrum of activity of antibacterial PFTMC-*b*-PDMAEMA 1D nanofibers by investigating their activity against gram-positive *Staphylococcus epidermidis* 12228 (*S. epi*). Employing our previously reported drug-loading procedure,[56,57] we also investigate the selective enhancement in antibacterial activity against *S. epi* upon loading of tetracyline and erythromycin. We also determine the antibacterial activity of 1D nanofibers and amorphous-core nanospheres against an extremely resistant strain of bacteria *Burkholderia vietnamiensis* BAA-248 (*B. vietnamiensis*) and investigate the nanoparticle ability to sensitize the bacteria to the more commonly employed AMP, polymyxin B.[62–65] Finally, we explore the effect coronal-chemistry on the targeting ability of nanoparticles against *B. vietnamiensis.*

## 5.3 Results

### 5.3.1 Synthesis of PFTMC-based polymers and living CDSA into controlled nanoparticles

#### 5.3.1.1 Synthesis and living CDSA of $PFTMC_{26}$-*b*-$PDMAEMA_{424}$ and $PFTMC_{20}$-*b*-$PDMAEMA_{300}$

The synthesis and purification of $PFTMC_{26}$-*b*-$PDMAEMA_{424}$ (P1) has been previously reported.[42,66] Further polymer was required for conducting the antibacterial assays against *B. vietnamiensis* and thus $PFTMC_{20}$-*b*-$PDMAEMA_{300}$ (P2) was also synthesized according to previously published procedures.[67–69] The PFTMC core-forming block was generated through ring-opening polymerization of the respective ring-closed monomer, using a reversible-addition

fragmentation-chain transfer (RAFT) agent as the initiator (Scheme S5.1).[70] The degrees of polymerization were determined through $^{1}$H NMR spectrometry and matrix-assisted laser desorption/ionization mass spectrometry. The PDMAEMA corona-forming block was integrated through controlled RAFT polymerization (Scheme S5.1, Figure S5.1). Final degrees of polymerization of the PDMAEMA were determined through relative $^{1}$H NMR integrations of the PDMAEMA protons relative to those found in the aromatic rings of the PFTMC core. Purification of P2 was performed through an updated procedure, which involved simple vacuum filtration of the dissolved polymer through basic alumina (Figure S5.1). Full details can be found in the supplementary information.

Living CDSA was performed on both BCPs to yield length-controlled 1D nanofibers or nanospheres (Figure 5.1A). P1 was employed for all testing against *S. epi*, whereas P2 was employed for all experiments involving *B. vietnamiensis.* No significant trend in antibacterial activity governed by differences in core or corona-forming block degrees of polymerization has been identifiable.[41,42] The self-assembly procedure for both polymers was identical. Unimer solution (20 mg/mL in tetrahydrofuran) was added into the selective solvent ethanol in a volume ratio of 1:4 *v/v*. The mixture (1 mg/mL polymer) was heated to 70° C for 2 h, and allowed to cool to 22° C overnight. For both polymers, this generated length-disperse morphologically pure 1D nanofibers (Figure 5.1A). The long nanofibers were then sonicated for 3 h at 10° C to yield short seed nanofibers (ca. 25 nm) (Figure 5.1B). Various amounts of unimer solution (20 mg/mL tetrahydrofuran) was added to the seed solution to give length-controlled and morphologically pure nanofibers, which were subsequently transferred into water by solvent addition-evaporation.

In the case of P1 final nanofibers employed were of length ($L_n$) 109 nm ($Đ_L$ = 1.07), and 483 nm ($Đ_L$ = 1.10), as determined by transmission electron microscopy (TEM) (Figure 5.1B). Seed nanofibers of length 23 nm ($Đ_L$ = 1.05) were also evaluated. Nanospheres (core diameter ($d_{core}$) = 16 nm, $Đ_L$ = 1.03, Figure S5.2) were assembled through the direct addition of unimer solution into water to give nanospheres at a final concentration of 1 mg/mL. Nanofibers generated from P2 were of final lengths 141 nm ($Đ_L$ = 1.07) and 557 nm ($Đ_L$ = 1.02), as well as nanoseeds of length 25 nm ($Đ_L$ = 1.15) (Figure S5.2). Nanospheres were also assembled with a final $d_{core}$ of 10 nm ($Đ_L$ = 1.05) (Figure S5.2).

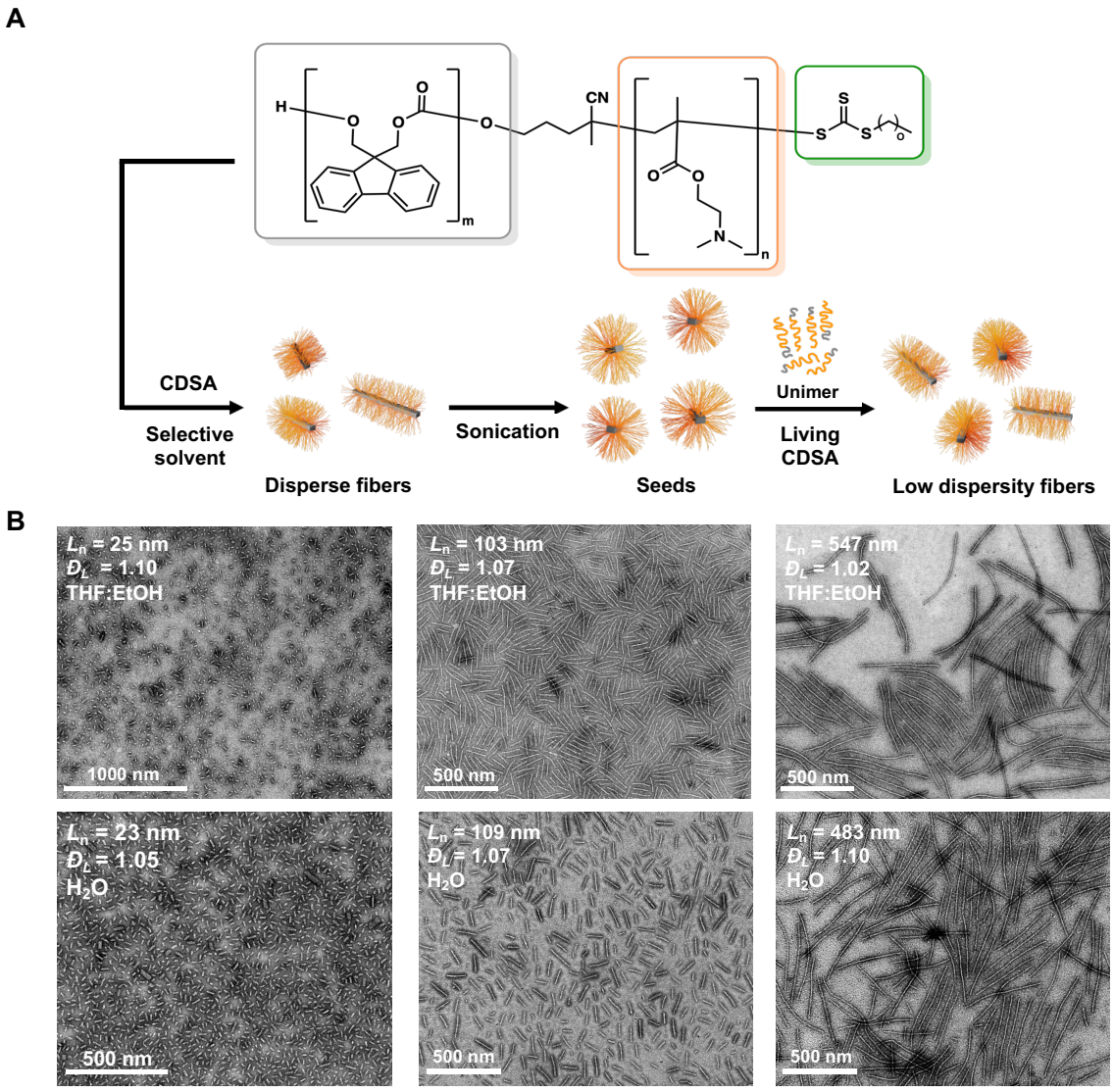


**Figure 5.1.** General schematic of the living CDSA process to generate length-controlled nanofibers with representative TEM micrographs of the nanofibers used in this work shown below. (A) The structure of the BCP PFTMC$_m$-*b*-PDMAEMA$_n$ used to generate 1D nanofibers evaluated for antibacterial activity against *S. epi* and *B. vietnamiensis*. The crystalline-core disperse nanofibers are sonicated to yield seeds, which then grow upon the addition of further dissolved polymer. (B) TEM micrographs of PFTMC$_{26}$-*b*-PDMAEMA$_{424}$ seed nanofibers (25 nm) upon addition of unimer solution to yield 103 nm nanofibers and 547 nm nanofibers. Each image below represents the same nanofiber sample upon transfer into water, yielding nanofibers of length 23

nm, 109 nm, and 483 nm. Figure is reproduced and adapted with permission of the American Chemical Society and the Royal Society of Chemistry.

#### 5.3.1.2 Synthesis and living CDSA of PFTMC$_{18}$-*b*-PNIPAM$_{425}$ and PFTMC$_{18}$-*b*-PEG$_{530}$

To investigate the effect of coronal chemistry on the ability of 1D nanofibers to target the less charged *B. vietnamiensis* membrane, more neutral nanofibers were desired. We hypothesized that rather than targeting the membrane through electrostatic interactions, which could prove challenging as the membrane of *B. vietnamiensis* is not highly charged, that hydrophobic interactions may also be capable of promoting association. Therefore, PFTMC$_{18}$-*b*-poly(N-isopropylacrylamide)$_{425}$ (PNIPAM) (P3) and PFTMC$_{18}$-*b*-poly(ethylene glycol)$_{530}$ (PEG) (P4) were also synthesized and living CDSA of the resulting polymers was performed, according to previously published procedures (Figure S5.2).[56,57,69] P3 was synthesized through ring-opening polymerization followed by subsequent RAFT polymerization of the N-isopropylacrylamide methacrylate monomer. P4 was generated through ring-opening polymerization which instead utilized the methoxy-PEG itself as a macroinitiator for ring-opening. Living CDSA of P3 was conducted in mixtures of tetrahydrofuran and methanol at 1:4 *v/v*, as previously reported. Colloidally stable nanofibers of $L_n$ = 241 nm ($Đ_L$ = 1.04) and 467 nm ($Đ_L$ = 1.04) were successfully prepared, as determined by TEM analysis (Figure S5.2). Living CDSA of P4 was performed in tetrahydrofuran and methanol, also at 1:4 *v/v* and length-controlled nanofibers of $L_n$ = 114 nm ($Đ_L$ = 1.12) were generated (Figure S5.2). Full polymer characterization and nanofiber details can be found in the supplementary information (Table S5.1). A brief summary of the polymers and nanoparticles utilized in this work is given below in Table 5.1.

**Table 5.1.** Polymer composition and nanoparticle measurements upon transfer into water, followed by the strain of bacteria employed for antibacterial activity evaluation.

| Polymer composition | Nanoparticle details | Antibacterial activity evaluation |
|---|---|---|
| $PFTMC_{26}$-*b*-$PDMAEMA_{424}$ (**P1**) | **F*** 23 nm, $Đ_L$ = 1.05<br>**F** 109 nm $Đ_L$ = 1.07<br>**F** 483 nm $Đ_L$ = 1.10<br>**S**$^+$ 16 nm $Đ_L$ = 1.03 | *S. epi* |
| $PFTMC_{20}$-*b*-$PDMAEMA_{300}$ (**P2**) | **F** 25 nm, $Đ_L$ = 1.15<br>**F** 141 nm $Đ_L$ = 1.07<br>**F** 557 nm $Đ_L$ = 1.02<br>**S** 10 nm $Đ_L$ = 1.05 | *B. vietnamiensis* |
| $PFTMC_{18}$-*b*-$PNIPAM_{425}$ (**P3**) | **F** 241 nm, $Đ_L$ = 1.04<br>**F** 467 nm $Đ_L$ = 1.04 | *B. vietnamiensis* |
| $PFTMC_{18}$-*b*-$PEG_{530}$ (**P4**) | **F** 114 nm, $Đ_L$ = 1.12 | *B. vietnamiensis* |
| *F = nanofiber $^+$S = nanosphere | | |

### 5.3.2 Evaluation of nanoparticle antibacterial activity against Staphylococcus epidermidis

#### 5.3.2.1 Drug loading of tetracycline onto P1 nanofibers evaluated by dynamic light scattering

To determine the versatility of 1D nanofibers to serve as antibacterial drug delivery vehicles, tetracycline was loaded onto 23 nm seed nanofibers, 109 nm and 483 nm nanofibers, and 16 nm nanospheres. Previous work by our group has demonstrated that 20 wt % is likely the maximum drug-loading capacity of crystalline-core nanofibers, as evidenced by dynamic light scattering (DLS) and flow cytometry.[42] The same 109 nm nanofibers, 23 nm seed nanofibers, and 16 nm nanospheres, were previously loaded with 20 wt % tetracycline and the antibacterial activity was

evaluated against gram-negative *E. coli*. These combination treatments exhibited potent antibacterial activity, especially when nanoparticles with small dimensions (seeds, nanospheres) were employed. In this work, we wished to evaluate the antibacterial activity against a new strain of bacteria, gram-positive *S. epi*. One important consideration is the difference in membrane characteristics of gram negative and gram-positive bacteria. The former contain an additional outer membrane which normally reduces the permeation and potency of treatments, as it provides an additional barrier that needs to be surpassed.[71] Therefore, we would expect the 1D nanofibers to be more potent antibacterials against *S. epi* than against *E. coli*.

Drug-loading was performed according to the procedure previously reported.[42] Nanofiber solutions (50 μL, 1 mg/mL, THF:EtOH) were added into a vial. Tetracycline (10 μL, 1 mg/mL, EtOH) was then added into the same vial. Water (100 μL) was then added by dropwise addition. Samples were left open to air for 48 h to afford evaporation of the organic solvents. Nanosphere solutions (50 μL, 1 mg/mL, $H_2O$) were prepared by direct addition of tetracyline (10 μL, 1 mg/mL, EtOH), and again 100 μL of water was added, and the EtOH was allowed to evaporate. After evaporation, samples were gravimetrically returned to 1 mg/mL through addition of water. DLS was utilized to ensure no major changes in the hydrodynamic radius occurred upon addition of the drug tetracycline. No change in the hydrodynamic radius was observed for any sample, and furthermore no species representing the measured hydrodynamic radius of free tetracycline were observed in solution (Figure 5.2A).

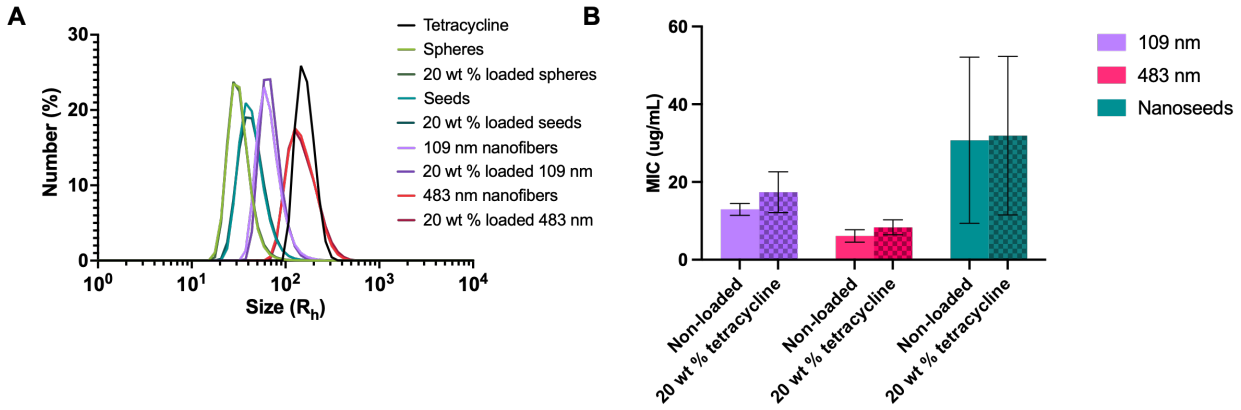


**Figure 5.2.** Data obtained for non-loaded and tetracycline-loaded P1 nanoparticles. (A) Traces of the hydrodynamic radius of particles before and after loading 20 wt % tetracycline, relative to that of free tetracycline (black trace). In order from left to right is the hydrodynamic radius of nanospheres (light green trace), and loaded nanospheres (dark green trace), seed nanofibers (teal trace) and loaded seed nanofibers (dark blue trace), 109 nm nanofibers (light purple trace) and those loaded with 20 wt % tetracycline (dark purple trace), and finally 483 nm nanofibers (bright pink trace) and tetracycline-loaded 483 nm nanofibers (red trace). (B) Minimum inhibitory concentrations determined for pristine and tetracycline-loaded nanofibers against *S. epi*, with pure nanofibers shown in solid colour and drug-loaded nanofibers shown in patterned bars. No significant difference in antibacterial activity was demonstrated upon tetracycline loading, and no antibacterial activity was observed upon incubation of *S. epi* with nanospheres (Figure S5.3, S5.4).

#### 5.3.2.2 Evaluation of the antibacterial activity of tetracycline-loaded P1 nanoparticles against S. epi

Antibacterial activity was determined through monitoring of the absorbance at 600 nm ($OD_{600}$) over the course of 4 h, according to previously reported procedures.[41,42] Nanoparticles were serially diluted in a 96 well-plate from 100 µg/mL to 0 µg/mL, and *S. epi* (diluted to an $OD_{600}$ of 0.6 in tryptic soy broth) was added into the wells. The minimum inhibitory concentration (MIC), which

represents the minimum amount of therapeutic required to inhibit bacterial growth, was calculated using GraphPad prism software.[72] The MICs were first determined for non-loaded P1 nanoparticles. Nanofibers of $L_n$ = 109 nm displayed an MIC of 13 μg/mL (Figure 5.2B, S5.3). This is approximately a 2-fold increase in activity relative to that observed against *E. coli* (37 μg/mL).[42] 483 nm nanofibers displayed an MIC of 6 μg/mL (Figure 5.2B, S5.3), representing again increased potency against *S. epi* relative to that previously observed against *E. coli* (17 μg/mL),[41] although slightly different degrees of polymerization exist between the two polymers in each work. Upon observation of samples containing 23 nm seed nanofibers, an MIC of 34 μg/mL was determined (Figure 5.2B, S5.4). Finally, when nanospheres were incubated with *S. epi*, no significant antibacterial activity was demonstrated, and no MIC was determinable (Figure S5.4).

We next evaluated the antibacterial activity of the same nanoparticle samples, but loaded at 20 wt % with tetracycline. In contrast to our previous results, the addition of tetracycline did not improve the antibacterial activity of any of the nanoparticles trialed and in most cases resulted in an increased MIC, though this difference was not statistically significant (Figure 5.2B, S5.3, S5.4). We determined that this lack in activity may be due to the inherent susceptibility of the bacteria to the selected antibiotic, as tetracycline is more commonly employed for combatting gram-negative bacteria. Therefore, we sought to select an antibiotic to which *S. epi* is more susceptible and determine if enhanced activity is then demonstrated.

### 5.3.3 Determination of erythromycin-loaded nanoparticle antibacterial activity against S. epi

Erythromycin is a hydrophobic antibiotic to which *S. epi* has been previously recorded to be susceptible.[73] Therefore, drug-loading was repeated for 109 nm P1 nanofibers, but using 20 wt % erythromycin instead of tetracycline. DLS evidenced that no disruption of the nanofibers occurred upon addition of erythromycin (Figure S5.5). Antibacterial assays were repeated over a concentration range of 100 µg/mL to 0 µg/mL nanofibers. After 4 h of incubation, the $OD_{600}$ was measured. Upon calculation of the MIC, more potent antibacterial activity was observed, with an MIC of 3 µg/mL obtained, an approximately 4-fold increase in activity (Figure 5.3A,B). Importantly, no MIC was determinable for an equivalent amount of erythromycin on its own (Figure S5.6), demonstrating a synergy occurring between the nanofibers and the antibiotic. Furthermore, the MIC reported herein represents potent antibacterial activity and falls within the range of MICs reported for commonly prescribed antibiotics.

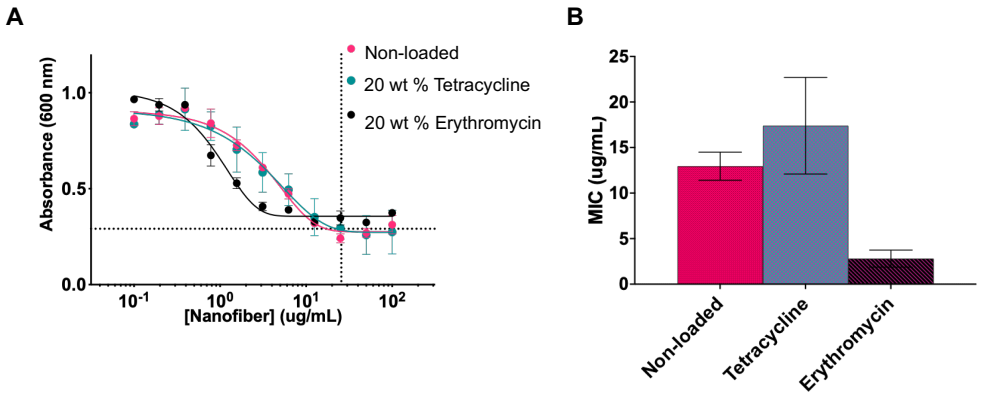


**Figure 5.3.** Antibacterial activity of 109 nm P1 nanofibers loaded with erythromycin, relative to non-loaded and those loaded with tetracycline. (A) Bacterial growth curves plotted as the absorbance at 600 nm as a function of nanofiber concentration. The point of inflection of each curve represents the MIC for that material. The point of inflection upon loading with erythromycin occurs at a lower concentration than that for tetracycline-loaded and pure 109 nm nanofibers. (B)

MIC values obtained for each material plotted as a bar chart, with error bars representing the 95 % confidence interval for each mean value. Much more potent antibacterial activity is observed upon loading of erythromycin.

### 5.3.4 Investigations of P2 nanoparticles against drug-resistant *B. vietnamiensis*

#### 5.3.4.1 Investigations into synergistic antibacterial action between P2 nanoparticles with polymyxin B

In the subsequent sections of this work, we explore the antibacterial activity of P2, P3, and P4 nanoparticles against drug-resistant *B. vietnamiensis*. This genus of bacteria, *Burkholderia*, is notoriously resistant to cationic AMPs, as well as most traditional antibiotics, with concentrations upwards of 1 mg/mL occasionally being required to exert any antibacterial effect.[61,65] Over time, these organisms have developed several characteristics which allow them to evade the effects of commonly prescribed as well as novel treatments, which include having a more neutral membrane, as well as increased amounts of efflux pumps which quickly excrete therapeutics from their interior.[74–76] In human pathology, these organisms are largely found in patients who have cystic fibrosis, a disease characterized by large amounts of mucus in the lungs.[59] Their presence results in infections which are extremely difficult to treat. Therefore, the development of new materials which either contain inherent activity against these bacteria, or are able to sensitize them to existing medications is highly valuable.

To investigate if our cationic P2 nanoparticles were still able to target the bacterial membrane, despite the lack of significant negative charge, we conducted the same antibacterial assays as those outlined in the previous sections. P2 Nanofibers of $L_n$ = 25 nm (seeds, $Đ_L$ = 1.15), 141 nm ($Đ_L$ = 1.07), and 557 nm ($Đ_L$ = 1.02) were prepared via living CDSA (Figure S5.2) and evaluated for

antibacterial activity against *B. vietnamiensis*. P2 nanospheres of $d_{core}$ = 10 nm ($Đ_L$ = 1.05) were also prepared (Figure S5.2). Additionally, we wished to determine if the presence of nanoparticles could enhance the activity of the cationic AMP, polymyxin B, to which *B. vietnamiensis* is resistant.[25,26] This AMP functions in a similar manner to most cationic AMPS, in that association by electrostatic interactions occurs first, followed by insertion of hydrophobic residues into the membrane.[63,65] Once the membrane is permeabilized, further molecules of polymyxin B can enter the bacterium and interrupt the synthesis of new lipopolysaccharide molecules, a process that is crucial for bacterial replication and membrane repair. As polymyxin B is hydrophilic, no drug-loading was necessary, and instead the nanoparticles and polymyxin B were simply co-incubated with the bacteria at concentrations from 100 μg/mL to 0 μg/mL (Figure S5.7). Upon calculation of the MIC for P2 nanoparticles in the presence and absence of polymyxin B, no bactericidal antibacterial activity was observed (Figure S5.8, S5.9). Despite this, we did notice that upon incubation with 141 nm and 557 nm nanofibers in particular, the absorbance values at t = 0 h were quite high, but not much change occurred over the course of 4 h, indicating only a small increase in bacterial number over this time course. Thus, we decided to plot the change in absorbance at 600 nm (or $\Delta$ $OD_{600}$) to decipher if any further information about the antibacterial activity could be elucidated.

Upon analysis of the overall change in bacterial number, we were able to identify that 557 nm nanofibers inhibit the replication of *B. vietnamiensis* to the greatest extent ($\Delta$ $OD_{600}$ = 0.16), and this inhibition is enhanced when polymyxin B is present ($\Delta$ $OD_{600}$ = 0.05) at 100 μg/mL (Figure 5.4), representing reasonable bacteriostatic activity. Polymyxin B (100 μg/mL) alone did not inhibit bacterial replication to any extent ($\Delta$ $OD_{600}$ = 0.48) (Figure 5.4, S5.10). Upon incubation

with 50 µg/mL of 557 nm nanofibers with and without polymyxin B, the bacterial replication was also slowed, with $\Delta$ $OD_{600}$ = 0.28 and $\Delta$ $OD_{600}$ = 0.18 identified, respectively (Figure 5.4B). All nanoparticles at concentrations below 50 µg/mL did not induce any bacterial response. Nanofibers of $L_n$ = 141 nm also exhibited a reasonable effect, with a $\Delta$ $OD_{600}$ = 0.16 obtained for non-loaded nanofibers at 100 µg/mL, and a $\Delta$ $OD_{600}$ = 0.13 obtained in the presence of polymyxin B at the same concentration, however, the difference is not statistically significant (Figure 5.4B). While we have previously determined that small nanoparticles are superior for drug-delivery to bacteria, neither 23 nm seed nanofibers or 10 nm nanospheres significantly inhibited the growth of *B. vietnamiensis* with or without polymyxin B (Figure 5.4C, S5.9).

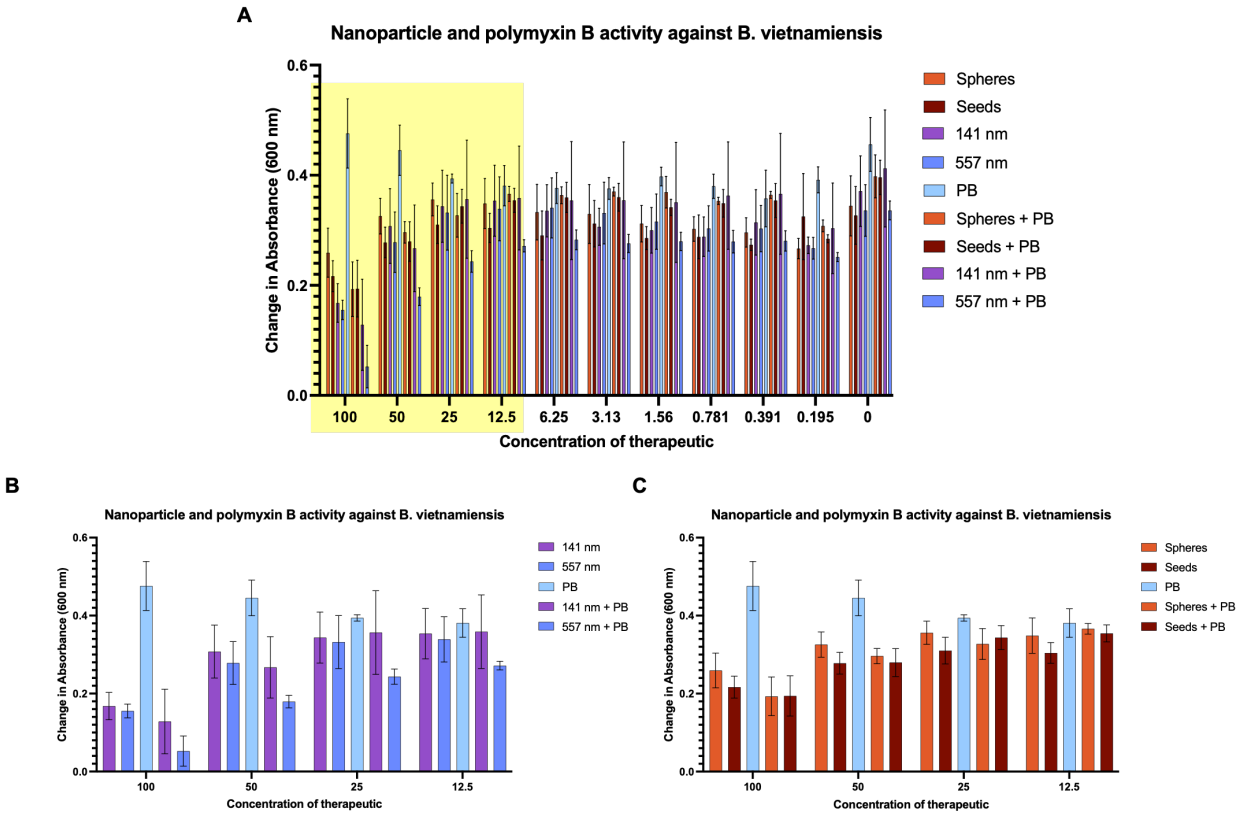


**Figure 5.4.** P2 nanoparticle antibacterial activity against *B. vietnamiensis*, represented in the change in absorbance at 600 nm at concentrations from 100 µg/mL to 0 µg/mL. (A) All data obtained for P2 nanospheres, seed nanofibers, 141 nm nanofibers, and 557 nm nanofibers in the

presence and absence of polymyxin B, as well as pure polymyxin B. (B) Data obtained of 141 nm and 557 nm nanofibers from the region highlighted in yellow from chart (A), with data for nanospheres and seed nanofibers removed. The change in absorbance is much smaller upon incubation with both polymyxin B and 557 nm nanofibers. (C) Data obtained upon incubation of nanospheres and seed nanofibers from the region highlighted in yellow in chart (A). No difference in absorbance is present upon incubation of nanoparticles with or without polymyxin B.

### 5.3.5 Investigation of the targeting capabilities of P3 and P4 nanofibers containing neutral corona-forming blocks

Finally, as the targeting displayed from the cationic P2 nanofibers was not as high as that previously identified against *S. epi* and *E. coli*, which contain much more anionic membranes, we hypothesized that perhaps the use of a neutral corona-forming block could mediate hydrophobic interactions between the nanoparticles and the bacteria. Therefore, P3 (containing a PNIPAM corona) nanofibers of $L_n$ = 241 nm ($Đ_L$ = 1.04) and 467 nm ($Đ_L$ = 1.04) were prepared via living CDSA (Figure S5.2). Furthermore, P4 (PEG corona) nanofibers of $L_n$ = 114 nm ($Đ_L$ = 1.12) were also evaluated (Figure S5.2). Materials were incubated with bacteria at concentrations from 100 μg/mL to 0 μg/mL in the presence and absence of polymyxin B, and the MICs were calculated; no bactericidal antibacterial activity was observed (Figure S5.11). The change in absorbance was plotted once more. Upon observation of cultures containing P3 nanofibers, the $\Delta$ $OD_{600}$ at all concentrations was higher than those observed for P2 nanofibers (Figure 5.5A). However, differences depending on the length of the nanofibers were observable. When 100 μg/mL of nanofibers are present, the $\Delta$ $OD_{600}$ = 0.36 and 0.38 for 241 nm and 467 nm nanofibers, respectively. These values are not statistically significantly different from that recorded for free polymyxin B ($\Delta$ $OD_{600}$ = 0.48). However, upon the co-incubation of P3 nanofibers with polymyxin

B, a decrease in bacterial growth is observed with the Δ $OD_{600}$ = 0.26 and 0.25 when $L_n$ = 241 nm and 467 nm respectively (Figure 5.5A). The Δ $OD_{600}$ of 241 nm nanofibers in combination with polymyxin B remains at 0.26 down to 25 μg/mL, whereas that for 467 nm nanofibers with polymyxin B increases to 0.29 and 0.30 at 50 μg/mL and 25 μg/mL respectively (Figure 5.5A). Some fluctuations are observed at lower concentrations (< 25 μg/mL) of therapeutic, but the values never drop below those observed at higher concentrations (> 25 μg/mL). P4 nanofibers of $L_n$ = 114 nm ($Đ_L$ = 1.12) were also subjected to the same screening, however, at no concentration did the Δ $OD_{600}$ drop below that observed for free polymyxin B (Figure 5.5B). The results herein demonstrate that nanofibers containing a lower degree of positive charge could be promising for targeting bacteria with these characteristics, however some degree of electrostatic interaction is likely required for effective activity.

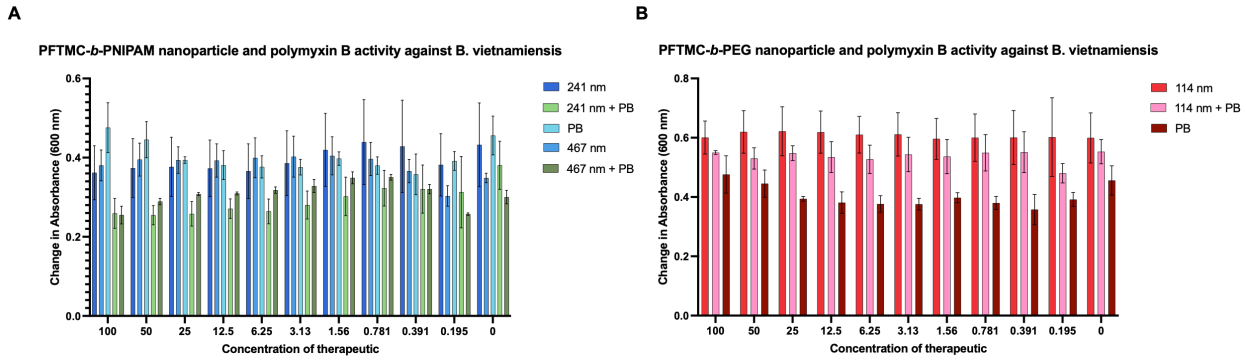


**Figure 5.5.** P3 and P4 nanofiber antibacterial activity against *B. vietnamiensis*, graphed as the change in absorbance at 600 nm over 4 h. (A) P3 nanofibers of length 241 nm and 467 nm demonstrate no inhibition of bacterial growth alone, but hinder bacterial replication upon co-incubation with polymyxin B at concentrations > 25 μg/mL. (B) P4 nanofibers of length 114 nm cause no significant decrease in bacterial growth at any of the concentrations tested, with or without polymyxin B.

## 5.4 Discussion

Recently, a major focus has been placed on the development of broad spectrum antibacterials which either avoid the development of resistance or can help more common treatments to overcome mechanisms of resistance. Due to the promising results of our previous work, which demonstrated that 1D nanofibers possess a general mechanism of action which involves indiscriminate puncture of the bacterial membrane against *E. coli*, we wished to explore the ability of these materials further for specifically overcoming antibacterial resistance. First, we expanded the scope of the 1D nanofibers through testing their activity against gram-positive *S. epi.* All of the P1 anisotropic nanofibers displayed increased antibacterial activity against *S. epi* relative to that recorded against *E. coli*. This can be explained by the differences in membrane composition between the two types of bacteria, as gram-negative bacteria have an additional and less permeable outer membrane. Therefore, we can recognize that the membrane permeation mechanism is likely still at play against gram-positive bacteria, and that membrane disruption is more facile in these strains due to the presence of fewer membrane barriers. Interestingly, the nanospheres, which were not predicted to cause membrane damage in the same manner, did not display enhanced activity relative to *E. coli*, and thus we observe once more how the crystalline-core is crucial for imparting antibacterial activity. Furthermore, through the loading of both tetracycline and erythromycin, we demonstrate that selective enhancements in antibacterial activity can be generated through careful selection of the added antibiotic at the core-corona interface. For example, seed nanofibers loaded with tetracycline would inhibit *E. coli* growth at approximately 4 μg/mL, whereas at this concentration *S. epi* would remain unaffected. If however an infection was caused by *S. epi*, erythromycin could be loaded onto the seed nanofibers to exert an effect. Therefore, the drug-loading procedure can be performed identically regardless of the therapeutic selected, and this can

mediate differences in the observed antibacterial activity. We next determined the ability of P2, P3, and P4 nanofibers to target the drug-resistant bacteria *B. vietnamiensis*. It is important to note that none of the nanofibers or nanospheres evaluated against this strain, over the concentration range, inhibited the bacterial growth enough to calculate an MIC. Some insight was provided by monitoring the overall change in bacterial growth from t = 0 to t = 4. When P2 nanofibers were employed, both 109 nm and 483 nm from 100 – 50 μg/mL, the bacterial growth was significantly hindered upon co-incubation with polymyxin B. Interestingly, the 483 nm nanofibers exhibited the highest overall effect. We postulate that this could be due to each nanoparticle containing a higher amount of charged groups, and thus, as targeting the bacterium is more difficult, this could be advantageous. It is also possible that in alignment with our previous results, the longer nanofibers better intercalate the membrane upon interaction, allowing increased entry of polymyxin B, resulting in slowed replication. Considering the complete resistance to polymyxin B historically demonstrated by *B. vietnamiensis*, the results presented herein highlight that the physical action of the nanofibers is incredibly promising for overcoming antibacterial resistance, as synergy is displayed when none would be expected. While no MIC is calculable, it is important to note that the experiments were performed using a bacterial concentration of $5.0 \times 10^8$ colony forming units/mL, which is a substantially high concentration relative to standard tests, but is consistent with our previous publications. Therefore, the ability of the 1D nanofibers to sensitize such an incredibly resistant bacteria to a compound with no solo effect, at relatively low therapeutic concentrations, shows great promise for overcoming both mild and severe antibacterial resistance. We were also interested in determining if less highly charged nanofibers or neutral nanofibers could cause increased association with the more neutral bacteria. P3 nanofibers displayed some level of targeting, although this was not as significant as observed for P2 nanofibers. For these P3

nanofibers, it appeared that shorter 241 nm nanofibers outperformed the 467 nm nanofibers. This may be because when the polymers are at a given concentration, there are more 241 nm nanofibers than 467 nm nanofibers present in solution. If no significant targeting is occurring then the increased chance of a 241 nm nanofiber encountering a bacterium in solution could lead to this increased effect. Finally, we were able to determine that P4 nanofibers displayed no antibacterial activity, which was also observed against *E. coli*. Therefore, regardless of membrane composition, PEG-based nanofibers are not useful for targeting bacterial membranes. In summary, we can conclude that cationic functional groups are the most effective currently for targeting the bacterial cell membrane, and that longer nanofibers are the most promising for use in overcoming antibacterial resistance.

## 5.5 Conclusion

In this article, we present exploratory work meant to expand the knowledge surrounding the versatility of 1D nanofibers for overcoming antibacterial resistance. The scope of antibacterial activity of nanofibers containing a cationic corona is demonstrated to also include *S. epi* and should be applicable to other gram-positive bacteria. We also highlight the ability of the nanofibers to permeabilize the membrane of the very drug-resistant organism *B. vietnamiensis*. While further work is required to increase the potency and synergy of the combination treatment containing 1D nanofiber and polymyxin B, we demonstrate that bacterial growth is inhibited, especially upon incubation with 483 nm cationic nanofibers and polymyxin B. Finally, this confirms the mechanism of action of 1D nanofibers is general and physical, and that anisotropic crystalline-core nanofibers possess significant advantages for antibacterial treatment over isotropic nanosphere equivalents.

## 5.6 Supporting Information

### 5.6.1 General considerations

The synthesis and characterization of $PFTMC_{26}$-*b*-$PDMAEMA_{424}$ have been previously reported by Street et al. and Parkin et al.[42,66] $PFTMC_{20}$-*b*-$PDMAEMA_{300}$ was synthesized according to previously published procedures.[42,66,69] The synthesis and characterization of $PFTMC_{18}$-*b*-$PEG_{530}$ and $PFTMC_{18}$-*b*-$PNIPAM_{425}$ have been previously reported by Garcia-Hernandez et al.[56] The PFTMC homopolymer degree of polymerization was determined by matrix-assisted laser desorption/ionization mass spectrometry and the coronal-block degree of polymerization was determined by integrations of coronal block peaks in $^1$H NMR relative to peaks of the PFTMC block. RAFT-CTA was dried via vacuum desiccation over phosphorus pentoxide prior to use. Methoxy PEG was purchased from Polymer Source (Montreal, Canada). All other reagents and solvents were purchased from Sigma-Aldrich (Canada), Combi-Blocks (USA), VWR (Canada), or Fisher Scientific (Canada) and used without further purification. Solvents for self-assembly were HPLC grade and were filtered through PTFE, nylon, or cellulose filters with a pore size of 200 nm before use. All reactions were carried out in an MBraun 200B glove box under a nitrogen atmosphere or using standard Schlenk line techniques. RAFT polymerizations were performed in custom-made Schlenk-vials to fit dry heating blocks. 1,8 Diazabicyclo[5.4.0]undec-7-ene (DBU) was dried over CaH2, and purified by distillation under reduced pressure. Anhydrous solvents were dried and purified using an MBraun Grubbs/Dow solvent purification system.

### 5.6.2 Instrumentation

**Gel permeation chromatography (GPC)**

Gel permeation chromatograms were acquired on a Malvern OMNISEC triple-detector (refractive index, UV-Vis photodiode detector, light scattering detector and viscometer) chromatograph. Prepared samples were of 1 mg/mL concentration in HPLC grade THF, and were filtered through a PTFE filter with a 200 nm pore size prior to measurement. The eluent used was Triethylamine/THF (1 % *v/v*) at a flow rate of 1 mL/min. Two columns were employed, the first of grade T3000 and the second of grade T5000, operated at 35 °C. Universal calibration was constructed using a polystyrene standard. Samples were prepared at 1 mg/mL in eluent and filtered through a PTFE membrane filter, pore size = 200 nm.

**Preparatory Gel permeation chromatography (Prep GPC)**

Preparatory gel permeation chromatography was performed on a Shimadzu Prep GPC equipped with a CBM-20A communications bus module, LC-20AP solvent delivery unit, SIL-10AP autosampler, CTO-40C column oven, SPD-40 UV-Vis detector, RID-20A refractive index detector, and FRC-10A fraction collector. An initial injection of polymer in THF (1 mL, 10 mg/mL) at a flow rate of 3 mL/min using HPLC grade THF as eluent was used to gather the retention times of the species in solution. Using this data, the fraction collector was calibrated to separate the desired peaks into separate vials. Subsequent injections (3 mL, 10 mg/mL, 3 mL/min) were repeated until the desired volume was collected. The resulting solutions were concentrated in vacuo to yield the final polymer.

**Ultrasonication**

Micelle sonication was carried out using a Fisherbrand 112xx series advanced ultrasonic cleaner (FB-11203), operated in sweep mode at 80 % power and 37 MHz at 10 °C.

**Matrix-assisted laser desorption/ionization-time of flight mass spectrometry (MALDI-TOF MS)**

MALDI-TOF MS measurements performed using a Bruker Ultraflextreme running in linear mode. Samples were prepared using a trans-2-[3-(4-tert-butylphenyl)-2-methyl-2-propenylidene]malononitrile matrix (20 mg/mL in THF) and the polymer sample (2 mg/mL in THF), mixed in a 10:1 (v/v) ratio. Approximately 3 μL of the mixed solution was deposited onto a stainless-steel sample plate and allowed to air dry.

**Transmission electron microscopy (TEM)**

TEM images were obtained on a JEOL 1011 microscope equipped with an 11 Megapixel CCD camera, operated at 80 kV. Nanoparticle solutions (1.5 μL, 1 mg/mL) were drop-casted onto a carbon-coated copper grid. Uranyl acetate solution (8 μL) in EtOH (3 wt %) was subsequently drop-casted on top, and the grids were left to dry overnight. Copper grids (400 mesh) were purchased from Ted Pella. Carbon films (ca. 6 nm) were prepared by carbon sputtering mica sheets with a Leica ACE 600 carbon coater. The carbon films were deposited onto copper grids via floatation on water and the grids were allowed air dry.

For micelle length analysis, a minimum of 200 nanofibers were traced manually using the FIJI software package. The number average micelle length ($L_n$) or width ($W_n$) and weight average micelle length ($L_w$) were calculated using eq. S1-2 from the individual contour lengths ($L_i$) of the

micelles. Here, $N_i$ is the number of micelles of length $L_i$, and $n$ is the number of micelles examined in each sample. The distribution of micelle lengths is characterized by $Đ = L_w/L_n$.

$$L_n = \frac{\sum_{i=1}^{n} N_i L_i}{\sum_{i=1}^{n} Ni} \qquad L_w = \frac{\sum_{i=1}^{n} N_i L_i^2}{\sum_{i=1}^{n} NiLi} \qquad \text{(eq. S1-2)}$$

**Dynamic Light Scattering (DLS) Measurements**

Dynamic light scattering (DLS) experiments were carried out using a Malvern Zetasizer Pro. Aqueous samples for DLS were prepared at 50 $\mu$L of 1 mg/mL. The correlation function was acquired in real-time and analysed by Cumulant analysis. This process allowed the diffusion coefficients for the nanoparticles to be determined. These were expressed as the effective hydrodynamic radius ($R_h$) using the Stokes-Einstein relationship for coated spheres in water (Refractive Index = 1.33, Dispersant Viscosity = 0.887, Dispersant Dielectric Constant = 78.5) with core properties of polystyrene latex (Refractive Index = 1.590, Absorption = 0.010).

### 5.6.3 Synthetic Procedures

**Synthesis of PFTMC$_{20}$-*b*-PDMAEMA$_{300}$**

**Scheme S5.1.** Ring-opening polymerization (ROP) of FTMC monomer followed by reversible addition-fragmentation chain-transfer (RAFT) polymerization to yield PFTMC$_{20}$-*b*-PDMAEMA$_{300}$

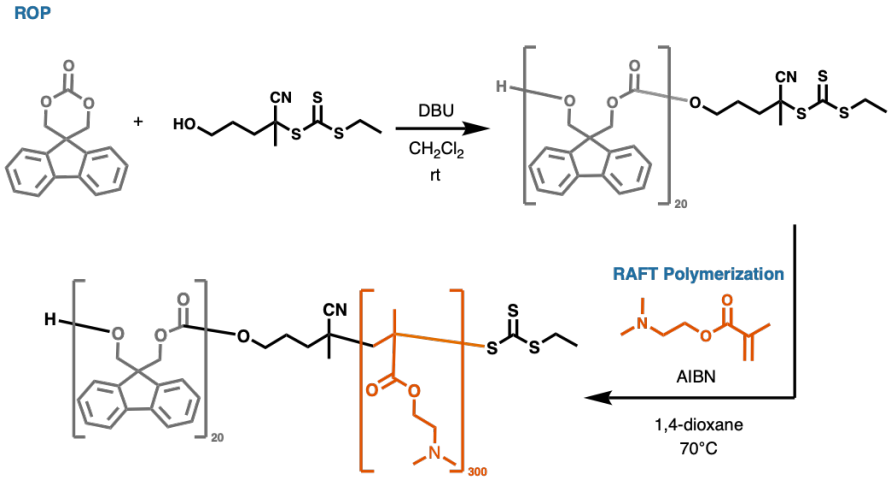


To a solution of 2-cyano-5-hydroxypentan-2-yl ethyl trithiocarbonate in anhydrous $CH_2Cl_2$ (500 µL, 100 mg/mL, 0.2 mmol, 1.0 eq), DBU (24 µL, 24.4 mg, 0.16 mmol, 0.8 eq) was added in an oven-dried round bottom flask equipped with a magnetic stirring bar. To the stirring solution,

FTMC (1.01 g, 4.0 mmol, 20 eq) in anhydrous $CH_2Cl_2$ (6 mL) was added, and the reaction mixture was stirred at room temperature for 1 h, before the reaction mixture was quenched by the addition of benzoic acid (100 mg). The crude product was purified by precipitation into ice-cold diethyl ether three times, followed by precipitation into ice-cold MeOH three times, and drying in vacuo to yield $PFTMC_{20}$-CTA as a yellow solid (872 mg g, 82 %).

GPC: Mn = 3,300, $Đ$M = 1.14.

$PFTMC_{20}$-CTA (60 mg, 0.011 mmol, 1 eq), Dimethylaminoethylmethacrylate (520.7 mg, 3.3 mmol, 300 eq),and AIBN (0.544 mg, 0.003 mmol, 0.3 eq) were dissolved in dioxane (4 mL) in a custom-made schlenk-vial followed by four freeze-pump-thaw cycles. The vial with the reaction mixture was placed in a preheated dry heating block and heated to 70 °C, and stirred under $N_2$ for 18 h. The reaction was quenched by submersion in liquid nitrogen. The product was precipitated once in ice-cold diethyl ether, and two subsequent times into ice-cold hexanes. The product was dried in vacuo to yield PFTMC-*b*-PDMAEMA as a white crystalline solid. GPC analysis indicated the presence of a small amount of water-initiated PFTMC homopolymer (as evidenced by a lower Mw shoulder with increased absorbance at 268 nm via UV/Vis). Water-initiated PFTMC homopolymer cannot subsequently polymerize other monomers via RAFT polymerization. The PFTMC homopolymer was removed via alumina filtration (flushed with $CH_2Cl_2$ to elute the diblock copolymer). The resulting polymer was dried and precipitated in ice-cold hexanes to yield $PFTMC_{20}$-*b*-$PDMAEMA_{300}$ as a white crystalline solid (30 mg).

GPC: Mn = 17,200, $Đ_M$ = 1.8. This value is likely overestimated due to GPC column absorption effects.

### 5.6.4 Self-Assembly Procedures

The composition of all solvent mixtures is given as *v:v*. All nanofibers were ultimately transferred into Milli-Q® water *via* a modified procedure of the preformed-nanoparticle solvent-switch loading (PNSL) method as reported by Garcia-Hernandez et al.[56] Modifications include slow drop-wise addition of water from a micropipette, followed by organic solvent evaporation over the course of 2 days. No filtration through a syringe filter was performed. Exact self-assembly procedures for $PFTMC_{26}$-*b*-$PDMAEMA_{424}$ can be found in reference 42, while those for $PFTMC_{18}$-*b*-$PDMAEMA_{425}$ and $PFTMC_{18}$-*b*-$PEG_{530}$ can be found in reference 56.

**General self-nucleation procedure**

A solution of diBCP dissolved in THF (unimer) (20 mg/mL – 200 mg/mL) was diluted with an appropriate amount of THF. Subsequently, unimer solution was slowly added via a micropipette into a selective solvent (EtOH) to yield solutions which had final diBCP concentrations between 1 mg/mL – 10 mg/mL with 20:80 THF:EtOH solvent ratios. Each solution was manually shaken for ~10 s, agitated using a vortex mixer for ~10 s, and heated to 70 °C for 3 h. The resulting length-disperse nanofibers were analyzed via TEM.

**General preparation of seed nanofibers**

Length disperse nanofibers (1 mg/mL – 10 mg/mL, 20:80 THF:EtOH) were sonicated for at least 3 h using a Fisherbrand 112xx series advanced ultrasonic cleaner (FB-11203) for 3 h at 10 °C in sweep mode at 37 MHz and 80% power. The resulting seed nanofibers were analyzed by TEM.

**General preparation of length-controlled nanofibers**

To a diluted seed solution (MeOH or EtOH, 0.6 – 1 mg/mL), unimer (10 – 20 mg/mL in THF) was added depending on the desired $m_{unimer}/m_{seed}$ (e.g. if seed length is 25 nm, and 100 nm nanofibers desired, 3 equivalents of unimer would be added). The self-assembly solution was manually shaken for ~15 s after each addition, and then aged either for 48 h at 20 °C, or for 2 h at 70 ˚C and cooled to 20 °C overnight. The resulting nanofibers were analyzed by TEM.

### 5.6.5 Bacterial Culture and Assays

All bacteria work was performed in a biological safety cabinet using sterile technique. All materials were autoclaved and disinfected with 70 % ethanol prior to being placed in the biological safety cabinet. Clear, sterile, 96-well plates were purchased from Corning. Lysogeny broth (LB) was used for streak plates and liquid culturing of *Burkholderia vietnamiensis* (*B. vietnamiensis*) BAA-248. Tryptic Soy broth (TSB) was used for culturing of *Staphylococcus epidermidis* (*S. epi*) 12228. The buffer was prepared by weighing out (4-(2-hydroxyethyl)-1-piperazineethanesulfonic acid) (HEPES) into a glass bottle, filling with distilled water, autoclaving, and balancing to pH 7.4. Minimum inhibitory concentration (MIC) curves were fitted using GraphPad Prism and the Lambert and Pearson method.[72] The procedure was previously reported by Parkin et al.[41,42]

**Preparation of bacteria for assays**

From a stock solution of bacteria that was kept at -80 °C (50 % glycerol, 50 % culture in broth), a single loop was used to make a streak plate (LB or TSB agar). These plates were placed in an incubator at 37 °C for 24 h. This was repeated. From these initial streak plates, a second

propagation was performed. A disposable loop was used to select one colony from each, and streaked onto another plate, respectively. The new plates were incubated at 37 °C for 24 h. Subsequently, they were moved into a 4 °C fridge. To grow a liquid culture, a single colony was selected from a plate using a disposable loop. This was placed in 5 mL of LB or TSB contained in a 15 mL Falcon tube. The loop was swirled in the broth until the colony was visibly deposited in the broth. The falcon tube was placed in an incubator at 37 °C with orbital shaking at 200 rpm. The culture was allowed to grow for 24 h. From the initial culture, 25 µL of solution was taken and added to a second 15 mL falcon tube containing 5 mL of broth. This new culture was placed in an incubator at 37 °C with orbital shaking at 200 rpm for 24 h.

**Plating of bacteria and nanofibers determining the minimum inhibitory concentration**

Liquid bacterial cultures were diluted in respective broth to a maximum volume of 3 mL and to an absorbance of 0.600 using an OD meter and a polystyrene cuvette. Once the appropriate dilutions were determined, they were performed on a larger scale to give at least 5 mL of bacterial suspension in a sterile reservoir. 10 mL of 40 mM HEPES buffer was added to a separate sterile reservoir. Using a multichannel pipette, 50 µL of buffer was added to each well, excluding the third column. The first row (A1-12) and the last row (H1-12) were topped up to 100 µL of buffer to be used as blanks and to prevent evaporation. The first column was also used as a buffer blank. To three wells in the third column (B3, C3, D3) 20 µL of 1 mg/mL material to be tested was added, and 20 µL of 1 mg/mL of a second material to be tested was added to the next three (E3, F3, G3). Each of these wells was then diluted with 80 µL of buffer solution. From the third column, 50 µL was taken from each well using a multichannel pipette and placed into the next column in order to dilute the material in half. This was repeated until the full plate was serially diluted to 0.2 µg/mL. Each time, the material was pipetted up and down three times to ensure proper mixing. Diluted bacterial suspension (50 µL) was added into each well, including the second column as a control (HEPES, broth, and bacteria). Therefore, the final volume in each well was 100 µL.

**Cytation 5 plate reading for kinetic assays**

Absorbance measurements (100 µL of sample per well) were obtained with the Biotek Cytation 5 multimode plate reader and were conducted at 37 °C in a Corning 96-well plate (clear plates, with the lid). The samples were excited at 600 nm and the absorbance values were recorded. Two readings were taken, 10 minutes apart. The reading at 10 minutes was used over the reading at 0 minutes as the blanks were consistent at this time point. After the 10-minute reading, the 96-well

plate was placed back in an incubator for 4 h at 37 °C with orbital shaking at 200 rpm. The absorbance of each well plate at 600 nm was recorded again after 4 h.

### 5.6.6. Supplementary Tables

**Table S5.1.** Polymers used in this work for antibacterial investigations of nanofibers formed via living CDSA. Data reproduced with permission from the Royal Society of Chemistry.[56,66] and from the American Chemical Society.[42]

| Polymer | $M_n$ (g/mol) GPC | $M_w$ (g/mol) GPC | $Đ_M$ GPC | $DP_n$ NMR | $DP_n$ MALDI-TOF |
|---|---|---|---|---|---|
| **PFTMC$_m$-*b*-PDMAEMA$_n$** | 87,900 | 102,100 | 1.16 | **m** = 26<br>**n** = 424 | **m** = 26 |
| **PFTMC$_m$-*b*-PDMAEMA$_o$** | 17,184 | 31,250 | 1.8 | **m** = 20<br>**o** = 300 | - |
| **PFTMC$_p$-*b*-PNIPAM$_q$** | 31,800 | 55,900 | 1.76 | **p** = 18<br>**q** = 425 | **p** = 18 |
| **PFTMC$_p$-*b*-PEG$_r$** | 26,600 | 30,300 | 1.14 | **p** = 18<br>**r** = 530 | **p** = 18 |

### 5.6.7. Supplementary Figures

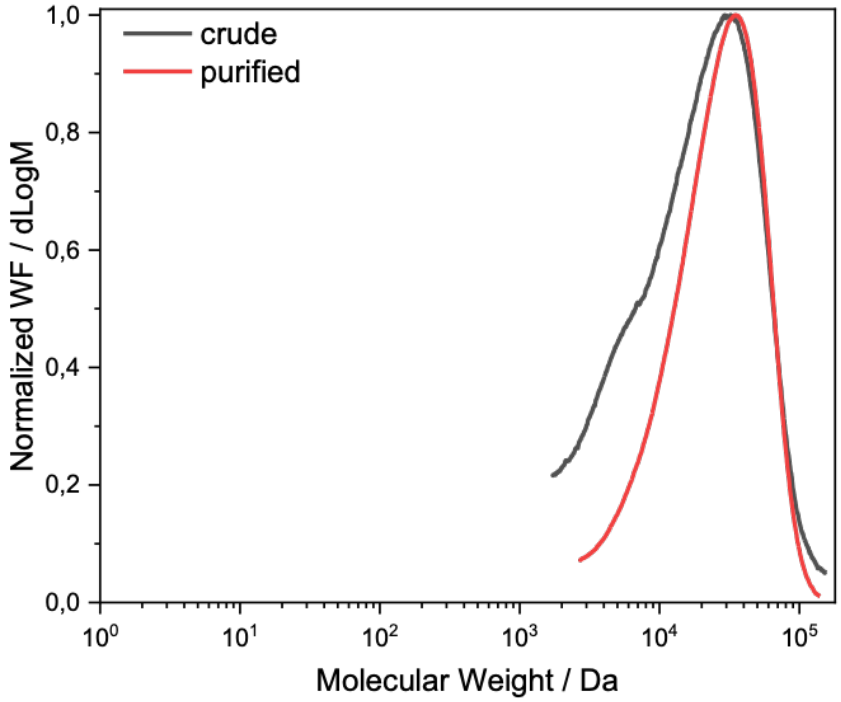


**Figure S5.1.** GPC chromatograph of $PFTMC_{20}$-*b*-$PDMAEMA_{300}$ before (black trace) and after purification (red trace). Each sample consisted of 100 uL of 1 mg/mL BCP in HPLC grade THF, filtered through a 0.2 µm syringe filter.

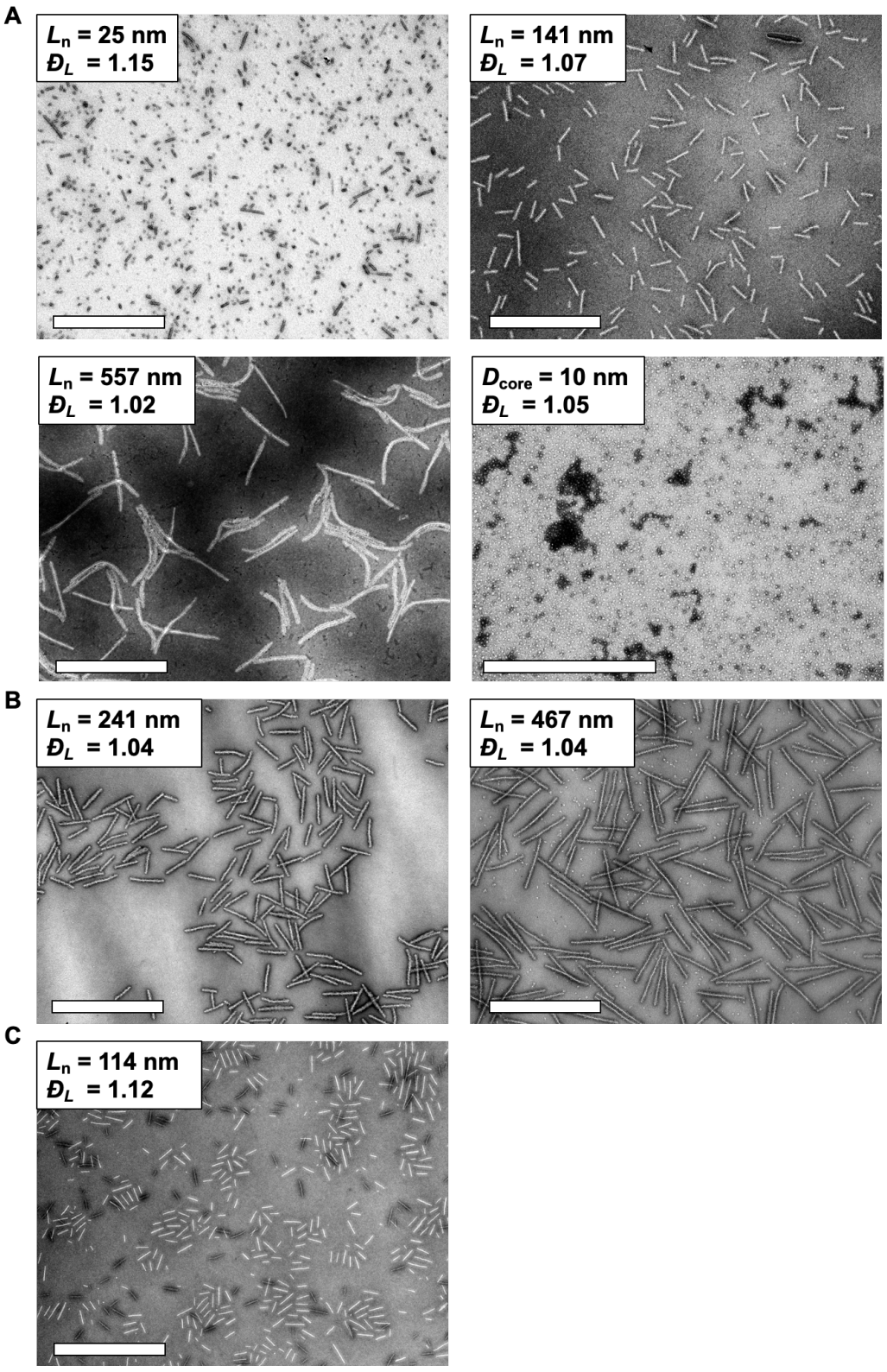


**Figure S5.2.** TEM micrographs of nanoparticles used in this work. (A) $PFTMC_{20}$-*b*-$PDMAEMA_{300}$ length-controlled nanofibers and morphologically pure nanospheres. (B)

PFTMC$_{18}$-*b*-PDMAEMA$_{425}$ length-controlled nanofibers prepared via living CDSA. (C) Low dispersity nanofibers from PFTMC$_{18}$-*b*-PEG$_{530}$.

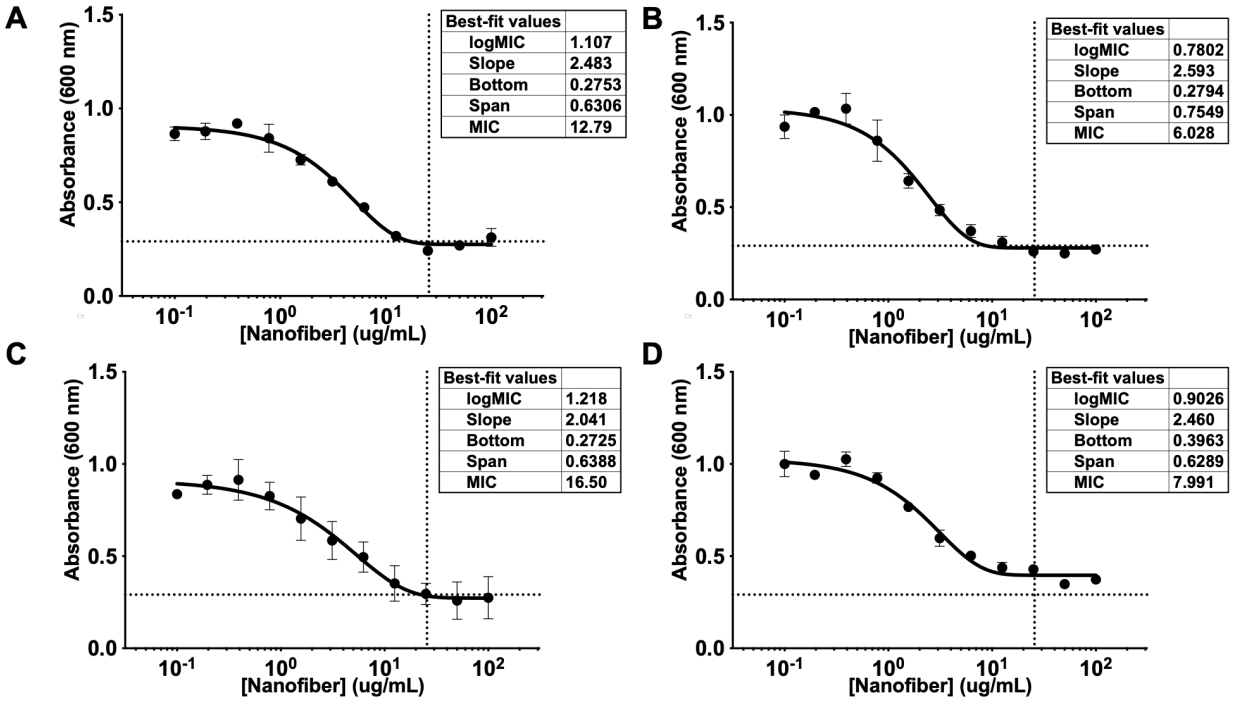


**Figure S5.3.** Antibacterial growth curves of *S. epi* in the presence of (A) 109 nm P1 nanofibers, (B) 483 nm P1 nanofibers, (C) 109 nm P1 nanofibers loaded with 20 wt % tetracycline, and (D) 483 nm P1 nanofibers loaded with 20 wt % tetracycline. No significant change in the bacterial growth is observed between samples containing or not containing tetracycline.

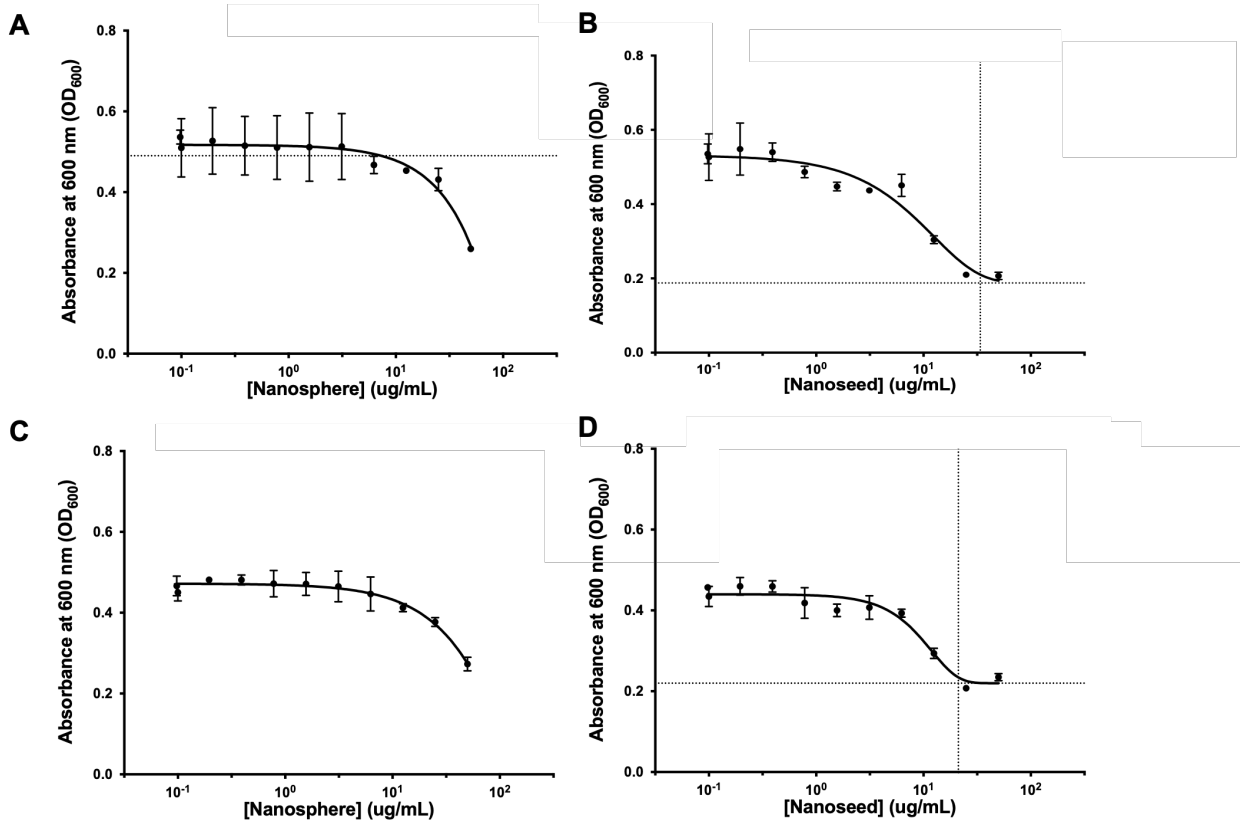


**Figure S5.4.** Bacterial growth curves of *S. epi* in the presence of nanofiber seeds or nanospheres. (A) Nanospheres, where no MIC is determinable (B) Seed nanofibers, (C) Nanospheres loaded with 20 wt % tetracycline, again no MIC is determinable, and (D) Seed nanofibers loaded 20 wt % with tetracycline. No statistically significant difference in MIC between loaded and non-loaded seed nanofibers was observed.

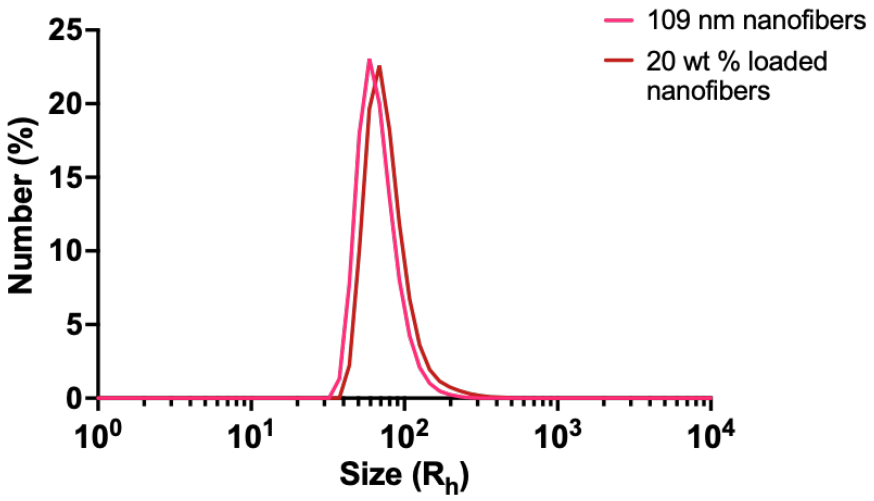


**Figure S5.5.** Hydrodynamic radius expressed by number of 109 nm P1 nanofibers without erythromycin (pink trace), and loaded with 20 wt % erythromycin (red trace).

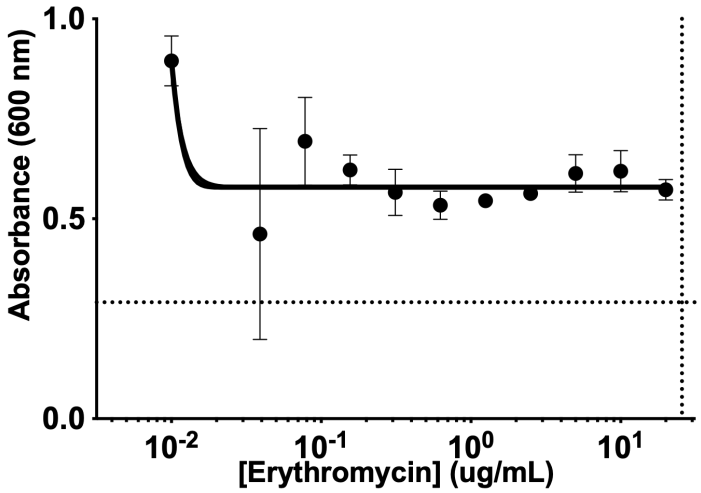


**Figure S5.6.** Bacterial growth curve of *S. epi* in the presence of erythromycin alone, from a concentration of 20 µg/mL to 0.1 µg/mL.

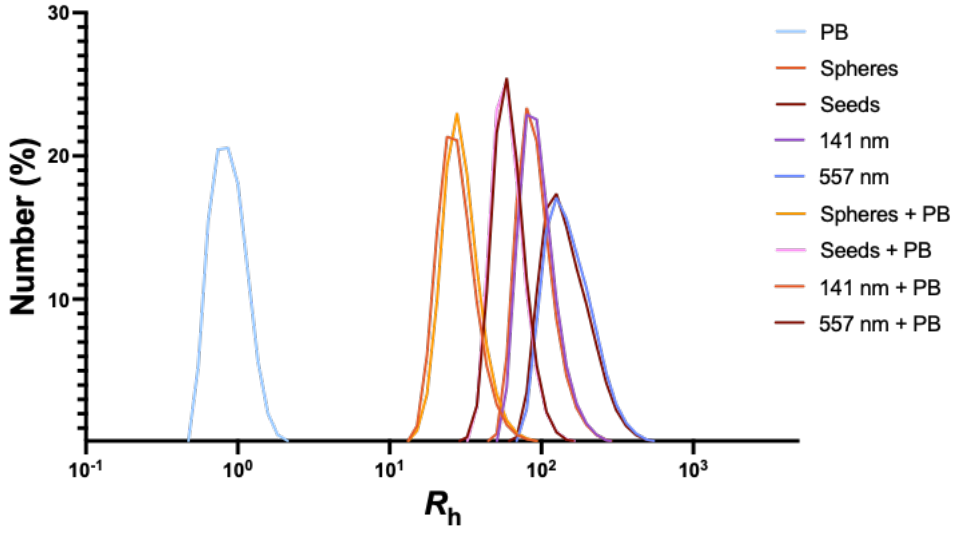


**Figure S5.7.** Hydrodynamic radii of P2 nanoparticles in the presence and absence of polymyxin B. No significant change in hydrodynamic radius is observed at any time, indicating the nanoparticles do not interfere with the structure of polymyxin B or vice versa.

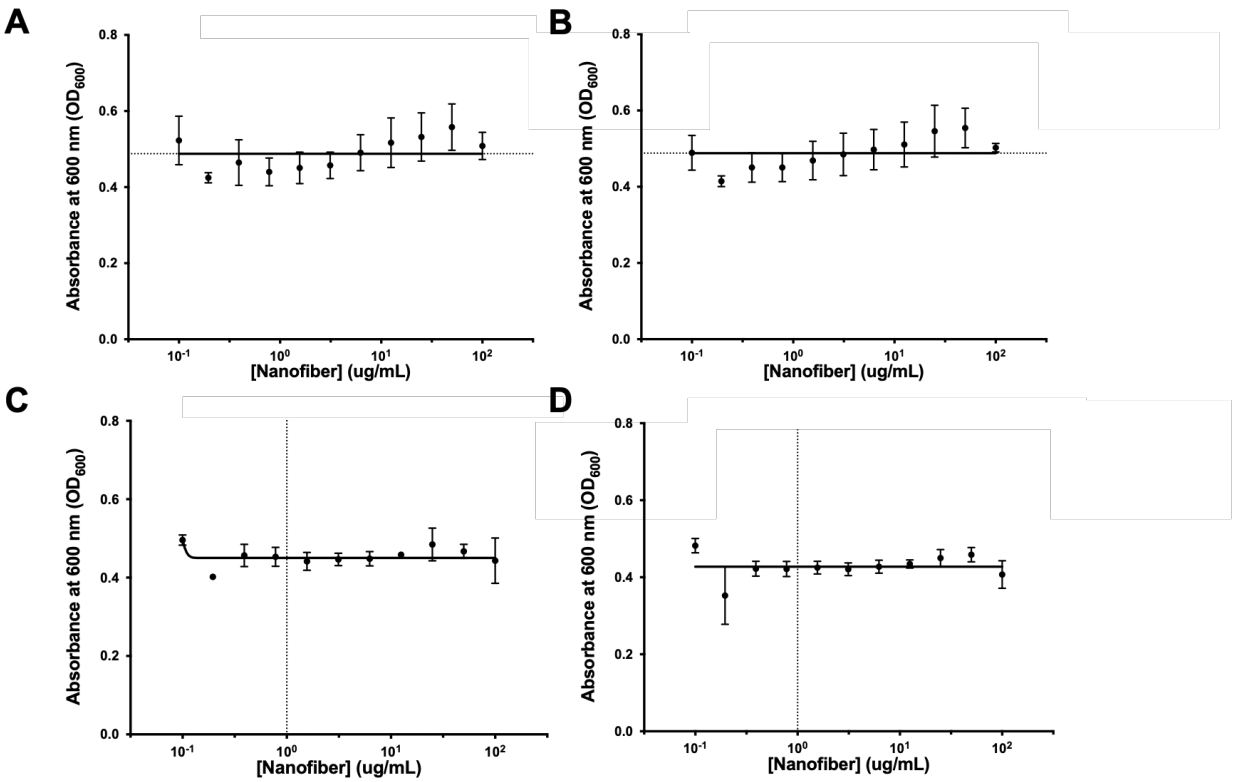


**Figure S5.8.** Bacterial growth curves of *B. vietnamiensis* in the presence of (A) P2 141 nm nanofibers (B) 557 nm nanofibers (C) 141 nm nanofibers and polymyxin B and (D) 557 nm nanofibers and polymyxin B.

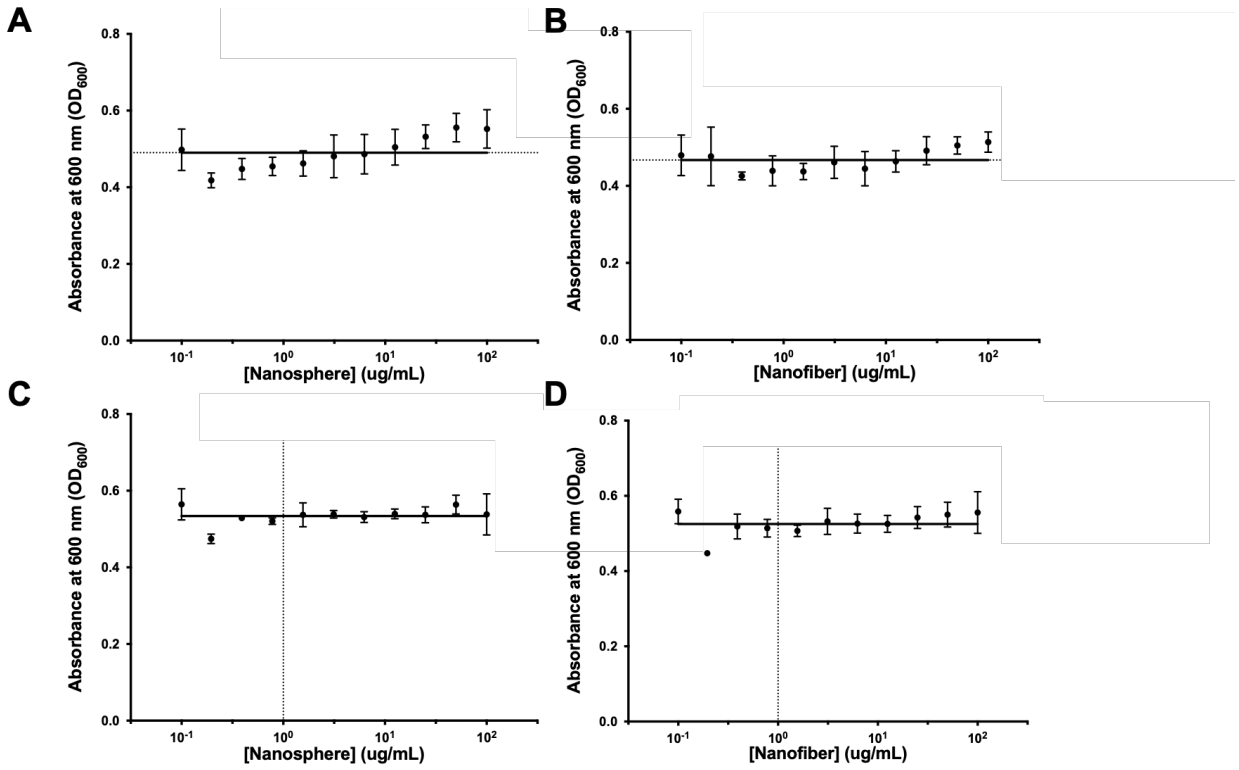


**Figure S5.9.** Bacterial growth curves of *B. vietnamiensis* in the presence of P2 nanoparticles including (A) Nanospheres of 10 nm core diameter (B) Seed nanofibers 25 nm in length, (C) Nanospheres co-incubated with polymyxin B and (D) Seed nanofibers co-incubated with polymyxin B.

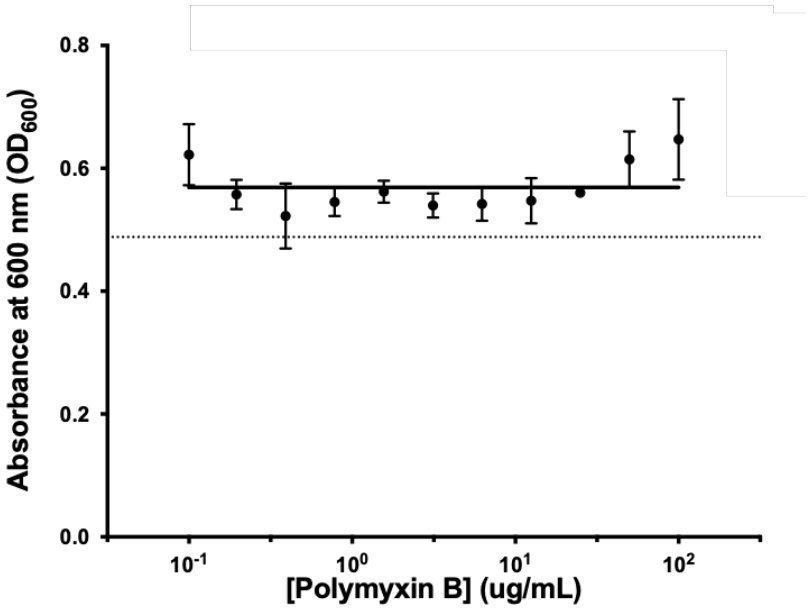


**Figure S5.10.** Bacterial growth curve of *B. vietnamiensis* in the presence of polymyxin B from a concentration of 100 µg/mL to 0.1 µg/mL. No inhibition of growth is observed, and no MIC is determinable.

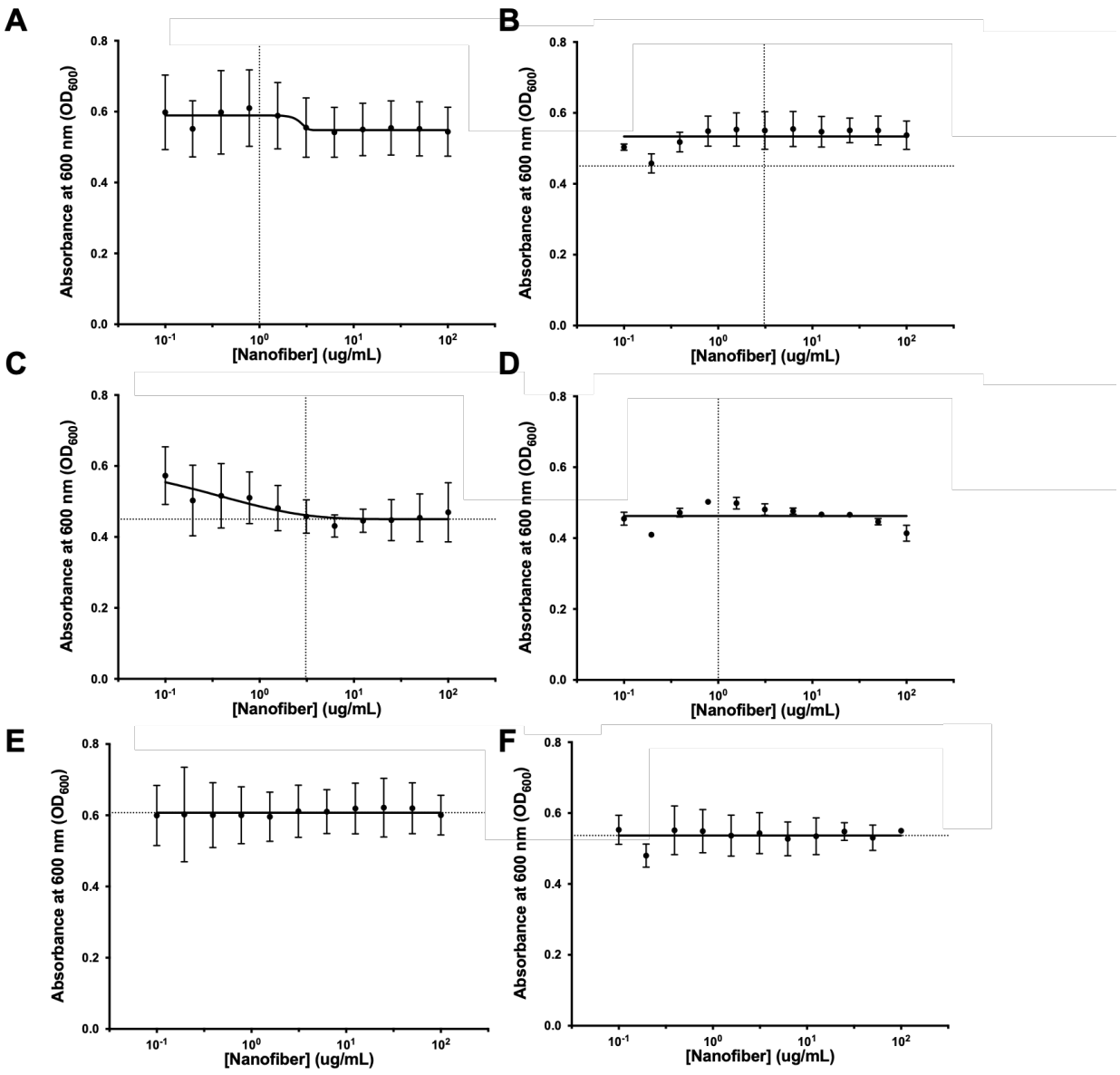


**Figure S5.11.** Bacterial growth curves of *B. vietnamiensis* with P3 and P4 nanofibers, with and without polymyxin B, where (A) is P3 nanofibers, (B) is P3 nanofibers (C) is P3 nanofibers with polymyxin B, (D) is P3 nanofibers with polymyxin B, (E) is P4 nanofibers and (F) is P4 nanofibers with polymyxin B. No sample caused significant bacterial death.

## 5.7 References


1. Lobanovska, M.; Pilla, G. Penicillin's Discovery and Antibiotic Resistance: Lessons for the Future? *Yale Journal of Biology and Medecine* **2017**, *20*, 135–145.
2. D'Costa, V. M.; King, C. E.; Kalan, L.; Morar, M.; Sung, W. W.; Schwarz, C.; Froese, D.; Zazula, G.; Calmels, F.; Debruyne, R.; Golding, G. B.; Poinar, H. N.; Wright, G. D. Antibiotic Resistance Is Ancient. *Nature* **2011**, *477* (7365), 457–461. DOI:10.1038/nature10388.
3. Munita, J. M.; Arias, C. A. Mechanisms of Antibiotic Resistance. *Microbiol. Spectr.* **2016**, *4* (2), 482–490. DOI:10.1128/microbiolspec.vmbf-0016-2015.
4. Blair, J. M.; Webber, M. A.; Baylay, A. J.; Ogbolu, D. O.; Piddock, L. J. Molecular Mechanisms of Antibiotic Resistance. *Nat. Rev. Microbiol.* **2014**, *13* (1), 42–51. DOI:10.1038/nrmicro3380.
5. Darby, E. M.; Trampari, E.; Siasat, P.; Gaya, M. S.; Alav, I.; Webber, M. A.; Blair, J. M. Molecular Mechanisms of Antibiotic Resistance Revisited. *Nat. Rev. Microbiol.* **2022**, *21* (5), 280–295. DOI:10.1038/s41579-022-00820-y.
6. Davies, J.; Davies, D. Origins and Evolution of Antibiotic Resistance. *Microbiol. Mol. Biol. Rev.* **2010**, *74* (3), 417–433. DOI:10.1128/mmbr.00016-10.
7. Albrich, W. C.; Monnet, D. L.; Harbarth, S. Antibiotic Selection Pressure and Resistance in *Streptococcus pneumoniae* and *Streptococcus pyogenes*. *Emerg. Infect. Dis.* **2004**, *10* (3), 514–517. DOI:10.3201/eid1003.030252.
8. Kolář, M.; Urbánek, K.; Látal, T. Antibiotic Selective Pressure and Development of Bacterial Resistance. *Int. J. Antimicrob. Agents* **2001**, *17* (5), 357–363. DOI:10.1016/s0924-8579(01)00317-x.

9. Magana, M.; Pushpanathan, M.; Santos, A. L.; Leanse, L.; Fernandez, M.; Ioannidis, A.; Giulianotti, M. A.; Apidianakis, Y.; Bradfute, S.; Ferguson, A. L.; Cherkasov, A.; Seleem, M. N.; Pinilla, C.; de la Fuente-Nunez, C.; Lazaridis, T.; Dai, T.; Houghten, R. A.; Hancock, R. E.; Tegos, G. P. The Value of Antimicrobial Peptides in the Age of Resistance. *Lancet Infect. Dis.* **2020**, *20* (9), e216–e230. DOI:10.1016/s1473-3099(20)30327-3.
10. Hancock, R. E.; Sahl, H.-G. Antimicrobial and Host-Defense Peptides as New Anti-Infective Therapeutic Strategies. *Nat. Biotechnol.* **2006**, *24* (12), 1551–1557. DOI:10.1038/nbt1267.
11. Zhou, C.; Qi, X.; Li, P.; Chen, W. N.; Mouad, L.; Chang, M. W.; Leong, S. S.; Chan-Park, M. B. High Potency and Broad-Spectrum Antimicrobial Peptides Synthesized via Ring-Opening Polymerization of α-Aminoacid-*n*-Carboxyanhydrides. *Biomacromolecules* **2009**, *11* (1), 60–67. DOI:10.1021/bm900896h.
12. Zhong, C.; Zhang, F.; Yao, J.; Zhu, Y.; Zhu, N.; Zhang, J.; Ouyang, X.; Zhang, T.; Li, B.; Xie, J.; Ni, J. New Antimicrobial Peptides with Repeating Unit against Multidrug-Resistant Bacteria. *ACS Infect. Dis.* **2021**, *7* (6), 1619–1637. DOI:10.1021/acsinfecdis.0c00797.
13. Fjell, C. D.; Hiss, J. A.; Hancock, R. E.; Schneider, G. Designing Antimicrobial Peptides: Form Follows Function. *Nat. Rev. Drug Discov.* **2011**, *11* (1), 37–51. DOI:10.1038/nrd3591.
14. Haney, E. F.; Straus, S. K.; Hancock, R. E. Reassessing the Host Defense Peptide Landscape. *Front. Chem.* **2019**, *7*, 43. DOI:10.3389/fchem.2019.00043.
15. Hale, J. D.; Hancock, R. E. Alternative Mechanisms of Action of Cationic Antimicrobial Peptides on Bacteria. *Exp. Rev. Anti-infective Ther.* **2007**, *5* (6), 951–959. DOI:10.1586/14787210.5.6.951.
16. Hancock, R. E.; Scott, M. G. The Role of Antimicrobial Peptides in Animal Defenses. *Proc. Natl. Acad. Sci.* **2000**, *97* (16), 8856–8861. DOI:10.1073/pnas.97.16.8856.

17. Falla, T. J.; Karunaratne, D. N.; Hancock, R. E. W. Mode of Action of the Antimicrobial Peptide Indolicidin. *J. Biol. Chem.* **1996**, *271* (32), 19298–19303. DOI:10.1074/jbc.271.32.19298.

18. Hancock, R. E. Peptide Antibiotics. *Lancet* **1997**, *349* (9049), 418–422. DOI:10.1016/s0140-6736(97)80051-7.

19. Huang, Y.; Huang, J.; Chen, Y. Alpha-Helical Cationic Antimicrobial Peptides: Relationships of Structure and Function. *Protein Cell* **2010**, *1* (2), 143–152. DOI:10.1007/s13238-010-0004-3.

20. Brown, K. L.; Hancock, R. E. Cationic Host Defense (Antimicrobial) Peptides. *Curr. Opin. Immunol.* **2006**, *18* (1), 24–30. DOI:10.1016/j.coi.2005.11.004.

21. Bechinger, B.; Gorr, S.-U. Antimicrobial Peptides: Mechanisms of Action and Resistance. *J. Dental Res.* **2016**, *96* (3), 254–260. DOI:10.1177/0022034516679973.

22. Yeaman, M. R.; Yount, N. Y. Mechanisms of Antimicrobial Peptide Action and Resistance. *Pharmacol. Rev.* **2003**, *55* (1), 27–55. DOI:10.1124/pr.55.1.2.

23. Rawlinson, L.-A. B.; O'Gara, J. P.; Jones, D. S.; Brayden, D. J. Resistance of Staphylococcus Aureus to the Cationic Antimicrobial Agent Poly(2-(Dimethylamino Ethyl)Methacrylate) (Pdmaema) Is Influenced by Cell-Surface Charge and Hydrophobicity. *J. Med. Microbiol.* **2011**, *60* (7), 968–976. DOI:10.1099/jmm.0.025619-0.

24. Moore, R. A.; Hancock, R. E. Involvement of Outer Membrane of Pseudomonas Cepacia in Aminoglycoside and Polymyxin Resistance. *Antimicrob. Agents Chemother.* **1986**, *30* (6), 923–926. DOI:10.1128/aac.30.6.923.

25. Loutet, S. A.; Mussen, L. E.; Flannagan, R. S.; Valvano, M. A. A Two-tier Model of Polymyxin B Resistance in *Burkholderia cenocepacia*. *Environ. Microbiol. Rep.* **2010**, *3* (2), 278–285. DOI:10.1111/j.1758-2229.2010.00222.x.

26. Loutet, S. Extreme Antimicrobial Peptide and Polymyxin B Resistance in the Genus Burkholderia. *Front. Cell. Infect. Microbiol.* **2011**, *1*, 6. DOI:10.3389/fcimb.2011.00006.

27. Shommu, N. S.; Vogel, H. J.; Storey, D. G. Potential of Metabolomics to Reveal Burkholderia Cepacia Complex Pathogenesis and Antibiotic Resistance. *Front. Microbiol.* **2015**, *6*, 668. DOI:10.3389/fmicb.2015.00668.

28. Vermis, K.; Vandamme, P. A. R.; Nelis, H. J. Burkholderia Cepacia Complex Genomovars: Utilization of Carbon Sources, Susceptibility to Antimicrobial Agents and Growth on Selective Media. *J. Appl. Microbiol.* **2003**, *95* (6), 1191–1199. DOI:10.1046/j.1365-2672.2003.02054.x.

29. Kamaruzzaman, N. F.; Tan, L. P.; Hamdan, R. H.; Choong, S. S.; Wong, W. K.; Gibson, A. J.; Chivu, A.; Pina, M. de. Antimicrobial Polymers: The Potential Replacement of Existing Antibiotics? *Int. J. Mol. Sci.* **2019**, *20* (11), 2747. DOI:10.3390/ijms20112747.

30. Lam, S. J.; Wong, E. H. H.; Boyer, C.; Qiao, G. G. Antimicrobial Polymeric Nanoparticles. *Prog. Polym. Sci.* **2018**, *76*, 40–64. DOI:10.1016/j.progpolymsci.2017.07.007.

31. Carmona-Ribeiro, A.; de Melo Carrasco, L. Cationic Antimicrobial Polymers and Their Assemblies. *Int. J. Mol. Sci.* **2013**, *14* (5), 9906–9946. DOI:10.3390/ijms14059906.

32. Roy, D.; Knapp, J. S.; Guthrie, J. T.; Perrier, S. Antibacterial Cellulose Fiber via Raft Surface Graft Polymerization. *Biomacromolecules* **2007**, *9* (1), 91–99. DOI:10.1021/bm700849j.

33. Kuroki, A.; Kengmo Tchoupa, A.; Hartlieb, M.; Peltier, R.; Locock, K. E. S.; Unnikrishnan, M.; Perrier, S. Targeting Intracellular, Multi-Drug Resistant Staphylococcus Aureus with

Guanidinium Polymers by Elucidating the Structure-Activity Relationship. *Biomaterials* **2019**, *217*, 119249. DOI:10.1016/j.biomaterials.2019.119249.

34. Ding, X.; Wang, A.; Tong, W.; Xu, F. Biodegradable Antibacterial Polymeric Nanosystems: A New Hope to Cope with Multidrug-resistant Bacteria. *Small* **2019**, *15* (20), 1900999. DOI:10.1002/smll.201900999.
35. Yao, D.; Guo, Y.; Chen, S.; Tang, J.; Chen, Y. Shaped Core/Shell Polymer Nanoobjects with High Antibacterial Activities via Block Copolymer Microphase Separation. *Polymer* **2013**, *54* (14), 3485–3491. DOI:10.1016/j.polymer.2013.05.005.
36. Song, J.; Jang, J. Antimicrobial Polymer Nanostructures: Synthetic Route, Mechanism of Action and Perspective. *Adv. Colloid Interface Sci.* **2014**, *203*, 37–50. DOI:10.1016/j.cis.2013.11.007.
37. Lim, Y. H.; Tiemann, K. M.; Heo, G. S.; Wagers, P. O.; Rezenom, Y. H.; Zhang, S.; Zhang, F.; Youngs, W. J.; Hunstad, D. A.; Wooley, K. L. Preparation and *in Vitro* Antimicrobial Activity of Silver-Bearing Degradable Polymeric Nanoparticles of Polyphosphoester-*Block*-Poly(L-Lactide). *ACS Nano* **2015**, *9* (2), 1995–2008. DOI:10.1021/nn507046h.
38. Guo, L.; Wang, H.; Wang, Y.; Liu, F.; Feng, L. Organic Polymer Nanoparticles with Primary Ammonium Salt as Potent Antibacterial Nanomaterials. *ACS Appl. Mater. Interfaces* **2020**, *12* (19), 21254–21262. DOI:10.1021/acsami.9b19921.
39. Li, Z.; Pearce, A. K.; Du, J.; Dove, A. P.; O'Reilly, R. K. Uniform Antibacterial Cylindrical Nanoparticles for Enhancing the Strength of Nanocomposite Hydrogels. *J. Polym. Sci.* **2022**, *61* (1), 44–55. DOI:10.1002/pol.20210853.

40. Inam, M.; Foster, J. C.; Gao, J.; Hong, Y.; Du, J.; Dove, A. P.; O'Reilly, R. K. Size and Shape Affects the Antimicrobial Activity of Quaternized Nanoparticles. *J. Polym. Sci. Part A: Polym. Chem.* **2018**, *57* (3), 255–259. DOI:10.1002/pola.29195.

41. Parkin, H. C.; Garcia-Hernandez, J. D.; Street, S. T.; Hof, R.; Manners, I. Uniform, Length-Tunable Antibacterial 1D Diblock Copolymer Nanofibers. *Polym. Chem.* **2022**, *13* (20), 2941–2949. DOI:10.1039/d2py00262k.

42. Parkin, H. C.; Street, S. T. G; Gowen, B.; Da-Silva-Correa, L. H.; Hof, R.; Buckley, H. L.; Manners, I. Mechanism of Action and Design of Potent Antibacterial Block Copolymer Nanoparticles. *J. Am. Chem. Soc.* **2024**, *146* (8), 5128–5141. DOI:10.1021/jacs.3c09033.

43. Sikder, A.; Pearce, A. K.; Kumar, C. M.; O'Reilly, R. K. Elucidating the Role of Multivalency, Shape, Size and Functional Group Density on Antibacterial Activity of Diversified Supramolecular Nanostructures Enabled by Templated Assembly. *Mater. Horiz.* **2023**, *10* (1), 171–178. DOI:10.1039/d2mh01117d.

44. Wang, X.; Guerin, G.; Wang, H.; Wang, Y.; Manners, I.; Winnik, M. A. Cylindrical Block Copolymer Micelles and Co-Micelles of Controlled Length and Architecture. *Science* **2007**, *317* (5838), 644–647. DOI:10.1126/science.1141382.

45. Gilroy, J. B.; Gädt, T.; Whittell, G. R.; Chabanne, L.; Mitchels, J. M.; Richardson, R. M.; Winnik, M. A.; Manners, I. Monodisperse Cylindrical Micelles by Crystallization-Driven Living Self-Assembly. *Nat. Chem.* **2010**, *2* (7), 566–570. DOI:10.1038/nchem.664.

46. Inam, M.; Cambridge, G.; Pitto-Barry, A.; Laker, Z. P.; Wilson, N. R.; Mathers, R. T.; Dove, A. P.; O'Reilly, R. K. 1D vs. 2D Shape Selectivity in the Crystallization-Driven Self-Assembly of Polylactide Block Copolymers. *Chem. Sci.* **2017**, *8* (6), 4223–4230. DOI:10.1039/c7sc00641a.

47. MacFarlane, L.; Zhao, C.; Cai, J.; Qiu, H.; Manners, I. Emerging Applications for Living Crystallization-Driven Self-Assembly. *Chem. Sci.* **2021**, *12* (13), 4661–4682. DOI:10.1039/d0sc06878k.

48. Guérin, G.; Wang, H.; Manners, I.; Winnik, M. A. Fragmentation of Fiberlike Structures: Sonication Studies of Cylindrical Block Copolymer Micelles and Behavioral Comparisons to Biological Fibrils. *J. Am. Chem. Soc.* **2008**, *130* (44), 14763–14771. DOI:10.1021/ja805262v.

49. Vespa, M.; Hudson, Z. M.; Manners, I. Homogeneous and Segmented Nanofibers with a Conjugated Poly[3-(2′-Ethylhexyl)Thiophene] Core via Living Crystallization-Driven Self-Assembly. *Macromolecules* **2024**, *57* (4), 1509–1520. DOI:10.1021/acs.macromol.3c02357.

50. Qiu, H.; Cambridge, G.; Winnik, M. A.; Manners, I. Multi-Armed Micelles and Block Co-Micelles via Crystallization-Driven Self-Assembly with Homopolymer Nanocrystals as Initiators. *J. Am. Chem. Soc.* **2013**, *135* (33), 12180–12183. DOI:10.1021/ja404100w.

51. Rupar, P. A.; Chabanne, L.; Winnik, M. A.; Manners, I. Non-Centrosymmetric Cylindrical Micelles by Unidirectional Growth. *Science* **2012**, *337* (6094), 559–562. DOI:10.1126/science.1221206.

52. Hudson, Z. M.; Lunn, D. J.; Winnik, M. A.; Manners, I. Colour-Tunable Fluorescent Multiblock Micelles. *Nat. Commun.* **2014**, *5*, 3372. DOI:10.1038/ncomms4372.

53. Tritschler, U.; Pearce, S.; Gwyther, J.; Whittell, G. R.; Manners, I. *50th Anniversary Perspective*: Functional Nanoparticles from the Solution Self-Assembly of Block Copolymers. *Macromolecules* **2017**, *50* (9), 3439–3463. DOI:10.1021/acs.macromol.6b02767.

54. Arno, M. C.; Inam, M.; Coe, Z.; Cambridge, G.; Macdougall, L. J.; Keogh, R.; Dove, A. P.; O'Reilly, R. K. Precision Epitaxy for Aqueous 1D and 2D Poly(ε-caprolactone) Assemblies. *J. Am. Chem. Soc.* **2017**, *139* (46), 16980–16985. DOI:10.1021/jacs.7b10199.

55. Ganda, S.; Stenzel, M. H. Concepts, Fabrication Methods and Applications of Living Crystallization-Driven Self-Assembly of Block Copolymers. *Prog. Polym. Sci.* **2020**, *101*, 101195. DOI:10.1016/j.progpolymsci.2019.101195.

56. Garcia-Hernandez, J. D.; Parkin, H. C.; Ren, Y.; Zhang, Y.; Manners, I. Hydrophobic Cargo Loading at the Core–Corona Interface of Uniform, Length-Tunable Aqueous Diblock Copolymer Nanofibers with a Crystalline Polycarbonate Core. *Polym. Chem.* **2022**, *13* (28), 4100–4110. DOI:10.1039/d2py00395c.

57. Garcia-Hernandez, J. D.; Street, S. T. G.; Kang, Y.; Zhang, Y.; Manners, I. Cargo Encapsulation in Uniform, Length-Tunable Aqueous Nanofibers with a Coaxial Crystalline and Amorphous Core. *Macromolecules* **2021**, *54* (12), 5784–5796. DOI:10.1021/acs.macromol.1c00672.

58. Garg, T.; Rath, G.; Goyal, A. K. Inhalable Chitosan Nanoparticles as Antitubercular Drug Carriers for an Effective Treatment of Tuberculosis. *Artif. Cells Nanomed. Biotechnol.* **2015**, *44* (3), 997–1001. DOI:10.3109/21691401.2015.1008508.

59. Jasim, R.; Schneider, ElenaK.; Han, M.; Azad, MohammadA. K.; Hussein, M.; Nowell, C.; Baker, MarkA.; Wang, J.; Li, J.; Velkov, T. A Fresh Shine on Cystic Fibrosis Inhalation Therapy: Antimicrobial Synergy of Polymyxin B in Combination with Silver Nanoparticles. *J. Biomed. Nanotechnol.* **2017**, *13* (4), 447–457. DOI:10.1166/jbn.2017.2355.

60. Messiaen, A.-S.; Forier, K.; Nelis, H.; Braeckmans, K.; Coenye, T. Transport of Nanoparticles and Tobramycin-Loaded Liposomes in Burkholderia Cepacia Complex Biofilms. *PLoS ONE* **2013**, *8* (11), e79220. DOI:10.1371/journal.pone.0079220.

61. Jassem, A. N.; Zlosnik, J. E.; Henry, D. A.; Hancock, R. E.; Ernst, R. K.; Speert, D. P. *In Vitro* Susceptibility of Burkholderia Vietnamiensis to Aminoglycosides. *Antimicrob. Agents Chemother.* **2011**, *55* (5), 2256–2264. DOI:10.1128/aac.01434-10.

62. Loutet, S. A.; El-Halfawy, O. M.; Jassem, A. N.; López, J. M.; Medarde, A. F.; Speert, D. P.; Davies, J. E.; Valvano, M. A. Identification of Synergists That Potentiate the Action of Polymyxin B against Burkholderia Cenocepacia. *Int. J. Antimicrob. Agents* **2015**, *46* (4), 376–380. DOI:10.1016/j.ijantimicag.2015.05.010.

63. Olaitan, A. O.; Morand, S.; Rolain, J.-M. Mechanisms of Polymyxin Resistance: Acquired and Intrinsic Resistance in Bacteria. *Front. Microbiol.* **2014**, *5*, 643. DOI:10.3389/fmicb.2014.00643.

64. Moffatt, J. H.; Harper, M.; Boyce, J. D. Mechanisms of Polymyxin Resistance. *Adv. Exp. Med. Biol.* **2019**, 55–71. DOI:10.1007/978-3-030-16373-0_5.

65. Zavascki, A. P.; Goldani, L. Z.; Li, J.; Nation, R. L. Polymyxin B for the Treatment of Multidrug-Resistant Pathogens: A Critical Review. *J. Antimicrob. Chemother.* **2007**, *60* (6), 1206–1215. DOI:10.1093/jac/dkm357.

66. Street, S. T. G; Parkin, H. C.; Shopperly, L.; Chrenek, J.; Letwin, K.; Willerth, S. M.; Manners, I. Optimization of Precision Nanofiber Micelleplexes for DNA Delivery. *Biomater. Sci.* **2023**, *11* (10), 3512–3523. DOI:10.1039/d2bm02014a.

67. Street, S. T. G; He, Y.; Harniman, R. L.; Garcia-Hernandez, J. D.; Manners, I. Precision Polymer Nanofibers with a Responsive Polyelectrolyte Corona Designed as a Modular, Functionalizable Nanomedicine Platform. *Polym. Chem.* **2022**, *13* (20), 3009–3025. DOI:10.1039/d2py00152g.

68. Street, S. T. G; Chrenek, J.; Harniman, R. L.; Letwin, K.; Mantell, J. M.; Borucu, U.; Willerth, S. M.; Manners, I. Length-Controlled Nanofiber Micelleplexes as Efficient Nucleic Acid Delivery Vehicles. *J. Am. Chem. Soc.* **2022**, *144* (43), 19799–19812. DOI:10.1021/jacs.2c06695.

69. Finnegan, J. R.; He, X.; Street, S. T.; Garcia-Hernandez, J. D.; Hayward, D. W.; Harniman, R. L.; Richardson, R. M.; Whittell, G. R.; Manners, I. Extending the Scope of "Living" Crystallization-Driven Self-Assembly: Well-Defined 1D Micelles and Block Comicelles from Crystallizable Polycarbonate Block Copolymers. *J. Am. Chem. Soc.* **2018**, *140* (49), 17127–17140. DOI:10.1021/jacs.8b09861.

70. He, X.; Finnegan, J. R.; Hayward, D. W.; MacFarlane, L. R.; Harniman, R. L.; Manners, I. Living Crystallization-Driven Self-Assembly of Polymeric Amphiphiles: Low-Dispersity Fiber-like Micelles from Crystallizable Phosphonium-Capped Polycarbonate Homopolymers. *Macromolecules* **2020**, *53* (23), 10591–10600. DOI:10.1021/acs.macromol.0c02075.

71. Madigan, M. T.; Bender, K. S.; Buckley, D. H.; Sattley, W. M.; Stahl, D. A.; Brock, T. D. *Brock Biol. Microorg.*; Pearson, 2022.

72. Lambert, R. J. W.; Pearson, J. Susceptibility Testing: Accurate and Reproducible Minimum Inhibitory Concentration (MIC) and Non-Inhibitory Concentration (NIC) Values. *J. Appl. Microbiol.* **2000**, *88* (5), 784–790. DOI:10.1046/j.1365-2672.2000.01017.x.

73. Sabath, L. D.; Garner, C.; Wilcox, C.; Finland, M. Susceptibility of *Staphylococcus aureus* and *Staphylococcus epidermidis* to 65 Antibiotics. *Antimicrob. Agents Chemother.* **1976**, *9* (6), 962–969. DOI:10.1128/aac.9.6.962.

74. Fehlner-Gardiner, C. C.; Valvano, M. A. Cloning and Characterization of the *Burkholderia vietnamiensis Norm* Gene Encoding a Multi-Drug Efflux Protein. *FEMS Microbiol. Lett.* **2002**, *215* (2), 279–283. DOI:10.1111/j.1574-6968.2002.tb11403.x.

75. Rhodes, K. A.; Schweizer, H. P. Antibiotic Resistance in Burkholderia Species. *Drug Resist. Updat.* **2016**, *28*, 82–90. DOI:10.1016/j.drup.2016.07.003.

76. Podnecky, N. L.; Rhodes, K. A.; Schweizer, H. P. Efflux Pump-Mediated Drug Resistance in Burkholderia. *Front. Microbiol.* **2015**, *6*, 305. DOI:10.3389/fmicb.2015.00305.

# Chapter 6

# Conclusions

## 6.1 Conclusions and Future Work

The work outlined in this thesis expands on the use of 1D nanofibers for biomedical applications, specifically for antibacterial activity and drug delivery. Chapter 2 investigates the inherent antibacterial activity of 1D PFTMC-*b*-PDMAEMA nanofibers against *E. coli*, and determines that long nanofibers possess higher inherent antibacterial activity over nanospheres. Furthermore, the cationic corona was found to be essential for mediating antibacterial activity. Chapter 3 then explores the antibacterial mechanism of action of such 1D nanofibers relative to nanospheres through the use of high-resolution microscopy and flow cytometry. We determine that long nanofibers display enhanced targeting of the bacteria relative to other nanoparticle sizes and shapes, and are better able to intercalate the bacterial membrane, resulting in their higher amounts of membrane damage. Chapter 4 expands upon previous work detailing the delivery of nucleic acids to mammalian cells through targeting of the cell surface with PDMAEMA-based 1D nanofibers, which demonstrated that short seed nanofibers (ca. 25 nm) are the most efficient for cargo delivery. Therefore, the anticancer drug paclitaxel was loaded at the core-corona interface of 25 nm 1D nanofibers. The cell viability of glioblastoma cells was then determined in both 2D and 3D cell models. Importantly, while the anisotropic shape doesn't appear to offer many advantages in the 2D cell model, it appears to assist in spheroid penetration in the 3D cell model to deliver therapeutic in high yields. Finally, chapter 5 begins exploratory work into extending the

scope of antibacterial action of 1D nanofibers against gram-positive, and drug-resistant bacteria. Synergy is identified when both common antibiotics and antimicrobial peptides are co-incubated with nanofibers, but further work is required to improve the potency of 1D nanofibers against antibiotic-resistant bacterial strains such as *B. vietnamiensis*.

### 6.1.1 Modification of the corona-forming block for enhanced targeting and lower cytotoxicity

PDMAEMA has been demonstrated to be an exceptional corona-forming block for biomedical applications, as the cationic charge allows for efficient targeting of both mammalian and bacterial cell membranes, indiscriminately. While this is ideal for examining cell uptake and delivery mechanisms, issues remain with the inherent toxicity associated with this functionality. For example, while the antibacterial activity is high, the relative toxicity against mammalian cells is also high. Therefore, the development of corona-forming blocks that target either mammalian cells or bacterial cells would be of great interest. Carbohydrate receptors on the surface of mammalian cells are promising candidates for selective targeting, and due to the vast range of sugars utilized for mammalian metabolism, a multitude of corona-forming blocks could be explored. Work has recently begun on the development of bioactive block copolymers with polyfructose corona, but other synthetic targets include polyglucose and polymannose coronas (Figure 6.1). In particular, glucose receptors are prevalent at the blood-brain-barrier as glucose is the sole source of energy utilized by the brain, and thus integration of a glucose corona could be beneficial for targeting this area.[1,2] Due to the simplicity of the bacterial membrane, active targeting is more challenging. Lysine is an amino acid that is very similar in structure to PDMAEMA and that bears antibacterial activity, but may be more well-tolerated by mammalian cells.[3] Furthermore, most amino acids can be integrated into block copolymers through RAFT polymerization, and thus other cationic amino

acids may be promising for use as corona-forming blocks.[4] For example, *E. coli* possesses chemoreceptors that are bound directly by serine, and thus this may allow for nanofiber targeting to bacteria while diminishing off-target toxic effects.[5]

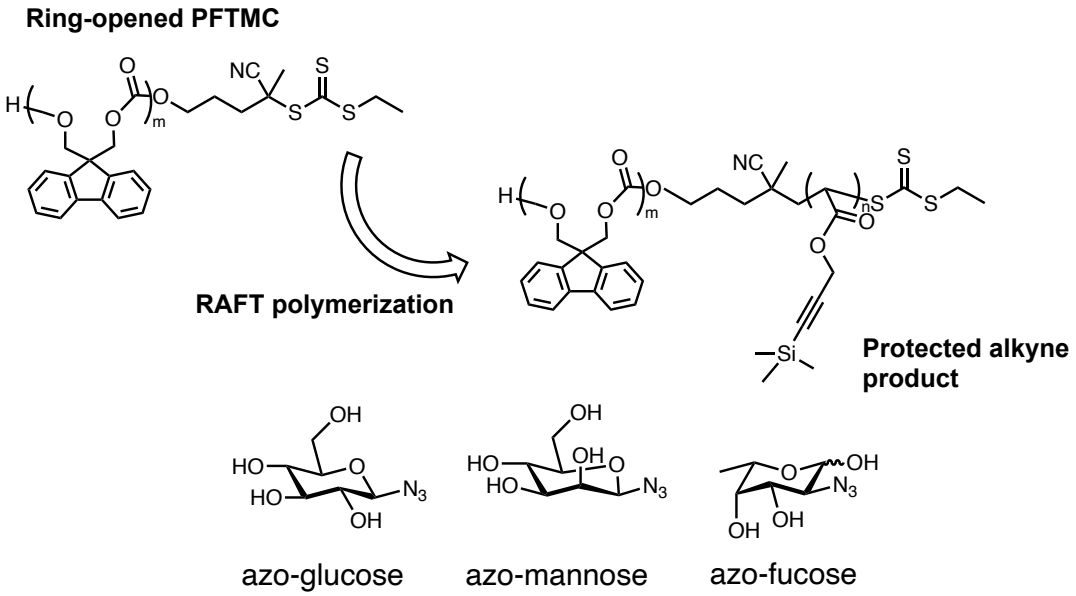


**Figure 6.1.** Synthetic route to PFTMC-based polymers containing sugar corona-forming blocks. Steps include ROP of the PFTMC monomer with the RAFT CTA, followed by RAFT polymerization using a methacrylate containing a protected alkyne functional handle. A deprotection and click reaction could then be performed to yield the final product.

### 6.1.2 Modification of cargo-loading for enhanced activity

While achieving more specific targeting is a major goal of future work, enhancing the activity by modifying the cargo delivered to the cell is also an option to reduce the effective concentration of the material. This is performed with antibiotics in chapters 3 and 5, and chemotherapeutics in chapter 4, but more options exist for such purposes. For example, in chapter 4 paclitaxel is selected as the loaded anticancer therapeutic; however, if paclitaxel is delivered to a healthy cell, it will still exert its cytotoxic effect. Loading nucleic acids, which only affect the growth of cancer cells and do not disturb healthy cells, is therefore a promising alternative. P53 is a gene that is disrupted in

about 50 % of cancer-causing cells and contributes to their uncontrolled division.[6,7] Wild type p53 regulates the cell-cycle and normally induces apoptosis when cells are unhealthy;[6] therefore, if wild type p53 could be complexed to the nanofibers and delivered to cells in which p53 is mutated, this would help transiently reinstate the proper function of p53 and lead to cell death (Figure 6.2). This may disproportionately affect cancer cells leading to tumor shrinkage, while having lower cytotoxic effects on quiescent cells. For loading nucleic acid cargo to target bacteria, bacteriophages are potent bactericidal viruses. Their mechanism of action involves attaching to the bacterial membrane, followed by injection of their DNA. This then hijacks the bacteria replicative machinery, producing several copies of the virus internally.[8,9] A limit is eventually reached where the bacterium is not able to withstand further virus replication, and cell lysis is triggered.[10] Therefore, bacteriophage DNA could be complexed to the nanofiber cationic corona and effectively delivered to the bacterium. This would be advantageous as any unwanted toxicity from the virus towards mammalian cells would also be limited.

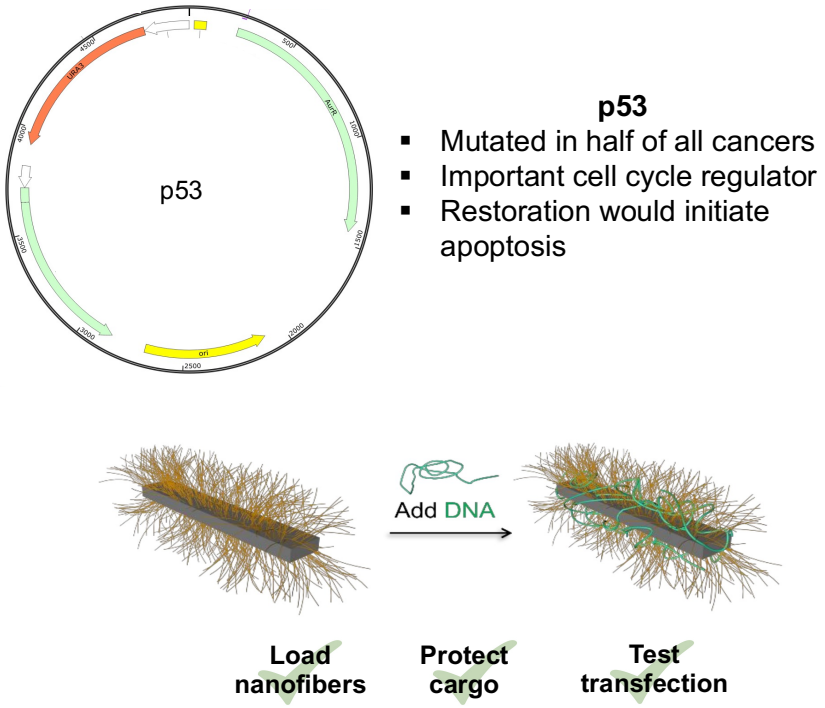


**Figure 6.2.** General schematic of the p53 plasmid which can be replicated in and isolated from bacterial cells, followed by the process of complexing the anionic nucleic acid to the cationic nanofiber corona for cargo delivery.

### 6.1.3 Scale-up of nanofiber production for clinical use

Finally, a significant challenge faced by these systems is the overall rate in which nanofibers can be produced. Traditional self-assembly to form polydisperse nanofibers takes place in about 1 mL of 1 mg/mL solution. Living CDSA is normally performed at volumes ranging from 50 µL – 1 mL and should not exceed concentrations of approximately 10 mg/mL, as self-nucleation can begin to compete with elongation. Therefore, two different processes have been investigated for scaling up nanofiber production: living CDSA in flow, and polymerization-induced CDSA (PI-CDSA) (Figure 6.3).[11,12] Living CDSA in flow allows for the continuous production of nanofibers, through control of the polymer concentration and flow rate through the reactor.[11] Initial studies by our group have shown promising results for the generation of uniform seed nanofibers at high

concentrations and volumes. However, further work is needed to extend this methodology to biocompatible systems, such as PFTMC-*b*-PDMAEMA and to generate length-controlled nanofibers at various unimer/seed ratios with low dispersities. PI-CDSA is another promising alternative which was applied to the synthesis and self-assembly of PFTMC-*b*-PEG, where PEG was utilized as a macroinitiator for ROP.[12] Upon addition of seeds into the reaction mixture, uniform fibers are formed through epitaxial growth as the polymer reaches a critical degree of polymerization. Another major advantage of this process is that a reduction in homopolymer byproduct is formed, which is traditionally a significant challenge to remove from the block copolymer product. The PDMAEMA homopolymer would need to be altered to contain a terminal alcohol functionality. which could be used for the initiation of the ROP of the FTMC monomer, and an appropriate solvent system would need to be chosen that can cause the crystallization of the PFTMC as the degree of polymerization increases. Overall, scale-up will significantly increase the potential of 1D nanofibers finding success in clinical applications.

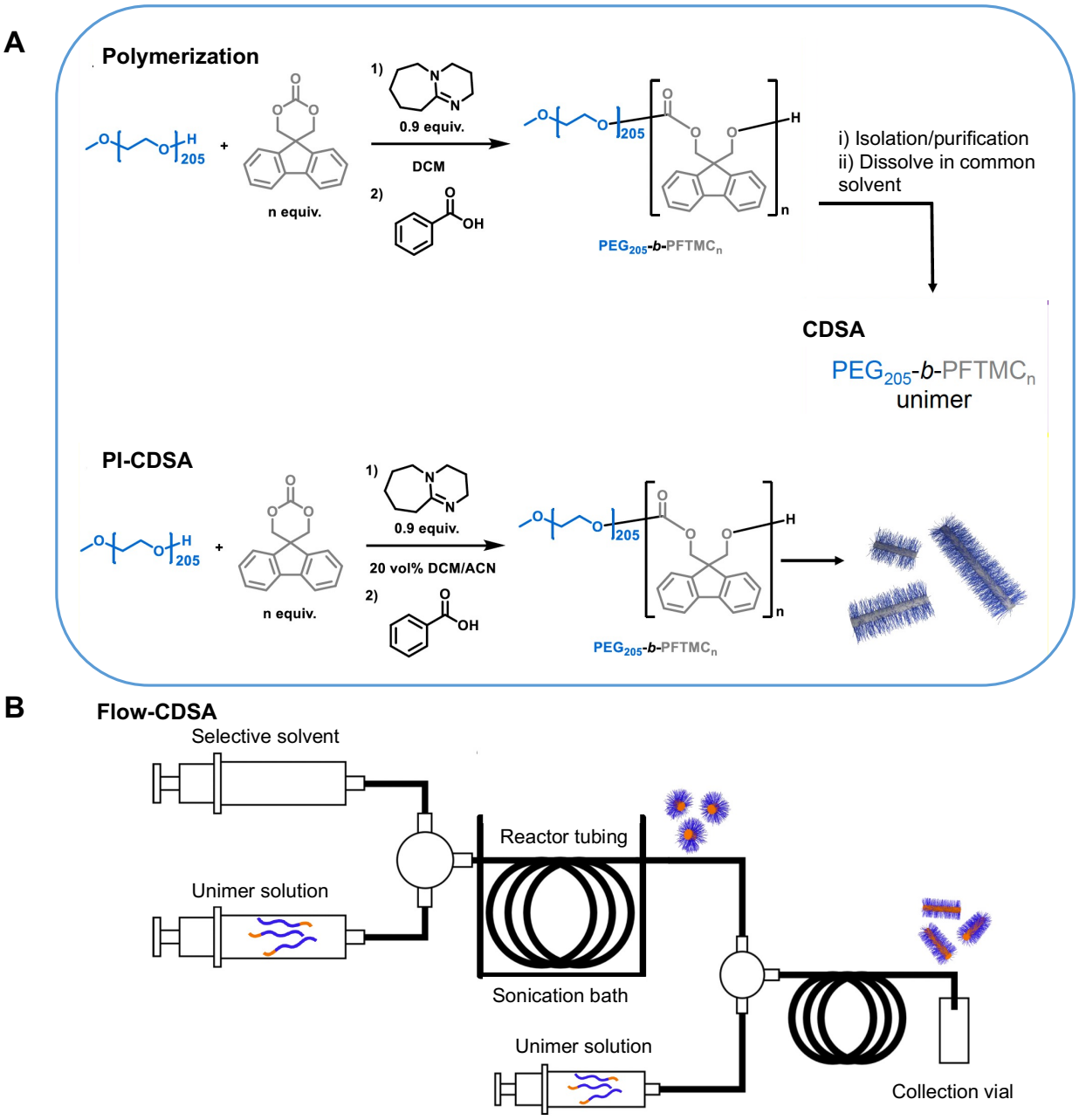


**Figure 6.3.** Two different approaches to scaled-up nanofiber production. (A) The PI-CDSA process is shown in contrast to traditional polymerization and subsequent living CDSA. In PI-CDSA, the ring opening polymerization and self-assembly occur in the same flask. As the core-forming block $DP_n$ increases, self-assembly of the core will occur. If this process takes place in the presence of pre-formed nanofiber seeds, the polymer will crystallize off the ends of the seeds

to yield morphologically pure and length-controlled nanofibers. (B) CDSA in flow is undergoing investigations for increased production of nanofibers. The unimer solution and selective solvent can be mixed in continuous flow to yield polydisperse nanofibers, which then immediately are sonicated. A second injection point can allow for the addition of further unimer solution to the seeds, generating length-controlled nanofibers at near continuous production rates and much higher concentrations.

## 6.2 Outlook

The results presented in this thesis have significantly advanced our fundamental knowledge on the biological properties of 1D polymer nanofibers prepared by living CDSA. The information obtained clearly showcases that anisotropic nanoparticles should be of great interest for biomedical applications, across a broad range of materials. Furthermore, we have demonstrated that understanding the mechanism of biological action is critical for learning how to design more active treatments. Finally, the work presented herein exemplifies living CDSA as a powerful tool for building modular nanoparticles that can be altered depending on the desired application, and represents a promising method for the generation of length-controlled, morphologically pure nanoparticles that are of increasing relevance for nanomedicine.

## 6.3 References


1. McAllister, M. S.; Krizanac-Bengez, L.; Macchia, F.; Naftalin, R. J.; Pedley, K. C.; Mayberg, M. R.; Marroni, M.; Leaman, S.; Stanness, K. A.; Janigro, D. Mechanisms of Glucose Transport at the Blood–Brain Barrier: An in Vitro Study. *Brain Res.* **2001**, *904*, 20–30. DOI: 10.1016/S0006-8993(01)02418-0.
2. Zhou, Y.; Peng, Z.; Seven, E. S.; Leblanc, R. M. Crossing the Blood-Brain Barrier with Nanoparticles. *J. Control. Rel.* **2018**, *270*, 290–303. DOI: 10.1016/J.JCONREL.2017.12.015.
3. Hyldgaard, M.; Mygind, T.; Vad, B. S.; Stenvang, M.; Otzen, D. E.; Meyer, R. L. The Antimicrobial Mechanism of Action of Epsilon-Poly-l-Lysine. *Appl. Environ. Microbiol.* **2014**, *80* (24), 7758. DOI: 10.1128/AEM.02204-14.
4. Mori, H.; Endo, T. Amino-Acid-Based Block Copolymers by RAFT Polymerization. *Macromol. Rapid Commun.* **2012**, *33* (13), 1090–1107. DOI: 10.1002/MARC.201100887.
5. Ortega, Á.; Zhulin, I. B.; Krell, T. Sensory Repertoire of Bacterial Chemoreceptors. *Microbiol. Mol. Biol. Rev.* **2017**, *81* (4), e00033-17. DOI: 10.1128/MMBR.00033-17.
6. Levine, A. J. P53, the Cellular Gatekeeper for Growth and Division. *Cell* **1997**, *88* (3), 323–331. DOI: 10.1016/s0092-8674(00)81871-1.
7. Hu, J.; Cao, J.; Topatana, W.; Juengpanich, S.; Li, S.; Zhang, B.; Shen, J.; Cai, L.; Cai, X.; Chen, M. Targeting Mutant P53 for Cancer Therapy: Direct and Indirect Strategies. *J. Hematol. Oncol.* **2021**, *14*, 1–19. DOI: 10.1186/S13045-021-01169-0.
8. Sulakvelidze, A.; Alavidze, Z.; Morris, J. Bacteriophage Therapy. *Antimicrob. Agents Chemother.* **2001**, *45* (3), 649. DOI: 10.1128/AAC.45.3.649-659.2001.

9. Egido, J. E.; Costa, A. R.; Aparicio-Maldonado, C.; Haas, P. J.; Brouns, S. J. J. Mechanisms and Clinical Importance of Bacteriophage Resistance. *FEMS Microbiol. Rev.* **2022**, *46* (1), 1–16. DOI: 10.1093/FEMSRE/FUAB048.
10. Kasman, L. M.; Porter, L. D. Bacteriophages. *Brenner's Encyclopedia of Genetics: Second Edition* **2022**, 280–283. DOI: 10.1016/B978-0-12-374984-0.00131-5.
11. Xiao, L.; Parkinson, S. J.; Xia, T.; Edge, P.; O'Reilly, R. K. Enhancing the Scalability of Crystallization-Driven Self-Assembly Using Flow Reactors. *ACS Macro Lett.* **2023**, *12* (12), 1636–1641. DOI: 10.1021/ACSMACROLETT.3C00600.
12. Ellis, C. E.; Garcia-Hernandez, J. D.; Manners, I. Scalable and Uniform Length-Tunable Biodegradable Block Copolymer Nanofibers with a Polycarbonate Core via Living Polymerization-Induced Crystallization-Driven Self-Assembly. *J. Am. Chem. Soc.* **2022**, *144* (44), 20525–20538. DOI: 10.1021/JACS.2C09715.